의학박사 학위논문

Translational Research on Blood-Retinal Barrier Breakdown in Diabetic Macular Edema and Age-related Macular Degeneration

당뇨망막병증 황반부종과 노인성 황반변성에서 망막혈액장벽 손상에 관한 중개연구

2017 년 8 월

서울대학교 대학원

의과학과 의과학전공

박 성 욱

A thesis of the Degree of Doctor of Philosophy

당뇨망막병증 황반부종과 노인성 황반변성에서 망막혈액장벽 손상에 관한 중개연구

Translational Research on Blood-Retinal Barrier Breakdown in Diabetic Macular Edema and Age-related Macular Degeneration

August 2017

The Department of Biomedical Sciences,

Seoul National University

College of Medicine

Sung Wook Park

Translational Research on Blood-Retinal Barrier Breakdown in Diabetic Macular Edema and Age-related Macular Degeneration

지도교수 김 정 훈

이 논문을 의학박사 학위논문으로 제출함

2017 년 4 월

서울대학교 대학원
의과학과 의과학전공
박 성 욱

박성욱의 의학박사 학위논문을 인준함
2017 년 7 월

위 원 장 _____ (인)
부위원장 _____ (인)
위 원 _____ (인)
위 원 _____ (인)
위 원 _____ (인)

Translational Research on Blood-Retinal Barrier Breakdown in Diabetic Macular Edema and Age-related Macular Degeneration

by

Sung Wook Park

A thesis submitted to the Department of Biomedical Sciences in partial fulfillment of the requirements for the Degree of Doctor of Philosophy in Medical Science at Seoul National University College of Medicine

July 2017

Approved by Thesis Committee:

Professor _____ **Chairman**

Professor _____ **Vice chairman**

Professor _____

Professor _____

Professor _____

ABSTRACT

Translational Research on Blood-Retinal Barrier Breakdown in Diabetic Macular Edema and Age-related Macular Degeneration

Sung Wook Park
Major in Biomedical Sciences
Department of Biomedical Sciences
Seoul National University Graduate School

Introduction: Diabetic retinopathy (DR) and age-related macular degeneration (AMD) are leading causes of blindness. In DR, macular edema (vascular leakage) and neovascularization (angiogenesis) cause severe vision loss. While neovascularization cause severe vision loss only in the later proliferative phase of DR, macular edema caused by vascular leakage can occur at any stage of DR and impair visual acuity. The two types of AMD are: dry and wet AMD. In wet AMD, new blood vessels (known as choroidal neovascularization) grow into the macula and damage the retina. Dry AMD is characterized by the presence of drusen and atrophy of the retinal pigment epithelium (RPE) cells.

For the treatment of DR, I focused on three cellular components of inner blood-retinal barrier (BRB); endothelial cells, pericytes, and astrocytes.

Especially, I aimed to investigate the role of Ang2 in pericyte loss and astrocyte loss in DR.

While laser-induced choroidal neovascularization has been extensively used in the studies of wet AMD, there is no single mouse model that fully recapitulates the cardinal features of human dry AMD. Here, I focused on the Aβ-related pathogenesis in dry AMD using 5XFAD mice and Aβ-injected mice. I investigated the mechanism of Aβ uptake via receptor for advanced glycation end product (RAGE) and the role of intracellular Aβ in autophagy dysfunction as a dry AMD pathogenesis.

Wet AMD is associated with retinal over-expression of, rather than mutations in, the *VEGFA* gene. RNA-guided genome surgery using CRISPR-Cas9 nucleases has shown promise for the treatment of diverse genetic diseases. Yet, the potential of such nucleases for therapeutic applications in non-genetic diseases is largely unexplored. Here, I used two genome editing tools; the preassembled, *Vegfa* gene-specific Cas9 ribonucleoproteins (RNPs) and the smallest Cas9 orthologue characterized to date, derived from *Campylobacter jejuni* (CjCas9) targeted to the *Vegfa* or *Hif1a* gene in RPE cells for the treatment of wet AMD.

Methods: In *in vivo* experiments, I used streptozotocin induced diabetic mice for DR study, 5XFAD mice and Aβ-injected mice for dry AMD study, and laser-induced choroidal neovascularization (CNV) mice for wet AMD study. In *in vitro* experiments, I performed cell viability assay, western blot, RT-PCR, flow cytometry, immunocytochemistry, ELISA, targeted deep

sequencing, and microarray, etc.

Results: Ang2 induced pericyte apoptosis under high glucose via α3β1 integrin/p53 pathway. Ang2 also induced astrocyte apoptosis under high glucose via αvβ5 integrin/GSK3β/β-catenin pathway. In addition, microglia derived-IL-6/STAT3 signaling in endothelial cell increased vascular leakage by attenuating tight junction proteins.

Intracellular Aβ contributed to dry AMD-like pathology in 5XFAD mice. RAGE-mediated p38 MAPK signaling contributes to endocytosis of Aβ in RPE. Intracellular Aβ induced breakdown of tight junction and autophagy dysfunction by lysosomal impairment.

Cas9 RNPs and CjCas9 effectively achieved *in vivo* genome editing in RPE cells. Both Cas9 RNPs and AAV/CjCas9 targeting *Vegfa* reduced the area of laser-induced CNV in a mouse model of wet AMD. Genome-wide profiling of Cas9 off-target effects via Digenome-seq showed that off-target mutations were rarely induced in the human genome.

Conclusions: Ang2/integrin signaling could be a potential therapeutic target to prevent pericyte loss and vascular leakage by astrocyte loss in DR. IL-6/STAT3 signaling is another therapeutic target to prevent vascular leakage in DR. Intracellular Aβ contributes to dry AMD pathogenesis. 5XFAD mice could be used a dry AMD mouse model. Targeting Aβ and modulating autophagy could be novel therapeutic approaches for the treatment of dry AMD. *In vivo* genome editing with Cas9 RNPs or CjCas9 has the potential for the local treatment for wet AMD, non-genetic degenerative diseases, expanding the scope of RNA-guided genome surgery to a new dimension.

* This work is based on published articles in Diabetes (1), Cell Death and Disease (2), Journal of Cellular Physiology (3), Neurobiology of Aging (4), Oncotarget (5, 6), Genome Research (7), and Nature Communications (8).

Keywords: Blood-retinal barrier, Retina, Age-related macular degeneration, Diabetic retinopathy, Diabetic macular edema, Pericyte loss, Vascular leakage, Angiogenesis, Antibody, Genome editing, Gene therapy

Student number: 2012-31158

CONTENTS

LIST OF TABLES AND FIGURES

General Introduction

Chapter 1

Chapter 2

Chapter 3

LIST OF ABBREVIATIONS

AAV, adeno-associated virus

Aβ, amyloid beta

AD, Alzheimer's disease

AMD, age-related macular degeneration

Ang, angiopoietin

BBB, blood-brain barrier

BM, Bruch's membrane

BRB, blood-retinal barrier

CFH, compliment factor H

CNV, choroidal neovascularization

Cas9, CRISPR associated protein 9

CRISPR, clustered regularly interspaced short palindromic repeats

crRNA, CRISPR RNA

DR, diabetic retinopathy

ELISA, enzyme-linked immunosorbent assay

FBS, fetal bovine serum

FITC, fluorescein isothiocyanate

GRGDS, glycine-arginine-glycine-aspartic acid-serine

GSK-3β, glycogen synthase kinase 3 beta

HIF, hypoxia-inducible factor

HRMEC, human retinal microvascular endothelial cell

IL-6, interleukin-6

MAPK, mitogen-activated protein kinase

MTT, 3-(4,5-dimethylthiazol-2-yl)-2,5-diphenyltetrazolium bromide

NG2, neural/glial antigen 2

NLS, nuclear localization signal

PAM, protospacer-adjacent motif

PBS, phosphate-buffered saline

PDGF, platelet derived growth factor

PE, phycoerythrin

pI, isoelectric point

RGD, arginine-glycine-aspartic acid

RPE, retinal pigment epithelium

RGEN, RNA-guided endonuclease

RNP, ribonucleoproteins

RT, room temperature

sgRNA, single-guide RNA

siRNA, small interfering RNA

STAT3, signal transducer and activator of transcription 3

STZ, streptozotocin

TEM, transmission electron microscope

tracrRNA, trans-activating crRNA

TUNEL, transferase-mediated dUTP nick-end labeling

VEGF, vascular endothelial growth factor

ZO-1, zonular occludens-1

GENERAL INTRODUCTION

The blood-retinal barrier (BRB) is composed of an inner BRB and an outer BRB. The outer BRB is the barrier formed at the retinal pigment epithelium (RPE) cells. The inner BRB is the barrier formed in retinal vessels. The BRB breakdown is closely related to the increase of vascular permeability as well as neovascularization in retinal diseases.

Diabetic retinopathy (DR) and age-related macular degeneration (AMD) are leading causes of blindness. In DR, macular edema (vascular leakage) and neovascularization (angiogenesis) cause severe vision loss. While neovascularization causes severe vision loss only in the later proliferative phase of DR, macular edema caused by vascular leakage can occur at any stage of DR and impair visual acuity. For the treatment of DR, I focused on three cellular components of inner blood-retinal barrier (BRB); endothelial cells, pericytes, and astrocytes. Especially, I aimed to investigate the role of Ang2 in pericyte loss and astrocyte loss in DR. Here, I demonstrated that Ang2 induced pericyte apoptosis under high glucose via α3β1 integrin/p53 pathway. Ang2 also induced astrocyte apoptosis under high glucose via αvβ5 integrin/GSK3β/β-catenin pathway. In addition, microglia derived-IL-6/STAT3 signaling in endothelial cell increased vascular leakage by attenuating tight junction proteins.

The two types of AMD are: dry and wet AMD. In wet AMD, new blood vessels (known as choroidal neovascularization) grow into the macula and damage the retina. Dry AMD is characterized by the presence of drusen and

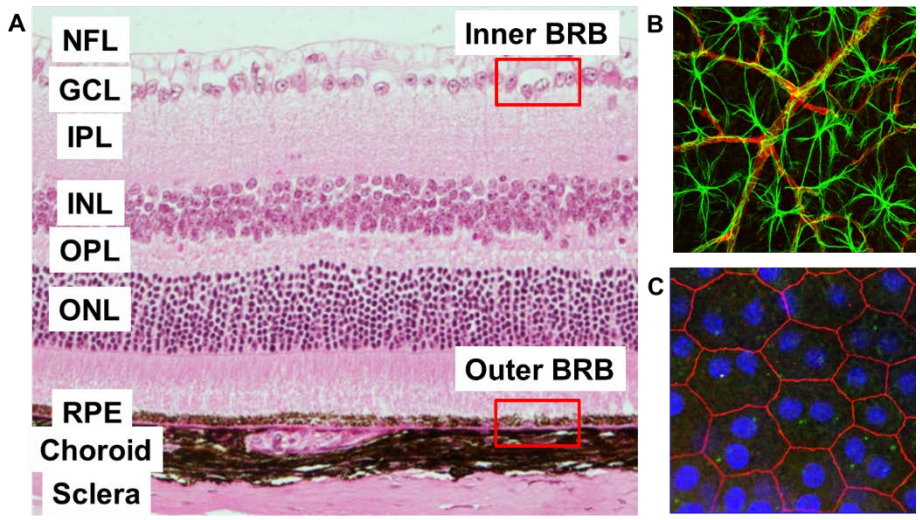

Figure 1. The blood-retinal barrier (BRB). (A) Cross-section of mouse retina. (B) Inner BRB is the barrier in the retinal vessels. (C) Outer BRB is the barrier formed at the retinal pigment epithelium (RPE) cells. NFL, nerve fiber layer; GCL, ganglion cell layer; IPL, inner plexiform layer; INL, inner nuclear layer; OPL, outer plexiform layer; ONL, outer nuclear layer; RPE, retinal pigment epithelium.

atrophy of the retinal pigment epithelium (RPE) cells. While laser-induced choroidal neovascularization (CNV) has been extensively used in the studies of wet AMD, there is no single mouse model that fully recapitulates the cardinal features of human dry AMD. Here, I focused on the Aβ-related pathogenesis in dry AMD using 5XFAD mice and Aβ-injected mice. I investigated the mechanism of Aβ uptake and the role of intracellular Aβ in autophagy dysfunction as a dry AMD pathogenesis. Intracellular Aβ contributed to dry AMD-like pathology in 5XFAD mice. RAGE-mediated p38 MAPK signaling contributes to endocytosis of Aβ in RPE. Intracellular Aβ induced breakdown of tight junction and autophagy dysfunction by lysosomal impairment.

Wet AMD is associated with retinal over-expression of, rather than mutations in, the *VEGFA* gene. RNA-guided genome surgery using CRISPR-Cas9 nucleases has shown promise for the treatment of diverse genetic diseases. Yet, the potential of such nucleases for therapeutic applications in non-genetic diseases is largely unexplored. Here, I used two genome editing tools; the preassembled, *Vegfa* gene-specific Cas9 ribonucleoproteins (RNPs) and the smallest Cas9 orthologue characterized to date, derived from *Campylobacter jejuni* (CjCas9) targeted to the *Vegfa* or *Hif1a* gene in RPE cells. Cas9 RNPs and CjCas9 effectively achieved *in vivo* genome editing in RPE cells. Both Cas9 RNPs and AAV/CjCas9 reduced the area of laser-induced CNV in a mouse model of wet AMD. Genome-wide profiling of Cas9 off-target effects via Digenome-seq showed that off-target mutations were rarely induced in the human genome.

Taken together, Ang2/integrin signaling could be a potential therapeutic target to prevent pericyte loss and vascular leakage by astrocyte loss in DR. IL-6/STAT3 signaling is another therapeutic target to prevent vascular leakage in DR. Intracellular Aβ contributes to dry AMD pathogenesis. 5XFAD mice could be used a dry AMD mouse model. Targeting Aβ and modulating autophagy could be novel therapeutic approaches for the treatment of dry AMD. *In vivo* genome editing with Cas9 RNPs or CjCas9 has the potential for the local treatment for wet AMD, non-genetic degenerative diseases, expanding the scope of RNA-guided genome surgery to a new dimension.

CHAPTER 1

Targeting Neurovascular Units to Treat Diabetic Retinopathy

INTRODUCTION

Diabetic retinopathy (DR) is the leading cause of the visual loss in working-aged people and the most common microvascular complication in the diabetic patients despite of the recent improvement in the management of DR via glycemic control and photocoagulation (9). Both the macular edema (vascular leakage) and neovascularization (angiogenesis) cause severe vision loss in DR (10). While neovascularization cause severe vision loss only in the later proliferative phase of DR, macular edema caused by vascular leakage can occur at any stage of DR and impair visual acuity (11).

Inner blood-retinal barrier (BRB) is composed of three cellular components; endothelial cells, pericytes, and astrocytes. I focused on these three cellular components regarding to the pathogenesis of DR (Figure 1-1). Firstly, I studied the mechanism of pericyte loss, the earliest characteristic change of DR. Secondly, I focused on the mechanism of astrocyte loss leading to vascular leakage. Thirdly, I directly studied endothelial cells with inflammation for vascular leakage.

In DR, a loss of pericyte is the earliest and most characteristic change of DR (12). Pericyte plays an important role in two major clinical reasons. First, pericyte enwraps endothelial cells to keep the integrity of inner BRB with the role of microvascular autoregulation (13). Thus, pericyte loss could weaken inner BRB even when endothelial cells are intact, and can lead to capillary instability as well as vascular leakage in macular edema. Second, microaneurysm and neovascularization occur in proliferating endothelial cells at the site of pericyte loss (14). As pericyte loss is an early diabetic change, it

would be beneficial to prevent pericyte loss for primary prevention of DR.

Although pericyte loss is an important phenotype in early DR, the mechanism by which hyperglycemia leads to pericyte loss remains largely unknown. Hyperglycemia causes pericyte apoptosis and ultimately pericyte loss (15-17). Angiopoietin 2 (Ang2) increases in vitreous of patients with proliferative DR (18). In addition, Ang2 is upregulated by hyperglycemia in diabetic retina and endothelial cells (19-21). Ang2 induces pericyte loss in normal mice retina and Ang2 overexpressing mice (19, 22). Thus, I postulated that hyperglycemia increases Ang2, which in turn induces pericyte apoptosis in DR.

The role of Ang2 in pericyte loss has been studied (19, 20, 22-24). Both apoptosis and migration are suggested mechanisms of pericyte loss by Ang2. However, the precise mechanism by which Ang2 induces pericyte loss has not been fully elucidated yet. Ang2 has been known to bind to the endothelial specific Tie-2 tyrosine receptor, with similar affinity to Ang1 (25). Ang2 acts as autocrine manner in the angiogenesis. This endothelial cell-derived antagonistic ligand of the vessel maturation and remodeling controls Ang1-Tie-2 signaling axis (26). Although it has been postulated that Ang2 naturally binds to Tie-2 receptor in pericyte as Ang-Tie system (20, 22), it is not clear whether Tie-2 indeed serves as a receptor for Ang2 induced pericyte loss. Recently, it was found that integrin mediates PDGF-BB-induced pericyte loss in tumor vessels (27). Also, Ang2 binds to integrin and regulates angiogenesis through integrin signaling (28). Thus, I hypothesized that Ang2 induces pericyte apoptosis via integrin signaling.

In the first part of chapter I, I demonstrated that Ang2 induced pericyte apoptosis via p53 pathway under high glucose. Interestingly, integrin, not Tie-2 receptor, was important for Ang2 induced pericyte apoptosis under high glucose. High glucose increased integrin α3β1 in pericyte. Furthermore, Ang2 induced pericyte apoptosis was effectively attenuated by blocking integrin α3β1 *in vitro* and *in vivo*. Taken together, Ang2 induced pericyte apoptosis via α3β1 integrin signaling in diabetic retinopathy.

In brain, the role of astrocyte as a component of neurovascular unit in the regulation of the blood-brain barrier (BBB) is well established. The perivascular endfeet of astrocyte contribute to the BBB features (29). In addition, astroglial-endothelial signaling regulates the BBB under pathological conditions (29, 30). Recently, retinal dysfunction in diabetes is explained by a subsequent change of the retinal neurovascular unit in terms of retinal pathophysiology (9, 31). However, the precise role of astrocyte in the regulation of the BRB in diabetic retina has not been elucidated.

In the retina, both astrocyte and Müller cell are involved in vascular ensheathment. However, astrocyte and Müller cell are affected by diabetes in different ways (32, 33). Although astrocyte is limited to the ganglion cell layer, astrocyte plays an important role in vessel integrity both via direct contact and through humoral factors (34, 35). In addition, astrocyte is closely related to the formation of tight junction in developing retina (36-38). Moreover, retinal astrocyte may decrease in number at sites where vessel is damaged with increased permeability of the BRB in pathologic conditions (32, 39-41). Thus, I focused on the role of astrocyte loss regarding to the vascular leakage in

diabetic retina.

In the first part of chapter I, Ang2 induces pericyte apoptosis via integrin signaling in diabetic retinopathy (1). Hyperglycemia-induced Ang2 has a central role in pericyte apoptosis by Ang2/α3β1 integrin/p53 signaling pathway in streptozotocin (STZ) induced diabetic mice. Local vascular leakage occurs early in the experimental diabetic mice even before the pericyte loss (31). In addition, Ang2 is upregulated by hyperglycemia in endothelial cells and diabetic retina (19-21). Moreover, Ang2 binds to integrin and regulates angiogenesis (28). In view of neurovascular unit, I postulated that Ang2 could affect astrocyte via integrin signaling before the pericyte loss in diabetic retina.

In the second part of chapter I, I provide evidence for the role of Ang2 induced astrocyte loss in vascular leakage in early diabetic retina. I demonstrate that Ang2 shows synergistic effects with high glucose on astrocyte apoptosis via GSK-3β/β-catenin pathway. Furthermore, I demonstrate both *in vitro* and *in vivo* that blocking αvβ5 integrin effectively attenuate Ang2 induced astrocyte apoptosis. Taken together, Ang2 induced astrocyte apoptosis via αvβ5 integrin signaling contributes to the vascular leakage in diabetic retina.

Among the three neurovascular components, endothelial cells are directly linked to vascular hyperpermeability under inflammatory microenvironment. In diabetic retina, various inflammatory cytokines are elevated (42-44). In addition, the tight junctions of endothelial cells play an important role to maintain vascular integrity. Vascular endothelial growth factor (VEGF),

originally known as vascular permeability factor, induces vascular hyperpermeability by down-regulating the tight junction proteins. Thus, anti-VEGF agents are used for the treatment of diabetic macular edema.

In the third part of chapter I, microglia-derived IL-6 under hyperglycemia contributes to retinal vascular hyperpermeability through downregulating tight junction proteins via endothelial STAT3 activation (3). Thus, IL-6/STAT3 signaling pathway could be a potential therapeutic target for the treatment of vascular leakage in DR.

MATERIALS AND METHODS

1. Cell cultures

Human umbilical vein endothelial cells (HUVECs, Lonza), human retina microvascular endothelial cells (HRMECs, ACBRI), human brain astrocytes (ACBRI), and human pericytes (Promo cell) were maintained in EBM-2, M199 medium, DMEM with 20% FBS, and pericyte media containing growth factors (Promo cell), respectively. A human microglial cell line, HMO6, was established by immortalizing primary microglia using a retroviral vector encoding v-ras (45), which carries morphologic and phenotypic features of primary human microglia (45, 46). All cells were cultured at 37℃ in an incubator with a humidified atmosphere of 95% O_2 and 5% CO_2.

2. Reagents and antibodies

Recombinant mouse and human Ang2, human integrin α3β1, human integrin αvβ5, phycoerythrin (PE)-conjugated anti- endothelial-specific receptor tyrosine kinase 2 (Tie-2) mouse IgG antibody, PE-conjugated anti-Tie-2 and mouse IgG antibodies, mouse Ang2 ELISA kit, mouse VEGF ELISA kit, human phospho-kinase array kit, anti-integrin αvβ3, anti-integrin αvβ5 (clone P5H9, MAB2528) neutralizing antibodies were purchased from R&D systems (Minneapolis, MN, USA); anti-ZO-1, anti-occludin antibodies, Invitrogen (Carlsbad, CA, USA); anti-Bcl-2 family antibodies, EPITOMICS (Burlingame, CA, USA); anti-phospho-p53, anti-PARP, anti-cleaved caspase-3, anti-integrin β1 antibodies, anti-phospho GSK-3β (Ser9), anti-phospho β-catenin, anti-β-catenin, anti-phospho-STAT3, anti-STAT3, and anti-PARP

antibody, Cell Signaling Technology (Beverly, MA, USA); anti-p53, anti-Tie1, peroxidase-conjugated secondary antibodies, Santa Cruz Biotechnology(Dallas, TX, USA); MTT (3-(4,5-dimethylthiazol-2-yl)-2,5-diphenyltetrazolium bromide), streptozotocin, and FITC-dextran (70 kD), Sigma-Aldrich (St. Louis, MO, USA); FITC-conjugated annexin V/propidium iodide assay kit, BD Biosciences (Franklin Lakes, NJ, USA); anti-NG2, anti-Ang2 antibodies, anti-GFAP, anti-integrin αv, β1, β3, β5, α3β1, and anti-Ang2 antibodies, Abcam (Cambridge, MA, USA); TUNEL fluorescein kit, Roche. Anti-Tie-2 antibody, H-Gly-Arg-Gly-Asp-Ser-OH (GRGDS) peptide, SB 216763, anti-integrin α1 (clone FB12, MAB1973), anti-integrin α3 (clone P1B5, MAB1952), anti-integrin β1 (clone 6S6, MAB2253), and α integrin blocking and IHC kit (α1-6, v) were purchased from Millipore (Billerica, MA, USA) and used for functional blocking. siRNAs for p53 were purchased from Bioneer (Daejeon, Korea). Anti-mouse Ang2 blocking antibody (Angy-2-1) was purchased from Adipogen (San Diego, CA, USA). Mouse Ang1 ELISA kit was purchased from MyBioSource (San Diego, CA, USA). Anti-Tie-1 and peroxidase-conjugated secondary antibodies were purchased from Santa Cruz Biotechnology (Dallas, TX, USA).

3. Animals

All animal experiments in this study were in strict agreement with the Association for Research in Vision and Ophthalmology Statement for the Use of Animals in Ophthalmic and Vision Research and the guidelines of the Seoul National University Animal Care and Use Committee. Six or eight-

week-old, pathogen-free male C57BL/6J mice were purchased from Central Lab. Animal Inc. After, 8 h fast, diabetes was induced by a single intraperitoneal injection of freshly prepared streptozotocin (STZ; Sigma) at a concentration of 180 mg/kg body weight in 10 mmol/l citrate buffer (pH 4.5). Age-matched controls received citrate buffer only. Mice with blood glucose levels > 300 mg/dl 4 days after STZ-injection were deemed diabetic. Diabetic and nondiabetic mice were killed 6 months after diabetes induction, and eyes were collected under deep anesthesia and immediately frozen at -80℃ for ELISA, or fixed in 4% paraformaldehyde for retinal digestion. Glucose levels and body weight were monitored consecutively, and glycated hemoglobin was determined before sacrifice.

4. Retinal digest preparations

Vascular preparations of whole-mount retinas were performed using a trypsin digestion technique. Briefly, after at least 24 h fixation in 4% paraformaldehyde, retinas were incubated in water for 1 h. Then, retinas were digested in 2.5% trypsin (Gibco) at 37℃ for 1 h. After removal of inner limiting membrane carefully, the retinal vessels were isolated by careful irrigation with filtered water. The retinal digest samples were dried and stained with periodic acid and Schiff base for 15 min and hematoxylin.

5. Morphological quantification of pericyte and acellular capillary

To determine numbers of retinal pericytes and acellular capillary, retinal digest preparations (n = 7-8) were analyzed. Pericytes were identified

according to the morphology and relative location to capillary. Total numbers of pericytes were counted in 10 randomly selected areas (magnification ×400) in the middle one-third of the retinal capillary area. Number of pericytes and acellular capillaries were standardized to the capillary area (numbers of cells or acellular capillaries per mm^2 capillary area). The capillary area was calculated using NIS-elements AR 3.2 program (Nikon). Samples were evaluated in a masked fashion.

6. Quantitative & qualitative assessment of the retinal vascular leakage

To determine vascular leakage, 3-week STZ-induced diabetic mice were used. Deeply anesthetized mice were intravenously injected with a FITC–dextran dissolved in PBS. After 1 h perfusion, the eyes were enucleated and fixed in 4% paraformaldehyde for 1 h. The retinas were dissected in 2× PBS, flat-mounted and viewed by a fluorescent microscope (Eclipse 90i, Nikon, Tokyo, Japan) at a magnification of ×40 and ×100.

To analyze vascular leakage quantitatively, the four representative sites of leakage at the mid peripheral retina (0.5 μm x 0.5 μm) per each mice were selected (n = 6-7). The mid peripheral retina was designated as the mid one third of the retina from optic nerve head to ciliary body. The images were imported into Image J (1.47v, NIH, USA); thereby, images were adjusted for color threshold based on the automatic isodata algorithm, and the interested area with FITC were marked with red. Then, the area of red was measured. The data were expressed as vascular leakage (%) which was normalized to those of control mice.

7. Quantification of retinal vascular leakage using Evans blue dye

For measuring retinal vascular leakage, mice were received 200 μL of Evans blue dye (20 mg/mL) in PBS by intracardiac injection. Mice were sacrificed 2 h after the injection and blood was sampled. Retinas were harvested, flat-mounted, and examined by fluorescence microscopy (BX61; Olympus, Japan). For quantitative analysis, retinas of both eyes were harvested and weighed. Evans blue was extracted in formamide (Sigma-Aldrich) solution. The concentration of the dye in the extracts was assessed by spectrophotometric measurements and calculated as outlined in (47).

8. Quantification of retinal vascular coverage by astrocyte

To determine the morphology & quantitative vascular coverage of retinal astrocyte, retinal flat-mounts were immunostained against GFAP for astrocyte and IB4 for vessel. The retinas were observed by a confocal microscope (Leica TCS STED, Leica Microsystems, Wetzlar, Germany). Briefly, the eyes were enucleated and fixed in 4% paraformaldehyde for 1 h. The retinas were dissected out in 2× PBS and incubated in the 100% methanol overnight at -20℃. Then, the retinas were blocked in Perm/Block solution (0.3% Triton-X and 0.2% BSA in PBS) for 1 h at room temperature. Then, the retinas were incubated with anti-GFAP antibody (1:100) and Alexa 594 conjugated anti-IB4 antibody (1:100) in Perm/Block solution overnight at 4℃. Then, the retinas were repeatedly washed with PBS and incubated with secondary antibody (1:200) for 1 h at room temperature. After washed with PBS, the

retinas were mounted with Fluoromount™ Aqueous Mounting Medium (Sigma Aldrich). The representative site of astrocyte loss at the mid peripheral retina per each mice were selected (n = 6-8). The morphology of astrocyte was analyzed with maximal projection images of z-stack (magnification ×400). For the analysis of the vascular coverage by astrocyte, the colocalized area of astrocyte and retinal vessel was divided by the area of retinal vessel (astrocyte coverage = colocalized area / vascular area). The colocalized area was calculated by using the Leica Application Suite Advanced Fluorescence (LAS AF) software (Leica Microsystems; Threshold and background values are 30% and 20%, respectively). The images were imported to Imaris software (Ver.7.6.5, Bitplane), and analyzed for the vascular area. Then, the vascular coverage by astrocyte was normalized to that of control (Relative astrocyte coverage %).

9. Intravitreal injection of Ang2 and anti-integrin antibodies

One microliters containing 100 ng of Ang2 and 500 ng of anti-integrin α3 (clone P1B5) or anti-integrin β1 (clone 6S6) was injected intravitreally under deep anesthesia. Sterile PBS was injected for control. After 10 days, retinas were subjected to digestion preparation.

One microliter containing 1 μg of anti-Ang2 neutralizing antibody and 1 μg of anti-integrin αvβ5 antibody (clone P5H9) was injected intravitreally under deep anesthesia at 2 weeks after diabetes induction with streptozotocin. Sterile PBS was injected for control. After 7 days of injection, retinas were subjected to the retinal flat-mount for the vascular leakage and/or astrocyte analyses.

10. Transferase-mediated dUTP nick-end labeling (TUNEL) assay and immunofluorescence.

Retinal digestion preparations were incubated with anti-rabbit NG2 antibody (1:100) and TUNEL fluorescein kit. Nuclei were counter stained with 4', 6-Diamidino-2-Phenylindole (DAPI). TUNEL and NG2-double positive cells were evaluated with a fluorescence microscope (Nikon, Tokyo, Japan).

11. Cell viability assay.

In all experiments, 2.5×10^4 cells were seeded into 96-well plates. After 24 h, cells were treated with Ang1 (300 ng/mL), Ang2 (300 ng/mL) under normal glucose (5 mM glucose), high glucose (25 mM glucose), and high mannitol (5 mM glucose plus 20 mM mannitol) as an osmotic control for 48 h. Cell viability was determined by MTT assay according to the manufacturer's instructions. Three independent experiments were performed for each experimental condition.

12. FACS analysis

In order to evaluate the apoptosis, 5×10^5 cells were treated with Ang2 (300 ng/mL) under normal glucose, high mannitol, and high glucose at 37℃ for 48 h. To determine the effect of integrin blocking, anti-integrin blocking antibodies (5 or 10 μg/mL) was treated 1 h before the addition of Ang2. The cells were harvested and washed two times in PBS. Cells were stained with FITC annexin-V and PI for 15 min, and analyzed by flow cytometry. Annexin

V positive/PI negative cells were determined to apoptotic.

In order to evaluate Tie-2 expression, pericytes and HUVECs (1×10^6 cells) were suspended in the complete media (25 μL) for each experiment. PE-conjugated anti-Tie2 antibody was added to the each sample at 4℃ for 1 h. PE-conjugated mouse IgG antibody was used as a control.

13. Quantitative RT-PCR

All RNA was collected and isolated from cells using RNeasy Plus Mini kit (Qiagen). cDNAs were prepared from RNAs (1 μg) using 2.5 μM oligo-dT primers, 1mM dNTPs, and MuLV reverse transcriptase. qPCR assays were performed in qPCR mastermix for SYBR Green PCR Master MIX (Applied Biosystems) using 7900HT real-time PCR (Applied Biosystems). Reaction conditions were 50 cycles of 95℃ for 5 s and 60℃ for 20 s for qPCR. Quantitative real-time PCR was performed using the following primers: Ang2 (forward: 5'-ACTGTGTCCTCTTCCACCAC-3'and reverse: 5'-GGATGTTTAGGGTCTTGCTTT-3'); Tie-2 (forward: 5'-GCTTGCTCCTTTCTGGAACTGT-3' and reverse: 5'-CGCCACCCAGAGGCAAT-3') (48); Tie-1 (forward: 5'-AGAACCTAGCCTCCAAGATT-3' and reverse: 5'-ACTGTAGTTCAGGGACTCAA-3'); ITGA1 (forward: 5'-GGTTCCTACTTTGGCAGTATT-3' and reverse: 5'-AACCTTGTCTGATTGAGAGCA-3'); ITGA3 (forward: 5'-AAGGGACCTTCAGGTGCA-3' and reverse: 5'-TGTAGCCGGTGATTTACCAT-3'); ITGAV(forward: 5'-

AATCTTCCAATTGAGGATATCAC-3’ and reverse: 5’-AAAACAGCCAGTAGCAACAAT-3’); ITGB1(forward: 5’-GAAGGGTTGCCCTCCAGA-3’ and reverse: 5’-GCTTGAGCTTCTCTGCTGTT-3’); ITGB3 (forward: 5’-CCGTGACGAGATTGAGTCA-3’ and reverse: 5’-AGGATGGACTTTCCACTAGAA-3’); ITGB5 (forward: 5’-GGAGCCAGAGTGTGGAAACA-3’ and reverse: 5’-GAAACTTTGCAAACTCCCTC-3’); ITGB8 (forward: 5’-AATTTGGTAGTGGAAGCCTATC-3’ and reverse: 5’-GTCACGTTTCTGCATCCTTC-3’); β-actin (forward: 5’-GCCGCCAGCTCACCAT-3’ and reverse: 5’-TCGATGGGGTACTTCAGGGT-3’). A mean quantity was calculated from triplicate qPCR for each sample and it was normalized to the control gene.

For Tie-2 RT-PCR, different primers were used as following (Forward: 5’-TGTTCCTGTGCCACAGGCTG-3’ and reverse: 5’-CACTGTCCCATCCGGCTTCA-3’). PCR products were separated on 1% agarose gels and visualized using SYBR® Safe DNA gel stain (Invitrogen) under UV transillumination.

Total RNA was isolated from retina using TRI Reagent (Molecular Research Center, Cincinnati, OH, USA) according to the manufacturer’s instructions. cDNA was prepared with High Capacity RNA-to-cDNA kit (Life Technologies). Real-time PCR was performed with StepOnePlus Real-Time PCR System (Life Technologies) with TaqMan Fast Advanced Master Mix (Life Technologies) and specific Gene Expression Assays (cat. no.: 4331182;

Life Technologies). Product IDs of Gene Expression Assays for genes are as follows: for *Angpt1*, Mm00456503_m1, for *Angpt2*, Mm00545822_m1, for *Vegfa*, Mm00437306_m1, and for *Rn18s*, Mm03928990_g1. All procedures were performed in accordance with the MIQE guidelines.

14. Immunoprecipitation and immunoblotting

For immunoprecipitation of Ang2-integrin α3β1 complex, Ang2 (500 ng), integrin α3β1 (500 ng), and anti-integrin α3β1 antibodies (2 μg) were incubated with G-sepharose beads at 4℃ overnight (19). Immune complexes were collected by centrifugation and washed with buffer 3 times.

For immunoprecipitation of Ang2-integrin αvβ5 complex, Ang2 (500 ng) and integrin αvβ5 (500 ng) were precleared with G-sepharose beads at 4℃ for 1 h. Then, the complex and anti-integrin αvβ5 antibody (2 μg) were incubated with G-sepharose beads at 4℃ overnight. The immune complexes were collected by centrifugation and washed with buffer 3 times.

For immunoblotting, cells were harvested and lysed in RIPA buffer with a protease inhibitor cocktail. Protein lysates were resolved by SDS polyacrylamide gel and transferred onto nitrocellulose membrane. The membranes were incubated with primary antibodies (1:1,000) at 4℃ overnight and secondary antibodies (1:5,000-10,000) at room temperature for 1 h. The membranes were incubated with enhanced chemiluminescent substrate (Pierce) and exposed to film or LAS 4000 (GE healthcare, Piscataway, NJ, USA).

15. ELISA

Two retinas from mice were pooled (n = 6 per each group). Samples including retina, vitreous, and lens were homogenized and lysed with brief sonication in 500 μL RIPA buffer with a complete protease inhibitor cocktail (Roche). After centrifugation at 12,000 rpm for 20 min, supernatants were collected. Ang1, Ang2 and VEGF levels were measured using ELISA kits according to the manufactures' instructions. The protein concentration was measured using a BCA protein assay kit (Pierce, Rockford, IL, USA). Ang1 (ng), Ang2 (pg), and VEGF levels (pg) were standardized to the retina protein (mg).

The cell culture supernatants were harvested and centrifuged at 12,000 rpm to remove the cellular debris. The IL-6 protein levels were measured by using a Human IL-6 Quantikine ELISA kit (R&D Systems) according to the manufacturer's instruction.

16. Trans-endothelial permeability assay

The trans-endothelial permeability assay was performed (49). Briefly, the cells were cultured on transwell plates for 3 days. Then, the HRMECs were exposed to the indicated reagents. For the co-cultures, HMO6 cells were plated into the bottom chamber. To evaluate endothelial permeability, Evans blue dye (Sigma-Aldrich) with bovine serum albumin was added into the inserted upper chamber. After 10 min, the optical density of the medium in the lower chamber was measured using spectrophotometry (Infinite M200PRO, Tecan, Switzerland). To inhibit the IL-6 activity, a neutralizing antibody against IL-6 (5 μg/mL; R&D Systems, Minneapolis, MN, USA) was added to

the cultures. To inhibit STAT3 phosphorylation, WP1066 (Selleck Chemicals, Houston, TX, USA), an inhibitor of JAK2, which is responsible for STAT3 phosphorylation, was added at a concentration of 2 μM.

17. Chromatin immunoprecipitation assay

Chromatin immunoprecipitation (ChIP) was performed by using the ChIP Assay Kit (Millipore, MA) according to the manufacturer's instruction. Soluble chromatin samples were immunoprecipitated with anti-STAT3 antibody (Cell Signaling Technology) and IgG for control at 4°C overnight. The immunoprecipitated DNAs were analyzed by quantitative PCR analysis using the SYBR Green PCR Master Mix. The sequences of the PCR primers for ZO-1, occludin, and VEGF promoters are listed (3). The amplification with control primers was used as a negative control.

18. Statistical Analysis

Statistical analyses were performed using the standard two-tailed Student's *t*-test assuming unequal variances and 1-way ANOVA and post-hoc test with Bonferroni's multiple comparison for multiple groups, respectively (SPSS statistics 20.0). $P < 0.05$ was considered statistically significant. Quantitative data are given as mean ± SD. Figures are depicted as mean ± SEM.

RESULTS

The number of retinal capillary pericyte is decreased in the diabetic mice retina

The numbers of the pericyte and the acellular capillaries in retinal digestion were compared between mice with 6-month STZ-induced diabetes and age-matched nondiabetic control mice (Figure 1-1A). The number of retinal capillary pericyte was significantly decreased in the STZ-induced diabetic mice retina (932.6 ± 70.3) compared to that of the control group (1341.8 ± 55.9, $P < 0.001$) (Figure 1-1B). On the other hand, the number of retinal acellular capillary was significantly increased in the STZ-induced diabetic mice retina (93.0 ± 22.5) compared to that of the control group (28.1 ± 11.5, $P < 0.001$) (Figure 1-1C). Table 1-1 shows the metabolic and physical parameters of the experimental groups.

Ang2 is increased in diabetic retina and the source of Ang2 could be endothelial cells

The effect of hyperglycemia on Ang2 expression in STZ-induced diabetic retina was evaluated by qRT-PCR. In diabetic retinas at 6 months, *Angpt2* mRNA increased 1.87 fold compared to non-diabetic normal retina ($P = 0.004$) (Figure 1-2A). Also, *Angpt1* mRNA and *Vegfa* mRNA increased 2.54 fold ($P = 0.004$) and 1.6 fold ($P = 0.027$), respectively (Figure 1-3).

Next, to determine the source of Ang2 in diabetic retina, I examined the effects of high glucose on *in vitro ANGPT2* mRNA transcription by qRT-PCR

Table 1-1. Metabolic and physical parameters of the STZ-induced diabetic and age-matched non diabetic control mice at 6 months.

	Non-diabetic	Diabetic	*P*-value
Body weight (g)	32.46 ± 3.22	18.97 ± 0.69	< 0.001
Blood glucose(mmol/L)	10.11 ± 1.48	32.83 ± 1.34	< 0.001
HbA1c (%)	5.33 ± 0.88	8.90 ± 1.10	< 0.001
HbA1c (mmol/mol)	34.75 ± 9.74	73.75 ± 11.95	

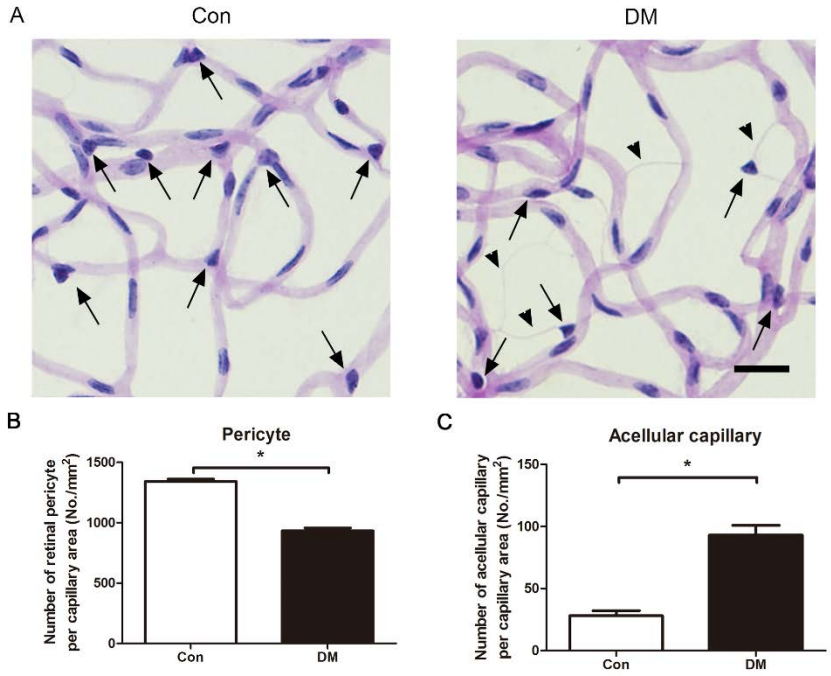

Figure 1-1. The number of retinal capillary pericyte is decreased in the diabetic mice retina. Pericytes were identified in retinal digest preparations by morphologic criteria (shape, staining intensity, and relative position in the capillary), and quantitated in 6 month streptozotocin (STZ) induced diabetic mice and age-matched controls. (A) Representative examples of retinal digest preparations of nondiabetic and diabetic mice after 6 months of diabetes are shown. Arrows indicate pericytes. Arrowheads indicate acellular capillaries. (B and C) The number of pericytes (B) and acellular capillaries (C) were normalized to the area of capillaries (mm^2) in which they were counted. A: periodic acid-Schiff (PAS) and hematoxylin-stained retinal digest preparations; original magnification ×400. Scale bar = 20 μm. B and C: n = 8 mice in each group. Bar graph represents mean ± SEM, Student's *t*-test: *$P < 0.01$.

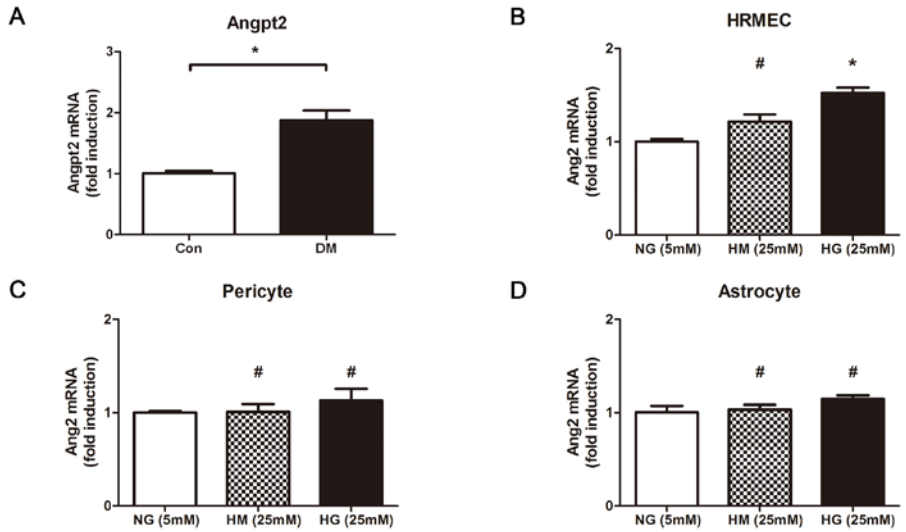

Figure 1-2. Ang2 is increased in diabetic retina and the source of Ang2 could be endothelial cells. (A) *Angpt2* mRNA level was determined in 6 month streptozotocin (STZ)-induced diabetic mice retina by qRT-PCR and normalized to *Rn18s* mRNA. Ang2 expression increased in 6 month STZ-induced diabetic mice retina. (B-D) *ANGPT2* mRNA transcription is induced by high glucose in HRMEC (B), not in pericyte (C) or astrocyte (D). HREMC, pericyte, and astrocyte were incubated for 48 h under 25 mM high glucose and 20mM mannitol + 5mM glucose, as an osmotic control. *ANGPT2* mRNA transcription were assessed by qRT-PCR. Actin was used as an internal control. *ANGPT2* mRNA levels were normalized to *ACTIN* mRNA and reported as fold induction compared to cells exposed to 5mM glucose. A: n = 6 mice in each group. Bar graph represents mean ± SEM, Con; age-matched normal mice, DM; streptozotocin induced diabetic mice. Student's *t*-test: $*P < 0.01$, $\#P > 0.05$.

in three major components of blood retinal barrier: HRMEC, pericyte, and astrocyte. In HRMEC, high glucose increased *ANGPT2* mRNA level more than 1.5-fold (1.52 ± 0.09, $P = 0.003$) compared with normal glucose (Figure 1-2B). On the other hand, high mannitol, an osmotic control, did not increase *ANGPT2* mRNA (1.21 ± 0.13, $P = 0.094$) in HRMEC (Figure 1-2B). Also, high glucose did not increase *ANGPT2* mRNA in pericyte (1.13 ± 0.22, $P = 0.418$) and astrocyte (1.13 ± 0.22, $P = 0.418$), respectively (Figure 1-2C and D). These data demonstrate that Ang2 increases in diabetic retina and the source of an Ang2 increase is retinal microvascular endothelial cells.

Ang2 plays synergistic role in pericyte apoptosis under high glucose condition

I determined the effect of Ang2 on the cell viability and apoptosis of pericyte under high glucose. Ang2 alone did not affect cell viability in pericyte (97.6 ± 3.6%, $P = 0.221$). High glucose reduced cell viability in pericyte (89.4 ± 7.9%, $P = 0.020$) (Figure 1-4A). Interestingly, Ang2 aggravated cell death under high glucose in pericyte (72.4 ± 2.9%, $P = 0.002$) (Figure 1-4A). Next, pericyte apoptosis was assessed by annexin-V/PI flow cytometric analysis. Of importance, the number of apoptotic pericyte was increased under high glucose (7.7 ± 0.3%, $P < 0.001$) compared that of the control group (2.4 ± 0.4%). Furthermore, high glucose induced pericyte apoptosis was significantly aggravated by Ang2 (25.9 ± 0.4%, $P < 0.001$) while Ang2 alone did not induced apoptosis (2.7 ± 0.1%, $P = 0.298$) under normal glucose (Figure 1-4B).

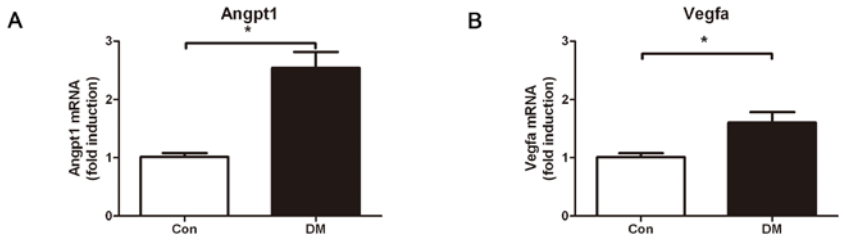

Figure 1-3. *Angpt1* and *Vegfa* mRNA expression in diabetic retina. *Angpt1* and *Vegfa* mRNA in 6 month streptozotocin-induced diabetic mice retina were assessed by qRT-PCR and normalized to *Rn18s* mRNA. n = 6 mice in each group. Bar graph represents mean ± SEM, Con; age-matched normal mice, DM; 6 month streptozotocin-induced diabetic mice, Student's *t*-test: $*P < 0.01$.

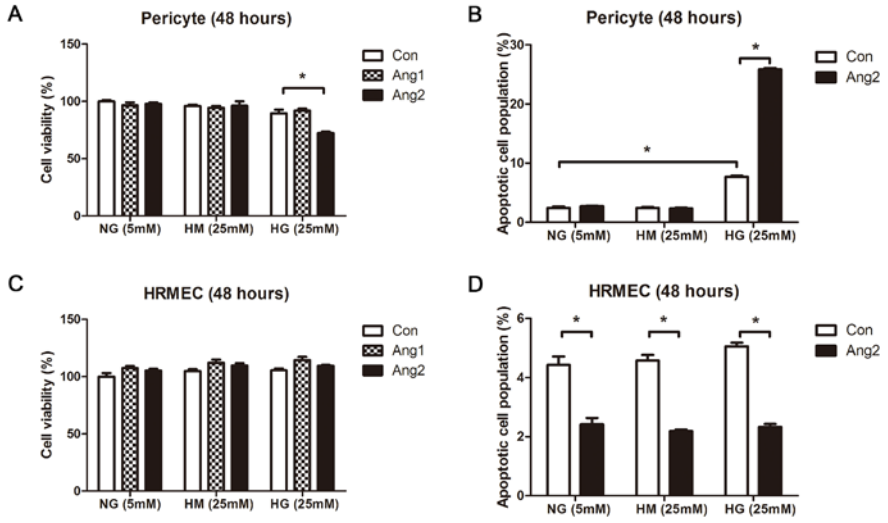

Figure 1-4. Ang2 plays synergistic role in pericyte apoptosis under high glucose condition. The effects of Ang2 on the cell viability and apoptosis of pericyte and HRMEC under high glucose condition were determined. Both pericyte and HRMEC were incubated for 48 h with/without Ang1 (300 ng/mL) or Ang2 (300 ng/mL) under high glucose (25 mM). (A, C) Cell viability was assessed by MTT assay. Ang2 induced cell death under high glucose in pericyte (A), but not in HRMEC (C). (B, D) Pericyte and HRMEC were stained with annexin-V FITC and propidium iodide and analyzed by flow cytometry. Cell apoptosis was expressed as the percentage of apoptotic cells in total cell populations. (B) High glucose induced pericyte apoptosis and Ang2 aggravated that apoptosis. (D) Ang2 showed protective effect on HRMEC apoptosis. Bar graph represents mean ± SEM of three independent experiments. NG; 5mM glucose, HM; 5mM glucose + 20mM mannitol, HG; 25mM glucose. Student's *t*-test: $*P < 0.01$.

Next, I determined the effect of Ang2 on the cell viability and apoptosis of HRMEC under high glucose condition. Ang1 and Ang2 increased cell viability in HRMEC under high glucose (114.4 ± 8.8%, P = 0.014, and 109.5 ± 2.3%, P = 0.040, respectively) (Figure 1-4C). As expected, apoptotic cell population was significantly decreased by Ang2 in HRMEC (Figure 1-4D). These data suggested that Ang2 plays synergistic role in pericyte apoptosis under high glucose condition and protective effect on endothelial cell.

Ang2 induces pericyte apoptosis via the p53 pathway under high glucose condition

Western blot studies confirmed that Ang2 induced apoptosis pathway with increase of Bax, cleaved PARP, and cleaved caspase-3 under high glucose, but not under normal glucose (Figure 1-5A). Next, I aimed to identify the mechanism that mediates Ang2 induced pericyte apoptosis under high glucose. I found that Ang2 induced p53 phosphorylation (Figure 1-5B) and subsequently p53 accumulation (Figure 1-5C) under high glucose. Then, to determine the role of the p53 pathway for the observed Ang2–mediated pericyte apoptosis, I treated pericytes with either control siRNA or two different p53 siRNAs. The p53 siRNAs effectively down-regulated p53 expression (Figure 1-5D), and they also attenuated Ang2 induced pericyte apoptosis under high glucose (Figure 1-5E). Interestingly, Ang2 phosphorylated ERK, but not Akt (Figure 1-5F). This ERK phosphorylation by Ang2 was inhibited by PD98059 (ERK inhibitor), and ERK inhibitor attenuated Ang2 induced p53 phosphorylation (Figure 1-5G). These data

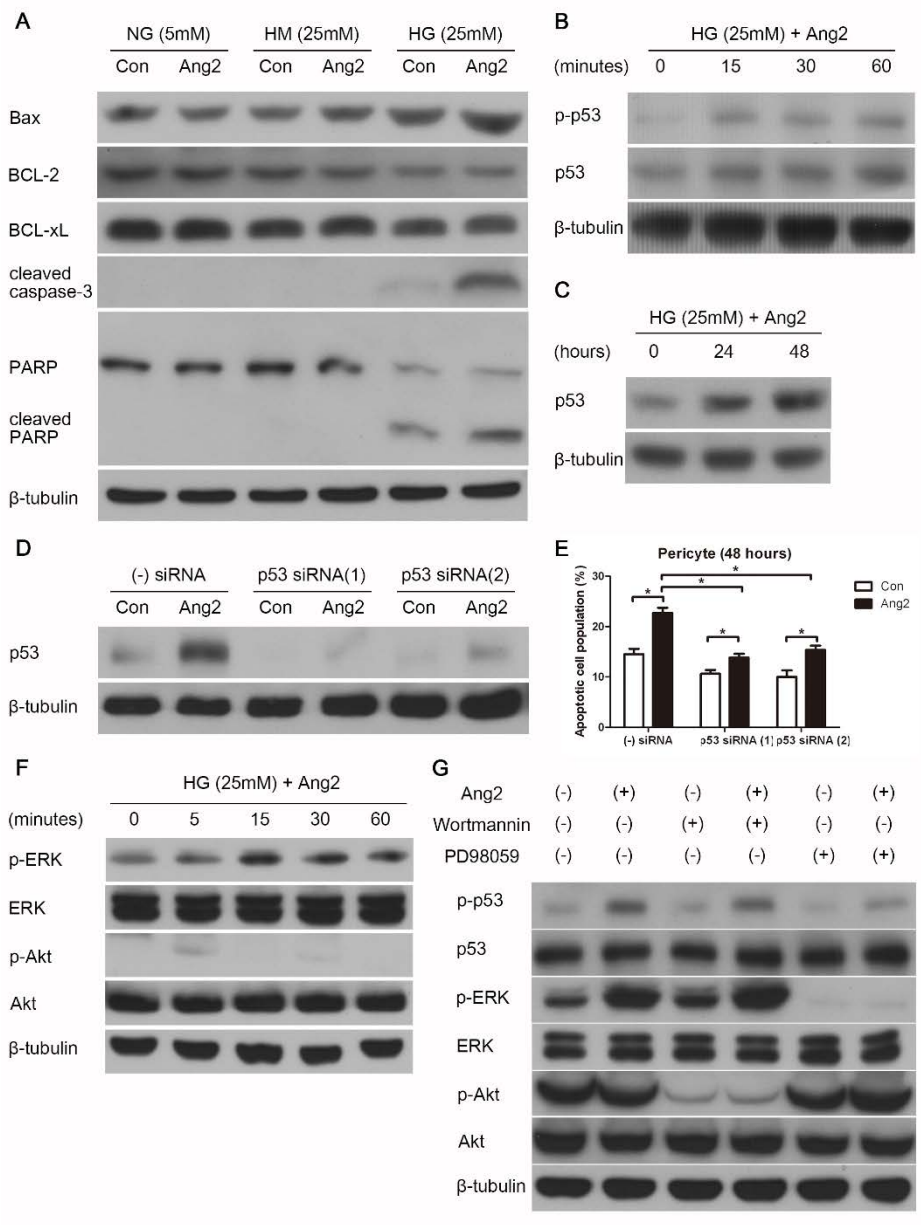

Figure 1-5. Ang2 induces pericyte apoptosis via the p53 pathway under high glucose condition. (A) Western blot analysis for Bax, Bcl-2, Bcl-xL, cleaved caspase-3, and cleaved PARP were performed on lysates obtained from pericyte treated with Ang2 (300 ng/mL) under 5mM glucose, 5mM

glucose + 20mM mannitol, and 25 mM glucose for 48 h. (B) Western blot analysis for phospho-p53 (Ser15) was performed on lysates obtained from pericyte treated with Ang2 for 15, 30, and 60 min under 25 mM high glucose. (C) Western blot analysis for p53 was performed on lysates obtained from pericyte treated with Ang2 for 24 and 48 h under 25 mM high glucose. (D) After the pericytes transfection with either control siRNA or p53 siRNA, western blot analysis for p53 was performed on cell lysates with Ang2 for 48 h under 25 mM high glucose. β-tubulin was used as a loading control. Data represent three independent experiments. (E) Apoptotic cell counts were assessed by FACS analysis 48 h after Ang2 treatment in siRNA transfected pericytes. Bar graph represents mean ± SEM of three independent experiments. Student's *t*-test: $*P < 0.01$. (F) Ang2 was treated for 5, 15, 30, and 60 min under 25mM high glucose. Phospho-ERK, ERK, phosphor-Akt, and Akt were determined by western blot. (G) Pericytes were pre-incubated with either Wortmannin (1 μM) or PD98059 (20 μM) for 1 h, and treated with Ang2 for 15 min under high glucose. Phospho-p53, p53, phospho-ERK, ERK, phosphor-Akt, and Akt were determined by western blot. . β-tubulin was used as a loading control.

suggest that Ang2 induces pericyte apoptosis via the p53 pathway under high glucose condition.

Integrin, not Tie-2, is important for Ang2 induced pericyte apoptosis under high glucose as an Ang2 receptor

To determine whether Tie-2 receptor is related with Ang2 induced pericyte apoptosis, western blot analysis (Figure 1-6A) and RT-PCR (Figure 1-6B) for Tie-2 and Tie-1 were performed on lysates obtained from HUVEC and pericyte. Interestingly, pericyte did not express Tie-2 or Tie-1 while HUVEC expressed Tie-2 and Tie-1. These data were confirmed by quantitative RT-PCR. *TIE2* mRNA and *TIE1* mRNA levels were significantly lower in pericyte than HUVEC (Figure 1-6C). Compared to HUVEC with Tie-2 expression, pericyte did not express Tie-2 in FACS analysis (Figure 1-6D).

To test whether or not integrins may serve as receptors for Ang2 in pericyte apoptosis under high glucose, I incubated pericyte under high glucose for 15 min with Ang2 and GRGDS peptides, which can inhibit integrins that bind RGD sequence (50). GRGDS (0.5 mg/mL attenuated Ang2 induced p53 phosphorylation (Figure 1-6D). This result showed that integrin signaling is involved in Ang2 induced p53 phosphorylation. Of importance, these data suggested that integrin, not Tie-2, is important for Ang2 induced pericyte apoptosis under high glucose as an Ang2 receptor.

High glucose increases integrin α1, α3, and β1 in pericyte.

As shown in Figure 1-4C and Figure 1-6E, Ang2 induced pericyte

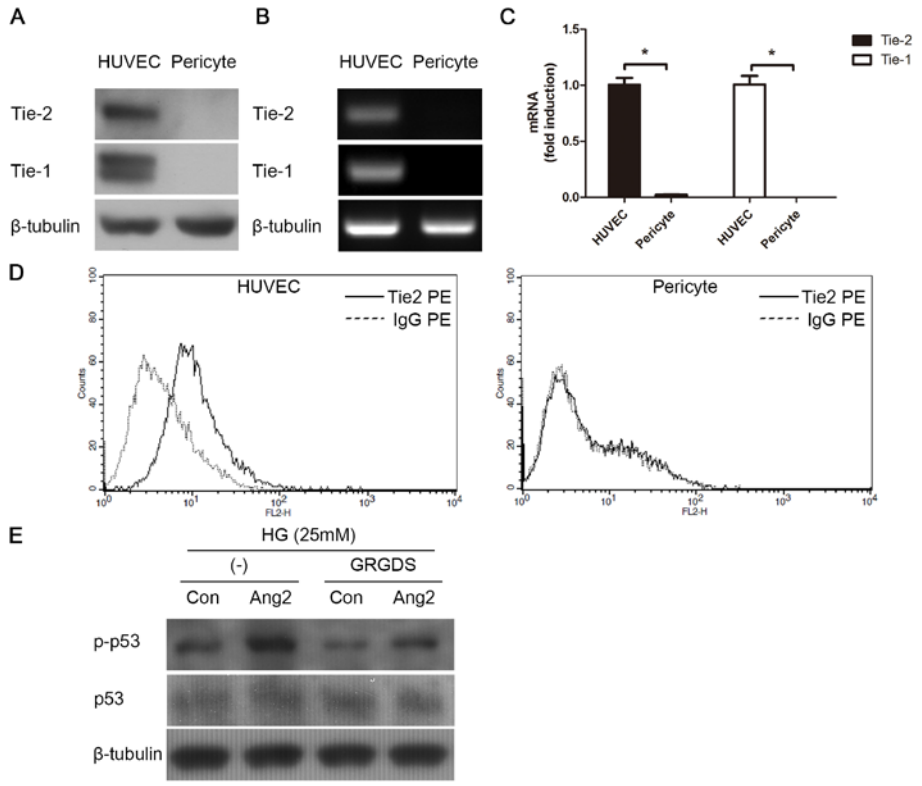

Figure 1-6. Integrin, not Tie-2, is important for Ang2 induced pericyte apoptosis under high glucose as an Ang2 receptor. Western blot (A) and RT-PCR (B) for Tie-2 and Tie-1 expression were performed on lysates obtained from HUVEC and pericyte. β-tubulin was used as an internal control. (C) *TIE2* and *TIE1* mRNA transcriptions were assessed by quantitative RT-PCR. Actin was used as an internal control. *TIE2* (C) and *TIE1* (D) mRNA levels were normalized to *ACTIN* mRNA and reported as fold induction compared to HUVEC. (D) Both HUVEC and pericyte were analyzed by flow cytometry for Tie-2 expression. (E) Western blot analysis for phospho-p53 (ser15) and p53 were performed on lysates obtained from pericyte treated with Ang2 (300 ng/mL) or RGDS (0.5 mg/mL) under 25 mM high glucose for

15 min. β-tubulin was used as a loading control. Data represent three independent experiments.

apoptosis via integrin receptor under high glucose, but not under normal glucose. I hypothesized that high glucose preconditioned pericyte susceptible to Ang2 by changing the integrin pattern. To determine which integrin subunit is responsible for Ang2 induced pericyte apoptosis, I screened the integrin α subunits (α1-6 and αv). Integrin α1 and α3 blocking antibodies attenuated Ang2 induced p53 phosphorylation (Figure 1-7A).

Next, to determine whether high glucose changes the integrin expression pattern, I performed quantitative RT-PCR and western blot studies for α1, α3, and β1. The choice was made because integrin α1, α3 can form the heterodimer with only integrin β1 (51). High glucose increased *ITGα1* (1.86-fold and 2.20-fold, $P < 0.01$) (Figure 1-7B), *ITGα3* (1.50-fold, 1.83-fold, $P < 0.01$) (Figure 1-7C), and *ITGβ1* (1.50-fold, 1.43-fold, $P < 0.01$) (Figure 1-7D) mRNA levels for 24 h and 48 h, respectively. In addition, high glucose increased integrin α1, α3, and β1 expression (Figure 1-7E). However, the integrin α1 was rarely expressed compared to integrin α3. In this regard, I performed co-immunoprecipitation assay to show direct binding of Ang2 to integrin α3β1. Indeed, Ang2 directly bound to integrin α3β1 (Figure 1-7F).

Ang2 induced pericyte apoptosis is inhibited by suppression of integrin α3β1

From the result of integrin expression in pericyte under high glucose, integrin α1β1 or α3β1 were supposed to be the possible receptor of Ang2. To determine whether Ang2 induced pericyte apoptosis through integrin α1β1 or α3β1, pericyte was incubated under 25 mM high glucose with Ang2 and anti-

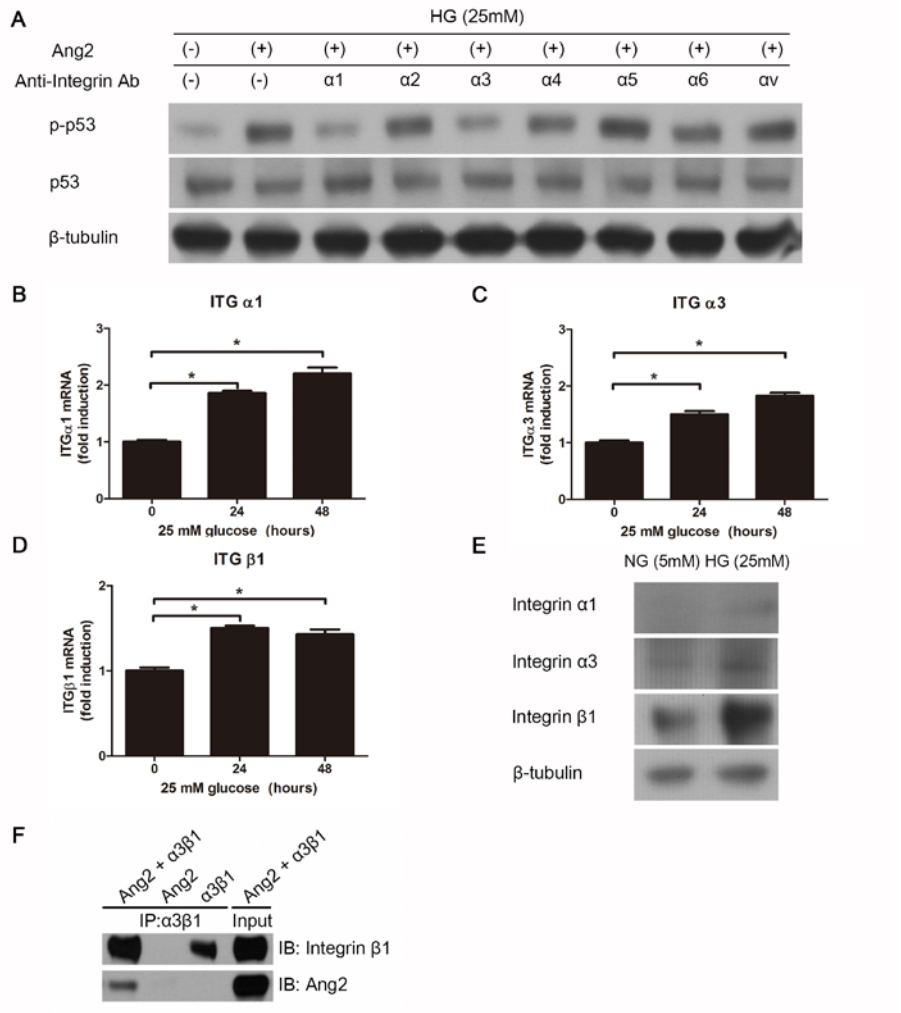

Figure 1-7. High glucose increases integrin α1, α3, and β1 in pericyte. (A) Western blot analysis for phospho-p53 (Ser15) and p53 were performed on lysates obtained from pericyte treated with Ang2 (300 ng/mL) or various integrin blocking antibodies (5 μg/mL, α1, α2, α3, α4, α5, α6, and αv) under 25 mM high glucose for 15 min. β-tubulin was used as a loading control. Data represent three independent experiments. (B-D) Pericyte were incubated under 25 mM high glucose for 24 and 48 h. *ITGα1* (B), *ITGα3* (C), and *ITGβ1* (D) mRNA transcriptions were assessed by quantitative RT-PCR. Actin was

used as an internal control. *ITGα1*, *ITGα3*, and *ITGβ1* mRNA levels were normalized to *actin* mRNA and reported as fold induction compared to control. (E) Western blot analysis for integrin α1, α3, and β1 were performed on lysates obtained from pericyte incubated under 25 mM high glucose for 48 h. β-tubulin was used as a loading control. Data represent three independent experiments. Student's *t*-test: $*P < 0.01$. (F) After incubation of Ang2 (500 ng), integrin α3β1 (500ng), and integrin α3β1 antibody, immune complexes were co-immunoprecipitated to show direct binding of Ang2 to integrin α3β1. Then, they were analyzed for Ang2 and integrin β1. Same amounts of recombinant Ang2 and integrin α3β1 were used as an input.

integrin α1, α3, and β1 antibodies for 48 h. Interestingly, Ang2 induced pericyte apoptosis under high glucose was attenuated by anti-integrin α3 and β1 antibodies, not by anti-integrin α1 antibody (Figure 1-8A). These results were confirmed for p53 expression on western blot analysis (Figure 1-8B). Ang2 significantly increased p53 expression under high glucose (2.7 ± 0.2, $P < 0.01$), but it was significantly attenuated by anti-integrin α1, α3, and β1 antibodies (1.5 ± 0.2, 1.0 ± 0.1, and 0.7 ± 0.1, respectively, $P < 0.01$).

On the basis of *in vitro* experiments, I next intravitreously injected 100 ng Ang2 with/without 500 ng anti-α3 or 500 ng anti-β1 antibodies to normal mice. Ten days after intravitreal injection, the isolated retinae were digested with trypsin for pericyte evaluation (Figure 1-8C). *In vivo*, intravitreal injection of Ang2 induced pericyte loss in the retina compared to that in PBS injected control mice (1047 ± 52 and 1401 ± 109 cells/mm^2, $P < 0.001$). Ang2 induced pericyte loss was significantly attenuated by anti-α3 or anti-β1 antibodies (1354 ± 148 and 1380 ± 66 cells/mm^2, $P < 0.001$) (Figure 1-8D). In addition, Ang2 induced TUNEL and NG2 double positive pericytes were decreased in anti-α3 or anti-β1 antibodies injected mice (Figure 1-8E). These *in vivo* data suggest that Ang2 induced pericyte loss via apoptotic mechanism in retina. Overall, these data demonstrated that integrin α3 and β1 important for Ang2 induced pericyte apoptosis via p53 pathway.

Retinal astrocyte loss occurs with retinal vascular leakage in early diabetic mice

To determine whether retinal astrocyte coverage to retinal vessel is attenuated

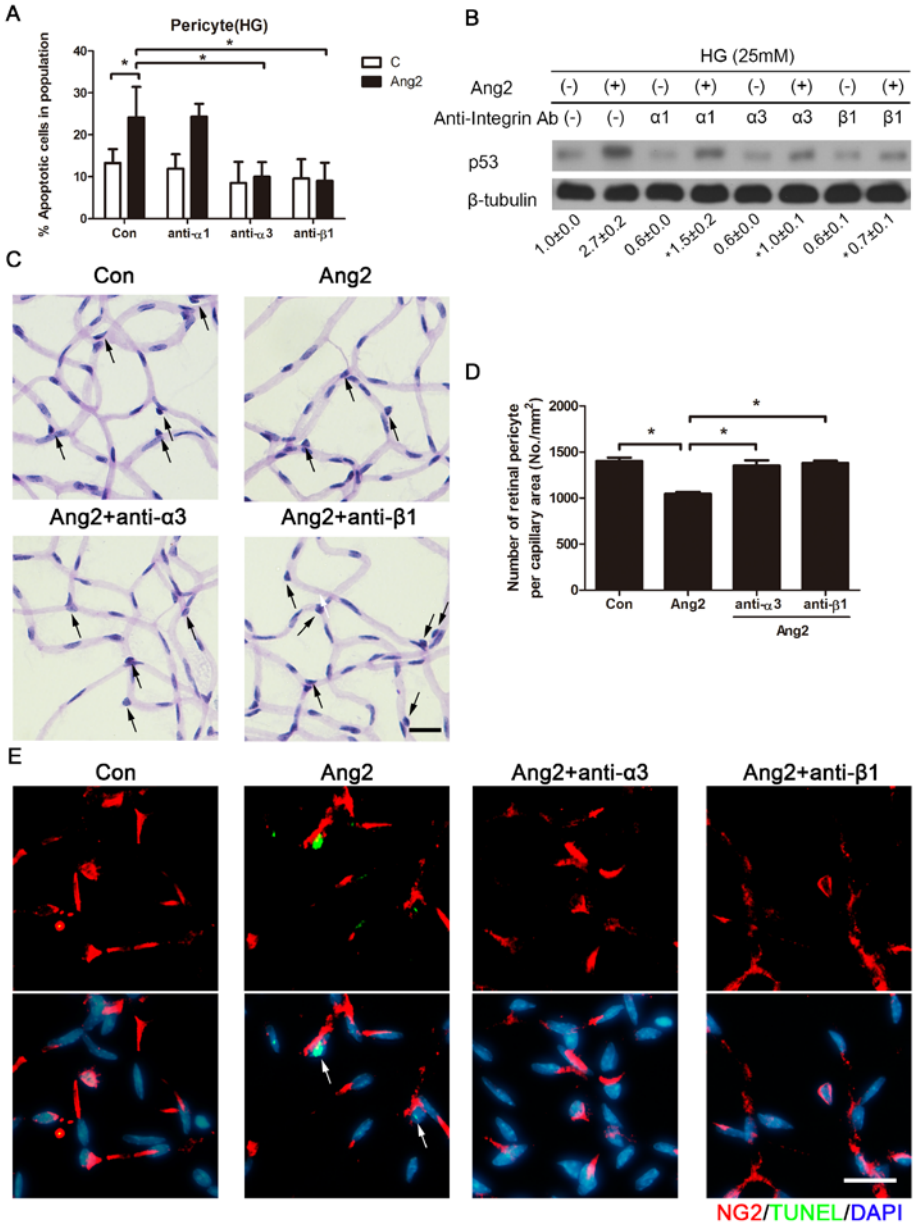

Figure 1-8. Ang2 induced pericyte apoptosis is inhibited by suppression of integrin α3β1. (A, B) Pericyte was incubated under 25 mM high glucose with Ang2 (300 ng/mL) and anti-integrin α1, α3, and β1 antibodies (5 μg/mL) for 48 h. (A*)* Pericyte apoptosis was analyzed by FACS and expressed as the

percentage of apoptotic cells in total cell populations. (B) Western blot analysis for p53 was performed on lysates obtained from pericyte. β-tubulin was used as a loading control. Data represent three independent experiments. (ImageJ quantitation; n = 3, mean ± SD, 2-tailed Student's *t*-test, $*P < 0.01$ compared to Ang2 treatment.) (C) Ang2 (100 ng) with/without anti-α3 or anti-β1 antibodies (500 ng) were intravitreously injected to normal mice. Ten days after intravitreal injection, eyes were enucleated and the isolated retinae were digested with trypsin for pericyte evaluation. Pericytes were identified in periodic acid-Schiff (PAS) and hematoxylin-stained retinal digest preparations by morphologic criteria. Representative examples of retinal digest preparations are shown. Arrows indicate representative pericytes. (D) The number of pericytes was normalized to the area of capillaries (mm^2) in which they were counted. (E) Retinal digest preparations were immunostained with NG2 (red), TUNEL (green), and DAPI (blue). White arrows indicate TUNEL positive pericytes. C and E: original magnification ×400. Scale bar = 20μm. C: n = 8 mice in each group. Bar graph represents mean ± SEM, Student's *t*-test: $*P < 0.01$.

in diabetic mice retina, I performed immunohistochemistry in retinal flat-mounts of diabetic mice. Retinal vascular coverage by GFAP labeled astrocyte was evaluated in 3 weeks of STZ-induced diabetes and age-matched non-diabetic control mice. Intriguingly, focal loss of astrocyte coverage to retinal vessel was observed in diabetic retina (Figure 1-9A). The relative astrocyte coverage to retinal vessel (42.0 ± 6.4%) was significantly decreased in the diabetic retina compared to that of the control retina (100.0 ± 5.4%, $P < 0.001$; Figure 1-9B). The retinal vascular leakage was also evaluated with fluorescein isothiocyanate (FITC)-dextran. The retinal vascular leakage (196.5 ± 7.1%) was significantly increased in the diabetic retina compared to that of the control retina (100.0 ± 16.0%, $P < 0.001$; Figure 1-9C). In early diabetic mice, retinal astrocyte loss occurred with increase of retinal vascular leakage.

Inhibition of Ang2 reduces astrocyte loss and vascular leakage in early diabetic retina

To determine which growth factor is linked to increased vascular leakage and astrocyte loss in early diabetic retina, I performed ELISA for retinal VEGF and Ang1/2. Retinal Ang2 level was increased at 1 and 3 weeks after diabetic induction (from 88.9 ± 1.3 pg/mg to 98.11 ± 2.2 and 102.7 ± 4.6 pg/mg, respectively, $P = 0.018$ by 1 way-ANOVA). With post-hoc test, retinal Ang2 at 3 weeks was significantly increased compared to control ($P = 0.017$). However, retinal VEGF and Ang1 levels were not significantly changed up to 3 weeks after diabetic induction. In qPCR in diabetic mice (up to 7 weeks after diabetic induction), *Ang2* and *Ang1* mRNA was significantly elevated

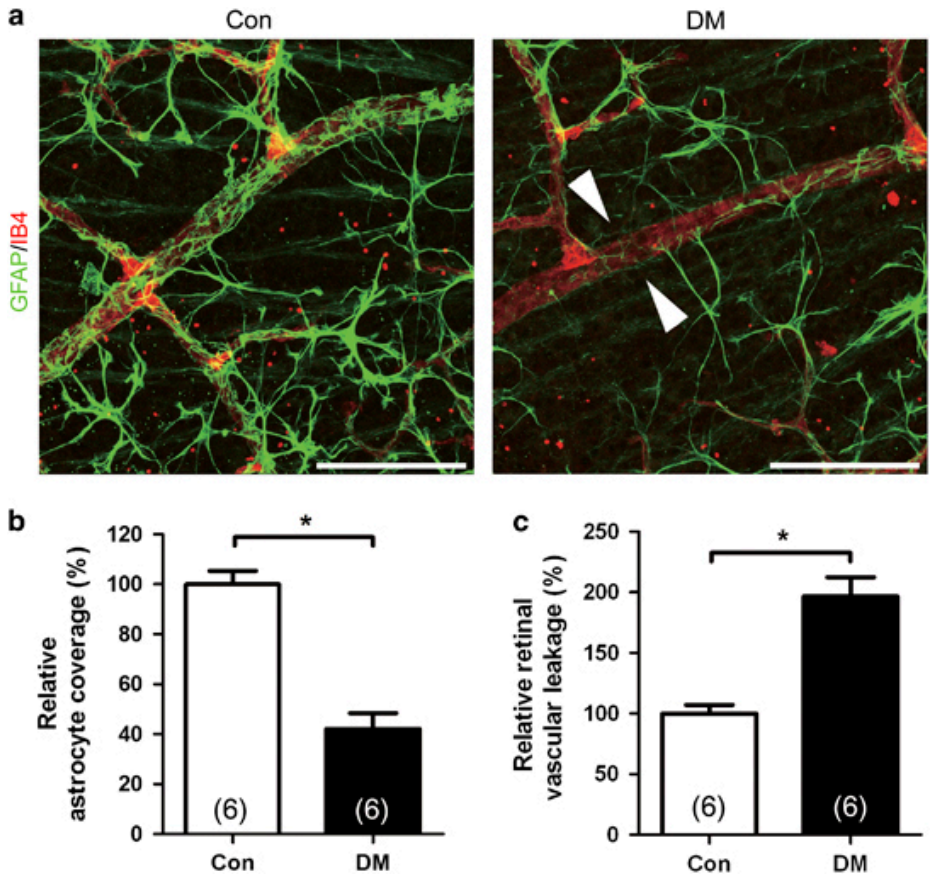

Figure 1-9. Retinal astrocyte loss occurs with retinal vascular leakage in early diabetic mice. Retinal vascular leakage and distribution of astrocyte were evaluated in 3 week streptozotocin-induced diabetic mice (DM) and age-matched controls (Con). (A) Representative site of focal astrocyte loss in mid peripheral retina is shown in diabetic retina (original magnification ×400; scale bar = 100 μm). White arrowheads indicate loss of astrocytes on diabetic retinal vessels. (B) Relative astrocyte coverage (colocalized area of astrocyte and vessel / vascular area) is shown and normalized to the value of control mice. (C) Retinal vascular leakage with FITC-dextran (70 kD) is evaluated and relative retinal vascular leakage (%) of diabetic retina is shown

normalized to the value of control mice. The sample size for each group is indicated on the bar graph. The bar graphs represent mean ± SEM, *$P < 0.01$ by Student's *t*-test.

after 3 weeks (Figure 1-10A and B). However, *Vegfa* mRNA was significantly increased after 5 weeks. (Figure 1-10C). The physical and metabolic parameters of the mice used in ELISA and qPCR were shown in Figure 1-10G. To explore the possibility that the increased vascular leakage was due to the astrocyte loss by Ang2, I injected Ang2 blocking antibody in diabetic mice at 2 weeks after STZ injection. The retina of anti-Ang2 blocking antibody injected mice showed increased astrocyte coverage (349.3 ± 49.8%) compared to the loss of astrocyte coverage in PBS injected diabetic mice ($P < 0.05$; Figure 1-10D and E). In addition, anti-Ang2 blocking antibody attenuated vascular leakage (72.4 ± 6.3%) compared to the vascular leakage in PBS injected diabetic retina ($P < 0.05$; Figure 1-10F). These findings suggested that astrocyte loss by Ang2 was associated with retinal vascular leakage and it could contribute to retinal vascular leakage in the STZ-diabetic mice.

Ang2 synergistically induces astrocyte apoptosis with high glucose

To determine the effect of Ang2 on cell viability of astrocyte *in vitro*, I performed MTT assay and fluorescence-activated cell sorting (FACS) analysis. Ang2 leads to pericyte death under high glucose condition (1). Similarly, it aggravated astrocyte cell death under high glucose (76.8 ± 2.2% from 85.5 ± 3.3%, $P < 0.05$; Figure 1-11A). Next, I examined whether astrocyte cell death is mediated by apoptotic pathway. Indeed, Ang2 induced apoptosis pathway with increase of Bax and cleaved poly ADP ribose polymerase (PARP) under high glucose (Figure 1-11B). Then, astrocyte apoptosis was assessed by

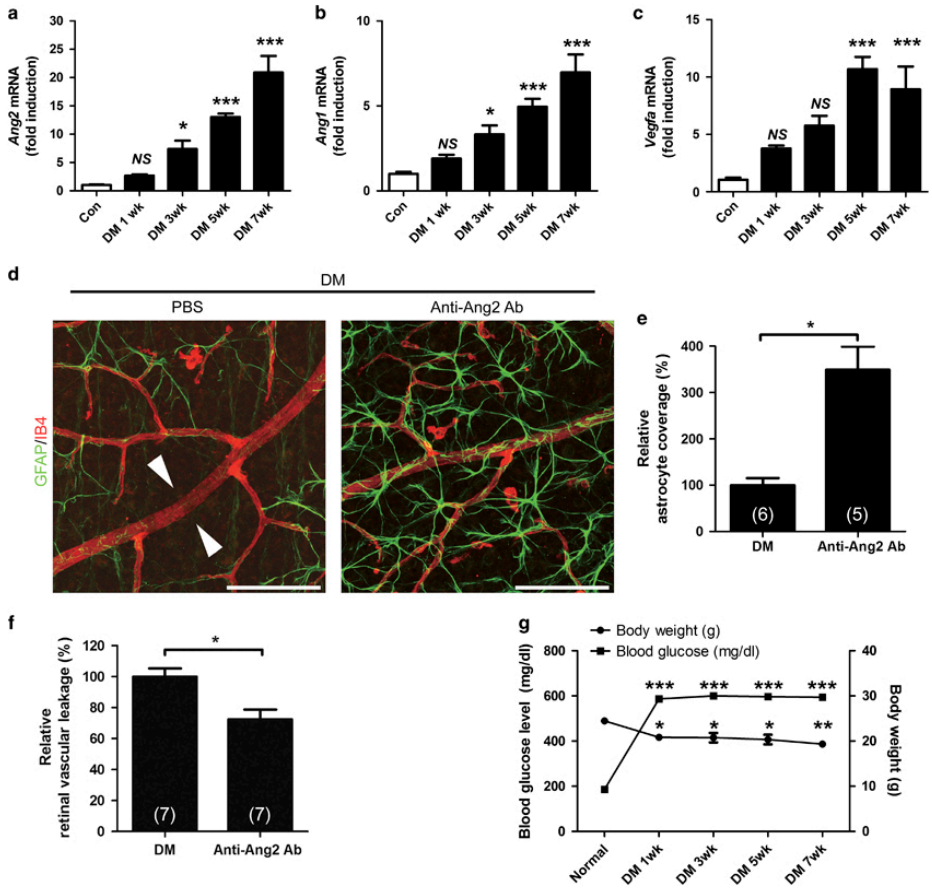

Figure 1-10. Inhibition of Ang2 reduces the astrocyte loss and vascular leakage in early diabetic retina. (A-C) Retinal mRNA was determined in 1, 3, 5, and 7 weeks from streptozotocin-induced diabetic mice (DM) and control mice (Con) retinas by qPCR, and normalized to Rn18s mRNA. (A) *Ang2* mRNA. (B) *Ang1* mRNA. (C) *Vegfa* mRNA. (D-F) Anti-Ang2 neutralizing antibody (Anti-Ang2 Ab, 1 μg) or PBS was intravitreally injected to 2 week DM mice. Retinal astrocyte and retinal vascular leakage were evaluated 1 week after the injection in 3 week DM mice. (D) Focal astrocyte loss shown in diabetic retina (PBS) is rescued in anti-Ang2 Ab injected

diabetic mice (original magnification ×400; scale bar = 100 μm). White arrowheads indicate loss of astrocytes on diabetic retinal vessels. (E) Relative astrocyte coverage (%; Anti-Ang2 Ab) is calculated by colocalized area per IB4+ vascular area and normalized to the value of control mice. (F) Relative retinal vascular leakage (%; Anti-Ang2 Ab) with FITC-dextran is shown normalized to the value of control mice. The sample size for each group is indicated on the bar graph. The bar graphs represent mean ± SEM, $*P < 0.05$, $**P < 0.01$, $***P < 0.001$ by ANOVA and Student's *t*-test.

annexin-V/propidium iodide (PI) FACS analysis. Ang2 increases apoptotic cell population regardless of the glucose level. Of importance, high glucose induced astrocyte apoptosis was significantly aggravated by Ang2 (32.6 ± 4.4% from 18.0 ± 2.6%, $P < 0.05$; Figure 1-11C). These data suggested that Ang2 induced astrocyte apoptosis especially under high glucose condition.

Ang2 induces astrocyte apoptosis via GSK-3β/β-catenin pathway under high glucose

I aimed to identify the mechanism that mediates Ang2 induced astrocyte apoptosis under high glucose. While astrocytes were incubated for 48 h under high glucose, Ang2 (300 ng/mL) was treated for the indicated time period. I found that Ang2 induced GSK3β activation by de-phosphorylation of GSK-3β (Ser9) and β-catenin phosphorylation (Figure 1-12A), which in turn, leaded to β-catenin degradation under high glucose (Figure 1-12B). Then, to determine the role of the GSK-3β/β-catenin pathway for the observed Ang2–mediated astrocyte apoptosis, I treated astrocyte with GSK3β inhibitor (SB216763, 10 μM, 1 h pretreatment). Inhibition of GSK-3β reduced Ang2 induced β-catenin phosphorylation at 30 min (Figure 1-12C), and subsequent β-catenin degradation at 48 h (Figure 1-12D). As expected, inhibition of GSK-3β effectively attenuated Ang2 induced astrocyte apoptosis under high glucose (13.4 ± 0.8% from 27.8 ± 3.2%, $P < 0.05$; Figure 1-12E). These data suggested that Ang2 induced astrocyte apoptosis via GSK-3β/β-catenin pathway under high glucose condition.

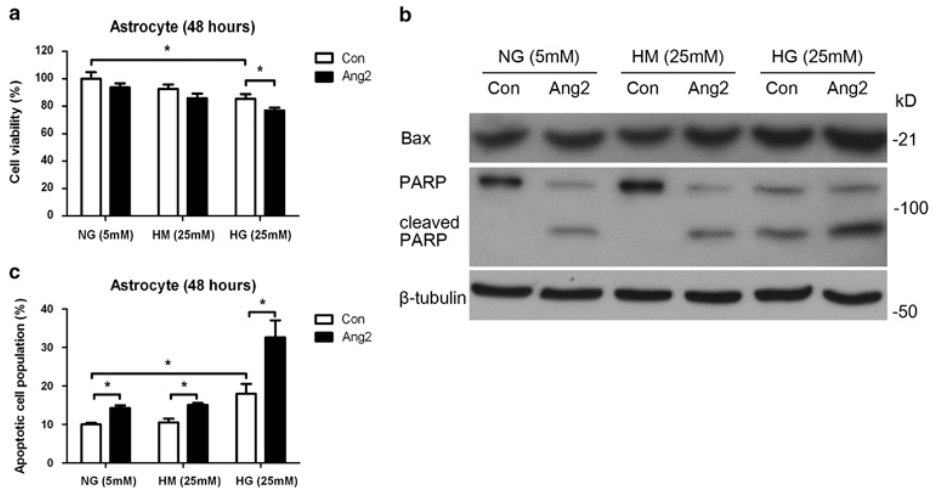

Figure 1-11. Ang2 synergistically induces astrocyte apoptosis with high glucose. The effects of Ang2 on the cell viability and apoptosis of astrocyte under high glucose (HG; 25 mM glucose) condition were determined. Astrocytes were incubated for 48 h with Ang2 (300 ng/mL) under HG and compared with control (Con). (A) Cell viability was assessed by MTT assay. (B) Western blot analysis for Bax and cleaved PARP were performed. β-tubulin was used a loading control. (C) Astrocytes were stained with annexin-V FITC and PI and analyzed by flow cytometry. Cell apoptosis was expressed as the percentage of apoptotic cells in total cell populations. The bar graph represents mean ± SEM of three independent experiments. HM, high mannitol (5 mM glucose + 20 mM mannitol); NG, normal glucose (5 mM glucose). *P < 0.05 by Student's t-test.

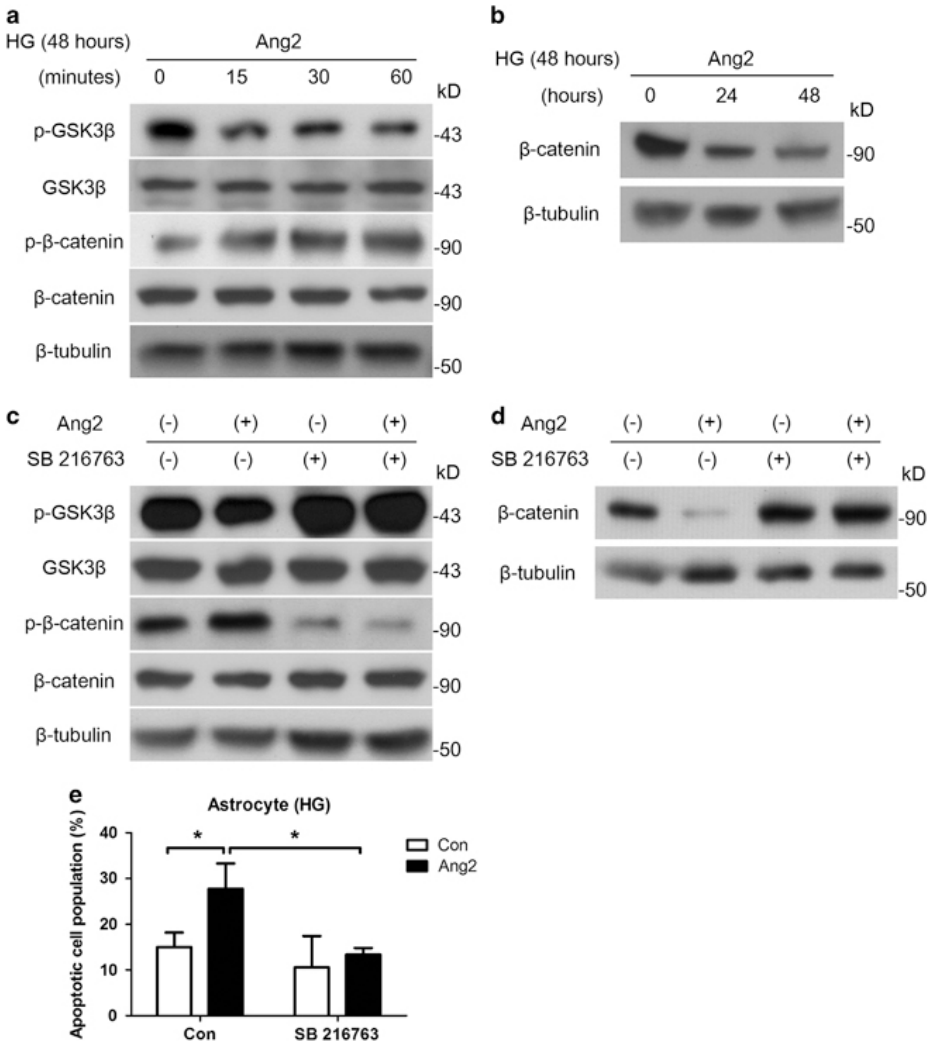

Figure 1-12. Ang2 induces astrocyte apoptosis via GSK-3β/β-catenin pathway under high glucose. While astrocytes were incubated for 48 h under HG, Ang2 (300 ng/mL) was treated for the indicated time period. (A) Western blot analysis for phospho-GSK-3β (Ser9) and phosphor-β-catenin (Thr41/Ser45) were performed on lysates obtained from astrocytes treated with Ang2 for 15, 30, and 60 min under HG (48 h). (B) Western blot analysis for β-catenin was performed on lysates obtained from astrocytes treated with

Ang2 for 24 and 48 h under total 48 h of HG. (C) After 48 h of HG incubation, SB 216763 (GSK-3β inhibitor, 10 μM) was pretreated for 1 h. Then, Ang2 was treated for 30 min. Western blot analysis was performed for phospho-GSK-3β (Ser9) and phosphor-β-catenin (Thr41/Ser45). (D, E) Astrocytes were incubated under HG with either Ang2 or SB 216764 for 48 h. (E) Western blot analysis for β-catenin was performed. (E) Apoptotic cell counts were assessed by FACS analysis. The bar graph represents mean ± SEM of three independent experiments. *$P < 0.05$ by Student's *t*-test. Data represent three independent experiments. β-tubulin was used as a loading control.

High glucose increases integrin αvβ5 as an Ang2 receptor in astrocyte

I aimed to reveal which receptor is responsible for mediating Ang2 induced apoptosis in astrocyte. To determine whether Tie-2 receptor, well known receptor for Ang2, is related with Ang2 induced astrocyte apoptosis, western blot analysis (Figure 1-13A) and real time-PCR (Figure 1-13B) for Tie-2 and Tie-1 were performed on lysates obtained from human retinal microvascular endothelial cells (HRMECs) and astrocyte. As shown in the previous study (1, 52), astrocyte did not express Tie-2 or Tie-1 while HRMECs expressed Tie-2 and Tie-1. Compared to HRMECs with Tie-2 expression, astrocyte did not express Tie-2 in FACS analysis (data now shown). Next, to determine whether integrin may serve as receptors for Ang2 in astrocyte apoptosis under high glucose, I incubated astrocyte under high glucose for 30 min with Ang2 and H-Gly-Arg-Gly-Asp-Ser-OH (GRGDS) peptides. GRGDS (0.5 mg/mL) attenuated Ang2 induced β-catenin phosphorylation (Figure 1-13C). This result showed that integrin signaling was involved in Ang2 induced β-catenin phosphorylation.

Next, to determine whether the high glucose changes the expression pattern of integrin, I performed quantitative RT-PCR and western blot studies for αv, β3, and β5, which are known to be expressed in astrocyte (52). Astrocyte mainly expressed αv and β5 integrin, and intriguingly, high glucose condition increased β5 integrin expression (Figure 1-13D). While high glucose did not increase *ITGαv* (Figure 1-13E), *ITGβ3* (Figure 1-13F) mRNA levels for 48 h, it significantly increased *ITGβ5* mRNA level ($P = 0.002$ by 1-way ANOVA, 24 h: 1.24 ± 0.04 fold, $P < 0.05$ and 48 h: 1.41 ± 0.00 fold, $P =$

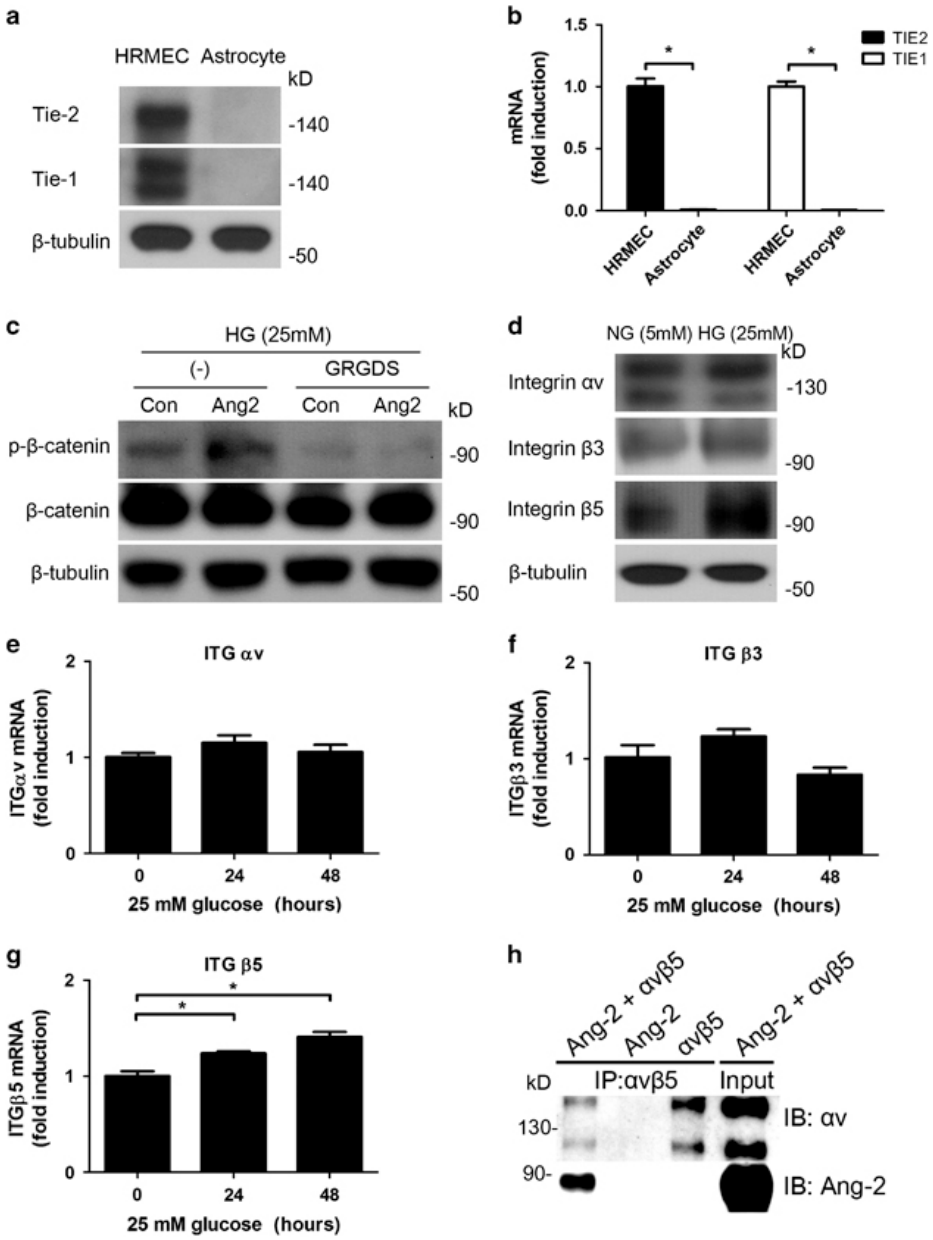

Figure 1-13. High glucose increases integrin αvβ5 as an Ang2 receptor in astrocyte. (A) Western blot for Tie-2 and Tie-1 expression were performed on lysates obtained from HRMECs and Astrocytes. (B) *TIE2* and *TIE1* mRNA transcriptions were assessed by quantitative RT-PCR. *TIE2* and *TIE1* mRNA levels were normalized to *β-ACTIN* mRNA and reported as fold induction

compared to HRMECs. *P < 0.001 by Student's t-test. (C) Western blot analysis for phosphor-β-catenin (Thr41/Ser45) and β-catenin were performed on lysates obtained from astrocytes treated with Ang2 (300 ng/mL) or GRGDS (0.5 mg/mL) for 30 min after 48 h of 25 mM high glucose (HG) incubation. (D) Western blot analysis for integrin αv, β3, and β5 were performed on lysates obtained from astrocytes under HG for 48 h. β-tubulin was used as a loading control. Data represent three independent experiments. *ITGαv* (E), *ITGβ3* (F), *ITGβ5* (G) mRNA transcriptions were assessed and normalized to *β-ACTIN* mRNA by quantitative RT-PCR. All mRNA levels were reported as fold induction compared to normal glucose (NG, 5 mM). *P < 0.05 by Student's t-test. (H) After incubation of Ang2 (500 ng), integrin αvβ5 (500 ng), and integrin αvβ5 antibody (2 μg), immune complexes were co-immunoprecipitated to show direct binding of Ang2 to integrin αvβ5. Then, they were analyzed for Ang2 and integrin αv. Same amounts of recombinant Ang2 and integrin α3β1 were used as an input. Con, control.

0.002 by post-hoc test, respectively; Figure 1-13G).

On the other hand, high glucose decreased *ITGβ8* mRNA (0.72 ± 0.01 fold for 48 h, $P < 0.01$). In addition, I aimed to show direct binding of Ang2 to integrin αvβ5 as αv is an exclusive partner for β5. Indeed, Ang2 was shown to directly bind to integrin αvβ5 in co-immunoprecipitation assay (Figure 1-13H). These data suggested that high glucose condition increased integrin αvβ5 as a receptor for Ang2 in astrocyte.

Ang2 induced astrocyte apoptosis is inhibited by suppression of αvβ5 integrin

To determine which integrin subunit is responsible for Ang2 induced astrocyte apoptosis, I screened the integrin α subunits (α1-6 and αv). Integrin α3 and αv blocking antibodies attenuated Ang2 induced β-catenin phosphorylation (Figure 1-14A). To further explore the precise integrin complex, I tested integrin α3, αv, and β1 blocking antibodies. Only integrin αv blocking antibody significantly prevented Ang2 induced β-catenin degradation (Figure 1-14B and D). Indeed, integrin α3 and β1 blocking antibodies did not affect Ang2 induced astrocyte apoptosis (Figure 1-14C and E). Thus, I could narrow down the candidate to αv and its counterpart subunit β3 and β5. Same experimental procedures were conducted with αvβ3 and αvβ5 integrin blocking antibodies, and Ang2 induced β-catenin degradation was inhibited only by blocking αvβ5 integrin (Figure 1-14F). Suppression of αvβ5 integrin effectively decreased Ang2 induced astrocyte apoptosis (19.3 ± 1.4% from 25.2 ± 1.2%, $P < 0.05$; Figure 1-14G).

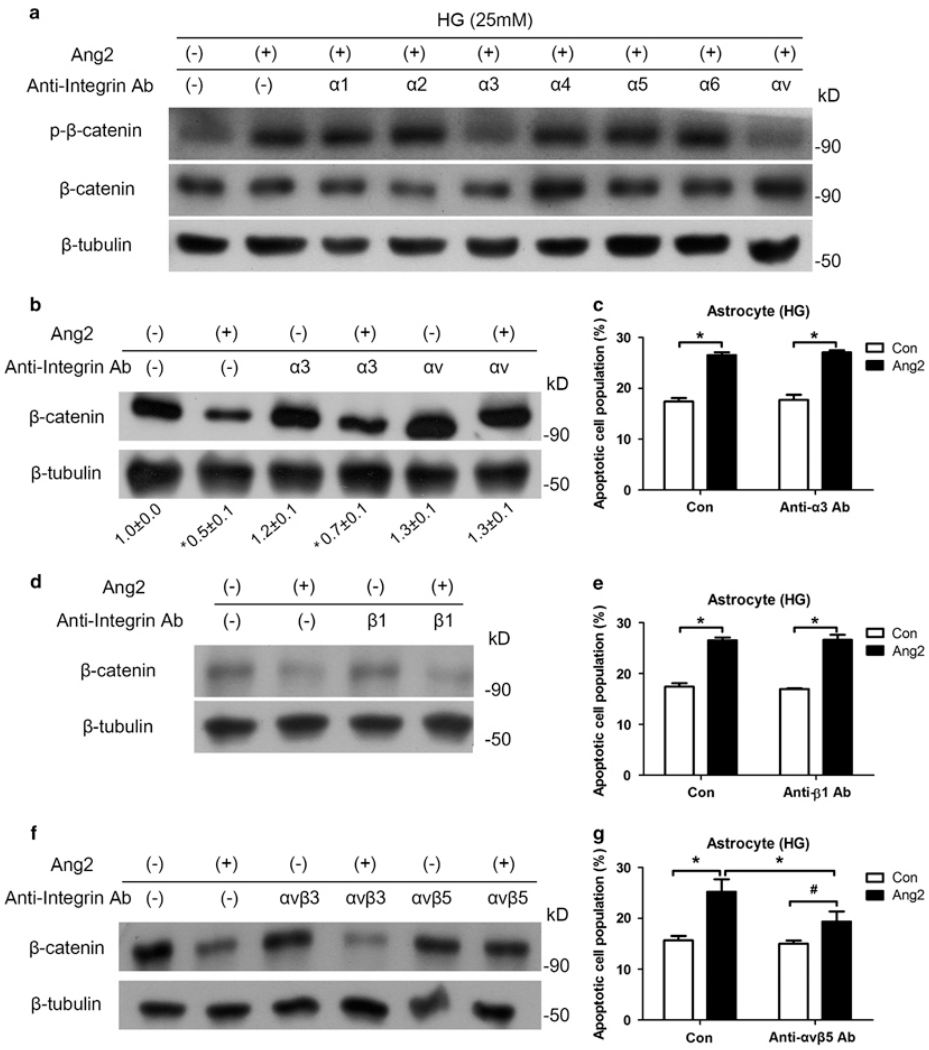

Figure 1-14. Ang2 induced astrocyte apoptosis is inhibited by suppression of αvβ5 integrin. (A) Western blot analysis for phosphor-β-catenin (Thr41/Ser45) and β-catenin were performed on lysates obtained from astrocytes treated with Ang2 (300 ng/mL) or various integrin blocking antibodies (10 μg/mL, α1, α2, α3, α4, α5, α6, and αv) under 25 mM high glucose (HG) for 30 min. (B, C) Astrocytes were incubated under HG with Ang2 and anti-integrin α3 or αv antibodies for 48 h. (B) Western blot analysis

for β-catenin was performed (ImageJ quantitation; n = 3, mean ± SEM). (C) Astrocyte apoptosis with anti-integrin α3 antibody was analyzed by FACS and expressed as the percentage of apoptotic cells in total cell populations. (D, E) Astrocytes were incubated under HG with Ang2 and anti-integrin β1 antibody (10 μg/mL) for 48 h. (D) Western blot analysis for β-catenin was performed. β-tubulin was used as a loading control. Data represent three independent experiments. (E) Astrocyte apoptosis with anti-integrin β1 antibody was analyzed by FACS and expressed as the percentage of apoptotic cells in total cell populations. (F, G) Astrocytes were incubated under HG with Ang2 and anti-integrin αvβ3 or αvβ5 antibodies (10 μg/mL) for 48 h. (F) Western blot analysis for β-catenin was performed. β-tubulin was used as a loading control. Data represent three independent experiments. (G) Astrocyte apoptosis with anti-integrin αvβ5 antibody was analyzed by FACS and expressed as the percentage of apoptotic cells in total cell populations. *$P < 0.05$ compared with Ang2 treatment by Student's *t*-test.

Inhibition of αvβ5 Integrin reduces astrocyte loss in diabetic retina

Based on *in vitro* experiments, I next intravitreally injected 1μg of anti-αvβ5 integrin antibodies to diabetic mice 2 weeks after STZ induction. One week after intravitreal injection, the isolated retinae were stained with GFAP for astrocyte evaluation (Figure 1-15A). *In vivo*, intravitreal injection of anti-αvβ5 integrin antibody effectively reduced astrocyte loss in diabetic retina (128.3 ± 16.4%) compared to the loss in PBS injected diabetic mice (53.1 ± 8.6%, P = 0.003; Figure 1-15B). These *in vivo* data suggested that astrocyte loss occurred via αvβ5 integrin in diabetic retina. In summary, I demonstrated that Ang2 induced astrocyte apoptosis via αvβ5 integrin in diabetic retina.

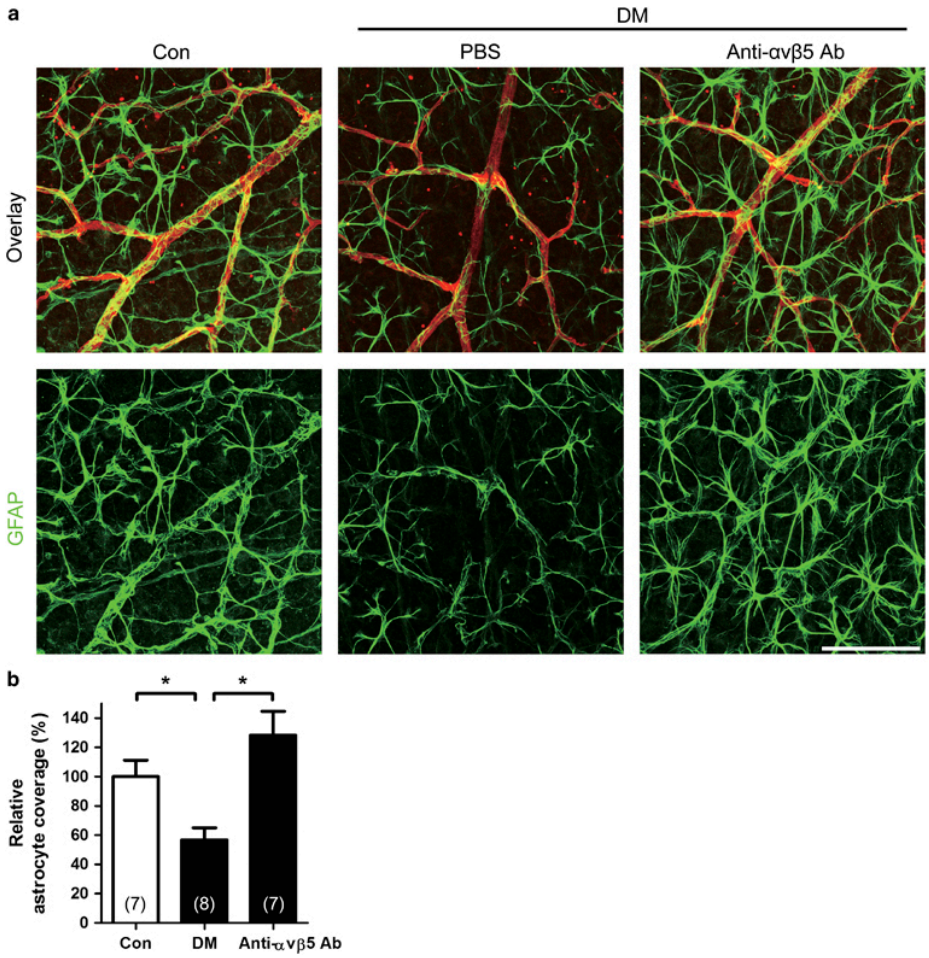

Figure 1-15. Inhibition of αvβ5 Integrin reduces astrocyte loss in STZ-induced diabetic mice. Anti-αvβ5 integrin neutralizing antibody (Anti-αvβ5 Ab, 1 μg) or PBS was intravitreally injected to 2 week DM mice. Retinal astrocyte was evaluated 1 week after the injection in 3 week DM mice. (A) Focal astrocyte loss shown in diabetic retina (PBS) is rescued in anti-αvβ5 Ab injected diabetic mice (original magnification ×400; scale bar = 100 μm). (B) Relative astrocyte coverage (%) is calculated by colocalized area of astrocyte and vessel per IB4+ vascular area and normalized to the value of control mice.

The sample size for each group is indicated on the bar graph. The bar graphs represent mean ± SEM, *$P < 0.001$ by Student's *t*-test.

High glucose-induced upregulation of IL-6 expression in microglia is associated with STAT3 activation in diabetic retina

In the retinas of STZ-induced diabetic mice, STAT3 phosphorylation was increased, whereas ZO-1 and occludin protein levels were decreased compared to that of control (Figure 1-16A). Since pro-inflammatory cytokines such as IL-6, IL-1β, and tumor necrosis factor-α (TNF-α) are known to be elevated in diabetic retina (42-44) and STAT3 could be activated by a variety of cytokines, I determined the expression of the pro-inflammatory cytokines in the retinas of STZ-induced diabetic mice. I found that the mRNA transcripts of IL-6 (*Il6*), IL-1β (*Il1b*), and TNF-α (*Tnfa*) were increased from 1 to 3 months in the STZ-induced diabetic retinas (Figure 1-16B).

Next, I determined the cellular source from which those cytokines are released under the diabetic condition. I used primary HRMEC, pericytes, astrocytes, and a cell line of human microglia (HMO6), which carries morphologic and phenotypic features of primary human microglia (45, 46). I exposed the cells to high glucose for 24 h and evaluated the gene expression of the cytokines observed in the diabetic retina (Figure 1-16C). Among the cytokines tested, the high glucose exposure only increased *IL6* mRNA level in the HMO6 cells (Figure 1-16C). These results demonstrate that the microglia are main source for the high glucose-induced IL-6 expression.

To address whether microglia exposed to high glucose could affect retinal endothelial permeability, I examined the endothelial permeability in co-culture model with HRMECs and HMO6 cells. When the cells were exposed to high glucose, HRMEC permeability was increased, whereas the addition of

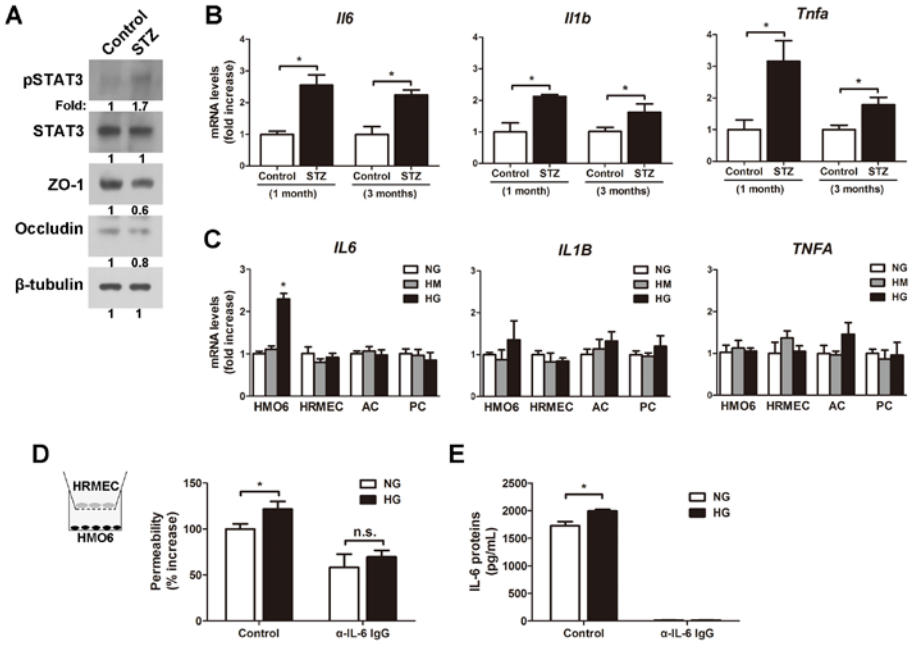

Figure 1-16. Effect of microglia-derived IL-6 on the retinal endothelial permeability. (**A**) The retina from STZ-induced diabetic mice (3 months) were examined for STAT3 phosphorylation (pSTAT3) and the protein expression of ZO-1 and occludin by western blot analysis. Representative blots are shown from 1 of 3 retinas with fold changes compared with age-matched control (Control) (**B**) Quantitative RT-PCR analysis of mRNA expression of the indicated cytokines in the retinas of STZ-treated (STZ) mice and age-matched controls (Control). The bars represent the means ± SD. * $P < 0.05$ vs Control (n = 3). (**C**) The indicated cells were exposed to normal glucose (NG), high glucose (HG), or high mannitol (HM) as a control. The mRNA expression levels of *IL6*, *IL1B*, and *TNFA* in the indicated cells were determined by quantitative RT-PCR. * $P < 0.05$ vs NG in each cell (n = 3). (**D**) The co-cultures of HRMECs and HMO6 cells (as depicted in the diagram)

were exposed to NG and HG for 48 h and the HRMEC monolayer integrity was evaluated. IL-6 activity was inhibited by a neutralizing antibody against IL-6 (α-IL-6 IgG). The results are percentage increases versus NG and plotted as the means ± SD (n = 4). * $P < 0.05$ between two values. n.s., no significance. (**E**) The IL-6 protein amounts in the supernatant media from (**D**) were determined by ELISA assay. The bar represents the means ± SD (n = 4). * $P < 0.05$ between two values.

an IL-6 neutralizing antibody to the co-culture plates completely abolished the high glucose-induced HRMEC permeability (Figure 1-16D). ELISA analysis of the co-culture medium confirmed the increased level of IL-6 protein from the HMO6 cells exposed to high glucose (Figure 1-16E). Microglia-derived IL-6 under high glucose condition increased retinal endothelial permeability.

STAT3 activation in ECs increases endothelial permeability through the downregulation of tight junction proteins

I investigated whether STAT3 activation in ECs affect an endothelial permeability. Since IL-6 has been known to strongly activate STAT3 signaling pathway (53), I determined IL-6-induced STAT3 phosphorylation in HRMECs. In HRMECs, IL-6 treatment increased the phosphorylation of STAT3 in a dose-dependent manner (Figure 1-17A). IL-6-induced STAT3 phosphorylation peaked at 15 min after treatment (Figure 1-17B). To address whether STAT3 activation is involved in the regulation of vascular integrity, I examined the HRMEC monolayer integrity using the trans-endothelial permeability assay. IL-6 (20 ng/mL) treatment began to increase trans-endothelial Evans blue dye permeability from 24 h (Figure 1-17C). The IL-6-induced increase in endothelial permeability was comparable to that of well-known permeabilizing agents such as TNF-α (100 ng/mL).

Since endothelial permeability is in large part regulated by intercellular junctions (54), I examined whether STAT3 activation affects the expression of adherens and tight junction proteins in retinal endothelial cells, I treated HRMECs with IL-6 (20 ng/mL) for 12 and 24 h and evaluated the mRNA

levels of junction proteins including ZO-1 (*TJP1*), occludin (*OCLN*), claudin-5 (*CLDN5*), and VE-cadherin (*CDH5*) by quantitative RT-PCR analysis (Figure 1-17D). IL-6 treatment downregulated the *TJP1* and *OCLN* mRNAs in a time-dependent manner, while *CLDN5* and *CDH5* mRNAs were not significantly altered (Figure 1-17D). IL-6 also reduced the protein levels of ZO-1 and occludin in the HRMECs under both normal and high glucose conditions (Figure 1-17E).

I next determined whether STAT3 inhibition could block the IL-6-induced changes in retinal endothelial cells. WP1066 treatment completely abolished the IL-6-induced downregulation of ZO-1 and occludin mRNA and protein levels in HRMECs (Figure 1-17F and G). Consistent with the effects on the expression levels of ZO-1 and occludin, the IL-6-induced elevation of HRMEC permeability was completely abolished by the WP1066 treatment (Figure 1-17H). These results suggest that STAT3 activation is responsible for the IL-6-induced downregulation of ZO-1 and occludin levels, leading to increasing the retinal endothelial permeability.

STAT3 activation downregulates ZO-1 and occludin expression through VEGF secretion in ECs

I wondered how STAT3 activation downregulates ZO-1 and occludin expression in ECs. Because a recent report showed the direct binding of STAT3 to the promoters of ZO-1 and occludin in epithelial cells (55), I first checked the binding of STAT3 to ZO-1 and occludin promoters in ECs. I treated HRMECs with IL-6 (20 ng/ml) in the presence and the absence of

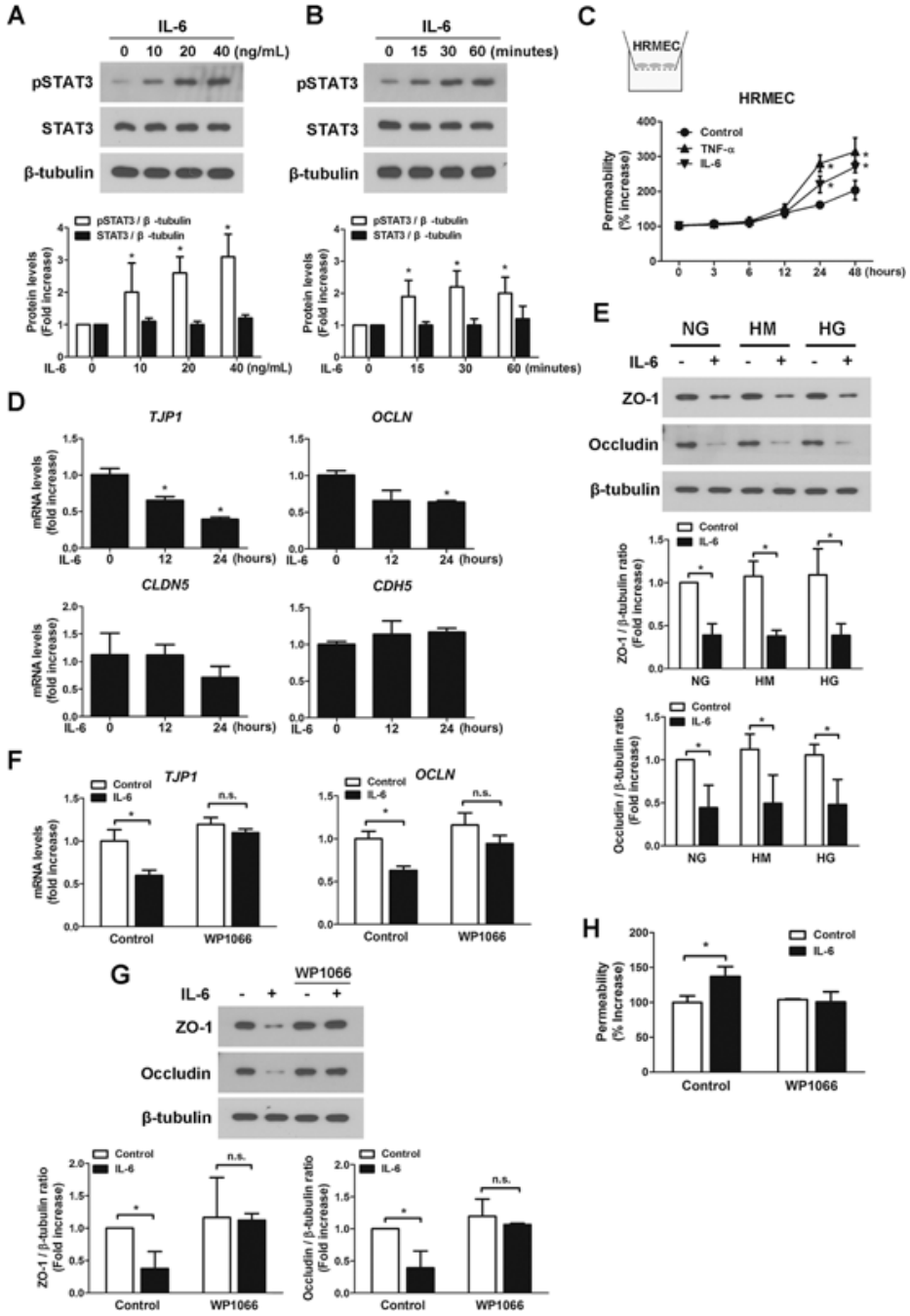

Figure 1-17. Effects of STAT3 activation on endothelial permeability and the tight junction protein expression in HRMECs. Dose- (A) and time-response (B) of STAT3 phosphorylation by IL-6 treatment in HRMECs.

STAT3 phosphorylation (pSTAT3) was determined by western blot analysis. The histograms on the bottom part show quantitative densitometric analysis of western blots to calculate the ratio of pSTAT3 or total STAT3 to β-tubulin. The results are fold increases versus 0 ng/mL or 0 min and plotted as the means ± SD (n = 3). *$P < 0.05$ versus control. (C) HRMECs were treated with IL-6 or TNF-α for the indicated times. The HRMEC monolayer integrity was evaluated by the trans-endothelial permeability assay as depicted in the diagram. The results are percentage increases versus 0 h and plotted as the means ± SD (n = 4). *$P < 0.05$ versus control. (D) HRMECs were treated with IL-6 for 12 and 24 h. The mRNA expression levels of the indicated genes were determined using quantitative RT-PCR. *$P < 0.05$ versus 0 h (n = 3). (E) HRMECs were treated with IL-6 for 48 h under NG, HM, or HG. The protein expression of ZO-1 and occludin was examined by western blot analysis. The histograms on the bottom part show quantitative densitometric analysis of western blots to calculate the ratio of ZO-1 or occludin to β-tubulin. The results are fold increases versus control under NG condition and plotted as the means ± SD (n = 3). *$P < 0.05$ between two values. (F) HRMECs were treated with IL-6 for 24 h in the presence and the absence of WP1066. The mRNA expression levels of TJP1 and OCLN were determined by quantitative RT-PCR. *$P < 0.05$ between two values (n = 3). n.s., no significance. The bars represent the means ± SD. (G) The protein expression of ZO-1 and occludin in the HRMECs treated with IL-6 for 48 h in the presence and the absence of WP1066 were examined by western blot analysis. The gels are representative. The histograms on the bottom part show quantitative densitometric analysis of

western blots to calculate the ratio of ZO-1 or occludin to β-tubulin. The results are fold increases versus control and plotted as the means ± SD (n = 3). *$P < 0.05$ between two values. n.s., no significance. (H) The HRMEC monolayer integrity in (G) was evaluated using a trans-endothelial permeability assay with Evans blue dye. The results are percentage increases versus control and plotted as the means ± SD (n = 4). *$P < 0.05$ between two values.

WP1066 for 24 h and then immunoprecipitated the cell lysates with anti-STAT3 antibody. The immunoprecipitated DNAs were analyzed by quantitative RT-PCR using the primers for putative STAT binding sites in each promoter (55, 56). ChIP analyses showed that the activated STAT3 did not bind to the promoters of both ZO-1 and occludin (Figure 1-18A and B).

Thus, I hypothesized that another protein may be involved in the STAT3-mediated responses in ECs. Because VEGF is one of the downstream effectors of STAT3 activation in many cells (57, 58) and can regulate the expression of tight junction proteins (59), I examined the induction of VEGF expression by STAT3 activation in ECs. In the ChIP assay, STAT3 binding to VEGF promoter was increased by IL-6 treatment in HRMECs, whereas WP1066 treatment abrogated the IL-6-induced STAT3 binding to the VEGF promoter (Figure 1-18C). IL-6 treatment upregulated *VEGFA* mRNA expression within 3–24 h in HRMECs (Figure 1-18D). VEGF protein level in the HRMEC culture medium was also upregulated by IL-6 treatment, which could be neutralized by anti-VEGF antibody (200 μg/mL, bevacizumab) treatment (Figure 1-18E). To further test whether VEGF is required for the IL-6-induced alterations in the retinal ECs, I examined the levels of tight junction proteins and the endothelial permeability in HRMECs treated with IL-6 in the presence and the absence of bevacizumab. I found that the IL-6-induced downregulation of ZO-1 and occludin protein levels in HRMECs was partially abrogated by the bevacizumab treatment (Figure 1-18F). In contrast, VE-cadherin protein level was not changed by the IL-6 and/or bevacizumab treatment (Figure 1-18F).

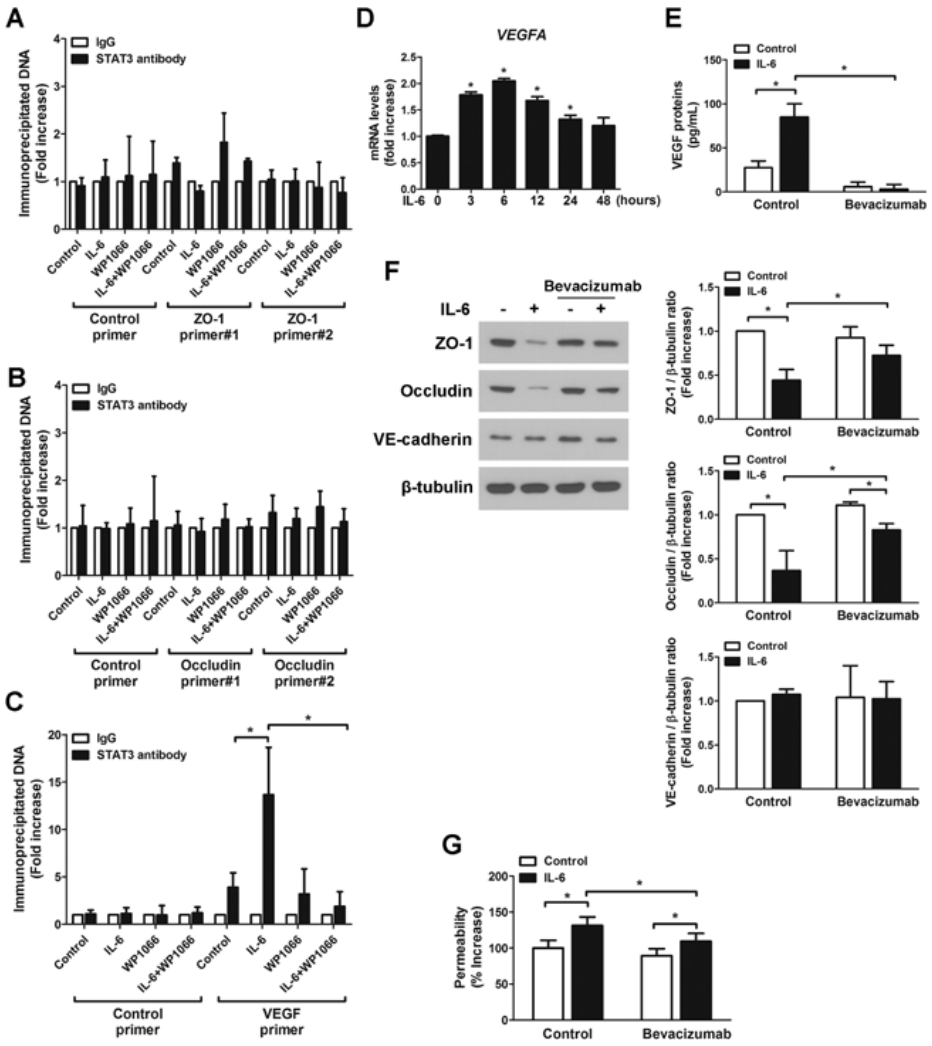

Figure 1-18. STAT3 activation downregulates ZO-1 and occludin levels through the induction of VEGF production. (A–C) HRMECs were treated with IL-6 for 24 h in the presence and the absence of WP1066. The immunoprecipitated DNAs from the HRMECs with anti-STAT3 antibody were analyzed by quantitative RT-PCR using primers for the putative STAT3 binding sites of the ZO-1 (A), occludin (B), and VEGF (C) promoters. The enrichment of DNAs with STAT3 antibody is expressed as fold increases

compared with that of IgG. Note that STAT3 binding to the VEGF promoter was increased by IL-6 treatment and reversed by WP1066 treatment (C). The bar represents the means ± SD (n = 3). *$P < 0.05$ between two values. (D) HRMECs were treated with IL-6 for the indicated times. The mRNA expression level of VEGFA in the HRMECs were determined by quantitative RT-PCR. *$P < 0.05$ versus 0 h (n = 3). (E) HRMECs were treated with IL-6 for 48 h in the presence and the absence of anti-VEGF antibody (bevacizumab). The VEGF protein amounts in the supernatant media were determined by ELISA assay. The bar represents the means ± SD (n = 4). *$P < 0.05$ between two values. (F) The protein expression of ZO-1, occludin, and VE-cadherin in the HRMECs treated with IL-6 and/or bevacizumab for 48 h were examined by western blot analysis. The gels are representative. The histograms on the right part show quantitative densitometric analysis of western blots to calculate the ratio of ZO-1, occludin, and VE-cadherin to β-tubulin. The results are fold increases versus control and plotted as the means ± SD (n = 3). *$P < 0.05$ between two values. (G) The HRMEC monolayer integrity treated with IL-6 and/or bevacizumab for 48 h was evaluated using the trans-endothelial permeability assay. The results are percentage increases versus control and plotted as the means ± SD (n = 4). *$P < 0.05$ between two values.

Moreover, the IL-6-induced elevation of HRMEC permeability was partially reduced by the bevacizumab treatment (Figure 1-18G). Taken together, these results suggest that STAT3 activation directly increases VEGF secretion, and that VEGF contributes to the IL-6-induced increased permeability of retinal endothelial cells through the reduction of ZO-1 and occludin levels.

STAT3 activation is involved in the IL-6-induced retinal vascular leakage *in vivo*

I next examined whether STAT3 activation is involved in the IL-6-induced vascular leakage in the retinas of mice. Two days after the intravitreal injection of mouse IL-6 (20 ng) with or without WP1066 (2 μM), a retinal vascular leakage was evaluated with Evans blue dye in the retinas of the mice. The vascular leakage was significantly increased in the IL-6-treated retinas compared to that of the control retinas (Figure 1-19A and B). WP1066 completely abolished the IL-6-induced elevation of vascular leakage in the retina. Consistently, IL-6-induced STAT3 phosphorylation in the retinas was abolished in the presence of WP1066 (Figure 1-19C). IL-6 treatment also reduced the protein levels of ZO-1 and occludin in the retinas, which was restored to normal levels in the presence of WP1066 (Figure 1-19D). These results suggest that STAT3 activation is responsible for the IL-6-induced vascular leakage through the downregulation of ZO-1 and occludin levels in the retinas of mice.

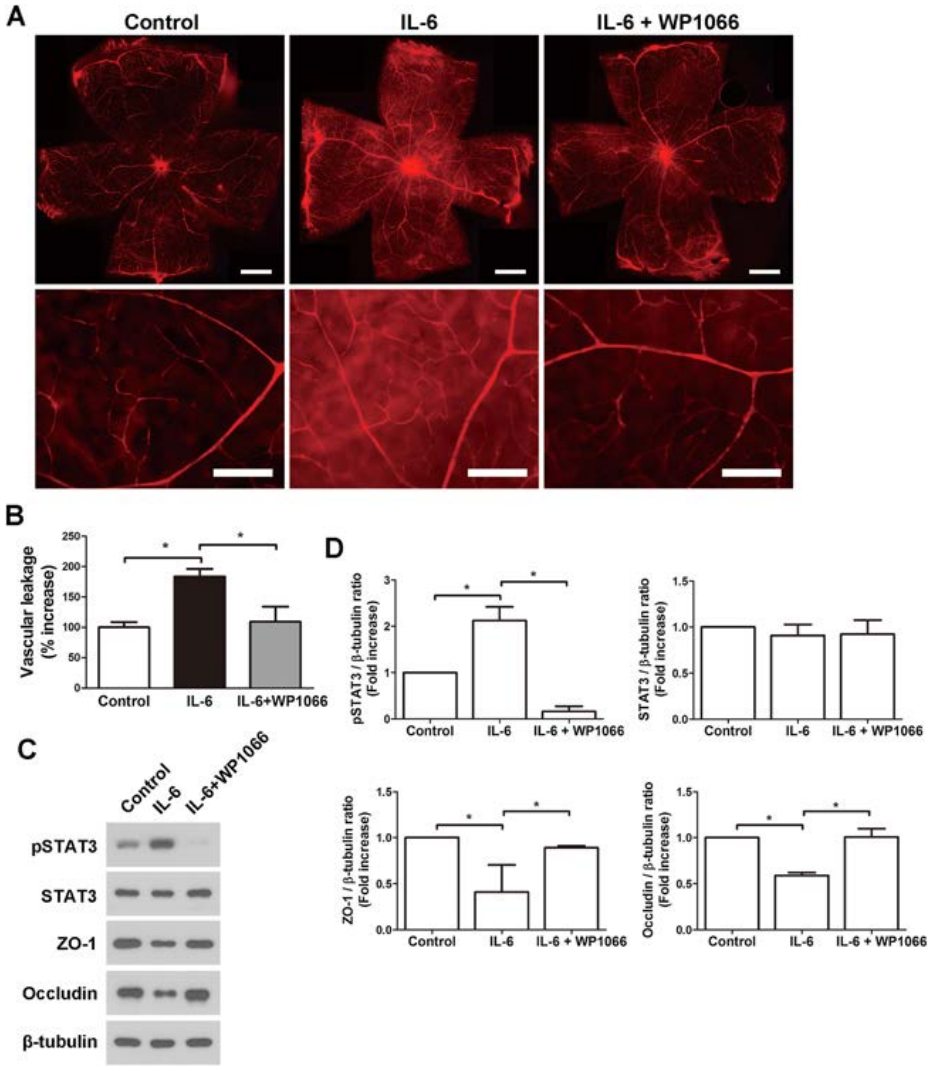

Figure 1-19. STAT3 inhibition effectively reduced IL-6 induced retinal vascular leakage. (A) Representative images of focal vascular leakage with Evans blue dye in the retinas of mice received IL-6 with and without WP1066. Scale bars are equal to 500 μm (upper row) and 100 μm (bottom row). (B) Quantitative analysis of retinal vascular leakage as measured by Evans blue dye in the retinas of mice received IL-6 with and without WP1066. Relative retinal vascular leakages are percent increases versus control and plotted as

the means ± SD (n = 3). *$P < 0.05$ between two values. (C) The STAT3 phosphorylation (pSTAT3) and the protein expression of ZO-1, occludin, and STAT3 in the retinas in (A) were examined by western blot analysis. Representative blots are shown from one of three retinas. (D) Quantitative densitometric analysis of western blots in (C) to calculate the ratio of pSTAT3, STAT3, ZO-1, and occludin to β-tubulin. The results are fold increases versus control and plotted as the means ± SD (n = 3). *$P < 0.05$ between two values.

DISCUSSION

In this study, I demonstrated that pericyte loss occurred with Ang2 increase in the diabetic mice retina (19, 20, 22). Previously, Tie-2 was known to be related with Ang-induced pericyte survival and recruitment (20). However, there was no direct evidence that Ang2 induced pericyte apoptosis via Tie-2. Unlike the previous study (20), pericyte did not express Tie-2 mRNA or protein in our study. While Ang2 alone did not induce apoptosis *in vitro* (20), Ang2 induced pericyte apoptosis under high glucose via p53 pathway. Thus, I postulated that Ang2 would induce Tie-2 independent apoptosis in pericyte. Accumulating evidence support the role of integrin in Ang2 activity in endothelial cells (28). However, little is known about Ang2/integrin system in the pericyte. Thus, I focused on the integrin receptors on pericytes.

Integrins are cell adhesion molecules that are expressed on the surface of endothelial cells and pericytes. The contribution of endothelial and mural cell integrins to angiogenesis has been studied. Pericytes express integrins including: the collagen receptors, α1β1, α2β1; the laminin receptors, α3β1, α6β1, α6β4, α7β1; the fibronectin receptor, α4β1, α5β1; and the osteoponin receptors, α8β1, α9β1 (51). Cytokines and extracellular matrix changes integrin subtypes in pericyte (60). Based on the differential response to Ang2 in pericyte depending on glucose concentration, I hypothesized that high glucose could change integrin subtype more susceptible to Ang2. During quantitative RT-PCR array for screening integrin subtype change response to high glucose, only *ITGα1*, *ITGα2*, *ITGα3*, and *ITGβ1* mRNA increased over 1.5-fold among *ITGα1*, *ITGα2*, *ITGα3*, *ITGα4*, *ITGα5*, *ITGα6*, *ITGα7, ITGαv,*

and *ITGβ1* mRNA (data not shown). In addition, basal *ITGα3* mRNA was over 6 times higher than *ITGα1 or ITGα2* mRNA in pericyte even under normal glucose condition. Thus, I concluded that integrin α3 and β1 are both predominant and high glucose inducible integrins in pericyte. The proportion of integrin α1 in pericyte is too minor to be responsible for Ang2 induced pericyte apoptosis. In addition, many integrins, including αvβ3, α5β1, αIIbβ3, αvβ6, and α3β1 recognize the tripeptide Arg-Gly-Asp (RGD) in their ligands (61). On the other hand, integrin α1β1 recognizes a configuration of residues formed by arginine and aspartic acid residues, not RGD. Attenuation of p53 by GRGDS supported that Ang2 induced pericyte apoptosis was effectively attenuated by blocking integrin α3β1. Integrin receptors induced by hyperglycemia in the diabetic retinopathy could make the pericyte more susceptible to the Ang2, in turn, lead to the pericyte apoptosis by Ang2/Integrin signaling pathway.

The laminin receptor α3β1 integrin is expressed in vascular endothelial cells and acts to suppress pathological angiogenesis in the retina and other organs (62, 63). However, a role for integrin α3β1 in pericyte is yet to be determined (51). Inhibition of β1 integrin induced a rounded morphology of the pericytes, suggesting pericyte adhesive properties were affected or that these cells were undergoing apoptosis (64). In this study, I suggested that integrin α3β1 was important for Ang2 induced apoptosis. This is notably different from classical concept that Tie-2 mediates the effect of Ang2 as an Ang2 receptor. Absence of Tie-2 in human pericyte used in this study was confirmed by various experiments including RT-PCR with two different

primers, western blot, and FACS analysis. In addition, both Ang1 and Ang2 can directly bind to some integrins and thereby signal in the absence of Tie-2 (65-68). Thus, I suggested that integrin mediated Ang2 induced apoptosis at least in Tie-2 negative pericyte.

Previous studies have shown that the primary source of Ang2 is vascular endothelial cells (69-72). High glucose increases Ang2 mRNA in HRMEC (73). Endothelial cell is regarded as potential source of Ang2 in the retina by transient rapid release from Weibel-Palade body and chronic upregulation of Ang2 (69, 74, 75). Chronic hyperglycemia upregulates Ang2 in the diabetic retina (73, 76) and Ang2 upregulation is causally involved in the pathogenesis of pericyte loss in diabetic retinopathy (19). Hyperglycemia induces pericyte loss not only by increasing Ang2 in endothelial cells, but also changing integrin subtype prone to Ang2 in pericytes. Our data support that glycemic control is important to prevent Ang2 induced pericyte loss in early diabetic retinopathy. Glycemic control is the effective treatment to reduce the progression of diabetic retinopathy (77-79).

I showed that Ang2 induced pericyte apoptosis under high glucose via p53 pathway. Furthermore, *in vitro* and *in vivo*, Ang2 induced pericyte apoptosis was effectively attenuated by blocking integrin $\alpha 3\beta 1$. Integrin $\alpha 3$ and $\beta 1$ blockers reduced p53 signaling by Ang2. Ser-15 of p53 is phosphorylated by a mitogen-activated protein kinase-dependent pathway (ERK1/2), and this step is required for apoptosis to occur (80).

It has been suggested that hyperglycemia causes pericyte loss by apoptosis (15-17). In this study, I postulated that hyperglycemia induced Ang2

overexpression in endothelial cells, in turn, caused apoptotic cell death of pericytes. In an animal model of diabetic retinopathy, high glucose was induced by STZ-injection as early as 3 days. Then, Ang2 increased upon 3 months with pericyte loss, and finally acellular capillary at 6 months (19, 81). The mechanism by which capillaries become acellular is largely unknown. Apoptosis preceding the formation of acellular capillaries in retinae from diabetic rats and humans is one mechanism by which endothelial cells could be eliminated from the diabetic capillary (17). Retinal capillary coverage with pericytes is crucial for the survival of endothelial cells. Loss of pericytes is related to the increase of acellular capillaries from hyperglycemic injury (14). Based on our data, Ang2 did not directly induce endothelial cell death. Thus, I postulated that acellular capillary could be endothelial cell death secondary to pericyte loss by Ang2.

In conclusion, I demonstrated that pericyte loss occurred with Ang2 increase in the diabetic mice retina. Ang2 induced pericyte apoptosis via p53 pathway under high glucose. High glucose increased integrin α3β1 in pericyte. Interestingly, integrin was involved in Ang2 induced pericyte apoptosis. Furthermore, Ang2 induced pericyte apoptosis was effectively attenuated by blocking integrin α3β1 both *in vitro* and *in vivo*. Taken together, Ang2 induced p53-dependent pericyte apoptosis via α3β1 integrin signaling in diabetic retinopathy. I suggest that glycemic control or blocking Ang2/integrin signaling could be a potential therapeutic target to prevent pericyte loss in early diabetic retinopathy.

In this study, I demonstrated that vascular leakage occurred in the diabetic

retina as early as 3 weeks after diabetic induction in mice. Interestingly, the vascular leakage in the early diabetic retinopathy was accompanied with loss of astrocytic endfeet. In terms of the neurovascular unit, astrocyte loss could contribute to vascular leakage in the retina. Of importance, our results showed that inhibition of Ang2 effectively attenuated both astrocyte loss and vascular leakage in the early diabetic retinopathy. Recently, I demonstrated that Ang2 induced pericyte loss via integrin signaling in diabetic retinopathy (1). Although pericyte loss is an early characteristic change in diabetic retinopathy, vascular leakage can occur even before the pericyte loss in diabetic mice (31). Thus, I postulated that astrocyte, as a component of neurovascular unit in retina along endothelial cell and pericyte, could play an important role in early vascular leakage in diabetic retina.

The early glial change in the diabetic retina has been described in diabetic animal models (32, 33, 41, 82-84). Retinal neuroglial abnormalities are observed predominantly in the inner retina before the characteristic vascular lesions are observed (33). In diabetic retina, it has been observed that Müller cells acquire strong GFAP immunoreactivity throughout the retina (reactive gliosis) later than astrocyte change, whereas astrocyte progressively decreased in number and GFAP immunoreactivity (32, 33, 41). However, there was no study to investigate the role of astrocyte loss in diabetic retinal vascular leakage in terms of neurovascular unit. Importantly, the molecular mechanism of astrocyte loss in diabetes has not been elucidated yet. Thus, I approached with this concept and also suggested that Ang2 induced astrocyte apoptosis via integrin signaling as the precise molecular mechanism of astrocyte loss in

diabetic retinopathy.

Ang2 induced astrocyte loss by apoptotic mechanism. I focused on the integrin as a receptor for Ang2 in astrocyte, since astrocyte lacked the expression of Tie-2, a known receptor for Ang2 (28, 52). Indeed, Ang2 could bind to integrin α3β1, αvβ5, and α5β1 (1, 28). Interestingly, integrin α3 or β1 blocking antibodies did not affect Ang2 induced astrocyte apoptosis, whereas they mediated Ang2 induced pericyte apoptosis (1). Because I showed integrin β1 was not responsible to Ang2 induced astrocyte apoptosis, I could rule out many integrin α subtypes and focus on the integrin αv complexes. Only αvβ5 integrin, not αvβ3 integrin, could mediate Ang2 induced astrocyte apoptosis. Although αv integrin did not change significantly, high glucose changed integrin subtype of astrocyte from β8 to β5, which was responsible for Ang2 mediated astrocyte apoptosis. Because αv integrin is the only α subtype for the integrin heterodimer with β5 subtype (85, 86), the increase of β5 subtype implied the increase of αvβ5 integrin. In addition, astrocyte mainly expressed αv and β5 integrin as previously reported (52, 87). I confirmed that inhibition of αvβ5 integrin effectively prevented Ang2 induced astrocyte loss *in vitro* and *in vivo*. Thus, integrin αvβ5 could be a therapeutic target in Ang2 induced astrocyte apoptosis.

Regarding to the molecular mechanism of Ang2 induced astrocyte apoptosis, I demonstrated that Ang2 activated GSK-3β and subsequently induced β-catenin phosphorylation and degradation. In addition, I showed that GSK-3β specific inhibitor blocked Ang2 induced astrocyte apoptosis. Inhibition of GSK-3β has been suggested as a therapeutic target in many

disease including diabetes and Alzheimer's disease (88, 89). Thus, I suggest that it could be also a therapeutic target in diabetic retina. Furthermore, nuclear translocation of β-catenin is critical to the activation of TCF/β-catenin target genes, including *survivin, cyclin D1, c-myc*. These target genes of *β-catenin, survinvin, c-Myc,* and *Cyclin D1* mRNA, were significantly decreased in astrocytes treated with Ang2 under high glucose (data not shown). Because survivin is a member of the inhibitor of apoptosis family of protein, decrease of β-catenin can lead to cellular apoptosis (90).

Previously, the most commonly used mouse models with diabetes are induced by chemical toxins such as streptozotocin or alloxan (91). This approach replicates some of the early features of DR and has the advantage that the onset of diabetes can be defined as the time of STZ injection. However, toxin-induced diabetes in mice has been less successful because of strain-dependent resistance to STZ (92). In addition, DR features could be compounded by inflammatory effect of STZ. Despite the drawbacks of STZ diabetic mice model, I showed high enough glucose levels during experimental periods. Recently, the availability of the Ins2Akita mouse line enables to use diabetic mice without STZ or toxins (93). Interestingly, this Ins2Akita mice also showed decreased GFAP immunoreactivity in astrocytes similar to our observation although there was no explanation about molecular mechanism. Thus, further study using Ins2Akita mice about Ang2 and its role in astrocyte loss via αvβ5 integrin signaling could strengthen our study.

In this study, I provided the evidence for the precise mechanism on the Ang2 induced astrocyte apoptosis under high glucose. These molecular

mechanisms gave us the insight for the therapeutic target of astrocyte loss in diabetic retina. In addition, high glucose increases Ang2 in HRMECs (1, 73) and the diabetic retina (73, 76). Thus, inhibition of each steps of Ang2/integrin αvβ5/GSK-3β axis could be potential therapeutic targets to treat vascular leakage in early diabetic retinopathy.

In conclusion, I demonstrated that Ang2 induced astrocyte loss and vascular leakage in early diabetic retinopathy. Ang2 induced astrocyte apoptosis via GSK-3β/β-catenin pathway under high glucose. High glucose increased αvβ5 in astrocyte. Furthermore, I showed that Ang2 induced astrocyte apoptosis was effectively attenuated by blocking αvβ5 integrin both *in vitro* and *in vivo*. Taken together, Ang2 induced astrocyte apoptosis via αvβ5 integrin signaling contributed to the vascular leakage in the early diabetic retina. I suggest that glycemic control or blocking Ang2/integrin signaling could be a potential therapeutic target to prevent astrocyte loss and vascular leakage in early diabetic retinopathy.

Endothelial hyperpermeability is a major pathogenesis of retinal vascular leakage in DR. Since STAT3 signaling in ECs is involved in the induction of ICAM-1 and VEGF expression (94-96), leading to increase leukocyte infiltration and vascular leakage, it has been proposed that STAT3 signaling in ECs plays a role in the pathogenesis of diabetic retinopathy. In the present study, I focused on the direct effect of STAT3 signaling on the regulation of tight junction proteins associated with endothelial permeability. I demonstrate that IL-6-induced STAT3 activation increases endothelial permeability through the reduced expression of ZO-1 and occludin, which are main

components of intercellular tight junction. The finding in IL-6-treated retinas of mice also supports for ZO-1 and occludin being an important target for activated STAT3.

With respect to the mechanism by which STAT3 activation contributes to the downregulation of ZO-1 and occludin, I found that the activated STAT3 did not directly bind to the promoters of ZO-1 and occludin, but rather bound to VEGF promoter and thereby increased VEGF transcription and production in retinal endothelial cells. The exact mechanism of VEGF expression by STAT3 has not been studied in retinal endothelial cells, but data obtained in various epithelial cancer cells show the direct binding of STAT3 to VEGF promoter.

Pro-inflammatory cytokines including IL-6, IL-1β, and TNF-α are elevated in diabetic retina (42-44) and linked to the pathology of DR (43, 97, 98). The inflammatory responses in the diabetic retina, of which adhesion molecules may be involved, is possibly elicited by IL-6 (99), IL-1β (100), and TNF-α (97). Although the pro-inflammatory responses induced by TNF-α and IL-1β mainly lead to activation of NF-κB and activator protein 1 (101, 102), STAT3 signaling is preferentially activated by IL-6 (103). In addition, IL-6 was reported to mediate angiotensin II-induced inflammation, in which the retinas of IL-6 knockout mice showed the decreased leukostasis induced by angiotensin II (99). However, the signaling pathways that link IL-6 to retinal endothelial permeability are not well characterized. I demonstrated that STAT3 activation is intrinsically important for altering endothelial permeability and vascular leakage through the regulation of tight junction

protein expression in retinal endothelial cells.

In the third study, I demonstrate that microglia-derived IL-6 is important for high glucose-induced retinal endothelial permeability. Although previous studies designated microglia as a source for IL-6 in response to inflammatory challenges such as angiotensin II-treated rat retina (99) and LPS-treated rat brain microglia (104), I found that high glucose alone is able to increase IL-6 expression in human HMO6 cells. Thus, I thought that microglia is a cellular source of IL-6 in diabetic retinopathy. Moreover, I demonstrated that high glucose alone did not affect the levels of tight junction proteins including ZO-1 and occludin in retinal endothelial cells. Rather, the retinal endothelial cells co-cultured with microglia produced the increased endothelial permeability in response to high glucose. This finding suggests the specific contribution of microglia to the high glucose-induced increase in endothelial permeability. There is a possibility that other cytokines such as TNF-α (105) from microglia may be involved in the increased endothelial permeability co-cultured with microglia. However, our finding that an IL-6 neutralizing antibody completely abolished the high glucose-induced increase in the endothelial permeability supports the hypothesis that IL-6 importantly mediates the microglia-induced change in endothelial permeability under high glucose condition.

In conclusion, microglia-derived IL-6 and endothelial STAT3 activation in retinal endothelial permeability is associated with vascular leakage in DR. Our findings indicate that STAT3 in retinal endothelial cells plays a causative role in downregulating ZO-1 and occludin levels. These results suggest the potential importance of IL-6/STAT3 signaling in regulating endothelial

permeability and provide a therapeutic target to treat vascular leakage in DR.

In this chapter, I studied three pathogenesis of DR with respect to three cellular components of blood-retinal barrier (Figure 1-20). Based on these mechanism studies, I suggest 1) inhibition of Ang2/integrin α3β1 signaling pathway to prevent pericyte loss, 2) inhibition of each steps of Ang2/integrin αvβ5/GSK-3β axis to treat astrocyte loss and early vascular leakage, and 3) inhibition of IL-6/STAT3 signaling pathway to treat vascular leakage in DR.

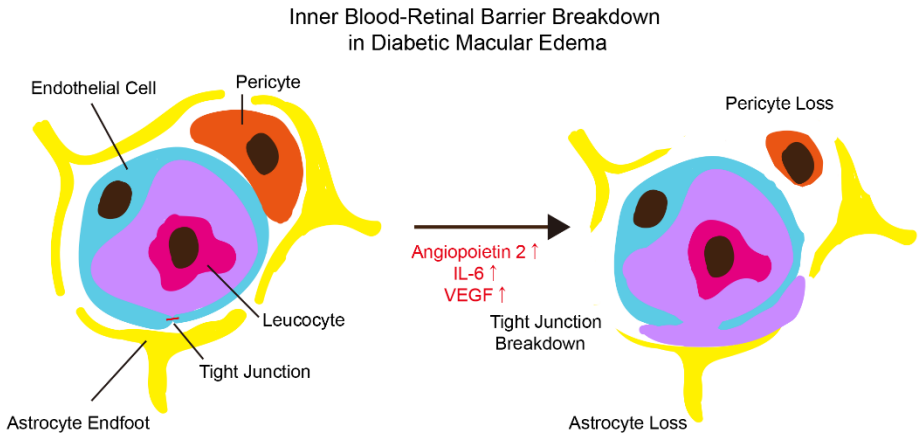

Figure 1-20. Inner blood-retinal barrier breakdown in diabetic macular edema. Inner blood-retinal barrier (BRB) is composed of three cellular components; endothelial cells, pericytes, and astrocytes. In diabetic macular edema, pericyte loss, astrocyte loss, and endothelial tight junction breakdown occurs.

CHAPTER 2

Targeting Amyloid Beta to Treat Dry Age-related Macular Degeneration

INTRODUCTION

Both age-related macular degeneration (AMD) and Alzheimer's disease (AD) increase dramatically with aging, and it has been suggested that they might share common risk factors and pathogenesis (106). The extracellular deposit of amyloid beta (Aβ) form senile plaque in brain, and it is one of the major hallmarks of AD. These deposits are also localized within the drusen between the basement membrane of the retinal pigment epithelium (RPE) and the Bruch's membrane in the human retina of AMD (107, 108), and the mouse retina of AD model (109). Furthermore, Aβ is only found in the drusen from the eyes of the AMD patients (110). The ε4 allele of apolipoprotein E (APOE), the major genetic risk factor for AD (111), may be also associated with AMD (112, 113). In addition, complement factor H (CFH), the main genetic risk factor of AMD, has been detected in Aβ plaques in the brain of AD patients (114), and decreased in the retina of AD mouse model (109).

Although the classical concept suggests that Aβ is deposited extracellularly, growing evidence from AD patients and transgenic mice indicates that Aβ can also accumulate intracellularly and it may contribute to disease progression (115). In the neprilysin gene disrupted mice, Aβ was localized within the subretinal deposits as well as in the cytoplasm of RPE (116). It has been also shown that extracellular Aβ could induce breakdown of the tight junction in RPE (117). However, the role of intracellular Aβ in RPE has not been elucidated yet. Recently, it is known that intracellular Aβ occurs prior to the formation of extracellular amyloid plaques in the subiculum of 5XFAD mice (118). In addition, 5XFAD mouse brain showed alterations in

cerebral tight junctions (119). These findings suggest that accumulation of intracellular Aβ might be an early process that triggers neuronal damage and alterations in outer blood-retinal barrier (BRB) in AD retina. While previous studies revealed the characteristics of the AD mouse retina, the retinal characteristics of 5XFAD mice was not evaluated except for exclusively high level of $A\beta_{42}$ (109, 116, 120). I postulated that intracellular Aβ might have an important role in the retina of 5XFAD mice.

In the first part of Chapter II, I focused on the role of intracellular Aβ and demonstrated that Aβ was intracellularly expressed in the RPE of 5XFAD mice, and that it attenuated the integrity of outer BRB. Taken together, these results suggest that intracellular Aβ could be important in the pathogenesis of dry AMD and retinal aging in AD.

AMD is a leading cause of blindness in the elderly (121). The two types of AMD are: dry and wet AMD. In wet AMD, new blood vessels (known as choroidal neovascularization) grow into the macula and damage the retina. Dry AMD is characterized by the presence of drusen and atrophy of the RPE cells. While laser-induced choroidal neovascularization has been extensively used in the studies of wet AMD (122), there is no single mouse model that fully recapitulates the cardinal features of human dry AMD, mainly due to its multifactorial nature (123, 124). Compared with humans, mice have a simpler Bruch's membrane (BM) structure without a macula. Furthermore, drusen, a hall-mark of dry AMD, is rarely found in mice. Therefore, it is essential to understand the ultrastructural pathology of dry AMD by analyzing basal deposits and BM at the ultrastructural level (124). Despite the efforts to

develop mouse models of dry AMD with various retinal lesions, a lack of an appropriate mouse model for dry AMD has impaired the translational research on the pathogenesis of the disease and the development of therapeutic agents. Thus, I aimed to validate the 5XFAD mouse, an animal model of AD that harbors five familial AD mutations, as a novel dry AMD mouse model that clearly shows amyloid beta deposits in the RPE.

Aβ has been implicated in the pathogenesis of both AD and AMD. Although 5XFAD mice are widely used as an animal model for the study of AD, the use of these mice for modeling dry AMD is largely unexplored. I recently suggested that 5XFAD mice could be used as a mouse model of dry AMD with regard to the Aβ-related pathology (4). In line with AD, I hypothesized that dry AMD is a neurodegenerative disease that involves the accumulation of Aβ. For the evaluation of dry AMD, it is essential to validate the ultrastructural changes in the RPE. However, the ultrastructure of the RPE and BM of aged 5XFAD mice has not yet been investigated. Here, I hypothesized that the eyes of 5XFAD mice would show an ultrastructural pathology consistent with dry AMD as a result Aβ accumulation in the eye.

In the second part of Chapter II, I focused on the ultrastructure of the RPE and BM and conducted a gene analysis of 5XFAD mice to investigate dry AMD like pathology. Using transmission electron microscopy (TEM), I found that aged 5XFAD mice had ultrastructural changes in the RPE and BM that were compatible with the cardinal features of human dry AMD. Furthermore, I analyzed the differential gene expression profiles of the RPE complex in 5XFAD mice to link the anatomical changes to the microarray-based

pathogenesis of dry AMD. These results demonstrate that aged 5XFAD mice have the potential to be used as a novel dry AMD model.

Aβ in drusen may be an important contributor to the development of AMD. Drusen in AMD and senile plaque cores in AD are similar in that deposition of Aβ is found in extracellular space at later stages of both diseases. The role of extracellular Aβ in RPE is known to alter the tight junction without apoptosis (117). Recent studies, on the other hand, suggest that accumulation of intraneuronal Aβ contributes neuronal apoptosis and may be an early event in the pathogenesis of AD (115, 125). In this regard, I recently reported that intracellular Aβ contributed to the breakdown of outer BRB in 5XFAD mice, a mouse model of AD, and suggested that intracellular Aβ could be also a key contributor to the development of AMD (4). However, the precise mechanism of intracellular uptake of Aβ in RPE remains to be elucidated.

Receptor for advanced glycation end products (RAGE), a member of the immunoglobulin superfamily, is a multi-ligand receptor capable of binding diverse range of molecules including Aβ (126). The receptor is known to be highly expressed in the RPE and levels of RAGE are significantly elevated in AMD, especially in RPE adjacent to drusen (127, 128). RAGE is also known to participate in the uptake of Aβ from the circulation into the brain by endocytosis and transcytosis in endothelial cells (129, 130). Recently, it has been suggested that RAGE-mediated signaling contributes to intraneuronal transport of Aβ (131). Thus, I hypothesized that RAGE could contribute to intracellular transport of Aβ in RPE. If Aβ uptake is mediated by RAGE in

RPE, anti-RAGE therapy could inhibit intracellular accumulation of Aβ, and subsequently prevent the breakdown of tight junction in RPE. This can expand the application of anti-RAGE therapy from AD to AMD (132, 133).

In the third part of Chapter II, I demonstrate that subretinal injection of Aβ leads to intracellular uptake of Aβ and subsequent breakdown of tight junction in RPE *in vivo*. I also present evidence that extracellular Aβ gets translocated into intracellular space via RAGE-mediated endocytosis in RPE. The Aβ/RAGE-mediated p38 MAPK signaling contributes to endocytosis of Aβ. Blocking of RAGE inhibits intracellular Aβ-induced tight junction breakdown in RPE. These findings indicate that RAGE contributes to the intracellular transport of Aβ, resulting in increased tight junction breakdown in RPE. Therefore, I suggest that blocking of RAGE can be a potential therapeutic target in AMD.

MATERIALS AND METHDS

1. Animal

Six-week-old, pathogen-free male C57BL/6J mice were purchased from Central Lab (Seoul, Korea). 5XFAD mice were purchased from the Jackson Laboratory (Bar Harbor, ME, USA). 5XFAD mice overexpress mutant human amyloid precursor protein 695 with the Swedish mutation (K670N, M671L: elevate the production of total Ab), Florida mutation (I716V: elevates the production of Ab42 specifically), and London mutation (V717I: elevates the production of Ab42 specifically) and human presenilin 1 with 2 FAD mutations (M146L and L286V: elevate the production Ab42 specifically) (4, 134). All 5XFAD transgenic mice (Tg6799, B6 ⁄ SJL hybrid background) used were heterozygotes with respect to the transgene, and nontransgenic wild-type littermate (WT) mice served as controls. In addition, to eliminate any possible confounding factor from carrying rd1/rd1 genotype (135), all 5XFAD mice used in this study were confirmed not to carry rd1 gene (WT/WT). Mice were maintained under a 12 h dark–light cycle. All animal experiments in this study were in strict agreement with the Association for Research in Vision and Ophthalmology Statement for the Use of Animals in Ophthalmic and Vision Research and the guidelines of the Gwangju Institute of Science and Technology Animal Care and Use Committee.

2. Reagents and antibodies

Rabbit anti-ZO-1 and anti-occludin antibodies, Lipofectamine RNAi max and other culture reagents were purchased from Life technologies (Gaithersburg,

MD, USA). Anti-p38, anti-phospho p38, and anti-β-actin antibodies were purchased from Cell Signaling Technology Inc. (Beverly, MA, USA). Mouse anti-$A\beta_{42}$ (12F4) antibody was purchased from Covance (Seoul, Korea). SB 203580 was purchased from EMD Millipore (Billerica, MA, USA). Anti-RAGE neutralizing mAb (MAB11451) and anti-RAGE antibody (AF1145) were purchased from R&D system Inc. (Minneapolis, MN, USA). EZ-Link Sulfo-NHS-SS-Biotin (Cat #21328) was purchased from Pierce Biotechnology Inc. (Rockford, IL, USA). RAGE siRNA and control negative siRNA were purchased from Bioneer (Daejeon, Korea). $A\beta_{42}$ and FITC labeled $A\beta_{42}$ were purchased from American peptide company Inc. (Sunnyvale, CA, USA).

3. Cell cultures

ARPE-19 cells (American Type Culture Collection, Manassas, VA, USA) were used for human RPE cells. The cells were routinely maintained in Dulbecco's modified Eagle's medium: Nutrient Mixture F-12 (DMEM/F12) containing 10% fetal bovine serum, 100 U/mL penicillin, and 100 μg/mL streptomycin. All culture reagents were purchased from Invitrogen (Carlsbad, CA, USA).

RAGE siRNA and negative siRNA (50 nM) were transfected using Lipofectamine RNAi max in opti-MEM® media according to the manufacturer's instructions. After reaching confluent, ARPE-19 cells were maintained in DMEM/F12 containing 1% FBS to make a polarization for the experiments (136).

4. Histology

Enucleated eyes were fixed in 4% paraformaldehyde for 24 h, and embedded in paraffin for histological analysis and cross section. Four-μm-thick serial sections were prepared from paraffin blocks. Sections were deparaffinized and hydrated by sequential immersion in xylene substitute and graded alcohol solutions. Then sections were stained with hematoxylin and eosin (H&E) for histological examination via light microscopy (Nikon, Tokyo, Japan).

5. Immunofluorescence staining

For immunofluorescence of cross-section of the retina, sections were treated with proteinase K (Sigma Aldrich, St. Louis, MO, USA) for 20 min at 37℃ and 70% formic acid (Sigma Aldrich) for 30 min at room temperature. Then they were rinsed with PBS, and treated with 0.2% Triton-X100 for 20 min at 37℃. After getting rinsed with PBS, the sections were treated with blocking solution (Vector Laboratories, Inc., Burlingame, CA, USA) for 1 h at 37℃. Slides were incubated with mouse anti-Aβ (4G8 or 12F4, 1:100, Covance, Princeton, NJ, USA) for 90 min at 37℃. Alexa 594 donkey anti-mouse IgG (1:400, Molecular Probes, Inc., Eugene, OR, USA) were used as secondary antibodies. The slides were mounted with aqueous mounting medium (DAKO, Glostrup, Denmark) and observed under fluorescence microscope (Nikon, Tokyo, Japan) and confocal microscopes (LSM 510 Meta, Carl Zeiss, Germany, and Leica TCS STED, Leica Microsystems, Germany).

I performed immunofluorescence staining of RPE complex as previously

described (5). After deep anesthesia, mice were sacrificed and enucleated eyes were fixed in 4% paraformaldehyde for 24 h. RPE complex was incubated in Perm/Block solution (0.2% Triton-X 100 and 0.3% BSA in PBS) at RT for 1 h. Then, it was incubated overnight at 4℃ with primary antibodies against rabbit anti-ZO-1 (1:100, cat# 61-7300, Invitrogen, Carlsbad, CA, USA) and mouse anti-Aβ (1:100, 4G8, Covance, Princeton, NJ, USA). After washing with PBS, it was incubated at RT for 2 h with secondary antibodies (Alexa Fluor 488 donkey anti-mouse IgG, 1:200 and Alexa Fluor 594 donkey anti-rabbit Ig G, 1:200). After washing with PBS, it was counterstained with 10 mg/mL DAPI (Sigma Aldrich, St. Louis, MO, USA). After washing with PBS, the RPE/choroid complex was mounted with Fluoromount™ Aqueous Mounting Medium (Sigma Aldrich) and observed under confocal microscope (Leica TCS STED, Leica Microsystems, Germany and LSM710, Carl Zeiss, Oberkochen, Germany).

6. Preparation of oligomeric $A\beta_{42}$ solution

$OA\beta_{42}$ solution was generated as the previously described method (4). $A\beta_{42}$ and FITC labeled $A\beta_{42}$ (62-0-80B and 62-0-82B) were dissolved in hexafluoro-2-propanol (Sigma Aldrich, St. Louis, MO, USA) to a final concentration of 1 mg/mL at room temperature for 3 days. The peptide was aliquoted and dried under vacuum for 1 h. The aliquoted peptide was dissolved in DMSO to a final concentration of 2 mM. The protein concentration was measured using a BCA protein assay kit (Pierce Biotechnology Inc.). The $A\beta_{42}$ stock in DMSO was diluted directly into

DMEM/F12 at 10 μM, and incubated for 24 h at 4℃ to make OAβ_{42}.

7. Cell Viability Assay

Cell viability was determined by WST-1 (2-(4-Iodophenyl)-3-(4-nitrophenyl)-5-(2, 4-disulfophenyl)-2H-tetrazolium, monosodium salt) assay. ARPE-19 cells were seeded into each well of 96-well plates at a concentration of 5×10^3 cells/well. After incubation for 24 h, cells were treated with either 1 μM Aβ_{42-1} as a control or various concentration of Aβ_{42} (0.01-10 μM) for 24 h. Then, 10uL of WST-1 solution was added into each well. After incubation at 37℃ for 2 h, absorption at 450 nm was measured using a microplate spectrophotometer (Molecular Devices, Sunnyvale, CA, USA). Three independent experiments were performed for each experimental condition.

8. Biotinylation of membrane proteins

Biotinylation of cell membrane proteins was performed as previously described method (131). ARPE-19 cells plated in 8-well culture slides were washed with PBS and incubated with PBS containing 300 μg/mL sulfo-NHS-SS-biotin at room temperature for 30 min. The biotinylation of membrane proteins was quenched using 1 M glycine in PBS at 4℃ for 15 min. After additional two brief wash with 100 mM glycine in PBS to remove the residual biotin, cells were incubated with OAβ_{42} at 37℃ for 1 h. Then, to terminate uptake of biotinylated proteins, cells were washed with cold NT buffer (150 mM NaCl, 1mM EDTA, 0.2% BSA, and 20 mM Tris, pH 8.6). Then, cells were incubated with 50 mM MesNa/NT buffer at 4℃ for 30 min.

9. Immunocytochemistry

ARPE-19 cells with confluence were incubated with OAβ_{42} (10 μM) in serum free DMEM/F12 medium for 24 h. After removal of the medium, cells were intensively washed with warm PBS and fixed with 4% paraformaldehyde at RT for 15 min. For the permeabilization, 0.2% Triton X-100 in PBS was treated for 10 min. After washing, the cells were incubated with 1% BSA in PBS at RT for 1 h. Cells were incubated overnight at 4℃ with rabbit anti-ZO-1 (1:1000), mouse anti-Aβ (1:1000), and goat anti-RAGE (1:500), or Alexa 488 conjugated phalloidin (1:500, Molecular Probes). After washing, cells were incubated at RT for 1 h with secondary antibodies (Alexa Fluor 488, 594, 647 anti-mouse, rabbit, goat IgG, 1:500). Nucleus was counterstained with DAPI at RT for 10 min. After washing, the slides were mounted and observed under confocal microscope (Leica TCS STED).

10. Western blotting

ARPE-19 cells were incubated with 10 μM OAβ_{42} and A$\beta_{42\text{-}1}$ for 24 h. ARPE-19 cells were incubated with 10 μM OAβ_{42} for 30 min to detect p38 MAPK and for 24 h to detect intracellular Aβ and tight junction proteins. SB 203580 (10 μM, p38 MAPK inhibitor, EMD Millipore, 559395) was pretreated 30 min prior to OAβ_{42} treatment. Anti-RAGE neutralizing antibody (20 μg/mL) was pretreated 2 h prior to OAβ_{42} treatment.

Cell proteins were extracted with RIPA buffer (Tris 50mM pH 7.4; NaCl 150 mM; SDS 0.1%; NaDeoxycholate 0.5%; Triton X-100 1%) with a

complete protease inhibitor cocktail (Roche, Indianapolis, IN, USA). Equal amounts of protein were separated by SDS-PAGE, and transferred to nitrocellulose membranes (GE healthcare, Piscataway, NJ, USA). After blocking in 5% skim milk in PBST (0.1% Tween 20 in PBS), the membranes were incubated with primary antibodies for ZO-1 (1:1,000), ZO-2 (1:1,000), occludin (1:2,000), claudin-1 (1:1,000), p38 (1:1,000), phospho-p38 (1:1,000), $A\beta_{42}$ (1:1000), and actin (1:5,000). The membranes were incubated with ECL substrate (DoGEN, Seoul, Korea) and exposed in ImageQuant™ LAS 4000 (GE healthcare life sciences). The band intensity analyzed using ImageJ 1.42 software (National Institutes of Health, Bethesda, MD, USA).

11. Transepithelial electrical resistance measurement

The measurement of TER was performed by impedance analysis using cellZscope® (NanoAnalytics GmbH, Munster, Germany) or EVOM2 TER (World Precision Instruments). Briefly, the cell covered transwell filters (0.4 μm, Corning Inc., NY, USA) coated with laminin were placed in this setup using 12-well plate. After stabilization of TER value on plateau, TER was measured with 10 μM $OA\beta_{42}$ and $A\beta_{42\text{-}1}$ over 24 h or with 10 μM $OA\beta_{42}$ and anti-RAGE neutralizing antibody (20 μg/mL) for 48 h. The TER value just after treatment was normalized to 100% for relative analysis.

12. $A\beta_{42}$ ELISA

For $A\beta_{42}$ ELISA, enucleated eyes were immediately separated into neural retina and RPE/choroid complex. Then, each sample was snap-frozen in liquid

nitrogen and kept in -80℃ until analysis. I measured Aβ level in retina and RPE complex with ELISA Human $A\beta_{42}$ Ultrasensitive ELISA Kit (Invitrogen, cat#KHB3544) according to the manufacturer's instructions. Each sample was lysed with RIPA buffer and centrifuged at 13,000 RPM for 20 min. Supernatants were designated to RIPA soluble fraction of $A\beta_{42}$. Then, the pellet, RIPA insoluble fraction, was further lysed with 70% formic acid and sonicated briefly. Then, the sample was ultracentrifuged at 100,000 g for 1 h. The supernatants after ultracentrifugation were isolated and neutralized by adding 1M Tris (pH 11). This fraction was designated as RIPA insoluble sample. Total tissue protein was measured from each sample using BCA kit.

13. Transmission electron microscopy (TEM)

For TEM, 8 eyes from 4 mice were used from each group of 9-month-old male WT, 9-month-old male 5XFAD, and 12-month-old male 5XFAD. Enucleated eyes were immediately fixed in 1.5% paraformaldehyde/1.5% glutaraldehyde in 0.1 M sodium cacodylate buffer (pH 7.4), postfixed in 1% osmium tetroxide in 0.1 M sodium cacodylate buffer (pH7.4), dehydrated in a graded ethanol series, and embedded in epoxy resin according to standard protocols. Semithin sections (1-μm thick) were stained with toluidine blue; ultrathin sections were stained with uranyl acetate and lead citrate and were examined with an electron microscope (H-7650, HITACHI, Japan). The thickness of Bruch's membrane was measured in two representative images per each case (n = 8). The thinnest and thickest parts of BM were measured and the average thickness was determined (137).

14. RNA extraction and Microarray based gene expression profiling

I performed global gene expression analyses using Affymetrix GeneChip® Mouse Gene 2.0 ST oligonucleotide arrays. For microarray-based expression profiling, RPE/choroid complex was isolated from neural retina immediately after enucleation. Then, each sample was snap-frozen in liquid nitrogen and kept in -80℃. Total RNA was isolated from RPE/choroid complex using TRIzol reagent (Invitrogen) according to the manufacturer's instructions. RNA quality was assessed by Agilent 2100 bioanalyser (Agilent Technologies, USA), and quantity was determined by ND-1000 spectrophotometer (NanoDrop Technologies, USA). Per RNA sample, 300 ng were used as input into the Affymetrix procedure according to the manufacturer's recommended protocol (http://www.affymetrix.com). For data analysis, Affymetrix GeneChip® Human Gene 2.0 ST oligonucleotide array was scanned using Affymetrix Model 3000 G7 scanner and the image data was extracted through Affymetrix Commnad Console software1.1. The raw .cel file generated through above procedure meant expression intensity data and was used for the next step. Expression data were generated by Affymetrix Expression Console software version1.1. For the normalization, RMA (Robust Multi-Average) algorithm implemented in Affymetrix Expression Console software was used. In order to classify the co-expression gene group which has similar expression pattern, I performed Hierarchical clustering in MEV (MultiExperiment Viewer) software 4.4 (www.tm4.org) using differentially regulated transcripts with a fold change (FC) greater than 1.2. The web-based tool, DAVID (the

Database for Annotation, Visualization, and Integrated Discovery) was used to perform the biological interpretation of differentially expressed genes (138). Then, these genes were classified based on the information of gene function in Gene ontology, KEGG Pathway database. (http://david.abcc.ncifcrf.gov/home.jsp). Array data are available in the GEO database under GSE85408. Database from microarray were available via files in online Supporting Information.

15. Subretinal injection

Twenty-week-old C57BL/6J mice were deeply anesthetized using a mixture of Zoletil 50® (Virbac, Carros, France) and Rompun® (Bayer Korea, Seoul, Korea) (3:1 ratio, 1mL/kg, i.p.). Then subretinal injection was done as previously described (139). Two microliter of 100 μM OAβ_{42} was injected using Nanofil syringe with 33 G blunt needle (World Precision Instruments Inc., Sarasota, FL, USA) under operating microscope (Leica Microsystems Ltd. Seoul, Korea). For the control mice, only 2 μL of DMEM/F12 media without Aβ was injected as a vehicle.

16. Real-time PCR

Total RNA was isolated from RPE cells using TRIzol reagent according to the manufacturer's instructions. cDNA was prepared with High Capacity RNA-to-cDNA kit. Real-time PCR was performed with StepOnePlus Real-time PCR System with TaqMan® Fast Advanced Master Mix and specific Gene Expression Assays (*AGER* and *GAPDH*). All procedures were performed in

accordance with the MIQE guidelines. All material and machine used in Real-time PCR was purchased from Life Technologies.

17. Statistical analysis

Statistical analyses were performed using SPSS software version 18.0 (SPSS Inc., Chicago, IL, USA). Two-tailed unpaired *t*-test was used. *P* values less than 0.05 were considered to be statistically significant. Data and figures are depicted as mean ± SEM.

RESULTS

5XFAD mice show the features of dry AMD in the outer retina with intracellular Aβ in RPE

It is known that Aβ deposits lead to retinal degeneration similar to dry AMD in AD mouse retina. Among AD mouse models, 5XFAD mice showed the highest retinal abundance of $A\beta_{42}$. However, the retinal pathology focusing on the RPE of 5XFAD mice has not been described yet. In order to evaluate whether 5XFAD mice show the features of dry AMD, light microscopic findings with H&E were evaluated in the 5XFAD mice retina. Retinas of 12 month old 5XFAD mice were different from those of control littermate mice. Similar to senescent neprilysin gene–disrupted mice (116), 5XFAD mice had large vacuoles, hypopigmentation in the RPE layer and thickened Bruch's membrane (Figure 2-1A and B). Of importance, 5XFAD mice had drusen-like deposit between RPE and Bruch's membrane (Figure 2-1B). In addition to thickened Bruch's membrane with Aβ deposits beneath the RPE layer, I found that retinal Aβ accumulated in the RPE layer of 5XFAD mice (Figure 2-1C and D).

Intracellular Aβ accumulates in RPE and attenuates the tight junction of RPE in 5XFAD mice

To visualize typical tight junction integrity of RPE cells, the flat mounts of RPE/choroid complex were performed and immunostained for the tight junction proteins and Aβ (Figure 2-2). In 8 month old 5XFAD mice, abundant intracellular Aβ (Figure 2-2B and D) were detected in the cytosol of RPE

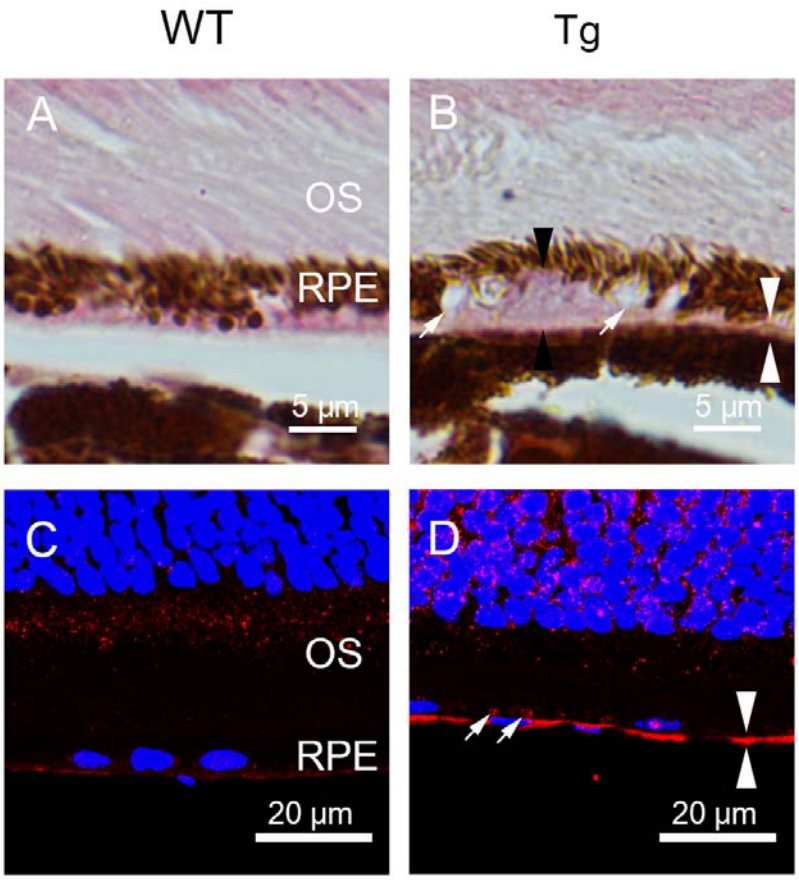

Figure 2-1. Retinal sections of 12 months old 5XFAD mice show the features of dry AMD in the outer retina and intracellular Aβ in RPE. The outer segment/retinal pigment epithelium (RPE)/choroid interface of cross sections are evaluated in 12-month old control and transgenic mice with 5 familial autosomal dominant mutations (5XFAD). In hematoxylin and eosin (H&E)-stained retinal sections, (A) WT mice show normal RPE layer and Bruch's membrane. (B) Those of 5XFAD mice show large vacuoles (arrows), hypopigmentation and thick Bruch's membrane (white arrowheads). Black arrowheads indicate sub-RPE drusen-like deposit. In retinal sections

immunostained with Aβ (red), (C) WT mice show no Aβ accumulates in the RPE layer. (D) Intracellular Aβ accumulates in the RPE layer of 5XFAD mice. There is a significant increase in Aβ immunoreactivity in RPE layer (arrows). White arrowheads indicate Bruch's membrane with Aβ. Nuclei were counterstained for DAPI. (A, B) Magnification ×1000. Scale bar = 5 μm. (C, D) Magnification ×1600. Scale bar = 20 μm. WT, wild type; Tg, 5XFAD transgenic mice; OS, outer segment; RPE, retinal pigment epithelium.

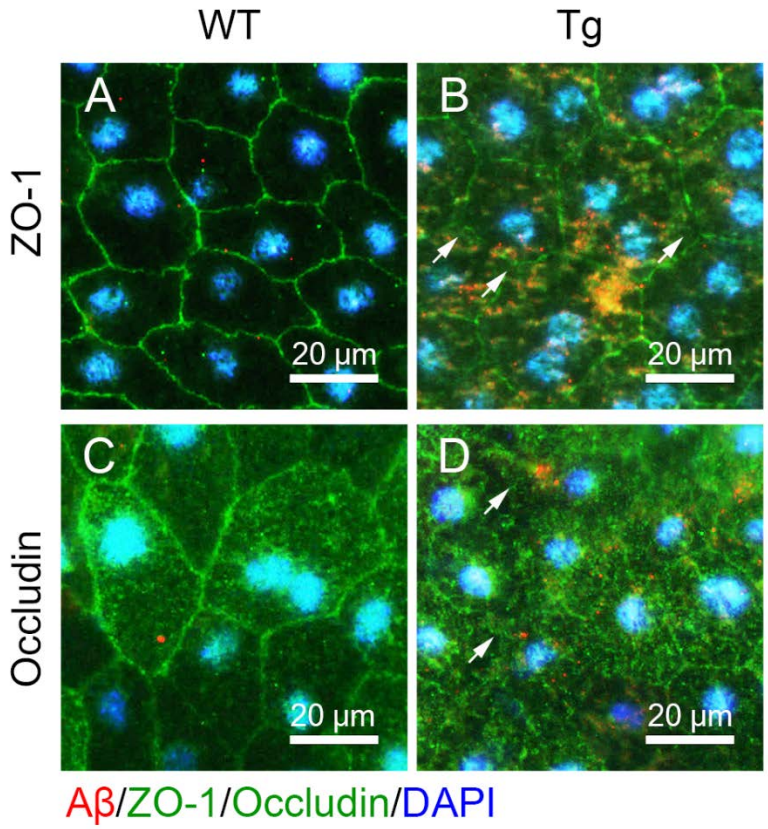

Figure 2-2. Intracellular Aβ accumulates in the RPE and attenuates RPE tight junction integrity in 5XFAD mice. (A, B) Representative flat mounts of RPE of WT (A) and Tg (B) mice stained for $A\beta_{42}$ (red) and ZO-1 (green). There is a significant increase in $A\beta_{42}$ immunoreactivity in the RPE of Tg retina with an attenuated and disorganized expression in ZO-1 (arrows). (C, D) Representative flat mounts of RPE of WT (C) and Tg (D) mice stained for $A\beta_{42}$ (red) and occludin (green). Occludin integrity is severely hampered where $A\beta_{42}$ immunoreactivity is detected in the RPE of Tg retina (arrows). All sections were counterstained for DAPI. Magnification ×400. Scale bar = 20 μm.

compared with control mice (Figure 2-2A and C). With increasing intracellular accumulation of Aβ in the RPE cell, ZO-1 labeled tight junction integrity was attenuated and disorganized (Figure 2-2B) compared to the typical hexagonal shape of RPE tight junction in control mice (Figure 2-2A). In addition, occludin labeled tight junction integrity was significantly attenuated in 5XFAD mice (Figure 2-2D) than those in controls (Figure 2-2C).

Exogenous oligomeric $A\beta_{42}$ is taken up by RPE and intracellular $A\beta_{42}$ attenuate tight junction integrity of ARPE-19 cells

To investigate the role of Aβ on the tight junction in RPE cells, I performed *in vitro* study. First, WST-1 assay was performed to determine the concentration of Aβ with sublethal cytotoxicity. $OA\beta_{42}$, which is known to have more potent cytotoxic effect than $A\beta_{42}$ monomer, did not affect the viability of ARPE-19 cells up to 10 μM. Then, I performed immunocytochemistry for Aβ and tight junction protein ZO-1 and occludin in ARPE-19 cells. After 24 h of exogenous $OA\beta_{42}$ treatment, Aβ was abundantly detected in RPE cells, mainly in the intracellular area under confocal microscopic evaluation. Furthermore, I confirmed that both ZO-1 and occludin were decreased and lost their integrity as tight junction in ARPE-19 cells with intracellular $OA\beta_{42}$ (Figure 2-3). On the other hand, ARPE-19 cells treated with reverse $A\beta_{42\text{-}1}$, an inactive control peptide, showed well organized tight junction with no detectable $A\beta_{42\text{-}1}$ accumulation

RPE took up exogenous oligomeric $A\beta_{42}$ time dependent manner (Figure 2-4). RPE cells showed relatively conserved ZO-1 integrity at 6 h.

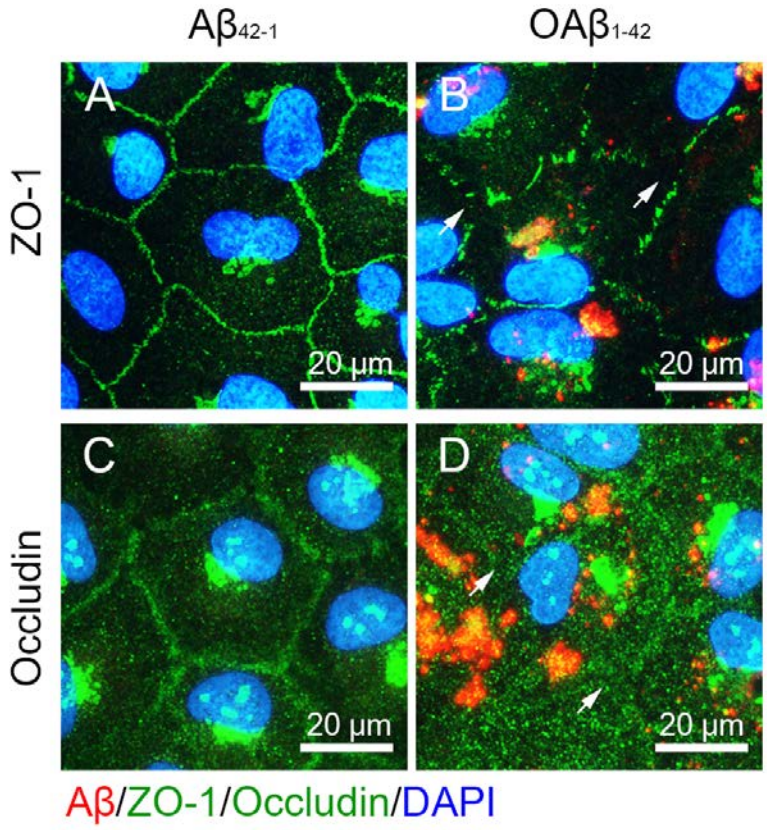

Figure 2-3. Exogenous oligomeric $A\beta_{42}$ is taken up by RPE and intracellular $A\beta_{42}$ attenuate tight junction integrity of ARPE-19 cells. Immunocytochemistry of $A\beta_{42}$ (red), and tight junction proteins (green) ZO-1 (A, B) and occludin (C, D) in ARPE-19 cells. ARPE-19 cells were incubated for 24 h with (A, C) reverse $A\beta_{42\text{-}1}$ 10 μM, and (B, D) $OA\beta_{42}$ 10 μM. (A, C) RPE cells show integrated and organized hexagonal shape with ZO-1 (A) and Occludin (C) expression as tight junctions without intracellular uptake of Aβ. (B, D) RPE cells show intracellular distribution of $A\beta_{42}$ (red) 24 h after exogenous $OA\beta_{42}$ treatment. Aβ uptaken RPE cells show disintegrated and disorganized hexagonal shape with attenuated ZO-1 and occludin expression

as tight junctions. Arrows indicate disrupted tight junction. Magnification ×400. Scale bar = 20 μm.

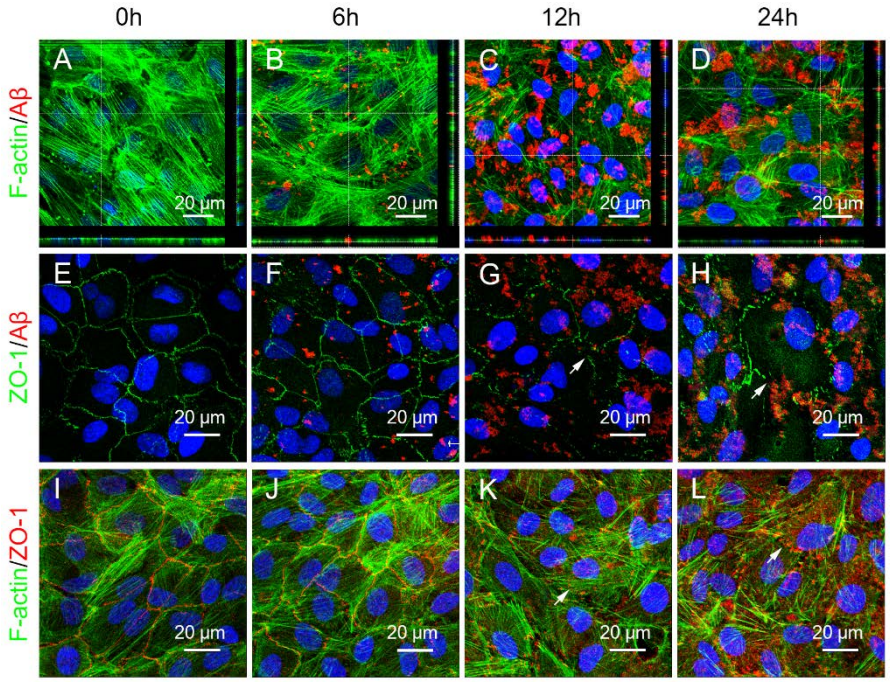

Figure 2-4. RPE takes up exogenous oligomeric $A\beta_{42}$ time dependent manner and intracellular $A\beta_{42}$ attenuate tight junction integrity. Immunocytochemistry were performed for Aβ, tight junction protein ZO-1, and cytoskeleton F-actin. ARPE-19 cells were incubated for 24 h with $OA\beta_{42}$ 10 μM. (A-D) Z-stack images were reconstructed with X and Y axis orthogonal views under confocal microscopy. RPE takes up exogenous oligomeric $A\beta_{42}$ time dependent manner. Intracellular $A\beta_{42}$ increases after 12 h. (E-H) RPE cells show relatively conserved ZO-1 integrity at 6 h (F). (G, H) Aβ-laden RPE cells show disrupted tight junction after 12 h. Arrows indicate disrupted tight junction. (I-L) Aβ induces tight junction breakdown without cell retraction. Arrows indicate disrupted tight junction. Magnification x1000. Scale bar = 20 μm.

Intracellular $A\beta_{42}$ dramatically increased after 12 h and Aβ-laden RPE cells showed disrupted tight junction after 12 h. Intracellular $A\beta_{42}$ induced tight junction breakdown without cell retraction (Figure 2-4).

Oligomeric $A\beta_{42}$ alters the tight junction protein in ARPE-19 cells

I also performed the western blot assay to evaluate the change of tight junction protein with $OA\beta_{42}$. ARPE-19 cells were treated with $OA\beta_{42}$ 10 μM, or inactive reverse control peptide $A\beta_{42\text{-}1}$ as a control. After 24 h of $OA\beta_{42}$ 10 μM treatment, while claudin-1 level was not changed, tight junction proteins including ZO-1, ZO-2 and occludin were decreased (Figure 2-5A and B). In addition, $OA\beta_{42}$ decreased occludin time dependent manner (Figure 2-5C). In accordance with this data, TER with $OA\beta_{42}$ 10 μM was sustained for 6 h, then declined abruptly (Figure 2-5D).

Breakdown of tight junctions with Aβ accumulation in the RPE of the aged 5XFAD mice

To validate the aged 5XFAD mouse as an animal model for dry AMD, I first investigated the integrity of the outer BRB. Compared with the hexagonal shape of the RPE in the 12 month-old wild type (WT) mice, the irregularly shaped apical tight junction (ZO-1) of the RPE in the 12 month-old 5XFAD mice indicated the breakdown of the outer BRB (Figure 2-6A). In addition to the loss of ZO-1 at the apical RPE, note that abundant Aβ deposits were present at the basal RPE juxta above the choroidal endothelial cells in the RPE/choroid complex flat-mounts (z-axis).

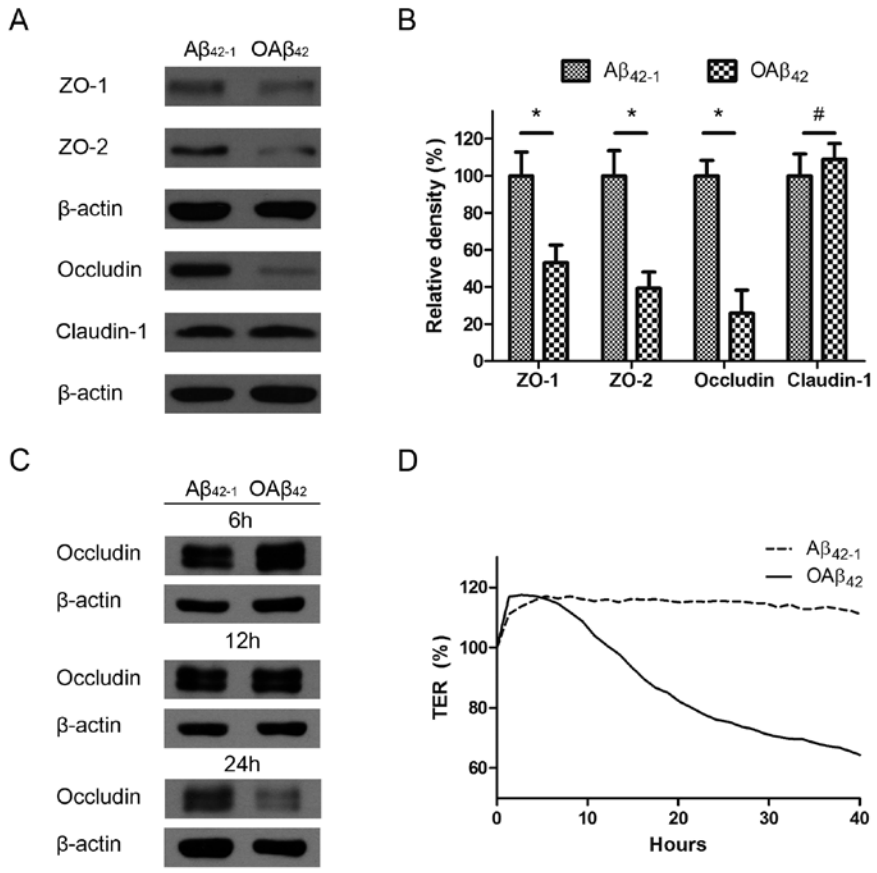

Figure 2-5. Oligomeric Aβ$_{42}$ alters the tight junction protein in ARPE-19 cells. (A, B) ARPE-19 cells were incubated for 24 h with 10 μM oligomeric Aβ$_{42}$ (OAβ$_{42}$) and inactive reverse peptide Aβ$_{42-1}$ as a control. (A) Tight junction proteins (ZO-1, ZO-2, occludin, and claudin-1) were evaluated by western blot. β-actin was used as an internal control. (B) Quantitative analysis was performed by measuring the densitometry of each band relative to β-actin. Each value represents the mean (± SEM) of three independent experiments (*P < 0.05, #P >0.05). (C) OAβ$_{42}$ induced significant decrease in occludin levels in a time-dependent manner in ARPE-19 cells. Cells were incubated for

6, 12, and 24 h with 10 μM OAβ_{42} and inactive reverse peptide A$\beta_{42\text{-}1}$ as a control. Occludin expression was evaluated by western blot. β-actin was used as an internal control. (D) Transepithelial electrical resistance (TER) was measured and normalized to the TER value just after Aβ treatment.

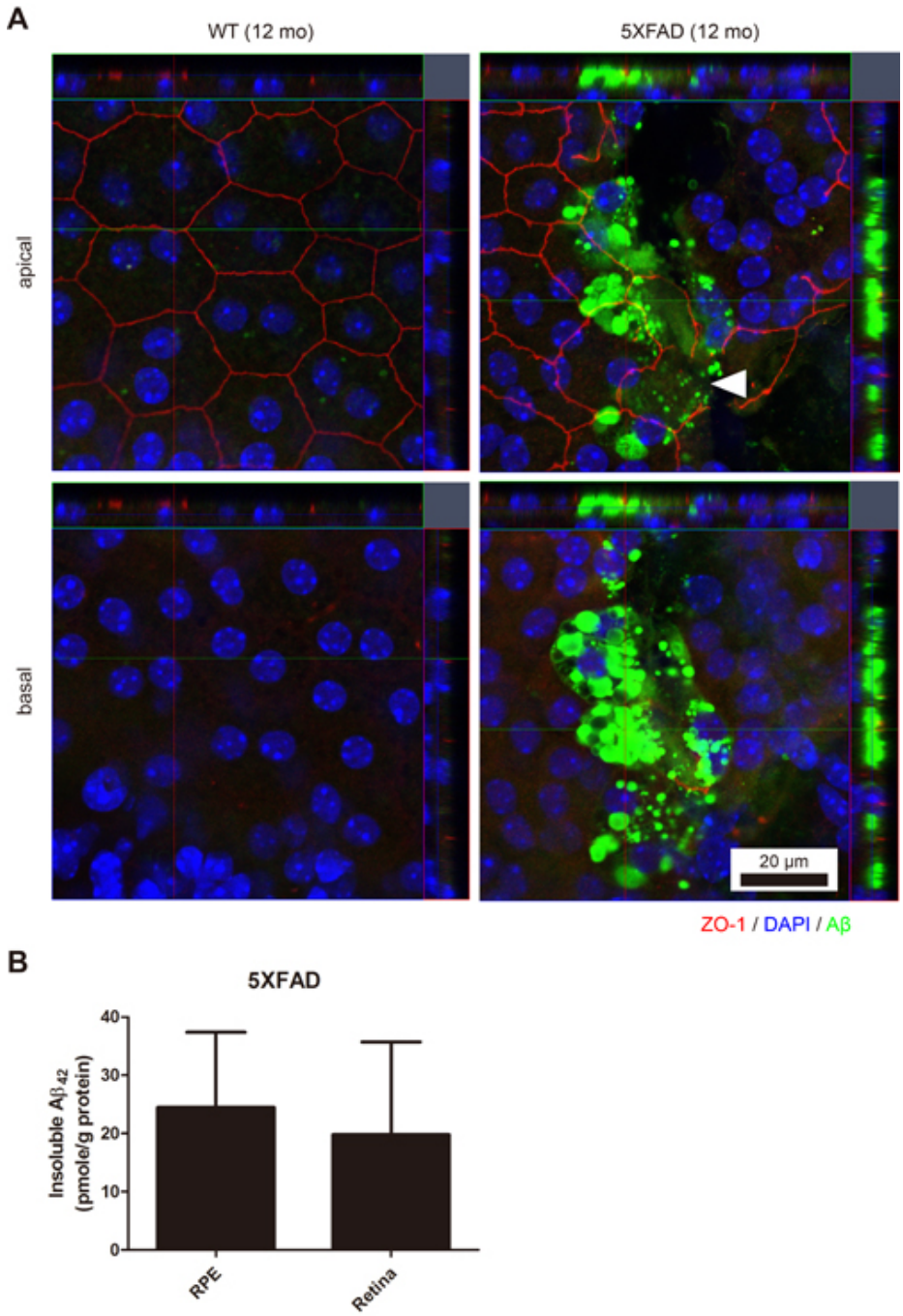

Figure 2-6. The RPE/choroid/scleral complex of aged 5XFAD mice with intracellular Aβ accumulation. (A) The RPE complex of the 12-month-old 5XFAD mice and the age-matched wild-type littermate mice (WT) were flat-

mounted (n = 4). Representative images of 5XFAD mice show irregular apical tight junctions (ZO-1, red) compared to typical hexagonal tight junctions in the aged-matched WT mice. Arrowhead indicates disrupted tight junction of the RPE. Abundant accumulation of Aβ (green) was occasionally observed in the RPE complex of 5XFAD mice. Scale bar = 20 μm. (B) $A\beta_{42}$ levels of the RPE complex and the retina in 5XFAD mice (n = 7).

These Aβ deposits at the RPE/choroid complex of the aged 5XFAD mice were also detected by ELISA as an insoluble form of $A\beta_{42}$ (Figure 2-6B), not as a soluble form of $A\beta_{42}$. The level of Aβ in the WT mice was below the detection limit of the ELISA.

Increased thickness of Bruch's membrane (BM) in the aged 5XFAD mice

Thickening of BM is one of the cardinal features of early dry AMD. I recently reported the thickening of BM in locations where Aβ deposits downregulate tight junctions in the RPE of aged 5XFAD mice (4). However, this observation was based on H&E stained cross-sections, not on TEM-based ultrastructure. Thus, I analyzed the ultrastructure of the RPE/choroid of the aged 5XFAD mice in this study. The average thickness of BM was 0.68 ± 0.05 μm in the 9-month-old WT mice, 1.06 ± 0.08 μm in the 9-month-old 5XFAD mice, and 1.03 ± 0.10 μm in the 12-month-old 5XFAD mice, respectively (Figure 2-7A-D). Although there was no significant change in the BM thickness between the 9-month-old and the 12-month-old 5XFAD mice, there was a significant increase in the BM thickness of the aged 5XFAD mice compared with that of the 9-month-old WT mice (n = 8, One-way ANOVA and Tukey's post hoc tests, $P < 0.01$, Figure 2-7D).

Basal laminar and basal linear deposits at BM of 5XFAD mice

Drusen is a hallmark of dry AMD. Although I did not find large-drusen, I observed both basal laminar deposits and basal linear deposits (Figure 2-8). Basal laminar deposits were occasionally found in the 9-month-old WT mice.

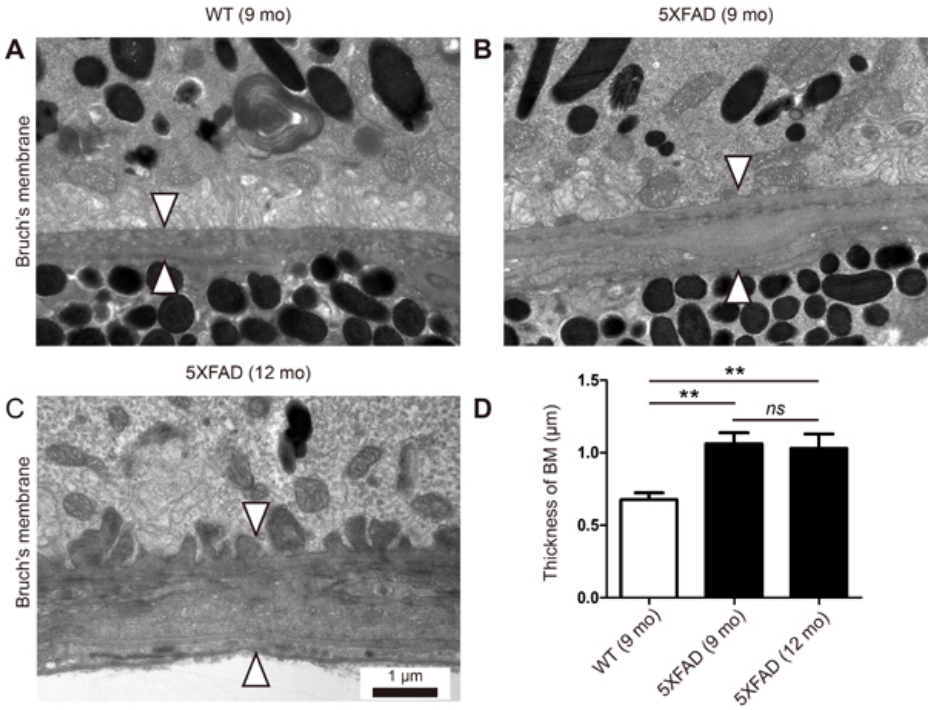

Figure 2-7. Thickening of Bruch's membrane in aged 5XFAD mice. (A) Representative transmission electron micrograph (TEM) images of the RPE complex from the 9 months old wild-type littermate mice (WT). (B and C) Representative TEM images of the RPE complex from the 9 and 12-month-old 5XFAD mice. (A) WT mice show normal structure and thickness of Bruch's membrane (arrowheads). (B and C) 5XFAD mice show thickening of Bruch's membrane (arrowheads) with basal linear deposits in outer collagenous layer (B) or with basal laminar deposits and loss of fenestration at choriocapillaris (C). Scale bars are 1 µm. (D) Thickness of Bruch's membrane (BM). Error bars indicate SEM. (n = 8). One-way ANOVA and Tukey's post hoc tests, $^{**}P < 0.01$.

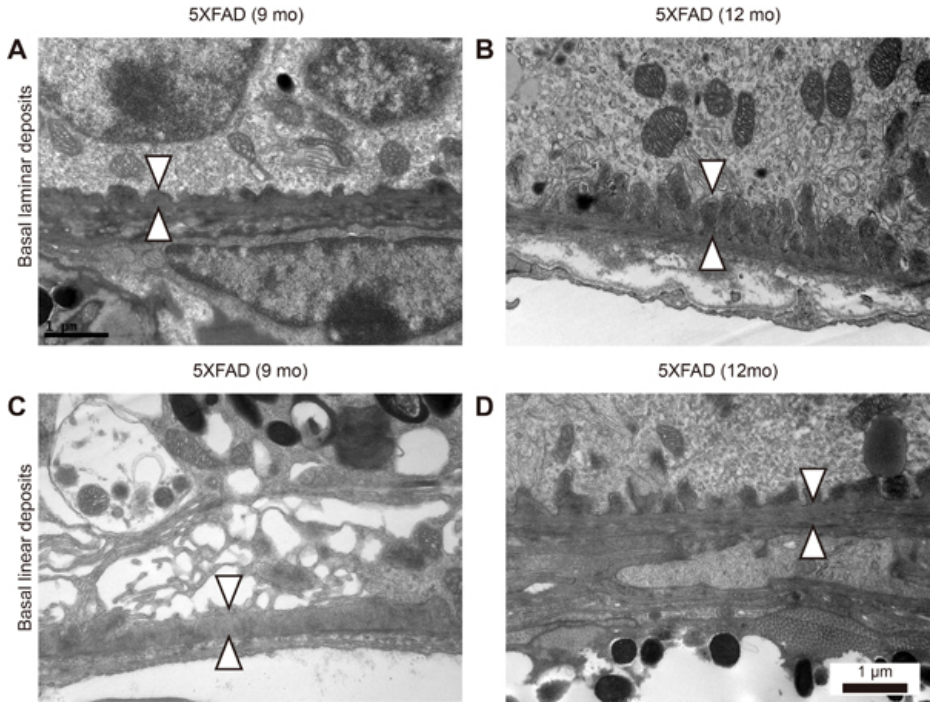

Figure 2-8. Basal laminar and linear deposits at Bruch's membrane in aged 5XFAD mice. (A-D) Representative transmission electron micrograph (TEM) images of RPE complex from 9 and 12-month-old aged 5XFAD mice. (A) 5XFAD mice showed undulating surface of Bruch's membrane with basal laminar deposits (arrowheads). (B) 5XFAD mice showed elongated basal laminar deposits (arrowheads) with loss of basal infolding. (C) 5XFAD mice showed basal linear deposits (arrowheads) at inner collagenous layer of Bruch's membrane and cystic degeneration of RPE. (D) 5XFAD mice showed both basal laminar and basal linear deposits (arrowheads). Scale bars are 1 μm.

However, the deposits in the aged 5XFAD mice were continuous and long enough to form undulating basal laminar deposits (Figure 2-8A and B). Basal linear deposits were found only in the aged 5XFAD mice (Figure 2-7B and C and Figure 2-8C and D) and they were associated with the increase in BM thickness. Note that the endothelial fenestrations were lost in the choriocapillaris underlying BM with the basal linear deposits (Figure 2-7C and Figure 2-8C).

Loss of apical microvilli and basal infolding in the RPE of the aged 5XFAD mice

The phagocytosis of shed photoreceptor rod outer segments (POS) by the RPE is essential for the maintenance of retinal function. In the 5XFAD mice, I observed a loss of the apical microvilli (Figure 2-9A and B). I performed a microarray-based differential expression gene analysis to investigate the relationship between the RPE structure and gene expression. Note the downregulation of *Itgav* (0.591 fold, $P = 0.0293$); the RPE requires αvβ5 integrin for binding to the shed POS (140). *Cldn1* (Claudin 1, 0.644 fold, $P = 0.0266$) is localized to the cilia of the RPE (141) and *Rrh* (retinal pigment epithelium derived rhodopsin homolog, 0.641 fold, $P = 0.00466$), also known as peropsin, is localized to the microvilli in the RPE (142). Thus, decreased expression levels of these genes might be strongly associated with a loss of microvilli (Figure 2-9). In addition, *F3* (coagulation factor III, 0.613 fold, $P = 0.00098$) is known to be upregulated in the RPE after POS uptake (143), as well as in the macrophages after phagocytosis (144). Thus, downregulation of

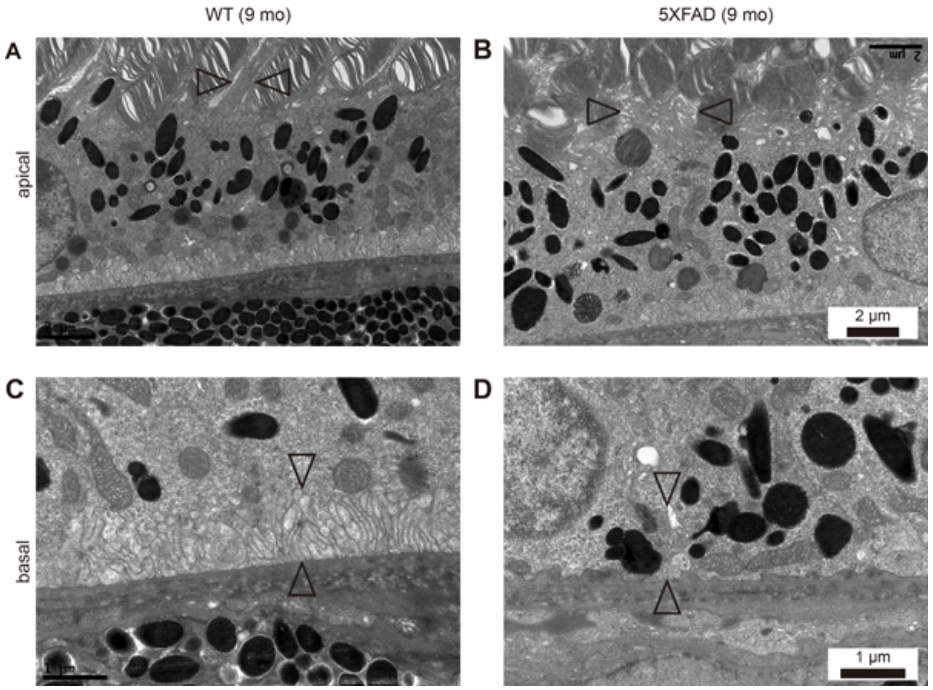

Figure 2-9. Loss of apical microvilli and basal infolding in aged 5XFAD mice. (A and C) Representative transmission electron micrograph (TEM) images of RPE complex from 9-month-old wild-type littermate mice (WT). (B and D) Representative TEM images of RPE complex from 9-month-old 5XFAD mice. (A) WT mice showed normal microvilli (arrowheads) surrounding photoreceptor outer segments (POS) at apical RPE. (B) 5XFAD mice showed disorganized apical microvilli (arrowheads) and POS. Scale bars are 2 μm. (C) WT mice showed well organized basal infolding (arrowheads) above Bruch's membrane, supporting intracellular organelles at basal RPE. (D) 5XFAD mice showed loss of basal infolding (arrowheads) and unsupported intracellular organelles juxta above Bruch's membrane. Scale bars are 1 μm.

F3 might be related to the decrease in POS uptake in the RPE resulting from the loss of microvilli. The differentially expressed gene profile associated with the apical microvilli is shown in Table 2-1.

I also observed a loss of basal infolding in the aged 5XFAD mice (Figure 2-9C and D), which supports intracellular organelles although the precise role of basal infolding is not well established. A loss of basal infolding, which led to direct contact between the intracellular vesicles, including lipofuscin and phagosomes, and BM, thereby affected the thickness of BM.

Increased number of intracellular granules of the RPE in the aged 5XFAD mice

One of the important functions of the RPE is to phagocytose POS and digest them for recycling. However, the incomplete digestion of POS may lead to the accumulation of undigested POS granules in phagosomes or accumulation of lipofuscin granules in the RPE. Indeed, the 9-month-old 5XFAD mice RPE contained more undigested POS granules (Figure 2-10B, 10.4 ± 0.8 per high power field, n = 8) than the age-matched WT mice (Fig. 5A, 5.0 ± 1.1 per high power field, n = 8, P = 0.0017). In addition to undigested POS-laden phagosomes, charcoal like granules (Figure 2-10C) or increased numbers of lipofuscin granules (Figure 2-10D) were observed in the RPE of the 5XFAD mice, especially at the basal side of the RPE, where the basal infolding was lost.

Table 2-1. Selected genes associated with phagocytosis and microvilli in differential gene expression profile of 5XFAD mice.

Gene symbol	Gene name	Fold change (TG/WT)	p-value
Itgav	integrin alpha V	0.591	0.029
Cldn1	claudin 1	0.644	0.026
Rrh	retinal pigment epithelium derived rhodopsin homolog	0.641	0.004
F3	coagulation factor III	0.613	0.009

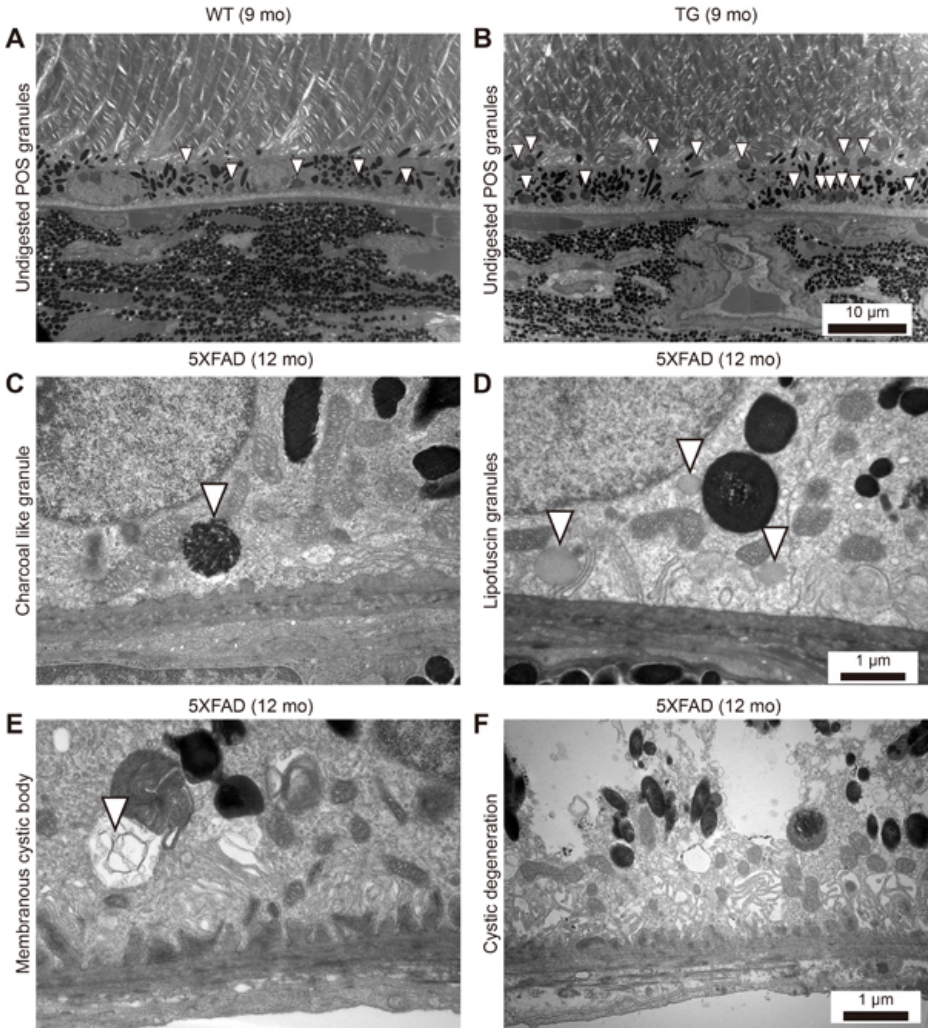

Figure 2-10. Increased number of intracellular granules of the RPE in aged 5XFAD mice. (A-D) Representative transmission electron micrograph (TEM) images of the RPE complex from 9 and 12-month-old 5XFAD mice and 9-month-old wild-type littermate mice. (A) WT mice showed normal distribution of melanin pigments and lysosomal granules (arrowheads). (B) 5XFAD mice showed increased number of undigested photoreceptor cell outer segments (POS) in lysosomal granules (arrowheads). Scale bars are 10 μm. (C) 5XFAD mice occasionally showed a charcoal-like granule

(arrowhead) with loss of basal infolding. (D) 5XFAD mice showed increased number of lipofuscin granules with disrupted basal infolding. Scale bars are 1 μm. (E) 5XFAD mice showed membranous cystic body (arrowhead). (F) 5XFAD mice showed marked cystic degeneration with ruptured cystic vacuole and disseminated undigested particles in RPE. Scale bars are 1 μm.

Differentially expressed gene profile associated with retinol metabolism and the inflammatory pathway in the RPE complex of the aged 5XFAD mice.

In the aged 5XFAD mice, I observed an intracellular membranous cystic body in the RPE as well as cystic degeneration (Figure 2-10E and F). Evidently, the cystic degeneration of the RPE led to RPE dysfunction other than phagocytosis or vice versa. One of the important roles of the RPE is retinol metabolism. Our microarray-based differential expression gene analysis revealed the down-regulation of several key enzymes involved in retinol metabolism (Figure 2-11A and B). *Adh7* (2.322 fold, $P = 0.012$) is associated with retinol metabolism. Furthermore, *Rpe65* (0.801 fold, $P = 0.0290$) is a major player in retinol metabolism, and its loss has been directly linked to retinal degeneration. Additional enzymes involved in retinol metabolism, including *Rdh5* (0.709 fold, $P = 0.0159$), *Rdh10* (0.651 fold, $P = 0.0070$), *Lrat* (0.638 fold, $P = 0.031473$), and *Ugt2b1* (0.711, $P = 0.032628$) were also decreased in the aged 5XFAD mice, which suggests overall dysfunctional retinol metabolism in the RPE (Figure 2-11B). In addition to the genes related to retinol metabolism, *Ttr* (transthyretin, 0.848 fold, $P = 0.0033$) acts as a carrier of retinol (vitamin A) through its association with retinol-binding protein (RBP) in the blood and CSF. *Rbp1* (retinol binding protein 1, 0.812 fold, $P = 0.0247$) was also down regulated in the aged 5XFAD mice. In addition, *Trf* (transferrin, 0.717 fold, $P = 0.0143$) is transcriptionally regulated by retinoic acid (145).

A

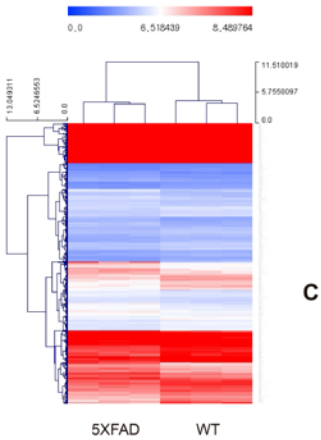

456 DAVID IDs for functional annotation

List of enriched KEGG pathways

Retinol metabolism
Drug metabolism
Cytokine-cytokine receptor interaction
Neuroactive ligand-receptor interaction
Cell adhesion molecules
Calcium signaling pathway
Nitrogen metabolism

B Differentially expressed gene profile associated with retinol metabolism

Gene symbol	Gene name	Fold-change	P value
Adh7	alcohol dehydrogenase 7 (class IV), mu or sigma polypeptide	2.322	0.012
Rpe65	retinal pigment epithelium 65	0.801	0.029
Ugt2b1	UDP glucuronosyltransferase 2 family, polypeptide B1	0.711	0.032
Rdh5	retinol dehydrogenase 5	0.709	0.016
Rdh10	retinol dehydrogenase 10 (all-trans)	0.651	0.007
Lrat	lecithin-retinol acyltransferase (phosphatidylcholine-retinol-O-acyltransferase)	0.638	0.031

C Differentially expressed gene profile associated with cytokine-cytokine receptor interaction

Gene symbol	Gene name	Fold-change	P value
Ccl3	chemokine (C-C motif) ligand 3	1.573	0.047
IL1r2	interleukin 1 receptor, type II	1.352	0.015
Tnfrsf21	tumor necrosis factor receptor superfamily, member 21	1.259	0.007
Tnfrsf8	tumor necrosis factor receptor superfamily, member 8	0.826	0.030
Ccr2	chemokine (C-C motif) receptor 2	0.804	0.0002
Ctf1	cardiotrophin 1	0.763	0.018
Met	met proto-oncogene	0.754	0.038
Pdgfc	platelet-derived growth factor, C polypeptide	0.747	0.036
Il2rb	interleukin 2 receptor, beta chain	0.743	0.039
Osmr	oncostatin M receptor	0.722	0.049
Ccl2	chemokine (C-C motif) ligand 2	0.709	0.046

Figure 2-11. Microarray based differentially expressed gene profile with retinol metabolism and cytokine-cytokine receptor interaction in the RPE complex of 5XFAD mice. (A) Hierarchical clustering map of 5XFAD mice and littermate wild type mice (WT) using gene identifiers (IDs) with 1.2 fold change with p value < 0.05, leading to list of enriched KEGG pathways in DAVID analysis for functional annotation. (B) Differentially expressed gene profile associated with retinol metabolism in 5XFAD mice. (C) Differentially expressed gene profile associated with cytokine-cytokine receptor interaction in 5XFAD mice.

It has been suggested that the inflammatory process is closely associated with the pathogenesis of dry AMD. Several mouse models using the inflammatory pathway have been developed. The aged 5XFAD mice show differential gene expression in cytokine-cytokine receptor interaction, and some of these interactions are closely related to the inflammatory response or immune reaction (Figure 2-11C). In the aged 5XFAD mice, the increased *Ccl3* (1.57 fold, $P = 0.047$), which interacts with CCL4 to attract macrophages, monocytes, and neutrophils, and *Mpeg1* (1.247 fold, $P = 0.0390$) suggested the possible involvement of macrophages in the RPE complex. Interestingly, the decreased *Ccl2* (0.71 fold, $P = 0.046$) and *Ccr2* (0.804 fold, $P < 0.0001$) in the aged 5XFAD mice is reminiscent of the *Ccl2* or *Ccr2* deficient mouse model of dry AMD (Fig. 6C) (146). Additionally, a mutation in *Cdhr1* (0.549 fold, $P = 0.0089$) has a known association with autosomal recessive retinal dystrophy (147).

Other differentially expressed gene profiles in the RPE complex of the aged 5XFAD mice are listed below. *Ilr1r2* (1.352 fold, $P = 0.0271$) may function as an IL-1 decoy by interacting with the IL-1 receptor accessory protein (148). *Gsto1* (3.80 fold, $P = 0.010$) and *Mgst1* (1.344 fold, $P = 0.0276$) are related to glutathione (GSH) homeostasis, and their upregulation leads to a decrease in reduced glutathione (149). *Sema3c* (0.537 fold, $P = 0.0358$) is a known inhibitor of pathological angiogenesis (150); therefore, downregulation of *Sema3c* may indicate the potential development of pathological angiogenesis in the 5XFAD mice.

Subretinal injection of Aβ leads to intracellular Aβ uptake and subsequent breakdown of tight junction in RPE

I have recently demonstrated that Aβ, endogenously generated from 5 mutant transgenes, accumulated in intracellular space at the RPE layer with thickened Bruch's membrane and Aβ deposits, thereby attenuating tight junction of RPE in aged 5XFAD mice (4). Exogenous oligomeric Aβ $(OA\beta)_{42}$ injection into subretinal space is also known to break tight junctions of RPE and result in disorganized and irregular staining of both ZO-1 and occludin on days 3 to 15 post-injection in both young and aged mice (117). These findings led us to probe whether extracellular Aβ translocates into intracellular space and subsequently induces breakdown of tight junction of RPE *in vivo*.

To evaluate cellular uptake of Aβ in RPE, I demonstrated intracellular Aβ uptake after subretinal injection of exogenous $OA\beta_{42}$. Seven days after subretinal $OA\beta_{42}$ injection, intracellular $A\beta_{42}$ was found concomitantly with the breakdown of tight junction (Figure 2-12). While typical hexagonal pattern of ZO-1 was not disrupted in vehicle injected mice (Figure 2-12A), the disrupted and irregular pattern of ZO-1 was found in $OA\beta_{42}$ injected mice which indicated a breakdown of tight junction in RPE (Figure 2-12B). These specific changes of tight junction were shown in details (Figure 2-12C and 1D). I also confirmed the intracellular uptake of Aβ using FITC-labeled $OA\beta_{42}$ (Figure 2-12E). These data suggest that RPE uptakes exogenous Aβ, and this, in turn, leads to tight junction breakdown *in vivo*.

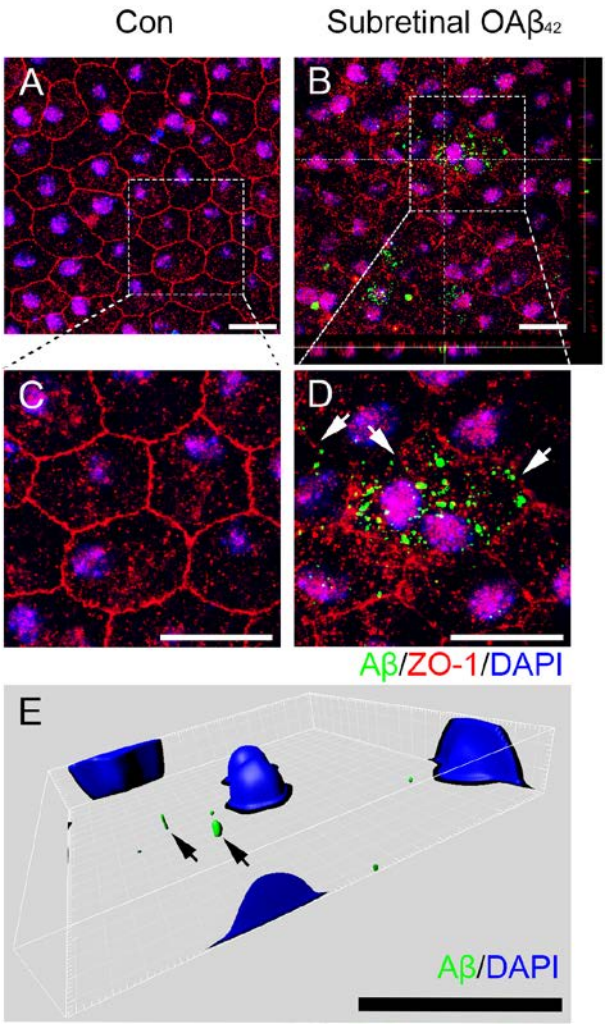

Figure 2-12. Subretinal injection of Aβ leads to intracellular Aβ uptake and subsequent breakdown of tight junction in RPE. Effect of subretinal injected $OA\beta_{42}$ (1 μg) on tight junction in retinal pigment epithelium (RPE) flat mount was evaluated at 1 week post injection. (A-E) RPE flat mounts with immunofluorescence staining against $A\beta_{42}$ (green), tight junction protein ZO-1 (red) and nucleus (DAPI, blue) are shown. (A) RPE flat mount after subretinal vehicle injection (Con) shows tight junction with typical hexagonal shape. (B) RPE flat mount after subretinal $OA\beta_{42}$ injection (Subretinal $OA\beta_{42}$)

shows intracellular Aβ and disrupted irregular expression of ZO-1. Orthogonal images indicates intracellular position of Aβ. (C and D) Optical zoom: ×2.4, a magnified portion of image a, b (enclosed in the white dotted box) to indicate intracellular Aβ and tight junction breakdown. (D) Arrows indicate disrupted tight junctions. (E) Representative images with 3-D reconstruction using Imaris software shows intracellular Aβ in RPE layer after subretinal injection of FITC-labeled $OA\beta_{42.}$ Arrows indicate intracellular Aβ (green). Magnification, ×1000. Scale bar = 20 μm. Figures were selected as representative data from three independent experiments.

Extracellular Aβ translocates into intracellular space via RAGE-mediated endocytosis in RPE

In order to determine the mechanism how extracellular Aβ gets translocated into intracellular space in RPE, I demonstrated intracellular Aβ uptake with plasma membrane and RAGE after exogenous $OA\beta_{42}$ treatment. First, I assessed intracellular distribution of Aβ and biotinylated-cell surface protein after Aβ treatment. After biotinylation of cell surface protein, cells were incubated with vehicle or $OA\beta_{42}$ for 1 h, and were treated with 2-mercaptoethanesulfonate (MesNa) to remove any remaining biotin on the cell surface. While control cells exposed to vehicle alone showed some biotinylated-proteins in cytosol (Figure 2A), RPE cells exposed to $OA\beta_{42}$ showed significantly increased biotinylated-proteins in cytosol with intracellular Aβ (Figure 2-13B). Intriguingly, intracellular Aβ was overlapped with some internalized biotinylated-proteins (Figure 2-13B, inset) suggesting that Aβ could bind to cell surface protein and translocate into intracellular space together.

To access possible colocalization of RAGE and Aβ, cells were incubated with vehicle or $OA\beta_{42}$ for 1h, and the distribution of RAGE and Aβ was examined under confocal microscope (Figure 2-13C and 2D). Indeed, the colocalization of RAGE and Aβ was detected in RPE exposed to $OA\beta_{42}$ (Figure 2-13D). These data suggested that Aβ interacts with RAGE and is internalized into RPE.

To analyze the effect of intracellular Aβ on tight junction integrity in RPE, I studied tight junction of RPE cells exposed to vehicle or $OA\beta_{42}$ for 24 h

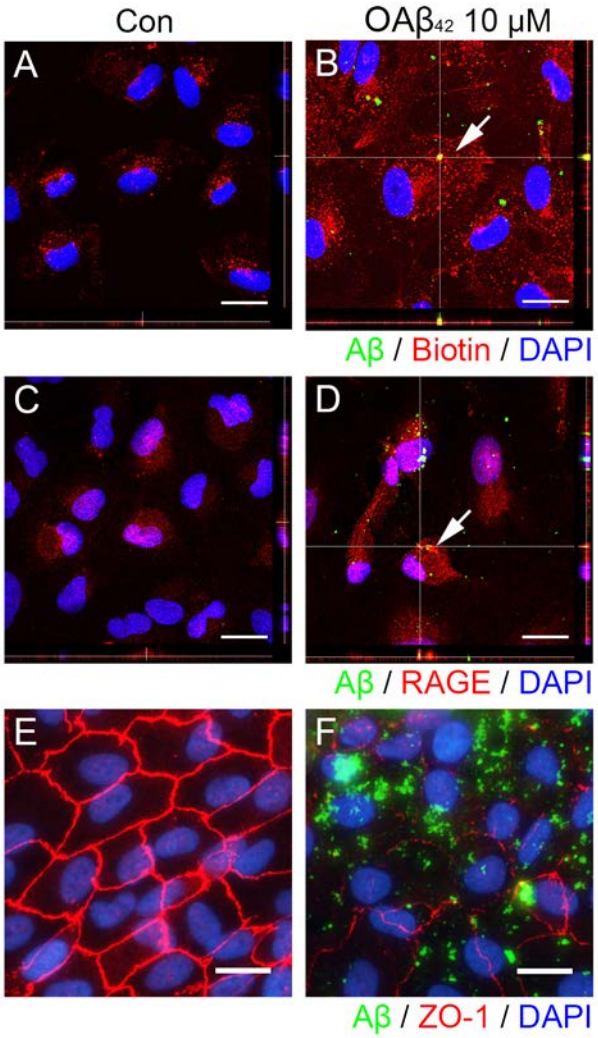

Figure 2-13. Extracellular Aβ translocates into intracellular space via RAGE-mediated endocytosis in RPE. ARPE-19 cells were exposed to vehicle control (A and C) or $OA\beta_{42}$ 10 μM (B and D) for 60 min, fixed in 4% PFA, and stained by anti-human $A\beta_{42}$ (green) and anti-biotin (red) or anti-RAGE (red). (A) RPE cells show basal level of endocytosis of cell membrane proteins (red). (B) RPE cells treated with $OA\beta_{42}$ 10 μM shows increased level of endocytosis of cell membrane proteins (red) in orthogonal view with a 0.49 μm Z-step interval. A magnified portion of image B (enclosed in the white

dotted box) indicates intracellular Aβ merged with biotinylated membrane proteins. Arrow indicates intracellular colocalization of Aβ and biotin. (C) RPE cells shows RAGE expression. (D) RPE cells treated with $OA\beta_{42}$ 10 μM shows internalized RAGE (red) in orthogonal view. A magnified portion of image D (enclosed in the white dotted box) indicates intracellular Aβ merged with internalized RAGE. Arrow indicates colocalization of Aβ and RAGE. (E and F) ARPE-19 cells were exposed to vehicle control (E) or $OA\beta_{42}$ 10 μM (F) for 24 h, fixed in 4% PFA, and stained by anti-human $A\beta_{42}$ (green) and anti-ZO-1 (red). (E) RPE cells show typical hexagonal shape tight junction. (F) RPE cells show disintegrated and disorganized ZO-1 with intracellular Aβ. Magnification, ×1000. Scale bar = 20 μm. Figures were selected as representative data from three independent experiments.

(Figure 2-13E and 2F). Intracellular Aβ was concomitant with disrupted and disorganized ZO-1 expression (Figure 2-13F).

siRNA-mediated knockdown of RAGE suppresses Aβ uptake in RPE

To investigate the role of RAGE on Aβ uptake in RPE cells, I performed *in vitro* study in RPE cells treated with RAGE siRNA. siRNA-mediated knockdown effectively decreased *AGER* mRNA (0.16 ± 0.02 fold induction) compared to negative siRNA (1.00 ± 0.13, $p<0.05$; Figure 2-14A). In accordance with this result, it effectively decreased RAGE expression in RPE (Figure 2-14B). Then, I examined intracellular Aβ uptake in RPE cells with RAGE siRNA. Interestingly, intracellular Aβ uptake was decreased in RPE with RAGE siRNA compared to RPE with negative siRNA under confocal microscope (Figure 2-14C). Consistent with these data, western blot results also showed that intracellular Aβ was significantly decreased in RPE with RAGE siRNA compared to RPE with negative siRNA (Figure 2-14D and E). These data showed that siRNA-mediated knockdown of RAGE suppressed Aβ uptake in RPE. This implied that RAGE played an important role in intracellular Aβ uptake in RPE

RAGE-mediated p38 MAPK signaling contributes to endocytosis of Aβ in RPE

RAGE is known to activate multiple downstream signaling pathways as a signal transduction receptor (151). Based on the previous study (131), I demonstrated that Aβ-induced RAGE signaling activation might lead to Aβ

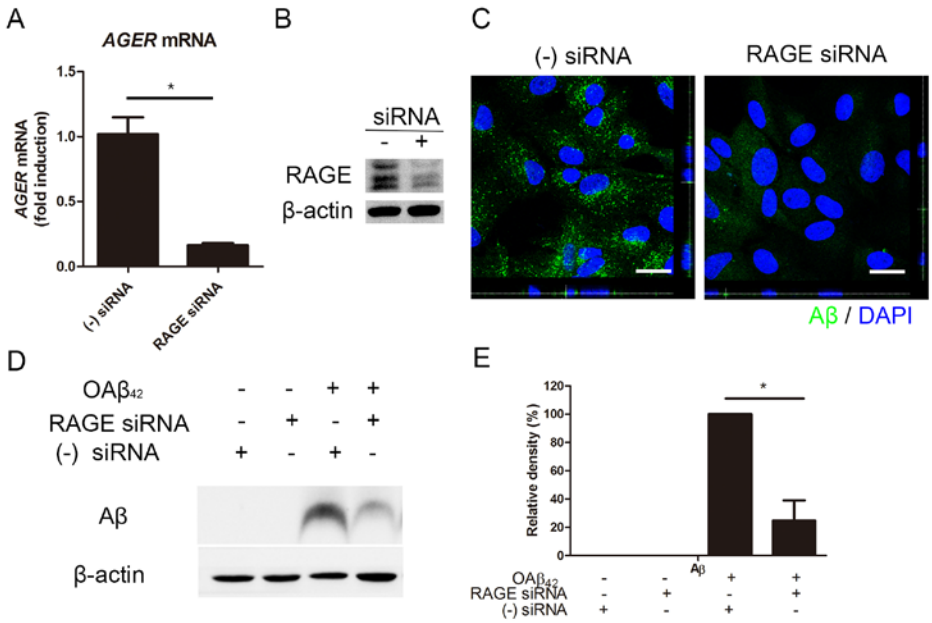

Figure 2-14. siRNA-mediated knockdown of RAGE suppresses Aβ uptake in RPE. RAGE siRNA was transfected in ARPE-19 cells. Negative siRNA was used as a control. RPE cells were treated $OA\beta_{42}$ 10 μM for 24 h. Intracellular Aβ uptake is decreased in RPE with RAGE siRNA compared to RPE with negative siRNA. (A) Relative expression of *AGER* mRNA is decreased in RPE cells with RAGE siRNA. (B) RAGE expression is decreased in RPE cells with RAGE siRNA. (C) Immunocytochemistry of $A\beta_{42}$ (green) shows decreased intracellular Aβ in RPE cells with RAGE siRNA. (D) Intracellular Aβ was evaluated by Western blot. (E) Relative band density of Aβ was analyzed using ImageJ 1.42 software. β-actin was used as a loading control. Data are presented as mean ± SEM. in graphs. $*P < 0.05$ (two tailed, unpaired *t*-test). Figures were selected as representative data from three independent experiments.

uptake into RPE. I first examined the effect of Aβ treatment on phosphorylation of p38 MAPK. Treatment of $OA\beta_{42}$ for 30 min showed a dose-dependent increase in phosphorylated p38 MAPK although it did not affect total protein levels of p38 MAPK (Figure 2-15A).

Next, I studied whether Aβ-induced phosphorylation of p38 MAPK is mediated by RAGE. RAGE siRNA effectively suppressed Aβ-induced p38 MAPK phosphorylation, and reduced intracellular Aβ accumulation (Figure 2-15B). In addition, RPE cells pretreated with p38 MAPK inhibitor (SB 203580) showed strong inhibition of Aβ uptake, similar to RPE cells pretreated with anti-RAGE neutralizing antibody (Figure 2-15C). Thus, Aβ/RAGE-mediated p38 MAPK signaling contributes to intracellular Aβ uptake in RPE.

Blockade of RAGE inhibits intracellular Aβ-induced tight junction breakdown in RPE

To determine whether inhibition of intracellular Aβ uptake could prevent Aβ-induced tight junction breakdown in RPE, I analyzed tight junction expression in RPE using western blot. I demonstrated that intracellular uptake of exogenous $OA\beta_{42}$ was decreased in RPE with siRNA-mediated knockdown of RAGE (Figure 2-15B). Indeed, siRNA-mediated knockdown of RAGE diminished the uptake of Aβ which subsequently inhibited intracellular Aβ-induced tight junction breakdown in RPE (Figure 2-16A and B). Consistent with these data, treatment of p38 MAPK inhibitor (SB 203580) and anti-RAGE neutralizing antibody also showed protective effect on Aβ-induced decrease of occludin expression in RPE (Figure 2-16C).

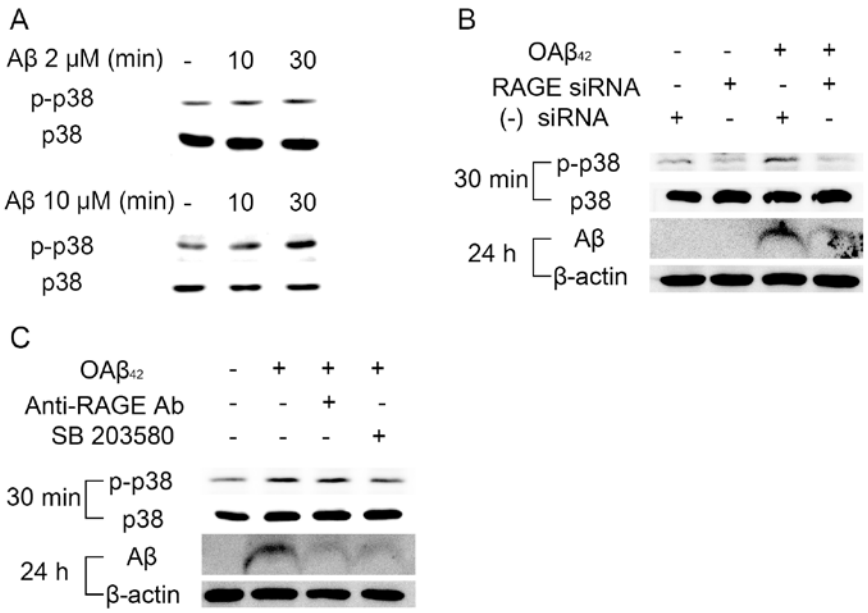

Figure 2-15. RAGE-mediated p38 MAPK signaling contributes to endocytosis of Aβ in RPE. (A) RPE cells were treated $OA\beta_{42}$ 2 μM or 10 μM for 30 min. Phosphorylation of p38 MAPK is increased at 30 min. (B) RAGE siRNA was transfected in ARPE-19 cells. Negative siRNA was used as a control. RPE cells were treated $OA\beta_{42}$ 10 μM for indicated time (30 min and 24 h). Phosphorylation of p38 MAPK and intracellular Aβ uptake are decreased in RPE with RAGE siRNA compared to RPE with negative siRNA. (C) RPE cells were pretreated with anti-RAGE neutralizing antibody (20 μg/mL, 2h) and SB 203580 (10 μM, 30 min) and were treated with $OA\beta_{42}$ 10 μM for indicated time (30 min and 24 h). Anti-RAGE neutralizing antibody and SB 203580 decrease intracellular Aβ in RPE. β-actin was used as an internal control. Figures were selected as representative data from three independent experiments.

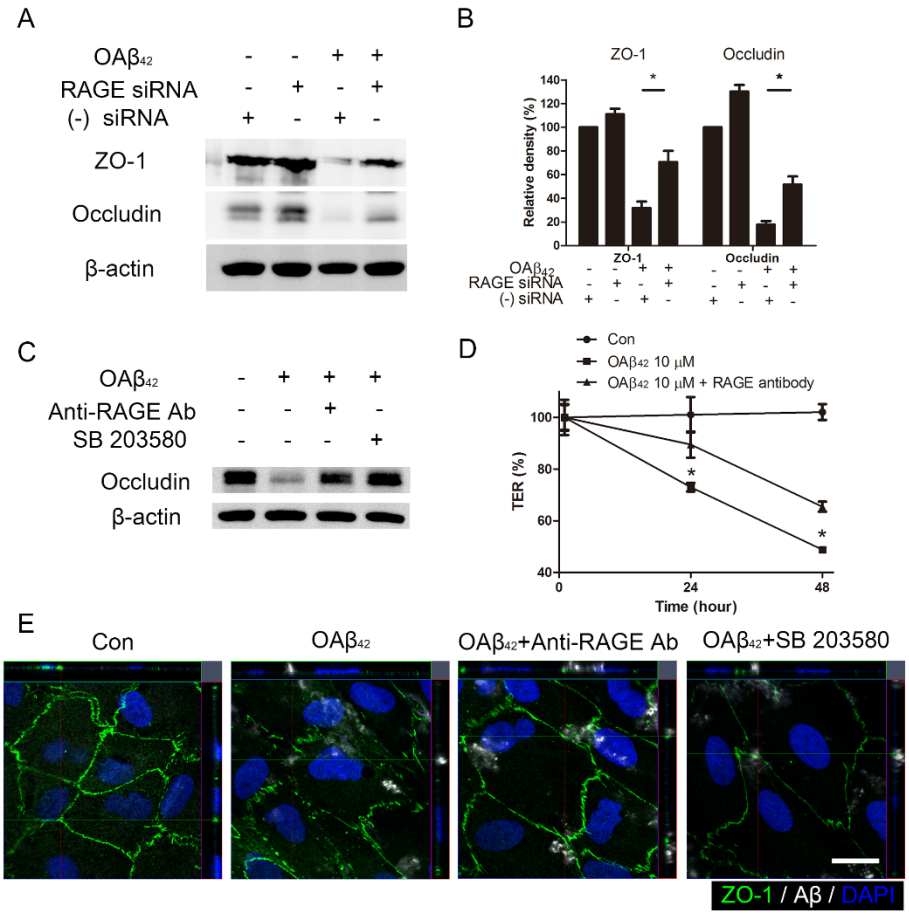

Figure 2-16. Blockade of RAGE inhibits intracellular Aβ-induced tight junction breakdown. (A) RAGE siRNA was transfected in ARPE-19 cells. Negative siRNA was used as a control. RPE cells were treated $OA\beta_{42}$ 10 μM for 24 h. Tight junction proteins (ZO-1 and occludin) were evaluated by Western blot. β-actin was used as an internal control. (B) Relative band density was analyzed using ImageJ 1.42 software. (C) RPE cells were pretreated with anti-RAGE neutralizing antibody (20 μg/mL, 2h) and SB 203580 (10 μM, 30 min) and were treated with $OA\beta_{42}$ 10 μM for 24 h. Occludin was evaluated by Western blot. β-actin was used as an internal

control. (D) Transepithelial electrical resistance (TER) was measured for 48 h and normalized to the TER value just after Aβ treatment. TER values with anti-RAGE neutralizing antibody (triangle) are compared to TER with OAβ_{42} treatment alone (square) at indicated time point. Data are presented as mean ± SEM. in graphs. *P < 0.05 (two tailed, unpaired t-test). (E) RPE cells were pretreated with anti-RAGE neutralizing antibody (20 μg/mL, 2h) and SB 203580 (10 μM, 30 min), and were treated with OAβ_{42} 10 μM for 24 h. Cells were stained by anti-human Aβ_{42} (white) and anti-ZO-1 (green). Magnification, ×1000. Scale bar = 20 μm. Figures were selected as representative data from three independent experiments.

To determine the role of RAGE on barrier function of RPE after Aβ treatment, I measured transepithelial resistance (TER) in RPE for 48 h. The mean initial TER of controls was 46 ± 4.5 ohms·cm2 when they reached a plateau. Anti-RAGE neutralizing antibody was sufficient to inhibit a decrease of TER during 48 h after $OA\beta_{42}$ treatment ($P < 0.05$; Figure 2-16D). In addition, tight junction breakdown with ZO-1 disruption after $OA\beta_{42}$ was also attenuated when ARPE-19 cells were treated with either p38 MAPK inhibitor or anti-RAGE neutralizing antibody (Figure 2-16E). These data suggested that intracellular Aβ uptake by RAGE contributed to breakdown of tight junction in RPE.

Aβ induced tight junction breakdown in RPE via RAGE/NF-κB signaling pathway

I postulated that RAGE involves not only in p38 mediated-Aβ uptake but also in downstream signaling pathway to directly regulate tight junction. I determined other RAGE-mediated signaling pathway after Aβ treatment except for p38 MAPK. I found that Aβ phosphorylated NF-κB p65 (Figure 2-17A). Treatment of IKK inhibitor (1 μM) prevented Aβ induced tight junction breakdown as well as phosphorylation of NF-κB p65 (Figure 2-17B). Taken together with Figure 2-16A, these data suggested that Aβ induced tight junction breakdown in RPE via RAGE/NF-κB signaling pathway

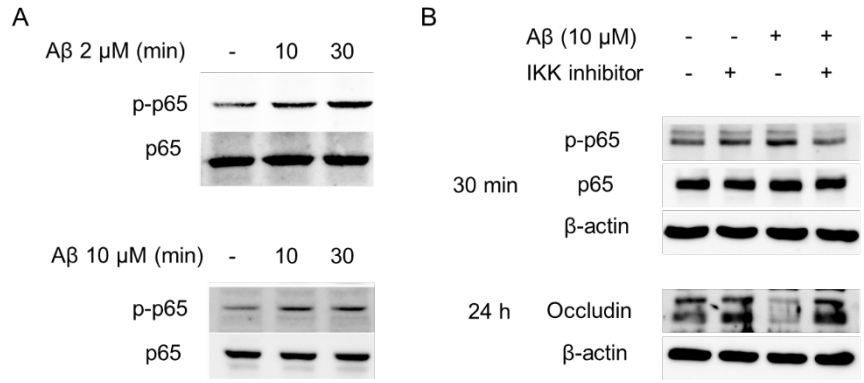

Figure 2-17. RAGE/NF-κB signaling contributes to Aβ-induced tight junction breakdown in RPE. (A) RPE cells were treated $OA\beta_{42}$ 2 μM or 10 μM for 30 min. Phosphorylation of NF-κB p65 is increased at 30 min. (B) IKK inhibitor (1 μM) was pretreated 30 min before treatment of $OA\beta_{42}$ 10 μM for indicated time (30 min and 24 h). Phosphorylation of NF-κB p65 and decrease of occludin are prevented by pre-treatment of IKK inhibtor. Tight junction proteins (occludin) was evaluated by Western blot. β-actin was used as an internal control.

DISCUSSION

In the first part of Chapter II, I demonstrated that intracellular Aβ was expressed in the RPE layer of 5XFAD mice which showed characteristic features of dry AMD. With intracellular $A\beta_{42}$, tight junction of RPE in 5XFAD mice was attenuated. Intriguingly, exogenous Aβ could be taken up by RPE cells and subsequently induce breakdown of the tight junction. Thus, intracellular $A\beta_{42}$ could play an important role in the pathogenesis of dry AMD. 5XFAD mice could be used as an animal model for the study of the relationship between dry AMD and AD with regard to Aβ related pathogenesis.

AMD is the leading cause of vision loss in adults over age of 65 in the developed countries. Both AD and AMD share common risk factors and suggestive pathogenesis. Aging is a major risk factor of both AD and AMD. Despite controversial debates in the role of apolipoprotein E4 (ApoE4) and CFH as common risk factors in both AD and AMD (112, 113, 115, 152), Aβ has been consistently considered as a pathologic molecule. $A\beta_{42}$ is more fibrillogenic than shorter $A\beta_{40}$, and elevated $A\beta_{42}$ and conversion of Aβ from monomeric form to oligomeric or aggregated form in the brain are considered key events in the pathogenesis of AD. Among the AD mice line, I used 5XFAD (Tg6799), the line with the highest $A\beta_{42}$ levels and intraneural Aβ in the brain than others (134). 5XFAD mice generated $A\beta_{42}$ almost exclusively in the brain and retina (109). Intracellular $A\beta_{42}$ accumulated in 5XFAD mice brain prior to plaque formation, implying potential role of intracellular Aβ in the pathogenesis of AD (109, 118). In this study, I found intracellular Aβ in the RPE and some characteristic features of dry AMD such as

hypopigmentation, large vacuoles, Bruch's membrane thickening and drusen like sub-RPE deposit in aged 5XFAD mice. Although 5XFAD mice did not show all the dry AMD features, there is no one model that recapitulated all of the features of human AMD yet (123). Thus, 5XFAD mice could be used as an animal model for dry AMD, especially studying the Aβ related pathogenesis in AMD.

Regarding to differentiate $A\beta_{42}$ from amyloid beta precursor protein (AβPP) or other Aβ peptides, consistent with previous studies in 5XFAD mice (134, 153), I showed the accumulation of 4G8-labeled intracellular Aβ in the early stages of plaque formation in this mouse model. Although 4G8 is known to react not only with Aβ but also with AβPP and its proteolytic derivatives, 4G8 antibody was needed to detect intracellular Aβ and thereof compare our results clearly with previous studies on intracellular Aβ that used this antibody. 4G8-stained hollow type plaques with nuclear remnants result from neuron-derived Aβ, not from cross-reactivity with AβPP using an end-specific Aβ antibody ($A\beta_{42}$) (118). Furthermore, 5XFAD specifically increased the expression of $A\beta_{42}$ and I used exogenous $A\beta_{42}$ in *in vitro* experiments. Thus, both 4G8 antibody and 12F4 antibody effectively detected intracellular Aβ in this study.

In the brain of AD patients, uptake of extracellular Aβ into neurons and intracellular production of Aβ could lead to the accumulation of intracellular Aβ, which in turn may gradually compromise neuronal function, by disrupting the Aβ-degrading pathway or by impairing the Aβ secretion of the neurons. As a result, highly Aβ-laden neurons may undergo death and lysis, releasing

intracellular Aβ into the surrounding extracellular space, and this becomes a seed for extracellular deposition. Same as in the brain neuronal cells, I suggest that intracellular Aβ accumulation could occur in the RPE cells as well by taking up extracellular Aβ, or producing Aβ intracellularly. This would disrupt the outer BRB, and potentially cause AMD.

Although the mechanism of intracellular uptake of exogenous Aβ in RPE cells is not well established yet, several endocytotic pathways were suggested as possible neuronal uptakes of soluble Aβ. They include α7 nicotinic acetylcholine (α7-NAch) receptor, N-methyl D-aspartate (NMDA) receptor, low density lipoprotein receptor-related protein 1 (LRP1)/apolipoprotein E (APOE), and receptor for advanced glycosylated end products (RAGE) (154). The RAGE, a member of the immunoglobulin superfamily, is expressed ubiquitously in brain (155, 156). It is known to be present in RPE cells (157) and is up-regulated in AMD (127). RAGE mediates Aβ transport from the periphery to the central nervous system (CNS) across the BBB (129, 130), and the interaction between Aβ and RAGE is believed to regulate the pathogenesis of AD (158). Aβ/RAGE-mediated signaling contributes to Aβ transport and Aβ internalization in neurons (131). Aβ induced occludin down-regulation is mediated by MAPK activation in hCMEC/D3 cells (159). Thus, I postulated that Aβ uptake might be mediated by RAGE-mediated endocytosis in RPE. However, the precise mechanism of RPE uptake of Aβ should be investigated in the further study. If Aβ uptake is mediated by RAGE, anti-RAGE therapy could block the intracellular accumulation of Aβ, and subsequently block the breakdown of tight junction in RPE.

In the first part of Chapter II, I demonstrated that intracellular Aβ contributed to the breakdown of outer BRB in 5XFAD mice. Thus, intracellular Aβ might play an important role in the pathogenesis of dry AMD. Also, I suggested that 5XFAD mice could be a mouse model of AMD with regard to the $A\beta_{42}$ related pathology and used for the study of the relationship between AD and AMD.

$A\beta_{42}$ has been implicated in dry AMD based on the parallel findings in AD and AMD (106). I recently suggested that the 5XFAD mouse could be a potential mouse model of dry AMD with regard to the Aβ-related pathology (4). In one mouse of dry AMD, APOE4 mice maintained on a high fat diet, Aβ accumulates in sub-RPE deposits (160). These mice also exhibit ZO-1 tight junction breakdown in RPE flat-mounts and thickening of BM. In this study, I demonstrated that the aged 5XFAD mice show outer BRB breakdown with Aβ accumulation. In addition, the aged 5XFAD mice show ultrastructural changes in the RPE and BM that are compatible with the cardinal features of human dry AMD, including a loss of apical microvilli and basal infolding of the RPE, increased BM thickness, basal laminar and linear deposits, and accumulation of lipofuscin granules and undigested POS-laden phagosomes.

In the second part of Chapter II, I noted that these pathognomonic ultrastructural changes in the RPE of the aged 5XFAD mice have also been found in previously established AMD animal models with various underlying mechanisms. Ramkumar et al. (124) have summarized the genetics and retinal pathology of other dry AMD models. The basal laminar and linear deposits beneath the RPE layer with a loss of basal infolding and numerous cystic

vacuoles in the 5XFAD mice have also been found in neprilysin gene-disrupted mice (116), another mouse model that suggests a possible role for Aβ in AMD. In mcd/mcd mice, a transgenic mouse line (mcd/mcd) expressing a mutated form of cathepsin D that is enzymatically inactive and thus impairs the processing of phagocytosed POS in the RPE cells, TEM has revealed the presence of basal laminar and linear deposits, which are considered to be the hallmarks of AMD, similar to those observed in the 5XFAD mice (161). Marked vacuolization and increases in lipofuscin granules and intracellular dense bodies have been observed in Ccl2-/- mice with TEM (146) and are also present in the aged 5XFAD mice. Cfh+/- mice fed with a high fat, cholesterol-enriched diet have RPE and photoreceptor dysfunction in response to basal laminar deposits (162).

CFH polymorphism (Y402H) is a risk factor for AMD (163, 164). The studies of multiple mouse models of AMD including human APOE4 knock-in mice (160), human CFH transgenic mice (165), and Cfh+/- mice (162) have focused on the complement activation. The advantage of using these CFH related mouse models is the support for a role for complement activation in AMD pathogenesis comes from studies implicating variations in the CFH gene as the strongest genetic factor associated with risk for AMD (163, 164). The precise mechanisms of complement system dysregulation in AMD are unknown, although there are several candidate molecules including Aβ. Aβ, a constituent of drusen, is a known activator of the complement system. Aβ is associated with drusen in human AMD eyes, but not with drusen in normal eyes (110). In particular, oligomeric Aβ presents in drusen from human AMD

eyes (108). In addition, Aβ accumulates and co-localizes with activated complement components within drusen (107, 166). Although I did not investigate the molecular mechanism of Aβ contribution to the pathogenesis of dry AMD, I directly used Aβ overexpressing mouse to recapitulate dry AMD-like pathology. This dry AMD-like pathology in 5XFAD mice might be associated with complement system dysregulation by Aβ. In this regard, 5XFAD mice have an advantage to study the contribution of Aβ to the complement system dysregulation without genetic modification of CFH-related genes.

Furthermore, the RPE complex of the aged 5XFAD mice shows differential gene expression profiles consistent with dry AMD in the inflammation response, immune reaction pathway, and decreased retinol metabolism. However, ultrastructural and gene profile changes have not been studied together in dry AMD animal models. Intriguingly, I can link the 5XFAD mouse differential gene expression profile with key ultrastructural changes, such as the loss of microvilli. Loss of microvilli and basal infolding has been found in various dry AMD models (124). However, we, for the first time, suggest that these changes might be linked to the decreased expression of *Itgav*, *Cldn1*, and *Rrh*. Note that RPE phagocytosis shows a remarkable specificity for POS mediated by αvβ5 integrin (140, 167). Most importantly, the decreased Ccl2 and Ccr2 in the aged 5XFAD mice is reminiscent of the Ccl2 or Ccr2 deficient mouse model of AMD (146), because it has been suggested that the inflammatory process is closely related to the pathogenesis of dry AMD. In addition, I postulate that the downregulation of the genes

related to retinol metabolism is the result of Aβ induced RPE dysfunction. Taken together, our findings suggest that aged 5XFAD mice can be used as a dry AMD mouse model.

A limitation of this study is the lack of extensive geographic atrophy in the aged 5XFAD mice, another cardinal feature of end stage dry AMD. Considering that no other animal models of dry AMD have completely recapitulated geographic atrophy, it is not surprising that I did not find geographic atrophy in the 12-month-old 5XFAD mice. Nonetheless, for the first time, this study demonstrated that 5XFAD mice show ultrastructural changes consistent with those of dry AMD.

Regarding the $A\beta_{42}$ related pathology in AD and AMD (106), I first suggested that 5XFAD mice could be used as a mouse model of dry AMD (4). Recently, hyperspectral imaging has detected amyloidopathy in the retina before the onset of cognitive dysfunction in 5XFAD mice (168). I thought that these findings indicated that 5XFAD mice could be used not only for the study of AMD, but also for the study of an early surrogate marker for the development of AD. Thus, I can use the eye as a window to the brain in the clinic.

In conclusion, I demonstrated that the ultrastructural changes in aged 5XFAD mice are comparable with the cardinal features of dry AMD. Thus, I suggest that aged 5XFAD mice can be used as a mouse model of dry AMD to study Aβ-related pathology and develop new therapeutic approaches.

In the third part of Chapter II, I demonstrated that subretinal injection of Aβ led to intracellular uptake of Aβ and subsequent breakdown of tight junction in RPE *in vivo*. I also showed that intracellular Aβ contributed to breakdown of tight junction in RPE via the RAGE/p38 MAPK-mediated endocytosis. RAGE contributed to intracellular uptake of Aβ which resulted in the increase of tight junction breakdown in RPE. Our study of the mechanism of intracellular Aβ uptake in RPE might help to investigate the role of intracellular Aβ in the pathogenesis of dry AMD. Furthermore, I also suggested that the research field of Aβ should be expanded from AD to AMD, and from extracellular Aβ to intracellular Aβ.

A growing body of evidence suggests that intraneuronal Aβ contributes neuronal apoptosis in the early pathogenesis of AD (115, 125). Intracellular $A\beta_{42}$ is known to accumulate in 5XFAD mice brain prior to plaque formation (118). I hypothesized that intracellular Aβ was also important in the early pathogenesis of AMD. However, the role of intracellular Aβ in RPE was only described in our previous study suggesting that intracellular Aβ in RPE could contribute to the development of AMD (4). Aβ is predominantly secreted from the neuronal cells, but the mechanism of Aβ transport into the RPE remains to be fully elucidated in AMD.

Regarding to Aβ uptake by RPE cells, the mechanism of intracellular uptake of exogenous Aβ is not established. Although the main role of RPE is phagocytosis, RPE phagocytosis showed a remarkable specificity toward ROS via αvβ5 integrin (140, 167). There were also several endocytosis pathways suggested as possible uptakes of Aβ in neurons and endothelial cells,

including α7-NAch receptor (169), NMDA receptor (170), LDL receptor-related protein 1 (171), and RAGE (130). Among these candidates, I demonstrated that RAGE contributed to intracellular Aβ uptake in RPE. RAGE is also important in retinal aging (172). It is known that RAGE distributed at apical membrane of the RPE (127, 173). In line with our results, Aβ/RAGE-mediated p38 MAPK signaling contributes to Aβ transport and neuronal dysfunction (131). Activation of endocytosis is essential in regulating the p38 MAPK activity in endothelial cells (174). Despite the evident role of RAGE in endocytosis of Aβ in this study, phagocytosis or other receptor mediated endocytosis could also contribute to intracellular uptake of Aβ. In addition, I also hypothesized that RAGE-mediated signaling itself (i.e. GSK-3β or NF-κB related signaling pathway) could affect tight junction or Aβ-related pathology in RPE. Thus, those Aβ-related mechanisms on RPE pathology should be investigated in further study.

The limitation of the study is that ARPE19 cells generate less effective tight junction than human fetal RPE (hfRPE) cells for *in vitro* study. It is also known that the staining with occludin in ARPE-19 cells is not good as that in hfRPE (175). Thus, it is better to show the distribution of ZO-1 tight junction protein in immunocytochemistry for tight junction evaluation in ARPE-19 cells. Nonetheless, this study for the first time demonstrated that intracellular Aβ uptake was mediated by RAGE via the RAGE/p38 MAPK-mediated endocytosis in RPE.

In conclusion, intracellular Aβ uptake was mediated by RAGE in RPE. Intracellular Aβ contributed to breakdown of tight junction in RPE via the

RAGE/p38 MAPK-mediated endocytosis. Blockade of RAGE with anti-RAGE antibody could block the intracellular accumulation of Aβ, and subsequently prevent the breakdown of tight junction in RPE. Thus, I suggest that blockade of RAGE can be a potential therapeutic target in AMD. Further study is warranted to develop new modality of RAGE-specific inhibitor for the treatment of AMD.

Taken together, in this chapter, I suggest that Aβ contributes to dry AMD pathogenesis and 5XFAD mice and Aβ-injected mice could be used as novel dry AMD mice model.

CHAPTER 3

In vivo Genome Surgery with CRISPR-Cas9 to Treat Wet Age-related Macular Degeneration

INTRODUCTION

AMD is the leading cause of blindness in aged populations in developed countries (121). Choroidal neovascularization (CNV) is a major pathologic feature of neovascular AMD and is caused primarily by angiogenic cytokines such as VEGF. In fact, VEGF is a major therapeutic target for the treatment of AMD using monoclonal antibodies or aptamers since it emerged as an important factor in angiogenesis (176). Currently, intravitreal injection of anti-VEGF therapy is a mainstay of treatment for neovascular AMD (177, 178). However, these anti-VEGF agents must be injected at least 7 times per year, because VEGF is continuously over-expressed in and secreted from diseased RPE cells. In this clinical circumstance, I reasoned that targeted inactivation of the *VEGFA* gene in RPE cells could reduce the VEGF level below a pathological threshold, leading to a long-term or permanent treatment of AMD, possibly in combination with current anti-VEGF therapy.

The type II clustered regularly interspaced short palindromic repeats (CRISPR)/CRISPR-associated (Cas) systems, repurposed from prokaryotic adaptive immune responses, are now widely used for targeted genome modifications in plants, animals, and human cells (179-181). In particular, Cas9 nucleases have shown promise for gene and cell therapy (182). Typically, these nucleases are expressed or delivered *in vivo* using plasmid DNA or viruses (183, 184). However, plasmid DNA delivery is often inefficient, especially *in vivo*, and can cause integration of small plasmid fragments degraded by endogenous nucleases at on-target and off-target sites

in the genome (181). Viral delivery of Cas9 can be highly efficient *in vivo* (184-187), but may be hampered by antibodies or T cells induced against the protein (188-190). Preassembled Cas9 ribonucleoproteins (RNPs) can be delivered to human primary and stem cells and mice to modify target genes (180, 181, 191). Cas9 RNPs are rapidly turned over in cells, reducing off-target effects. Furthermore, Cas9 RNPs are unlikely to be limited by host immune systems because they function and disappear before the generation of antibodies and T cells directed against them. Currently, despite these advantages of RNPs, the difficult delivery of Cas9 RNPs *in vivo* limits its utility for therapeutic applications (180).

In the first part of Chapter III, I show that *in vivo* genome editing of a wild-type gene, whose up-regulation is responsible for pathogenesis, could be a new therapeutic modality for the treatment of non-genetic degenerative diseases. Our ultimate goal is to harness Cas9 RNPs for a clinical application of therapeutic genome surgery in patients with AMD.

Genome editing has recently been democratized by the development of RNA-guided programmable nucleases repurposed from the type II CRISPR/Cas adaptive immune system against invading genetic elements in eubacteria and archaea (192). Cas9, the single effector protein component in the system, is complexed with CRISPR RNA (crRNA) and trans-activating crRNA (tracrRNA) or with single-guide RNA (sgRNA) composed of essential portions of crRNA and tracrRNA to form a sequence-specific RNA-guided endonuclease (RGEN) (193). A new RGEN with desired target specificity is

readily prepared by replacing crRNA or sgRNA, which hybridizes with a target DNA sequence. Cas9 RGENs cleave chromosomal DNA in a targeted manner, enabling genetic modifications or genome editing in cells and whole organisms (194-199).

Cas9 derived from *Streptococcus pyogenes* (SpCas9), the first Cas9 orthologue to enable targeted mutagenesis in human cells (194, 196, 197, 200), is still the most widely used among several Cas9 proteins available for genome editing. Owing to it large size (1,368 amino acids, 4.10 kbp), however, the SpCas9 gene and its sgRNA sequence cannot be packaged together into certain viral vectors such as adeno-associated virus (AAV) (201) for efficient delivery into cells *in vivo*. Instead, the SpCas9 gene alone can be packaged into a single AAV vector (186, 202). Alternatively, SpCas9 can be split into two parts (203, 204), each can be packaged into two AAV vectors (205, 206). However, split SpCas9 is less active than the intact SpCas9 (203, 204). Furthermore, co-delivery of two AAV vectors is less efficient than the delivery of a single AAV vector *in vivo*.

As an alternative to SpCas9, *Staphylococcus aureus* Cas9 (SaCas9) can be used for genome editing (184). SaCas9 is smaller (1,053 amino acids, 3.16 kbp) than SpCas9 and can be packaged, together with its sgRNA, into an AAV vector. Still, the SaCas9 gene cannot be packaged with a florescent reporter gene or two sgRNAs, essential for targeted chromosomal deletions or other rearrangements, into a single AAV vector. Furthermore, protospacer-adjacent motif (PAM) sequences recognized by SaCas9, 5’-NNGRRT-3’,

occur less frequently than those recognized by SpCas9, 5'-NGG-3', limiting targetable sites. In this regard, smaller Cas9 orthologues with different PAM sequences are highly desired to expand *in vivo* genome editing. Here, I present *Campylobacter jejuni*-derived Cas9 (CjCas9) for efficient genome editing *in vitro* and *in vivo*. CjCas9 is composed of 984 amino acid residues (2.95 kbp), much smaller than SpCas9 or SaCas9, but has never been shown to induce targeted mutagenesis in human or other eukaryotic cells or organisms. In this study, I characterized PAM sequences and optimized the sgRNA length to utilize CjCas9 for genome editing in mice.

MATERIALS AND METHODS

1. Data reporting

No statistical methods were used to predetermine sample size for *in vitro* and *in vivo* experiments. The investigators were not blinded to allocation during *in vivo* experiments, but single-blinded to the outcome assessment, especially measurement of CNV area.

2. Preparation of Cas9 RNPs

Purified Cas9 protein was purchased from ToolGen Inc. (South Korea). sgRNAs were generated by *in vitro* transcription using T7 polymerase (New England Biolabs) according to the manufacturer's protocol. Briefly, templates for sgRNA were generated by annealing and extension of two complementary oligonucleotides (Table S4). Templates were incubated with T7 RNA polymerase in reaction buffer (40 mM Tris-HCl, 20mM $MgCl_2$, 2 mM spermidine, 1 mM DTT, pH7.9) including NTPs (Jena bioscience) and RNase inhibitor (New England Biolabs) at 37°C for 16 h. Transcribed sgRNAs were incubated with DNase I (New England Biolabs) at 37°C for 30 min. sgRNAs were purified using RNeasy MinElute Cleanup kit (Qiagen) and quantified using Nano drop (Thermo Fisher Scientific). Purified sgRNAs (65 μg) were incubated with CIP (1000 units) (Alkaline Phosphatase, New England Biolabs) for the removal of 3-phosphate at 37°C for 1 h. sgRNAs were purified again using RNeasy MinElute Cleanup kit (Qiagen) and quantified using Nano drop

(Thermo Fisher Scientific). I also tested cell viability and indel efficiency using all Cas9 protein and sgRNA stocks, and high efficiency Cas9 protein and sgRNA stocks were used for *in vivo* eye injections.

3. Cy3-labeled Cas9 protein purification

After transformation of the pET28-NLS-Cas9 vector into *E. coli* strain BL21 (DE3), Cas9 protein expression was induced for 12 h at 18°C with 0.5 mM isopropyl β-D-1-thiogalactopyranoside (IPTG). The bacterial cells were lysed by sonication; after centrifugation at 20,000 g for 30 min, the soluble lysate was mixed with Ni-NTA beads (Qiagen) and Cy3 dye (GE Healthcare) was added at a 1:10 ratio (protein : dye molecules). The mixture was incubated overnight (> 12 h) at 4°C in the dark. Cy3-labeled Cas9 was eluted with elution buffer (50 mM Tris-HCl [pH 7.6], 150–500 mM NaCl, 10–25% glycerol, 0.2 M imidazole) and dialyzed against dialyzing buffer (20 mM HEPES pH 7.5, 150 mM KCl, 1 mM DTT, 10% glycerol). The purified Cy3-labeled Cas9 protein was concentrated using an Ultracel 100K cellulose column (Millipore). The purity of the Cy3-labeled Cas9 protein was determined by SDS-PAGE. The Cy3 labeling efficiency was measured by comparing the absorption spectra of the Cas9 protein (280 nm) and the conjugated Cy3 dye molecule.

4. Cell culture and transfection

NIH3T3 (ATCC® CRL-1658™) and ARPE-19 (ATCC® CRL-2302™) cell lines were cultured in Dulbecco's Modified Eagle Medium (DMEM) supplemented with 10% BCS or FBS at 37˚C in a humidified atmosphere containing 5% CO2. NIH3T3 and ARPE-19 cells were not authenticated or tested for mycoplasma contamination. One day before transfection, NIH3T3 and ARPE-19 cells were seeded into 24-well plates at 2 x 10^4 cells per well, with each well containing 250 µl growth medium lacking antibiotics. For plasmid delivery, cells were transfected with Cas9 (1 µg) and sgRNA (1 µg) expression plasmids using Lipofectamine 2000 (Thermo Fisher Scientific) according to the manufacturer's protocol. For RNP delivery, Cas9 protein (4 µg) was incubated with sgRNA (2.25 µg) at room temperature for 5 min, after which 50 µl Opti-MEM (Thermo Fisher Scientific) and 1 µl Lipofectamine 2000 (Thermo Fisher Scientific) were added. After 10 min, the RNP mixture was added to cells in the 24-well plates described above. Cells were harvested 48 h after transfection and analyzed using the T7E1 assay, targeted deep sequencing, and qPCR. For VEGFA expression in confluent RPE cells, ARPE-19 cells were maintained in DMEM/F12 containing 1% FBS after reaching confluency to allow formation of a polarized epithelial layer for the experiments (5). ARPE-19 cells in 12-well plates were transfected with 8 µg of Cas9 protein, 4.5 µg of sgRNA, and 3 µl of lipofectamine 2000. Two days after transfection, the transfection growth medium (DMEM + 1% FBS) was gently replaced with 0.5 ml of fresh serum-free medium. After 16 h, cells and media were harvested and analyzed using targeted deep sequencing, qPCR, and ELISA.

5. Cy3-labeled Cas9 RNP imaging and counting

One day after transfection, cells were fixed in 4% PFA for 10 min at room temperature and then stained with 4', 6-diamidino-2-phenylindole (DAPI, 1μg/ml, Sigma Aldrich) for 15 min at room temperature. Cells were visualized with a confocal microscope (LSM510, Carl Zeiss) at a magnification of ×630. The scanning parameters were as follows: scaling (x = 0.14 μm/pixel, y = 0.14 μm/pixel, z = 1 μm/pixel), dimensions (x = 1024, y = 1024, z = 6, channels: 3, 12-bit) with objective C-Apochromat 63x/1.20W Korr UV-VIS-IR. Cy3 positive nuclei were counted using ZEN 2 software (black edition, Ver 10.0, Carl Zeiss). To quantify the frequency of Cy3 positive nuclei, I counted the total number of cells and the number of cells with Cy3 staining in the nucleus in a field of view at a magnification of ×630 and calculated the average percentage of Cy3 positive nuclei over four fields of view (n = 3).

6. T7E1 assay

Genomic DNA was isolated from cells and tissues using a DNeasy Tissue Kit (Qiagen) according to the manufacturer's protocol. After target sites were amplified using PCR, the products were denatured and annealed using a thermal cycler. A list of primers used can be found in Table S5. Annealed PCR products were incubated with T7 endonuclease I (ToolGen, Inc.) at 37°C for 25 min and analyzed by agarose gel electrophoresis.

7. Targeted deep sequencing

On-target and potential off-target regions were amplified from genomic DNA using Phusion polymerase (Thermo Fisher Scientific). The PCR amplicons were subjected to paired-end sequencing using an Illumina MiSeq at LAS Inc. (South Korea). A list of primers used can be found in Tables S6, S7, and S8. Indels around the site 3 bp upstream of the PAM sequence were considered to be mutations resulting from Cas9 RNP activity.

8. RNA extraction and qPCR

Total RNA was isolated from NIH3T3 and ARPE-19 cells using an easy-spinTM Total RNA extraction Kit (iNtRON, South Korea) according to the manufacturer's protocol. 250 ng of RNA was then reverse transcribed using Superscript II (Enzynomics, South Korea). Quantitative PCR was performed using SYBR Green (KAPA) with following primers: mouse Vegfa, 5'-ACGTCAGAGAGCAACATCAC-3' (forward), 5'-CTGTCTTTCTTTGGTCTGCATTC-3' (reverse); mouse Gapdh, 5'-GCTGAGTATGTCGTGGAGTCTA-3' (forward), 5'-GTGGTTCACACCCATCACAA-3' (reverse); human VEGFA-1, 5'-CGAGTACATCTTCAAGCCATCC-3' (forward), 5'-GGTGAGGTTTGATCCGCATAAT-3' (reverse); human VEGFA-2, 5'-AGAAGGAGGAGGGCAGAAT-3' (forward), 5'-CACAGGATGGCTTGAAGATGTA-3' (reverse); human GAPDH, 5'-

CAATGACCCCTTCATTGACC-3’ (forward), 5’-TTGATTTTGGAGGGATCTCG-3’ (reverse).

9. VEGFA ELISA using confluent ARPE-19 cells

For human VEGFA ELISA, serum-free supernatants were collected from *Vegfa*-specific Cas9 RNP-treated confluent ARPE-19 cell cultures after cells were incubated in serum-free medium for 16 h. Secreted VEGFA protein levels were measured using a human VEGF Quantikine ELISA Kit (DVE00, R&D systems) according to the manufacturer’s instructions.

10. *In vitro* cleavage of genomic DNA and Digenome sequencing

Genomic DNA was isolated from ARPE-19 cells (ATCC) with a DNeasy Tissue Kit (Qiagen). *In vitro* cleavage of genomic DNA for Digenome sequencing was performed as described previously (207, 208). Briefly, genomic DNA (20 μg) was incubated with Cas9 protein (16.7 μg) and sgRNA (12.5 μg) in reaction buffer (100 mM NaCl, 50 mM Tris-HCl, 10 mM MgCl2, 100 μg/ml BAS, pH 7.9) at 37°C for 3 h. Cleaved genomic DNA was treated with RNase A (50 μg/ml, Sigma Aldrich) at 37°C for 30 min and purified with a DNeasy Tissue Kit (Qiagen). Whole-genome and Digenome sequencing were performed as described previously (208).

11. Animals

The care, use, and treatment of all animals in this study were in strict agreement with the ARVO statement for the Use of Animals in Ophthalmic and Vision Research and the guidelines established by the Seoul National University Institutional Animal Care and Use Committee. Adult (6 weeks old) male SPF C57BL/6J mice were used in the study. Mice were maintained under a 12 h dark–light cycle.

12. Subretinal injections

Subretinal injection was performed as previously described (139). Briefly, RNPs composed of Cas9 protein (8 μg), sgRNA (4.5 μg), and Lipofectamine 2000 (20% v/v) were mixed in 2 μL of injection volume. RNPs (2 or 3 μL) were injected into the subretinal space using a Nanofil syringe with a 33G blunt needle (World Precision Instruments Inc.) under an operating microscope (Leica Microsystems Ltd.). Subjects with retinal hemorrhage were excluded from the study.

13. Laser-induced CNV model

Mice were anesthetized with an intraperitoneal injection of a mixture of tiletamine and zolazepam (1:1, 2.25 mg/kg body weight) and xylazine hydrochloride (0.7 mg/kg body weight). Pupils were dilated with an eye drop containing phenylephrine (0.5%) and tropicamide (0.5%). Laser photocoagulation was performed using an indirect head set delivery system

(Iridex) and laser system (Ilooda). The laser wave length was 810 nm. Laser parameters were 200 μm spot size, 1 W power, and 100 ms exposure time. Laser burn was induced at the 12 (right eye) or 6 (left eye) o'clock positions around the optic disc with a modification18. Only burns that produced a bubble without vitreous hemorrhage were included in the study. Subretinal RNP injections were performed in the quadrant of laser burn. RNPs (sg*Rosa26* or sg*Vegfa*) were randomly allocated to the left or right eye in each mouse. Subretinal injection of Cas9 RNPs produced a bleb. I confirmed that the bleb overlapped with the laser-burn site. Subjects in which the bleb overlapped the laser-burn site were included in further studies. Seven days later, the eyes were fixed in 4% PFA for 1 h at room temperature. RPE complexes (RPE/choroid/sclera) were prepared for immunostaining with isolectin-B4 (Thermo Fisher Scientific, cat. no. I21413, 1:100) overnight at 4°C. The RPE complexes were flat-mounted and viewed with a fluorescent microscope (Eclipse 90i, Nikon) at a magnification of ×40. The CNV area was measured using Image J software (1.47v, NIH) by blind observers.

14. Immunofluorescent staining and imaging

The number of RPE cells in the RPE complex was calculated by counting DAPI stained nuclei in paraffin embedded 4 μm cross section samples in a high power field area (100 μm x 100 μm, n = 8). Cross section samples obtained at day 7 post-injection (n = 4) were immunostained with anti-opsin antibody (Millipore, AB5405, 1:1000) and Alexa Fluor 488 antibody (Thermo

Fisher Scientific, 1:500). The opsin positive area was measured using Image J software (1.47v, NIH) by blind observers. The intracellular distribution of Cy3-Cas9 protein in the RPE flat-mounts was imaged using a confocal microscope (LSM 710, Carl Zeiss). The scanning parameters were as follows: scaling (x = 0.042 μm/pixel, y = 0.042 μm/pixel, z = 0.603 μm/pixel), dimensions (x = 1024, y = 1024, z = 12, channels: 2, 8-bit), and zoom (5.0) with objective C-Apochromat 40x/1.20W Korr M27. ZEN 2 software was used to process the images.

15. Isolation of RPE sheets and genomic DNA extraction

RPE cell sheets at the RNP delivered site were harvested at day 3 post-injection with or without CNV according to the previously described protocol (209). Briefly, enucleated eyes were incubated with 0.1 % hyaluronidase (Sigma-Aldrich) at 37°C for 45 min after removal of lens, and then transferred in PBS for 30 min on ice. The RNP-injected area was separated from the RNP-free area. Next, neural retina was completely removed from enucleated eyes, and only RPE/choroid/scleral complex was incubated with Trypsin-ETDA solution at 37°C for 45 min. RPE cell sheets were isolated by shaking the eyecup using microforceps and only monolayer RPE sheets were collected using a glass capillary on the microscopy. Genomic DNA was directly extracted from the collected RPE sheets in the RNP-injected area and subjected to targeted deep sequencing. Briefly, the collected RPE sheets were

incubated with lysis buffer (25 mM NaOH, 0.2 mM EDTA) at 95°C for 20 min and pH adjusted to 7.4 using HEPES (50 mM).

16. Mouse VEGFA ELISA

For mouse VEGFA ELISA, a total of 30 laser burns were induced in the eye, after which RNPs (3 μL) were injected into the subretinal space. At day 3 post-injection, whole RPE complexes were isolated from the retina and frozen for further analysis. Cells were lysed with RIPA buffer and VEGFA levels were measured using a mouse VEGF Quantikine ELISA Kit (MMV00, R&D systems) according to the manufacturer's instructions.

17. Western blotting

To analyze RNP levels over time after *in vivo* RNP delivery, Western blotting of RPE complexes, obtained at 1 and 3 days post-injection, was performed. Samples containing equal amount of protein (20 μg) were analyzed; Cas9 and beta-actin were detected with an anti-HA high affinity antibody (Roche, 3F10, 1:1000) and an anti-beta-actin antibody (Sigma Aldrich, A2066, 1:1000), respectively. ImageQuant LAS4000 (GE healthcare) was used for digital imaging.

18. Statistics. Data were analyzed with SPSS software version 18.0 (SPSS Inc., Chicago, IL, USA). P values were determined by an unpaired, two sided

Student's *t*-tests or one-way ANOVA and Tukey post-hoc tests for multiple groups. Data are shown as mean with SEM.

19. Data access

The deep sequencing data from this study have been submitted to the NCBI Sequence Read Archive under accession number SRX1801343 and SRX1801344.

20. Animals

The care, use, and treatment of all animals in this study were in strict agreement with the ARVO statement for the Use of Animals in Ophthalmic and Vision Research and College of Veterinary Medicine and the guidelines established by the Seoul National University Institutional Animal Care and Use Committee, which granted permission to perform animal experiments. Eight-week old, male, specific pathogen free (SPF) C57BL/6J mice (n = 3-9) were used in this study. Mice were maintained under a 12 h dark–light cycle.

21. Laser-induced CNV model

After mice were anesthetized, pupils were dilated with an eye drop containing phenylephrine (0.5%) and tropicamide (0.5%). Laser photocoagulation was performed using an indirect head set delivery system (Iridex) and laser system (Ilooda). Laser parameters were 810 nm wave length, 200 μm spot size, 800 mW power, and 70 ms exposure time. Laser burn was induced 3 to 4 times around the optic disc. Only burns that produced a bubble without vitreous

hemorrhage were included in the study. Seven days later, the eyes were fixed in 4% paraformaldehyde for 1 h at room temperature. RPE complexes (RPE/choroid/sclera) were prepared for immunostaining and then incubated with isolectin-B4 (Thermo Fisher Scientific, cat. no. I21413, 1:100) and anti-GFP antibody (Abcam, ab6556, 1:100) overnight at 4°C. The RPE complex was flat-mounted and viewed with a fluorescent microscope (Eclipse 90i, Nikon) or a confocal microscope (LSM 710, Carl Zeiss) at a magnification of ×100. The CNV area was measured using Image J software (1.47v, NIH) by blinded observers. An average of 3-4 CNV areas per eye was analyzed. Each group consisted of 17–18 eyes.

22. Construction of cjCas9 and sgRNA plasmids

A human codon-optimized CjCas9-coding sequence, derived from *Campylobacter jejuni* subsp. *Jejuni* NCTC 11168, was synthesized with a nuclear localization signal (NLS) and an HA epitope at its C-terminal end (GeneArt™ Gene Synthesis, Thermo Fisher Scientific) and cloned into the p3s plasmid(195). The trans-activating crRNA (tracrRNA) sequence and the precursor CRISPR RNA (pre-crRNA) sequence were fused with a GAAA or TGAA linker to form a sgRNA sequence. sgRNAs were transcribed under the control of the U6 promoter. I used addgene plasmid (# 61591) for SaCas9 expression.

23. *In vitro* PAM identification. The recombinant Cas9 protein was expressed in E. coli and purified as described previously (194). sgRNAs were

transcribed using T7 RNA polymerase as described (194). To make a randomized PAM (N_{10}) library, the DNA sequence including the *AAVS1*-TS1 target site cloned in a plasmid was amplified with a randomized primer. After gel purification, the amplicon library (1 μg) was digested with the SpCas9 or CjCas9 protein and *in vitro* transcribed sgRNA for 30 min at 37℃. Digested library was purified by column filtration and subjected to deep sequencing using Miseq (Illumina). Miseq reads that perfectly matched the reference sequence were sorted. The randomized PAM region was extracted and analyzed with WebLogo.

24. PAM characterization using cell-based reporter assays

The *AAVS1*-TS1 target sites with variable PAM sequences, which were randomized at position X (5'-NNNNXCAC-3', 5'-NNNNAXAC-3', 5'-NNNNACXC-3', and 5'-NNNNACAX-3'), were synthesized (Macrogen, Inc.) and cloned in a surrogate reporter plasmid encoding RFP and GFP(210). To determine optimal PAM sequences, each of the resulting reporter plasmids (100 ng) and plasmids encoding CjCas9 and its sgRNA (225 ng and 675 ng, respectively) were co-transfected into HEK293 cells (1×10^5) using lipofectamine 2000 (Invitrogen). At day 2 post-transfection, the fraction of GFP and RFP double positive cells was determined by flow cytometry (BD Accuri™ C6, BD).

25. Cell culture and mutation analysis

HEK293 (ATCC, CRL-1573) cells and mouse NIH3T3 (ATCC, CRL-1658)

cells were maintained in Dulbecco's modified Eagle's medium (DMEM) supplemented with 100 units/mL penicillin, 100 mg/mL streptomycin, and 10% fetal bovine serum (FBS). sgRNA plasmid (750 ng) and CjCas9 plasmid (250 ng) were transfected into cells ($0.5\sim1\times10^5$) with lipofectamine 2000 (Invitrogen). After 48h of transfection, genomic DNA was isolated using a DNeasy Blood & Tissue kit (Qiagen) and on-target or off-target loci were amplified using specific primers (8) for targeted deep sequencing. Deep sequencing libraries were generated by PCR. TruSeq HT Dual Index primers were used to label each sample. Pooled libraries were subjected to paired-end sequencing (LAS, Inc.). Indel frequencies were calculated as described previously (207).

26. Digenome sequencing

Digenome-seq was performed as described previously (207, 211). Genomic DNA was isolated using a DNeasy Tissue kit (Qiagen) according to the manufacturer's instructions. Genomic DNA (8 μg) with CjCas9 or SaCas9 protein (300 nM) and sgRNA (900 nM) in a 400 μL reaction volume (100 mM NaCl, 50 mM Tris-HCl, 10 mM MgCl2, and 100 μg/mL BSA) and incubated the mixture for 8h at 37°C. Digested genomic DNA was incubated with RNase A (50 μg/mL) for 30 min at 37°C and purified again with a DNeasy Tissue kit (Qiagen). Digested DNA was fragmented using the Covaris system and ligated with adaptors for library formation. DNA libraries were subjected to WGS using an Illumina HiSeq X Ten Sequencer at Macrogen. I used the Isaac aligner to generate a Bam file using the following parameters: ver.

01.14.03.12; Human genome reference, hg19 from UCSC (original GRCh37 from NCBI, Feb. 2009), Mouse genome reference, mm10 from UCSC; Base quality cutoff, 15; Keep duplicate reads, yes; Variable read length support, yes; Realign gaps, no; and Adaptor clipping, yes (adaptor: AGATCGGAAGAGC*, *GCTCTTCCGATCT) (212).

27. AAV vectors encoding CjCas9 and its sgRNA sequences

AAV inverted terminal repeat-based vector plasmids carrying a sgRNA sequence and the CjCas9 gene with a nuclear localization signal (NLS) and an HA tag at the C terminus were constructed. sgRNA transcription was driven by the U6 promoter and CjCas9 expression was controlled by the EFS promoter in C2C12 myoblast cells or by the Spc512 promoter in TA muscles of C57BL/6 mice. For retinal delivery, an AAV vector encoding CjCas9 under the control of the EFS promoter, enhanced green fluorescent protein (eGFP) linked to the C-terminus of CjCas9 with the self-cleaving T2A peptide, and a U6 promoter-driven sgRNA specific to the *Vegfa* or *Hif1a* gene was constructed.

28. Production and characterization of AAV vectors

To produce AAV vectors, they were pseudotyped in AAVDJ or AAV9 capsids. HEK293T cells were transfected with pAAV-ITR-CjCas9-sgRNA, pAAVED2/9, and helper plasmid. HEK293T cells were cultured in DMEM with 2% FBS. Recombinant pseudotyped AAV vector stocks were generated using PEI coprecipitation with PEIpro (Polyplus-transfection) and triple-

transfection with plasmids at a molar ratio of 1:1:1 in HEK293T cells. After 72 h of incubation, cells were lysed and particles were purified by iodixanol (Sigma-Aldrich) step-gradient ultracentrifugation. The number of vector genomes was determined by quantitative PCR.

29. AAV transduction in mouse myoblast cells

Mouse myoblast cells were infected with AAVDJ-CjCas9 at different viral doses (multiplicity of infection (MOI): 1, 5, 10, 50, and 100 determined by quantitative PCR) and maintained in DMEM with 2% FBS. At different time points, cells were harvested for targeted deep sequencing. An MOI of 1 was estimated with one infectious virus particle in 100 total viral particles determined by quantitative PCR.

30. Intramuscular injection of AAV

AAV was administered to 8-week-old young adult male C57BL/6J mice anesthetized with 2–4% isoflurane. The mice were injected intramuscularly with AAV9-CjCas9 ($1x10^{11}$ viral genome) in physiological saline (40 μL) using an ultra-fine insulin syringe with a 31G needle (BD). As a negative control, C57BL/6J mice were injected with physiological saline (40 μL) only.

31. Intravitreal injection of AAV

8-week-old mice were anesthetized with an intraperitoneal injection of a mixture of tiletamine and zolazepam (1:1, 2.25 mg/kg body weight) and xylazine hydrochloride (0.7 mg/kg body weight). AAV9-CjCas9 (2×10^{10}

viral genome in 2 μL) was intravitreally injected using a Nanofil syringe with a 33G blunt needle (World Precision Instruments Inc.) under an operating microscope (Leica Microsystems Ltd.).

32. Immunofluorescent staining and imaging of retinal tissue

For the analysis of opsin positive area, formalin-fixed paraffin embedded samples were prepared at day 42 post-injection (n = 4). Cross-section samples were immunostained with anti-HA antibody (Roche, 3F10, 1:1000), anti-opsin antibody (Millipore, AB5405, 1:1000), and Alexa Fluor 488 or 594 antibodies (Thermo Fisher Scientific, 1:500). The opsin positive area corresponding to RPE cells expressing HA-tagged CjCas9 was measured using Image J software (1.47v, NIH) by blinded observers. For the distribution of CjCas9 and eGFP, the eyes were fixed in 4% paraformaldehyde for 1 h at room temperature. RPE complexes (RPE/choroid/sclera) were prepared for immunostaining and then incubated with anti-GFP antibody (Abcam, ab6556, 1:100) overnight at 4°C. After stain with Alexa Fluor 488 antibodies (1:500), the RPE flat-mounts were imaged using a confocal microscope (LSM 710, Carl Zeiss). The scanning parameters were as follows: scaling (x = 0.042 μm/pixel, y = 0.042 μm/pixel, z = 0.603 μm/pixel), dimensions (x = 1024, y = 1024, channels: 2, 8-bit) with objective C-Apochromat 40x/1.20W Korr M27. ZEN 2 software was used to process the images.

33. Genomic DNA extraction

For DNA extraction from muscle, muscle tissue was homogenized using

tungsten carbide beads (3mm; Qiagen) and a TissueLyser II (Qiagen). For extraction from RPE, after imaging of RPE flat-mounts, tissue samples were washed in PBS. RPE cells were mechanically isolated from choroid/sclera by vortexing for 30s in lysis buffer (NucleoSpin Tissue, Macherey-Nagel), as described (213). Genomic DNA from the remnant choroid/sclera tissues was analyzed to confirm complete isolation of RPE cells. Genomic DNA was analyzed by targeted deep sequencing.

34. Mouse Vegfa ELISA

At day 42 post-injection, whole RPE complexes were separated from neural retina tissue and frozen for further analysis. Sample tissues were lysed with Cell Lysis Buffer (120 μL) (CST #9803) and Vegfa protein levels were measured using a mouse VEGF Quantikine ELISA kit (MMV00, R&D systems) according to the manufacturer's instructions.

35. Electroretinography (ERG) analysis

Mice were dark-adapted over 16 h. Mice were anesthetized with an intraperitoneal injection of a mixture of tiletamine and zolazepam (1:1, 2.25 mg/kg body weight) and xylazine hydrochloride (0.7 mg/kg body weight). Pupils were dilated with an eye drop containing phenylephrine (0.5%) and tropicamide (0.5%). Contact lens electrodes were placed on both eyes with a drop of methylcellose. Full-field ERGs were recorded as described(214) by using the universal testing and electrophysiologic system 2000 (UTAS E-2000, LKC Technologies, Gaithersburg, MD). The responses were recorded at a

gain of 2 k using a notch filter at 60 Hz, and were bandpass filtered between 0.1 and 1500 Hz. In the light-adapted state (photopic), with a 30 cd/m2 background light to desensitize the rods and isolate cones, cone responses were recorded in response to single flashed of 0 dB for photopic response, and a flicker sequence of 30 Hz, averaging 20 responses. The amplitude of the a-wave was measured from the baseline to the lowest negative-going voltage, whereas peak b-wave amplitudes were measured from the trough of the a-wave to the highest peak of the positive b-wave.

36. Western blotting

The CjCas9 protein expressed in TA muscles of C57BL/6J mice at 8 month after injection of AAV was detected using Western blotting. Samples containing equal amounts of protein (20 μg) were analyzed; Cas9 and GAPDH were detected with an anti-HA high affinity antibody (Abcam, ab9110, 1:5,000) and an anti-GAPDH antibody (Abcam, ab9485, 1:2,500), respectively. Goat anti-rabbit IgG-HRP antibody (Abcam, ab6721, 1:5,000) was used for signal detection. ImageQuant LAS4000 (GE healthcare) was used for digital imaging.

37. Statistical analysis

No statistical methods were used to predetermine sample size for *in vitro* or *in vivo* experiments. All group results are expressed as mean ± SEM, if not stated otherwise. Comparisons between groups were made using the two-tailed Student's *t*-test or one-way ANOVA and Tukey post-hoc tests for

multiple groups. Statistical significance as compared to untreated controls was denoted with * ($P < 0.05$), ** ($P < 0.01$), *** ($P < 0.001$) in the figures and figure legends. Statistical analysis was performed in Graph Pad PRISM 5.

38. Data availability

The deep sequencing data from this study have been submitted to the NCBI Sequence Read Archive under accession number SRP095501 and SRP095507. The data that support the findings of this study are available from the corresponding author upon reasonable request.

RESULTS

Targeted mutagenesis in the *Vegfa/VEGFA* gene via Cas9 ribonucleoproteins (RNPs)

To investigate the potential of Cas9 RNP-mediated *in vivo* genome surgery for the treatment of AMD, I first identified Cas9 target sites that are conserved in both the human *VEGFA* gene and the mouse *Vegfa* gene using Cas-Designer (215) and that differ from any other site in the human genome by at least two or three nucleotides using Cas-OFFinder (216). I tested four single-chain guide RNAs (sgRNAs) targeting these sites in exons 3 and 4 (labeled as Vegfa-1, 2, 3 and 4), which encode binding sites for VEGF receptors 1 and 2, respectively, in the mouse NIH3T3 cell line (Figure 3-1) and the human RPE cell line (ARPE-19). The most active Vegfa-1 sgRNA complexed with the recombinant Cas9 protein and delivered via transfection using cationic lipid induced small insertions and deletions (indels) at the target site with a frequency of 82 ± 5% or 57 ± 3% in NIH3T3 cells or ARPE-19 cells, respectively (Figure 3-2A-D). At day 2 post-treatment, Cas9 RNP delivery was much more efficient than plasmid transfection in these cells (Figure 3-2C). I also carried out additional experiments using confluent ARPE-19 cells. Cells were harvested at 64 h after transfection and were analyzed using deep sequencing, qPCR, and ELISA to measure indel frequencies, mRNA levels, and protein levels, respectively. Indels were detected at a frequency of 40 ± 8% in the *Vegfa*-RNP-treated ARPE-19 cells (Figure 3-2E). The Cas9 RNP reduced the *VEGFA* mRNA level by 24 ± 4% and the VEGFA protein level

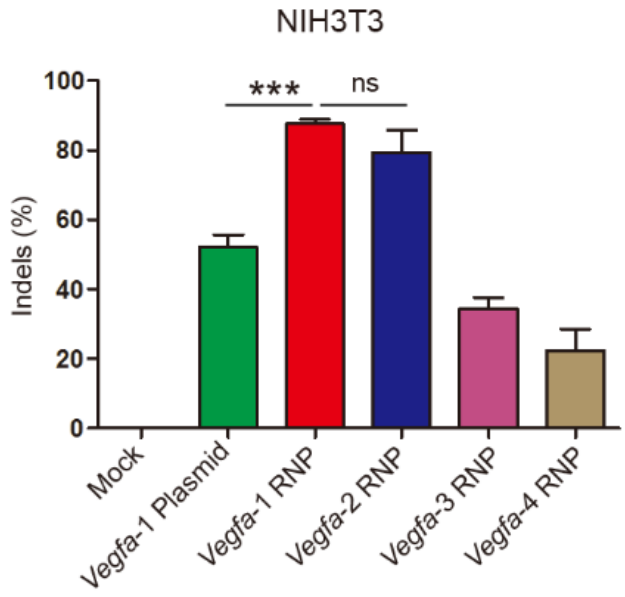

Figure 3-1. Mutation frequencies of *Vegfa*-specific Cas9 ribonucleoproteins (RNPs) in NIH3T3 cells. Mutation frequencies were measured using deep sequencing at day 2 post-transfection. Error bars indicate SEM. (n = 3). One-way ANOVA and Tukey post-hoc tests, *** $P < 0.001$.

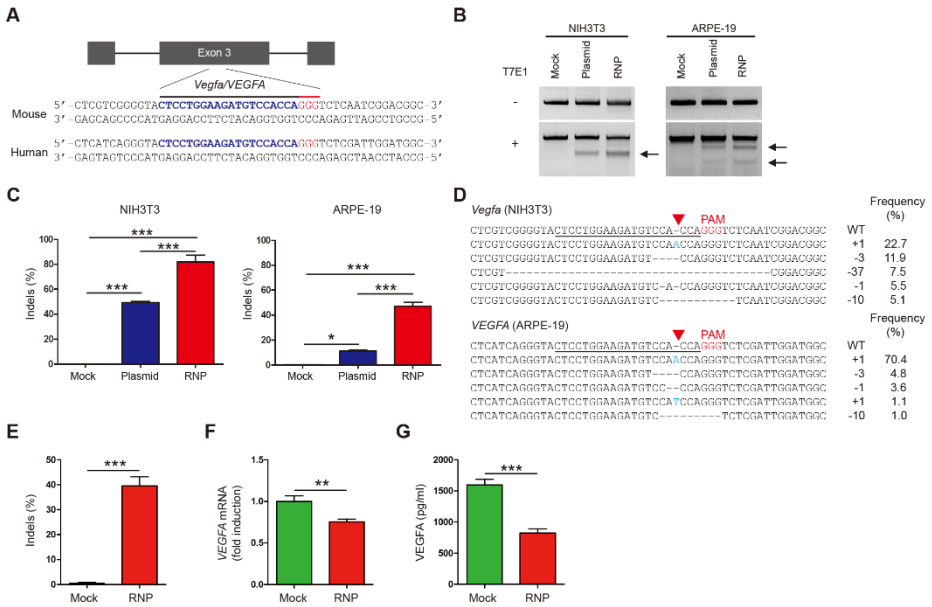

Figure 3-2. **Targeted mutagenesis in the *Vegfa/VEGFA* gene via Cas9 RNPs.** (A) The target sequence in the *Vegfa/VEGFA* locus. The PAM sequence and the sgRNA target sequence are shown in red and blue, respectively. (B) *Vegfa*-specific Cas9 RNP-driven mutations in NIH3T3 and ARPE-19 cells detected by the T7 endonuclease I (T7E1) assay. Arrows indicate the expected positions of DNA bands cleaved by T7E1. (C) Mutation frequencies measured by targeted deep sequencing. Error bars indicate SEM. (n = 3). One-way ANOVA and Tukey post-hoc tests, * $P < 0.05$, ** $P < 0.01$, *** $P < 0.001$. (D) Representative mutant DNA sequences at the *Vegfa/VEGFA* locus. The PAM sequence is shown in red and inserted nucleotides in blue. The target sequence is underlined. The red triangle indicates the cleavage position. The column on the right indicates the number of inserted or deleted bases and indel frequencies (%). WT, wild-type. (E)

Vegfa-specific Cas9 RNP-driven mutation frequencies in confluent ARPE-19 cells at 64 h post-transfection detected by targeted deep sequencing. (F) Relative *VEGFA* mRNA levels measured by quantitative PCR (qPCR). (G) Secreted VEGFA protein in the supernatant measured by ELISA. Error bars indicate SEM. (n = 5). Student's *t*-test, ** $P < 0.01$, *** $P < 0.001$.

by 52 ± 9 % in confluent ARPE-19 cells under post-mitotic conditions (Figure 3-2F and G).

To monitor the localization of Cas9 RNPs *in vitro* and *in vivo*, I used Cy3-conjugated Cas9 protein (217). Thus, Cy3-Cas9 combined with or without the Vegfa-1 sgRNA was mixed with cationic lipids and delivered into NIH3T3 cells. The Cy3-Cas9 RNP was detected in many nuclei (Figure 3-3A and B) and induced indels at the target site (Figure 3-3C and D). Interestingly, the proportion of Cy3 positive nuclei (42 ± 6%) (Figure 3-3B) was almost equal to the frequency of indels (40 ± 3%) (Figure 3-3D) at the target site, suggesting that target sites were almost completely cleaved in cells by nucleus-localized Cas9 and that the rate-limiting factor in genome editing was nuclear localization of Cas9. Cy3-Cas9 alone was rarely detected in nuclei and did not induce indels (Figure 3-3A and D). Note that Cas9 is a positively-charged protein with a pI value of 9.12 and cannot form a complex with cationic lipids in the absence of negatively-charged sgRNAs. The Cy3-Cas9 RNP, however, was less active than the unlabeled Cas9 RNP, which induced target-specific mutations at a frequency of 80%.

Next, I delivered the *Vegfa*-specific, Cy3-labeled or -unlabeled Cas9 RNP into the adult mouse eye via subretinal injection (139). Cy3 dye was observed in the nuclei of the RPE *in vivo* three days after the injection (Figure 3-3E). Notably, the subretinal injection of the Cy3-unlabeled Cas9 RNP gave rise to indels with a frequency of 25 ± 3% in RPE cells in the RNP-injected area at day 3 post-injection (n = 5, Figure 3-3F and Figure 3-4A).

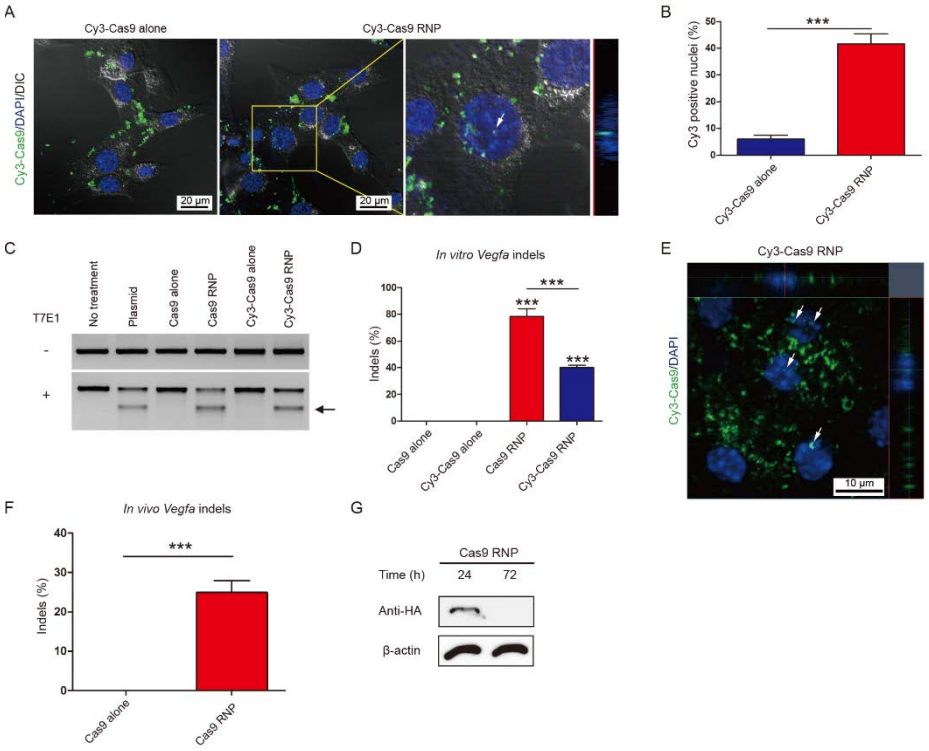

Figure 3-3. *In vitro* and *in vivo* delivery of Cy3-labeled Cas9 RNP. (A) Localization of Cy3 dye in NIH3T3 cells transfected with Cy3-labeled Cas9 RNP or Cy3-labeled Cas9 alone (as a control) at 24 h post-transfection. White arrows indicate nuclear colocalization of Cy3 dye. The z-axis image on the right shows that Cy3-Cas9 is localized inside the nucleus. (B) Proportion of Cy3 positive nuclei in total DAPI positive nuclei at 24 h post-transfection. Error bars indicate SEM. (n = 3). Student's *t*-test, *** $P < 0.001$. (C) *Vegfa*-specific Cas9 RNP-mediated mutations in NIH3T3 cells detected by the T7E1 assay. The arrow indicates the expected position of DNA bands cleaved by T7E1. (D) Mutation frequencies were measured using targeted deep sequencing. Error bars are SEM. (n = 3). One-way ANOVA and Tukey post-

hoc tests, *** $P < 0.001$. (E) Representative RPE flat-mount at day 3 post-injection of Cy3-labeled Cas9 RNP into mouse eye. White arrows indicate nuclear colocalization of Cy3 dye. (F) Frequencies of indels induced *in vivo* determined using genomic DNA isolated from the retinal pigment epithelium (RPE). Indels were analyzed by deep sequencing at day 3 post-injection. Error bars are SEM. (n = 5). Student's *t*-test, *** $P < 0.01$. (G) Representative Western blot analysis to measure the level of Cas9 protein in the RPE/choroid/scleral complex 24 and 72 h after injection (n = 4).

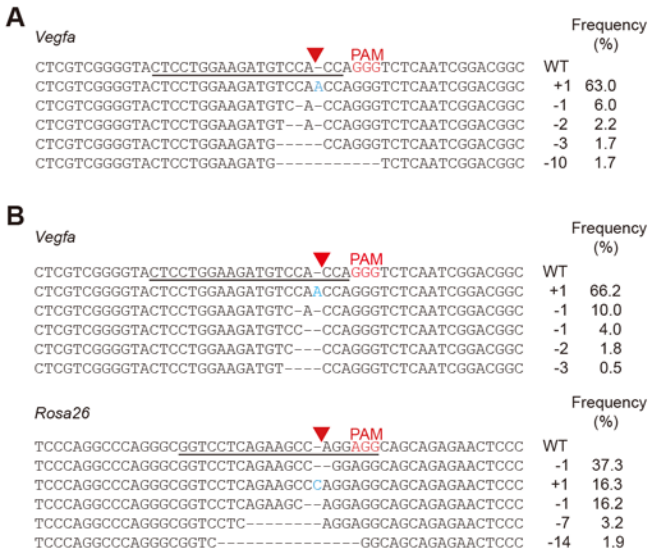

Figure 3-4. Mutant DNA sequences induced by *Vegfa*-specific Cas9 ribonucleoproteins (RNPs) *in vivo*. (A) Representative mutant DNA sequences in RPE at day 3 post-injection induced by the *Vegfa*–specific Cas9 RNP. (B) Mutant DNA sequences in RPE containing laser-induced choroidal neovascularization (CNV) at day 7 post-injection. The PAM sequence is shown in red. WT, wild-type. The column on the right indicates the number and frequency of inserted or deleted bases and indel frequencies (%).

Subretinal injection of RNPs did not induce detectable on-target indels in the neural retinal tissue or in the remnant RPE-choroid-sclera complex after RPE removal. Thus, in our experiments, subretinal injection of RNPs can induce indels in RPE cells in the injected area. I also performed Western blot analysis and found that the Cas9 protein was degraded completely at day 3 post-injection (Figure 3-3G), showing that Cas9 was rapidly turned over *in vivo*. Considering that Cas9 expression *in vivo* using adeno-associated virus (AAV) can evoke host immune responses with distinct cellular and molecular signatures (190), rapid degradation of Cas9 after RNP delivery has an advantage for *in vivo* application.

Encouraged by the efficient delivery and high mutation frequency of the *Vegfa*-specific Cas9 RNP *in vitro* and *in vivo*, I investigated whether the Cas9 RNP could be used for the treatment of CNV in a mouse model of AMD (122). Mice with laser-induced CNV were treated by subretinal injection of the *Vegfa*-specific Cas9 RNP or *Rosa26*-specific Cas9 RNP (Figure 3-5A). The *Rosa26*-RNP was used as a negative control. At day 3 post-injection, indels were analyzed in RPE cells in the Cas9 RNP-injected CNV area. Cas9-induced indels were detected at a frequency of 22 ± 5% or 24 ± 2% in the *Vegfa*-RNP-treated or the *Rosa26*-RNP-treated CNV (n = 5), respectively, (Figure 3-4B and Figure 3-5E and F), demonstrating that subretinal injection of the *Vegfa*-RNP can lead to local treatment in the eye. In addition, the *Vegfa*-RNP effectively reduced the concentration of the VEGFA protein in the CNV area (300 ± 20 pg/mL, n = 10), compared to the *Rosa26*-RNP (440 ± 30 pg/mL, n = 10, $P < 0.01$, Student's *t*-test) (Figure 3-5D).

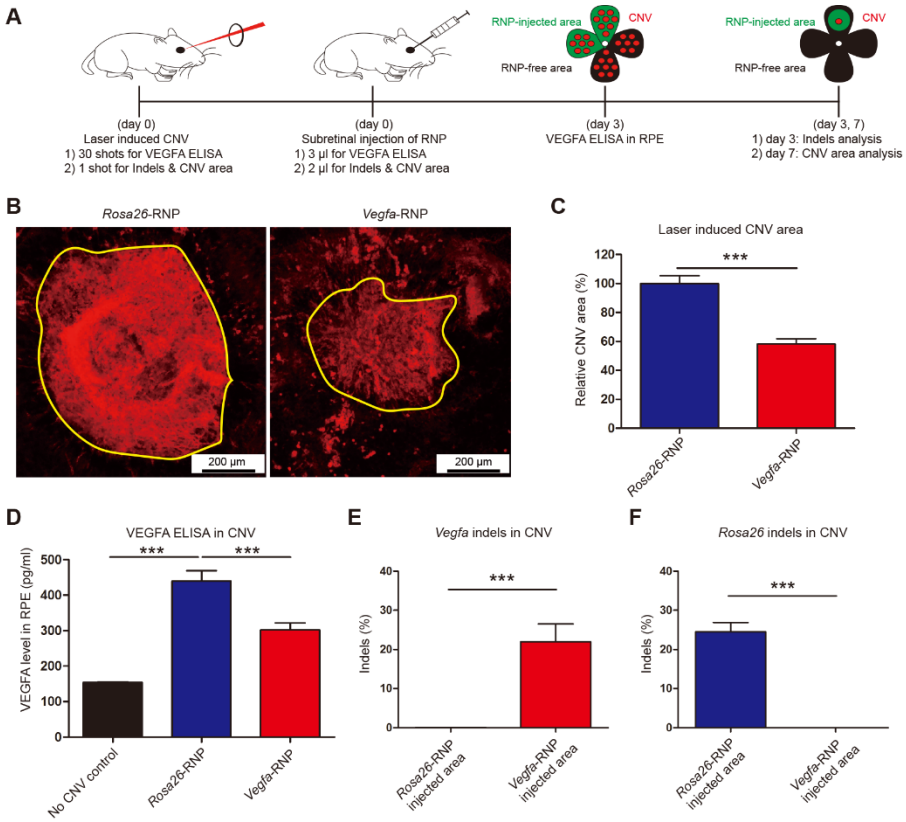

Figure 3-5. Subretinal injection of Cas9 RNPs targeting *Vegfa* reduces the area of laser-induced choroidal neovascularization (CNV) in a mouse model of age-related macular degeneration (AMD). (A) Mice with laser-induced CNV were treated with subretinal injection of the *Vegfa*-specific preassembled Cas9 RNP (*Vegfa*-RNP). After the retinal pigment epithelium (RPE) complex in the eye was flat-mounted, the CNV area was analyzed at day 7 post-injection. Genomic DNA isolated from the Cas9 RNP-injected area or from the opposite non-injected area (RNP-free area) was analyzed by deep sequencing. VEGFA ELISA was performed at day 3 post-injection. (B) Representative laser-induced CNV stained with isolectin B4 (IB4) in

C57BL/6J mice injected with the *Rosa26*-specific Cas9 RNP (as a control) or the *Vegfa*-RNP. The yellow line demarcates the area of CNV. (C) The CNV area. Error bars indicate SEM. (n = 15). Student's *t*-test, *** $P < 0.001$. (D) VEGFA level in CNV. Error bars indicate SEM. (n = 10). One-way ANOVA and Tukey post-hoc tests, *** $P < 0.001$. (E) Indel frequencies at the *Vegfa* target site in the RPE cells. Error bars indicate SEM. (n = 5). Student's *t*-test, *** $P < 0.001$. (F) Indel frequencies at the *Rosa26* target site in the RPE cells. Error bars indicate SEM. (n = 5). Student's *t*-test, *** $P < 0.001$.

At day 7 post-injection, a therapeutic effect was evaluated by assessing the CNV area. In mice treated with the *Vegfa*-RNP, the CNV area was significantly reduced (58 ± 4%, n = 15, $P < 0.001$, Student's *t*-test), compared to that in *Rosa26*-RNP injected mice (Figure 3-5B and C). Our results suggest that targeted inactivation of *Vegfa* in the RPE using Cas9 RNPs enables therapeutic genome surgery for the local treatment of AMD.

A critical issue in therapeutic genome surgery is the target specificity of CRISPR-Cas9 nucleases. I investigated whether the *Vegfa*-RNP used in this study caused any off-target mutations in the mouse eye or in human cells. First, using Cas-OFFinder (216), I identified 20 potential off-target sites in the mouse genome that are most highly homologous to the Cas9 target site. Genomic DNA was isolated from the CNV-free, RPE complex in the mouse eye treated with the Cas9 RNP and subjected to targeted deep sequencing. At these 20 sites, no Cas9-induced indels were detected with a frequency above 0.1%, demonstrating that no off-target mutations were induced above sequencing error rates (0.1%, on average) (Figure 3-6).

Next, I determined genome-wide off-target effects in the human genome rather than the mouse genome (Figure 3-7A and B). Note that the target sequence of this particular Cas9 RNP is conserved in the human *VEGFA* gene. I assessed the human genome-wide specificity using Digenome-seq (207, 208), in which cell-free human genomic DNA is digested *in vitro* using the *Vegfa*-specific Cas9 RNP and then subjected to whole genome sequencing.

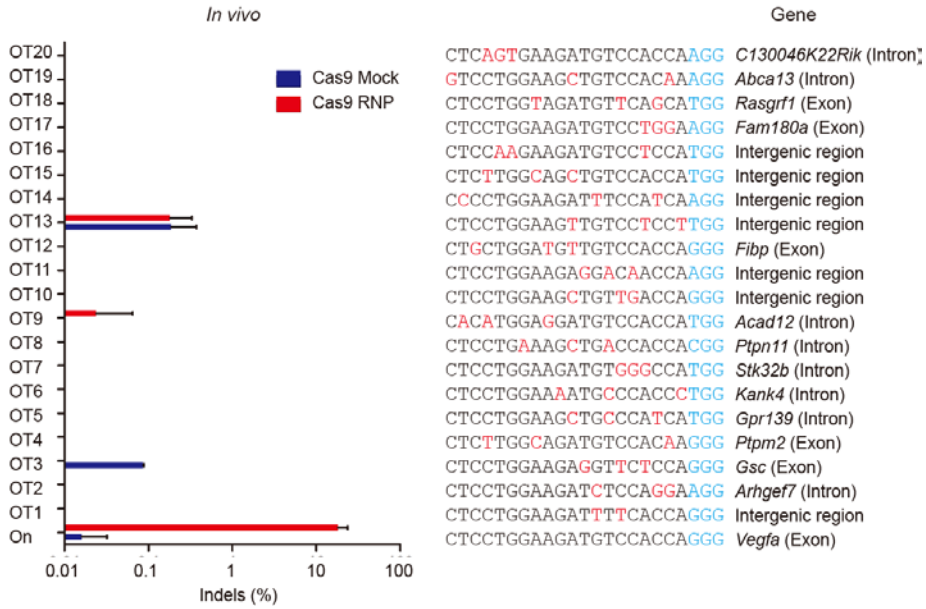

Figure 3-6. No detectable off-target effects of the *Vegfa*-specific Cas9 RNP in retinal pigment epithelium. Indel frequencies at 20 potential off-target sites identified by Cas-OFFinder. Error bars indicate SEM. (n = 3 for Cas9 Mock, n = 3 for Cas9 RNP, respectively). Mismatched nucleotides are shown in red and PAM sequences in blue.

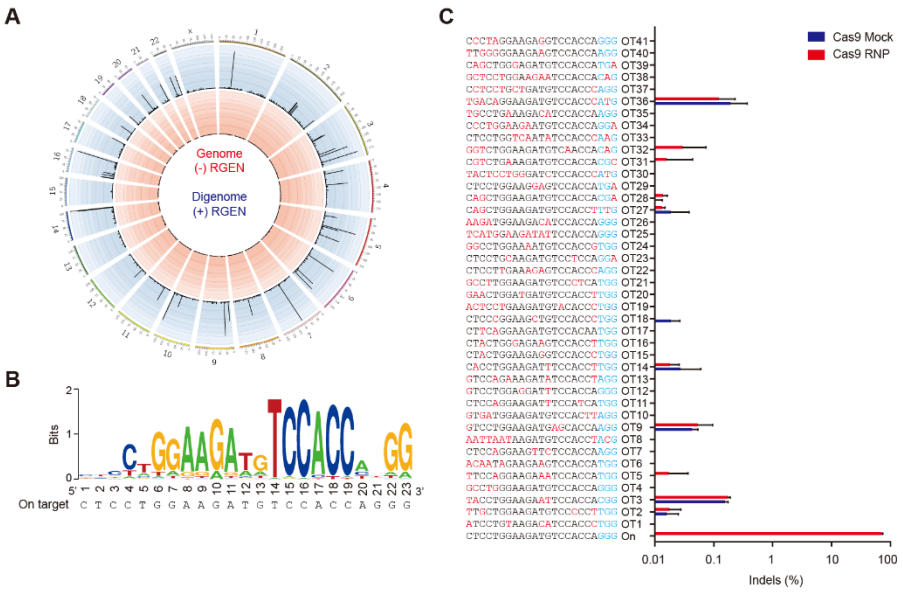

Figure 3-7. Genome-wide target specificity of the *Vegfa*-specific Cas9 RNP revealed by Digenome-seq. (A) Genome-wide Circos plot (218) showing in vitro cleavage sites. Human genomic DNA is shown in red and RGEN-digested genomic DNA in blue. (B) Sequence logo obtained using 42 Digenome-captured sites. (C) Off-target site validated in human ARPE-19 cells by targeted deep sequencing. The mismatched nucleotides are shown in red and PAM sequences in blue.

Uniform, rather than random, alignments of sequence reads at *in vitro* cleavage sites are computationally identified to provide a list of potential off-target sites. Digenome-seq using the *Vegfa*-RNP revealed *42 in vitro* cleavage sites including the on-target site (8). To validate or invalidate these sites, I carried out targeted deep sequencing using genomic DNA isolated from *Vegfa*-RNP-transfected ARPE-19 cells. Although these sites were cleaved efficiently *in vitro*, off-target indels were not detected at these 41 cleavage sites above sequencing error rates (Figure 3-7C). Use of Cpf1 (219, 220), Cas9 variants (221, 222) or modified gRNAs (223, 224) with improved specificity may avoid this residual off-target effect, if necessary. Taken together, these results show that the *Vegfa*-RNP is highly specific in both mouse and human cells.

Another major concern for mutating the *Vegfa* gene for the treatment of AMD is its trophic role in the eye. Cone dysfunction is the most significant change and is observed 3 days after conditional deletion of the *Vegfa* gene in mouse RPE (225). Note, however, that the *Vegfa* gene was mutated locally at the site of the RNP injection in our study. I evaluated the integrity of cone opsin at day 7, rather than day 3, post-injection and found that no cone dysfunction had occurred (Figure 3-8)

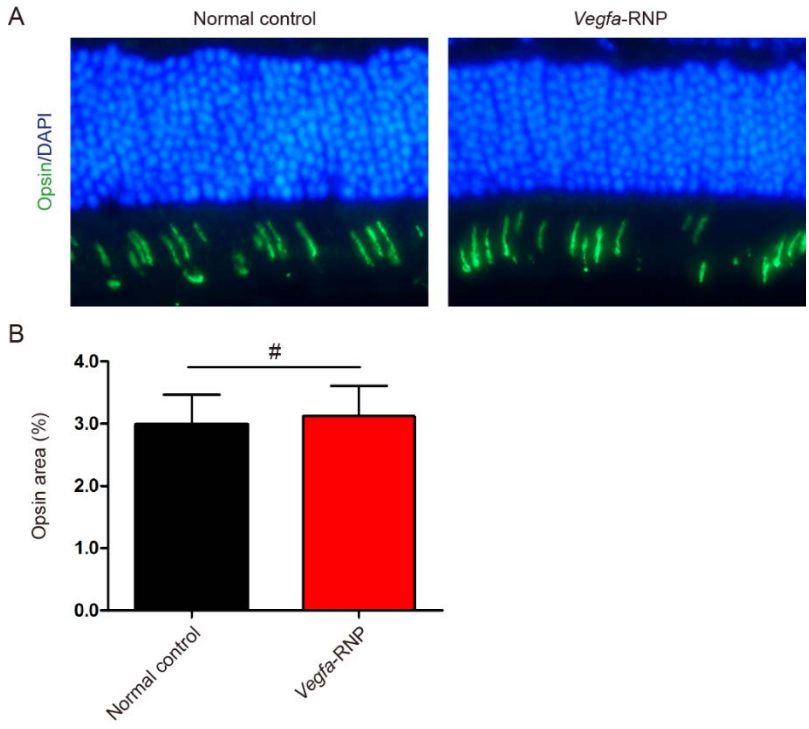

Figure 3-8. No cone dysfunction at day 7 post injection of the *Vegfa*-specific Cas9 RNP. (A) Representative cross section images with opsin (green) and DAPI (blue) stain from the retinas of *Vegfa*-RNP injected mice and un-injected control mice. (B) Relative opsin positive areas were compared between the normal control (3.0 ± 0.5%) and eyes injected with *Vegfa*-RNP (3.1 ± 0.5%). Error bars indicate SEM. (n = 4). #, $P > 0.05$ (Student's *t*-test).

Determination of PAM sequences recognized by CjCas9

First, I determined the PAM sequences recognized by CjCas9 *in vitro* (Figure 3-9B). A PCR amplicon library containing a CjCas9 target sequence followed by randomized 10-base pair (bp) sequences was cleaved by CjCas9 (and SpCas9 as a control) and a sgRNA specific to the target sequence. Cleaved duplexes were subjected to deep sequencing to identify PAM sequences recognized by CjCas9. This assay revealed that CjCas9 recognized 5'-NNNNACAC-3' or 5'-NNNNRYAC-3' (where R and Y stands for purines and pyrimidines, respectively) as PAMs *in vitro*. Using a different *in vitro* assay, Fonfara et al.(226) reported that the optimal PAM for CjCas9 was 5'-NNNNACA-3'.

To confirm the PAM specificity in human cells, I performed cell-based reporter assays by co-transfecting plasmids encoding CjCas9 and its sgRNA and reporter plasmids containing the target site with variable PAM sequences between RFP and GFP sequences(210) (Fig. 1c). Because the GFP sequence is fused to the RFP sequence out of frame in these reporter plasmids, cells express RFP but not GFP (RFP+ GFP-) in the absence of CjCas9. When CjCas9 cleaves the target site and induces small insertions or deletions (indels), the GFP sequence can be fused to the RFP sequence in frame. These reporter assays showed that CjCas9 cleaved target sites containing 5'-NNNNRYAC-3' PAM sequences in HEK 293 cells. Importantly, the cytosine nucleotide at the 3' end was essential.

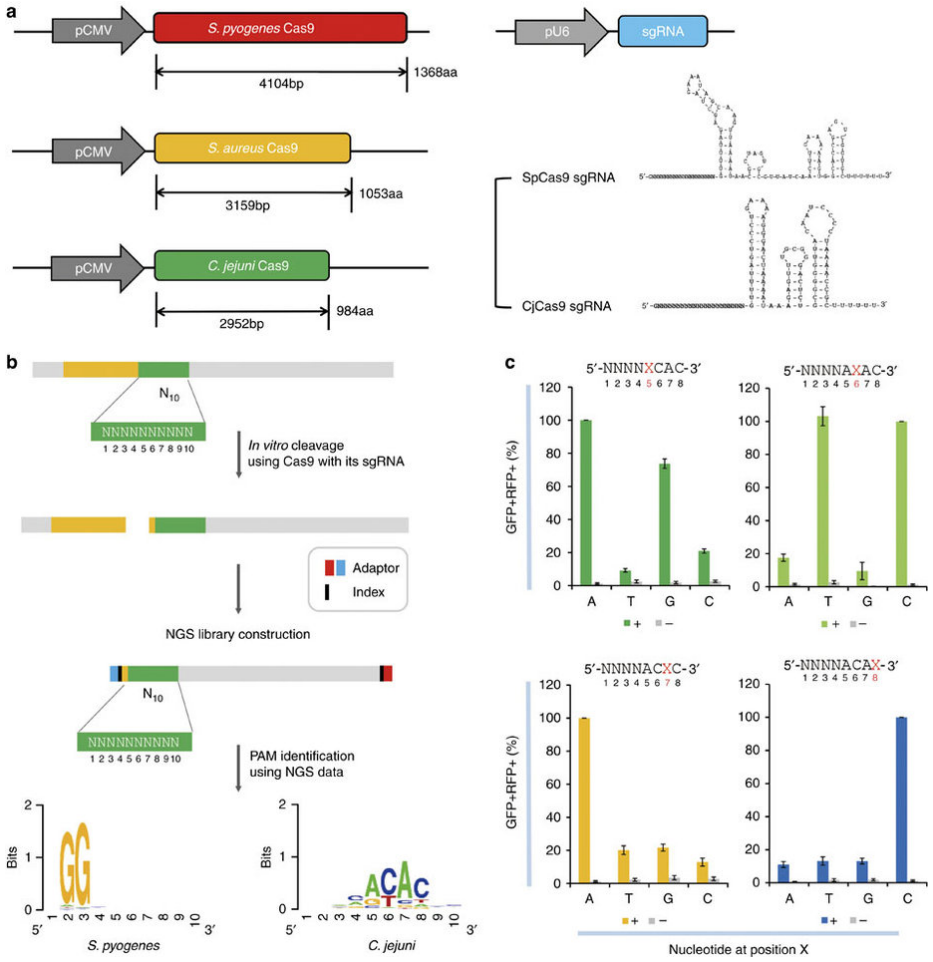

Figure 3-9. CjCas9 and its PAM specificity. (A) Cas9 orthologues and their sgRNAs. sgRNA structures were obtained using the mfold web server. (B) Schematic showing a PAM assay for characterization of PAM sequences recognized by Cas9. PCR amplicons containing a Cas9 target sequence (yellow) followed by randomized 10-bp (N10) sequences (green) were cleaved by CjCas9 in vitro. The sequence logo showing the PAM specificity was obtained using deep sequencing data. (C) PAM specificity in cells. Surrogate reporters encoding GFP and RFP and containing a CjCas9 target

sequence with degenerate PAMs were transfected with CjCas9 and its sgRNA plasmid into HEK 293 cells. The percentage of cells that express both GFP and RFP was normalized with that obtained using the optimal reporter containing the 5'-NNNNACAC-3' PAM sequence. (-) represents a mock control. Error bars indicate SEM (n = 3).

Optimization of CjCas9 sgRNA length

I next optimized the sgRNA length for CjCas9-mediated genome editing in human and mouse cells (Figure 3-10). I co-transfected CjCas9 and a series of sgRNAs with variable lengths into HEK293 cells or NIH3T3 cells and measured indel frequencies using targeted amplicon sequencing. The first nucleotide in the sgRNAs was fixed to an extra guanine (G) because sgRNAs are transcribed under the control of the U6 promoter, which requires a guanine at the 5' end. Unlike SpCas9, which is most active with GX_{20} sgRNAs that hybridize with a 20-nucleotide (nt) target DNA sequence upstream of a PAM, CjCas9 was most active with GX_{22} sgRNAs that hybridize with a 22-nt target sequence. GX_{20} and GX_{19} sgRNAs failed to induce indels at 8 out of 19 sites and 3 out of 4 sites, respectively in human or mouse cells.

I tested GX_{22} sgRNAs at 12 sites containing the optimal 5'-NNNNACAC-3' PAM in human cells. All of these sgRNAs co-transfected with CjCas9 were able to induce indels at frequencies that ranged from 1.0% to 64% (21 ± 5%, on average). CjCas9 also induced indels at sites with 5'-NNNNGCAC-3' PAMs, 5'-NNNNGTAC-3' PAMs, and 5'-NNNNATAC-3' PAMs albeit less efficiently (10 ± 3%, 10 ± 4%, and 16 ± 5%, respectively).

Genome-wide target specificities of CjCas9

I then determined genome-wide specificities of CjCas9 using nuclease-digested whole genome sequencing (Digenome-seq) (207, 211, 227). Cell-

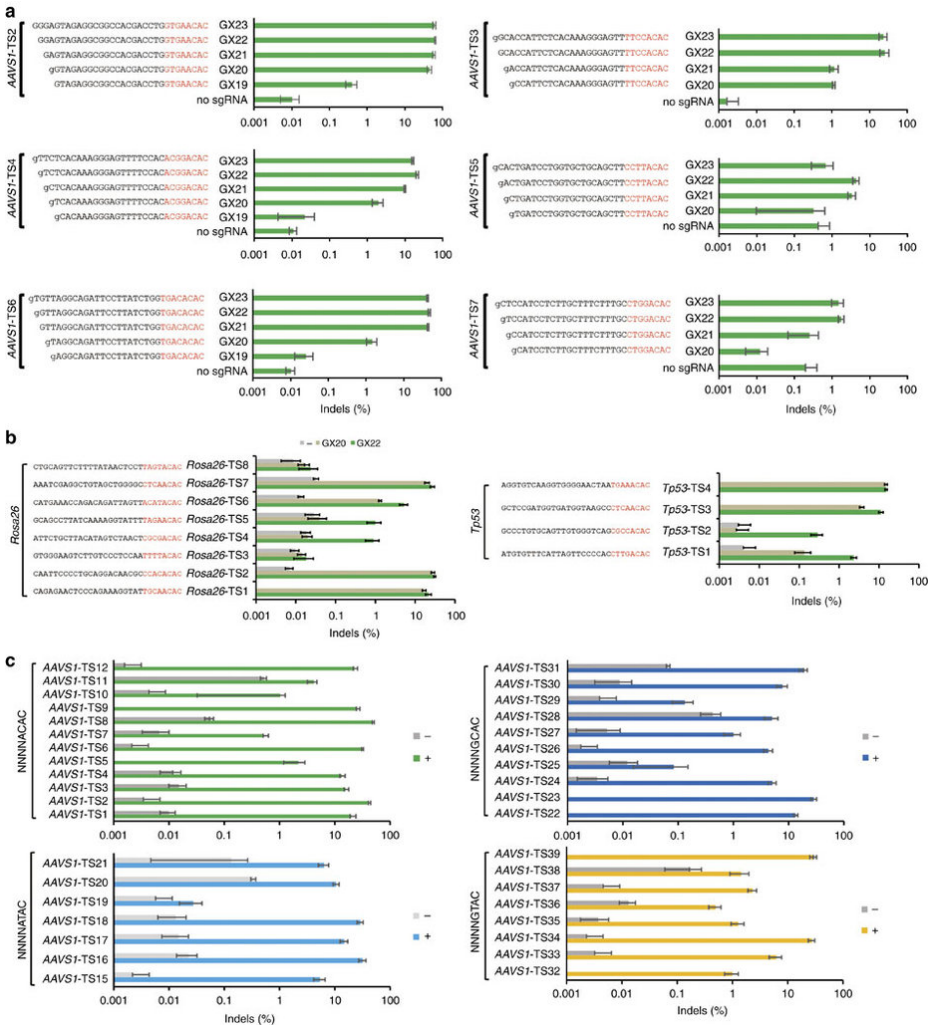

Figure 3-10. Optimization of sgRNA length for CjCas9. (A) sgRNAs with variable lengths (19 to 23 nucleotide complementary with a target DNA sequence) were designed and transfected with CjCas9 plasmid into human HEK293 cells. Genomic DNA was isolated 48 h after transfection. Indel frequencies were analyzed by targeted deep sequencing. The first guanine nucleotide at the 5' end that does not match the target sequence is shown in lower case. PAM motifs are shown in red. Error bars indicate SEM. (n = 3).

(B) Mutation frequencies at target sites in the mouse genome. *Rosa26* and *Tp53*-specific gX22 guide RNAs were designed and transfected into mouse NIH3T3 cells together with CjCas9 plasmid. Genome editing efficiencies were examined by deep sequencing using genome DNA isolated from cells after 48 h of transfection. PAM motifs are shown in red. Error bars indicate SEM (n = 3). (C) CjCas9-mediated genome editing at the human AAVS1 locus with different PAM sequences. sgRNAs targeting sites with a 5'-NNNNACAC-3' PAM (green; 12 sgRNAs), 5'-NNNNATAC-3' PAM (light blue; 7 sgRNAs), 5'-NNNNGCAC-3' PAM (dark blue; 10 sgRNAs), and 5'-NNNNGTAC-3' PAM (yellow; 8 sgRNAs) were designed and their activities examined in HEK293 cells with deep sequencing. Error bars indicate SEM (n = 3).

free genomic DNA digested with CjCas9 *in vitro* was subjected to whole genome sequencing (WGS). Uniform cleavage patterns corresponding to on-target and off-target cleavage sites were computationally identified. CjCas9 designed to target 6 different DNA regions cleaved between one and 27 sites (7 ± 4 sites, on average) in the human or mouse genome (Figure 3-11A-D). In parallel, I used Digenome-seq to test three SpCas9 nucleases designed to cleave sites that overlapped with CjCas9 target sites. SpCas9 cleaved 15 to 147 sites (70 ± 40 sites, on average) in the human or mouse genome, in line with our previous results showing that SpCas9 targeted to 11 different sites cleaved 90 ± 30 sites in the human genome (211). One target site in the human genome contained a 5'-NGGNACAC-3' PAM recognized by both CjCas9 and SpCas9. CjCas9 and SpCas9 cleaved human genomic DNA at 5 sites and 45 sites, respectively, although the two Cas9 orthologues showed comparable indel frequencies at this particular site. Thus, the higher specificity of CjCas9 was not gained at the expense of its lower editing efficiency. Strikingly, two CjCas9 nucleases targeting the *Rosa26* locus or the *Vegfa* gene in the mouse genome cleaved genomic DNA only at the single on-target site, reminiscent of the remarkable specificity of Cpf1 nucleases (227, 228). Sequence logos obtained computationally by comparing *in vitro* cleavage sites with each other unambiguously showed that these sites contained 5'-NNNNACAC-3' or 5'-NNNNRYAC-3' PAMs.

I chose the most promiscuous CjCas9 nuclease, which cleaved genomic DNA at 27 sites, and performed targeted amplicon sequencing to measure indel frequencies in human cells. Indels occurred at the on-target site but were

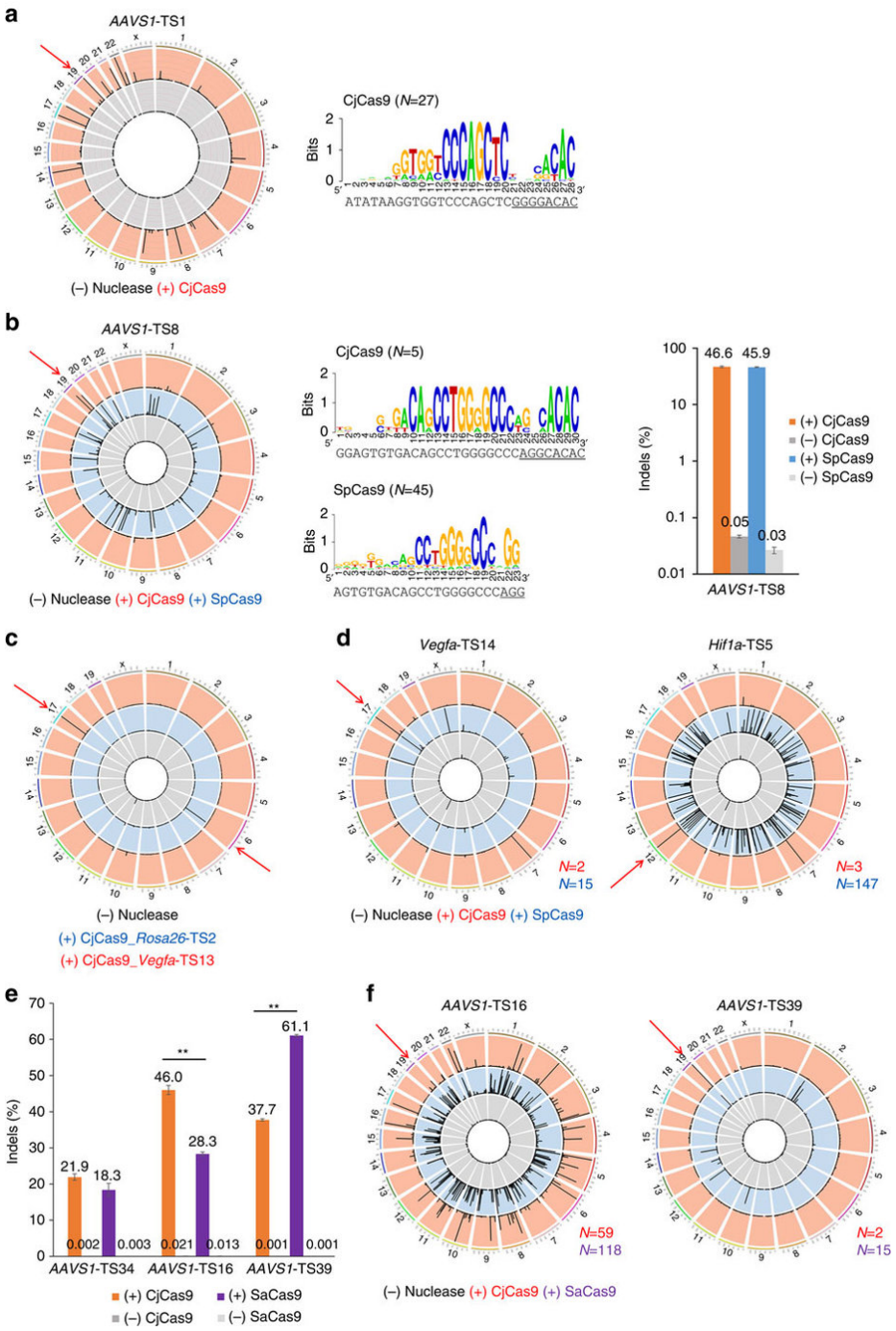

Figure 3-11. Genome-wide target specificities of CjCas9 nucleases examined using Digenome-seq. Human or mouse genomic DNA isolated

from HeLa cells or NIH3T3 cells (grey), respectively, was digested in vitro by Cas9 and its sgRNA targeted to the human *AAVS1* locus (A, B, F) and the mouse *Rosa26* (C), *Vegfa* (C and D) and *Hif1a* loci (D) and subjected to whole-genome sequencing. Circos plots show genome-wide DNA cleavage scores across the human or mouse genome. Red arrows indicate on-target sites. N indicates the number of *in vitro* cleavage sites identified by Digenome-seq. (A and B) Sequence logos were obtained by comparing DNA sequences at *in vitro* cleavage sites with each other. (B) Indel frequencies at the *AAVS1*-TS8 site measured using targeted deep sequencing. CjCas9 (orange) or SpCas9 (blue) targeted to the *AAVS1*-TS8 site was transfected into human HEK293 cells. Error bars indicate SEM (n =3). (E) Indel frequencies at three *AAVS1* sites targeted by CjCas9 (orange) and SaCas9 (violet).

not detectably induced at the other *in vitro* cleavage sites. Taken together, these results show that CjCas9 nucleases are highly specific in human cells. The remarkable specificity of CjCas9 can be at least partially attributed to its extended, 22-nt target and 4-nt PAM sequences, compared to the 20-nt target and 2-nt PAM sequences recognized by SpCas9.

Efficiency and specificity of CjCas9

I compared genome editing efficiencies and specificities of CjCas9 with those of SaCas9. I chose 3 overlapping sites in the human genome with 5'-NNGRRTAC-3' PAM sequences, which can be targeted by both CjCas9 and SaCas9. CjCas9 and SaCas9 generated indels at these sites in HEK293 cells with comparable frequencies of 35 ± 7% and 36 ± 13%, respectively (Figure 3-11E). I then determined genome-wide specificities of CjCas9 and SaCas9 nucleases targeted to two of these overlapping sites using Digenome-seq (Figure 3-11F). CjCas9 and SaCas9 targeted to the *AAVS1*-TS16 site cleaved human genomic DNA at 59 and 118 sites, respectively. CjCas9 and SaCas9 targeted to the *AAVS1*-TS39 site were more specific than were those targeted to the TS16 site, cleaving human genomic DNA at 2 and 15 sites, respectively. Note that CjCas9 targeted to the TS16 site was more efficient than SaCas9 in terms of on-target indel frequency (46% vs. 28%), suggesting that the higher specificity of CjCas9 was not gained at the expense of a lower on-target efficiency. These results demonstrate that CjCas9 is as efficient as SaCas9 but is more specific than SaCas9 at least at the sites I tested in human cells.

All-in-one AAV vector for *in vivo* genome editing

With its small size, the CjCas9 gene plus a sgRNA sequence can be packaged into an all-in-one AAV vector (Figure 3-12A). CjCas9 directed to the *Rosa26* locus was expressed in C2C12 mouse myotubes using an AAV serotype DJ (AAVDJ) vector. Indels accumulated at the target site in a time- and dose-dependent manner with a frequency of up to 79 ± 7% (Figure 3-12B). Because no sites other than the on-target site were cleaved by this particular CjCas9 nuclease in the mouse genome, as shown above using Digenome-seq, I identified, using Cas-OFFinder (229), potential off-target sites that differed from the on-target site by up to 4 nucleotides in the genome. No indels were detected at the resulting 20 homologous sites by targeted deep sequencing even at day 14 post-infection, confirming the high specificity of this CjCas9 nuclease.

I next packaged the muscle-specific Spc512 promoter-driven CjCas9 and the U6 promoter-driven *Rosa26*-specific sgRNA into a muscle-tropic AAV serotype 9 (AAV9) vector (230) (Fig. 4c). The resulting virus was administered via intramuscular injection into tibialis anterior (TA) muscles of C57BL/6 mice (n = 3 per group). CjCas9-induced indels were observed at the target site in TA muscles with a frequency of 17 ± 1% and 13 ± 2%, 8 weeks and 32 weeks, respectively, after injection. No indels were detectably induced at the 20 possible off-target sites in TA muscles even 32 weeks after injection (Figure 3-12D), although CjCas9 was still expressed. This result

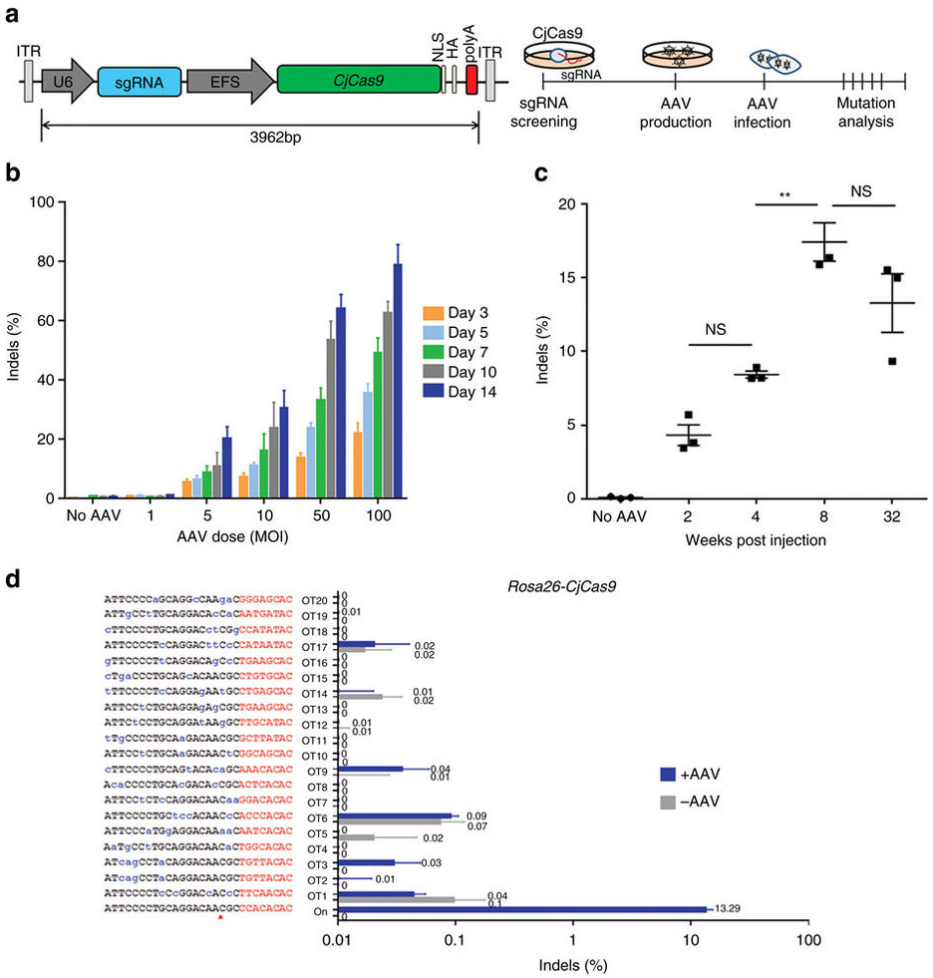

Figure 3-12. AAV-mediated mutagenesis *in vitro* and *in vivo*. (A) AAV vector encoding CjCas9 and its sgRNA. (B) Indel frequencies at the *Rosa26* target site in mouse C2C12 myotubes infected with AAV-CjCas9. (C) Indel frequencies at the *Rosa26* target site in TA muscles of C57BL/6 mice injected with AAV-CjCas9 measured at 2, 4, 8 and 32 weeks after injection. One-way ANOVA and Tukey post-hoc tests, ** $P < 0.01$, ns: not significant. (D) No off-target indels were detected at 20 homologous sites that differed from the

on-target site by up to 4 nucleotides in the mouse genome. Genomic DNA isolated from AAV-CjCas9-injected TA muscles of C57BL/6 mice at 32 weeks after injection was analyzed by targeted deep sequencing. Mismatched nucleotides are shown in blue and PAM sequences in red. Red arrows indicate cleavage positions within the 20-bp target sequences. Error bars indicate SEM (n =3).

suggests that a long-term expression of CjCas9 via AAV *in vivo* does not necessarily aggravate off-target effects.

In vivo genome editing in the mouse retina

To show that CjCas9 can be expressed via AAV in other tissues such as retina in mice and to investigate the therapeutic potential of CjCas9-mediated gene surgery for the treatment of AMD, a leading cause of blindness in adults, I prepared an AAV9 vector encoding CjCas9 under the control of the elongation factor-1 short (EFS) promoter, enhanced green fluorescent protein (eGFP) linked to the C-terminus of CjCas9 with the self-cleaving T2A peptide, and a U6 promoter-driven sgRNA specific to the *Vegfa* or *Hif1a* gene, whose expression in the retina is associated with choroidal neovascularization (CNV) (231, 232) (Figure 3-13A an B). I monitored the expression of CjCas9 in the eye and measured indel frequencies using targeted deep sequencing and Vegfa protein levels using ELISA, 6 weeks after the resulting viruses were administered into the eye via intravitreal injection.

In RPE cells, primary target cells for the treatment of AMD, AAV encoding the *Vegfa*-specific CjCas9 (AAV-CjCas9: *Vegfa*) achieved indels with frequencies that ranged from 22% to 30% at day 14, 28, and 42 post-injection (Figure 3-13C). As expected, CjCas9-linked eGFP was expressed in RPE cells (Figure 3-13D). At day 42 post-injection, CjCas9-induced indels were observed at *Rosa26*, *Vegfa*, and *Hif1a* target sites in the retina with a frequency of 44 ± 18%, 20 ± 5, 58 ± 12, respectively (Figure 3-13E) and in

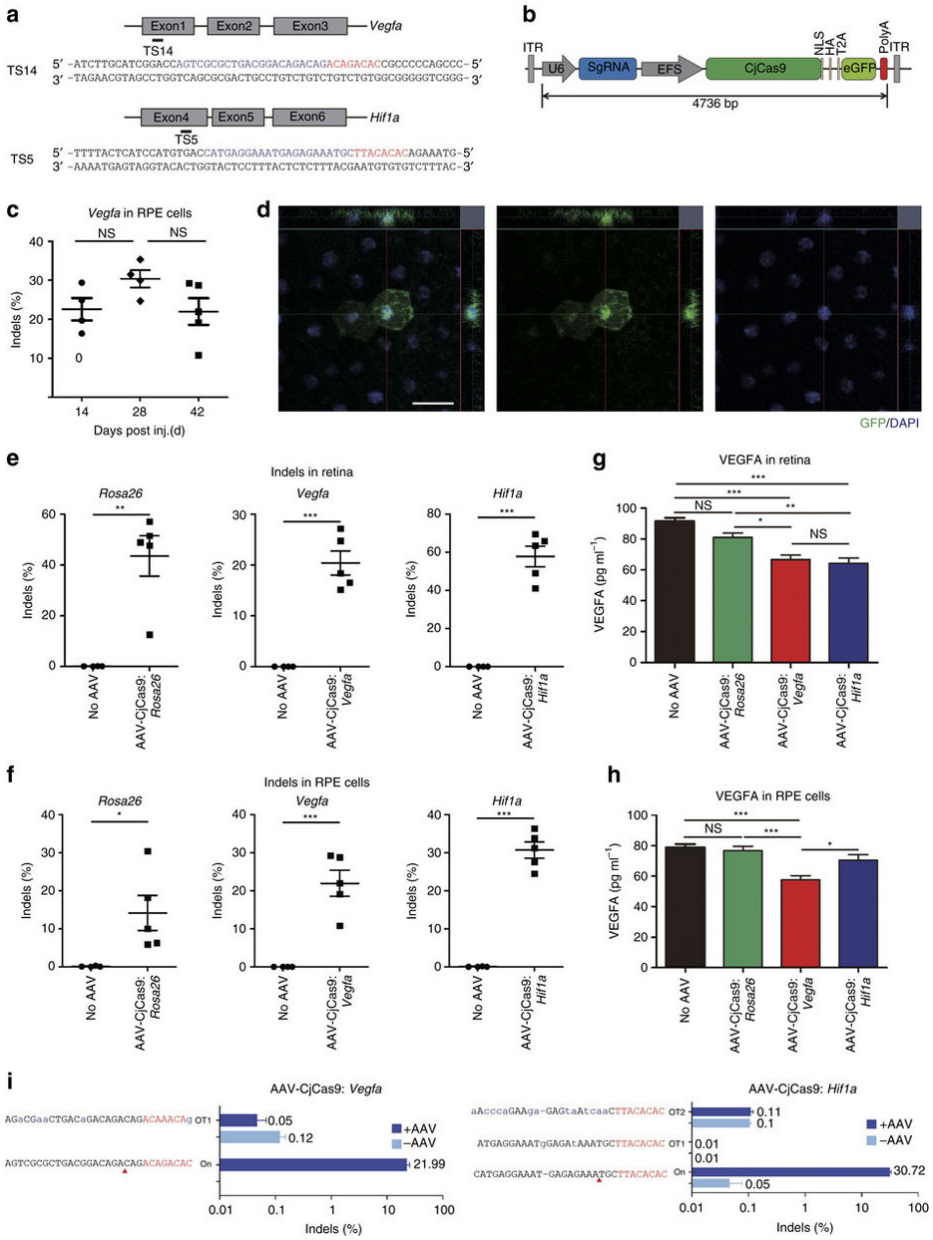

Figure 3-13. ***In vivo*** **genome editing with CjCas9 in the retina and retinal pigment epithelium.** (A) The CjCas9 target sequences in *Vegfa* and *Hif1a/HIF1A* genes. The PAM sequence and the sgRNA target sequence are shown in red and blue, respectively. (B) All-in-one AAV vector encoding

CjCas9. (C) Indel frequencies at the *Vegfa* target site were analyzed in RPE cells using deep sequencing at day 14, 28, and 42 post-intravitreal injection of AAV-CjCas9: *Vegfa*. Error bars indicate s.e.m. (n = 4-5). One-way ANOVA and Tukey post-hoc tests, ns; not significant. (D) Representative confocal images of in vivo eGFP expression in RPE cells of AAV-CjCas9-injected mice 6 weeks after injection (n = 6). eGFP was stained with anti-GFP antibody (green). Nuclei were counter-stained with DAPI (blue). Scale bar is 20 μm. (E-I) At day 42 post injection of AAV-CjCas9, indel frequencies and Vegfa protein levels were measured in retina and RPE cells using deep sequencing and ELISA, respectively. (E and F) Indel frequencies at the Rosa26, Vegfa, and Hif1a target sites in the retina (E) and RPE cells (F). Error bars indicate SEM (n = 4 for AAV-uninjected control, n = 5 for AAV-CjCas9). Student's *t*-tests, * $P < 0.05$, *** $P < 0.001$. (G and H) Vegfa levels measured by ELISA in the retina (G) and RPE cells (H), respectively. Error bars indicate SEM (n = 6-7). One-way ANOVA and Tukey post-hoc tests, * $P < 0.05$, *** $P < 0.001$. (I) Indel frequencies at in vitro cleavage sites identified by Digenome-seq. Genomic DNA isolated from RPE cells treated with AAV-CjCas9 at 6 weeks post-injection was subjected to targeted deep sequencing. Mismatched nucleotides are shown in blue and PAM sequences in red. Red arrows indicate cleavage positions within the 22-bp target sequences.

RPE cells with a frequency of 14 ± 5%, 22 ± 3%, and 31 ± 2%, respectively (Figure 3-13F). As expected, the Vegfa protein level measured using ELISA was decreased in the retina treated with AAV encoding the *Vegfa*- or *Hif1a*-specific CjCas9 (AAV-CjCas9: *Vegfa* and *Hif1a*) but not in those treated with AAV-CjCas9: *Rosa26* (Figure 3-13G). The Vegfa protein level was also decreased in RPE cells treated with the AAV-CjCas9: *Vegfa*. However, the protein level was not decreased in those with the AAV-CjCas9: *Hif1a* or *Rosa26* (Figure 3-13H), suggesting that Vegfa expression is differentially regulated in the retina and in RPE cells. I did not measure Hif1α protein levels because Hif1α is degraded under normoxia conditions. No off-target indels were detectably induced in these cells at one or two *in vitro* cleavage sites captured by Digenome-seq using the *Vegfa*-specific or the *Hif1a* specific sgRNA, respectively (Figure 3-13I), ruling out the possibility that the partial suppression of Vegfa expression in the retina and RPE cells were caused by CjCas9 off-target effects.

Therapeutic genome editing for the treatment of CNV

Next, I induced CNV in the eye by laser treatment 6 weeks after injection of AAV and measured the area of CNV one week later (Figure 3-14A). Both AAV-CjCas9: *Vegfa* and AAV-CjCas9: *Hif1a* reduced the area of CNV by 24 ± 4% and 20 ± 4%, respectively, compared to the AAV-uninjected negative control (Figure 3-14B-D). The *Rosa26*-specific CjCas9, used as another negative control, did not show any therapeutic effect. I noted that CjCas9

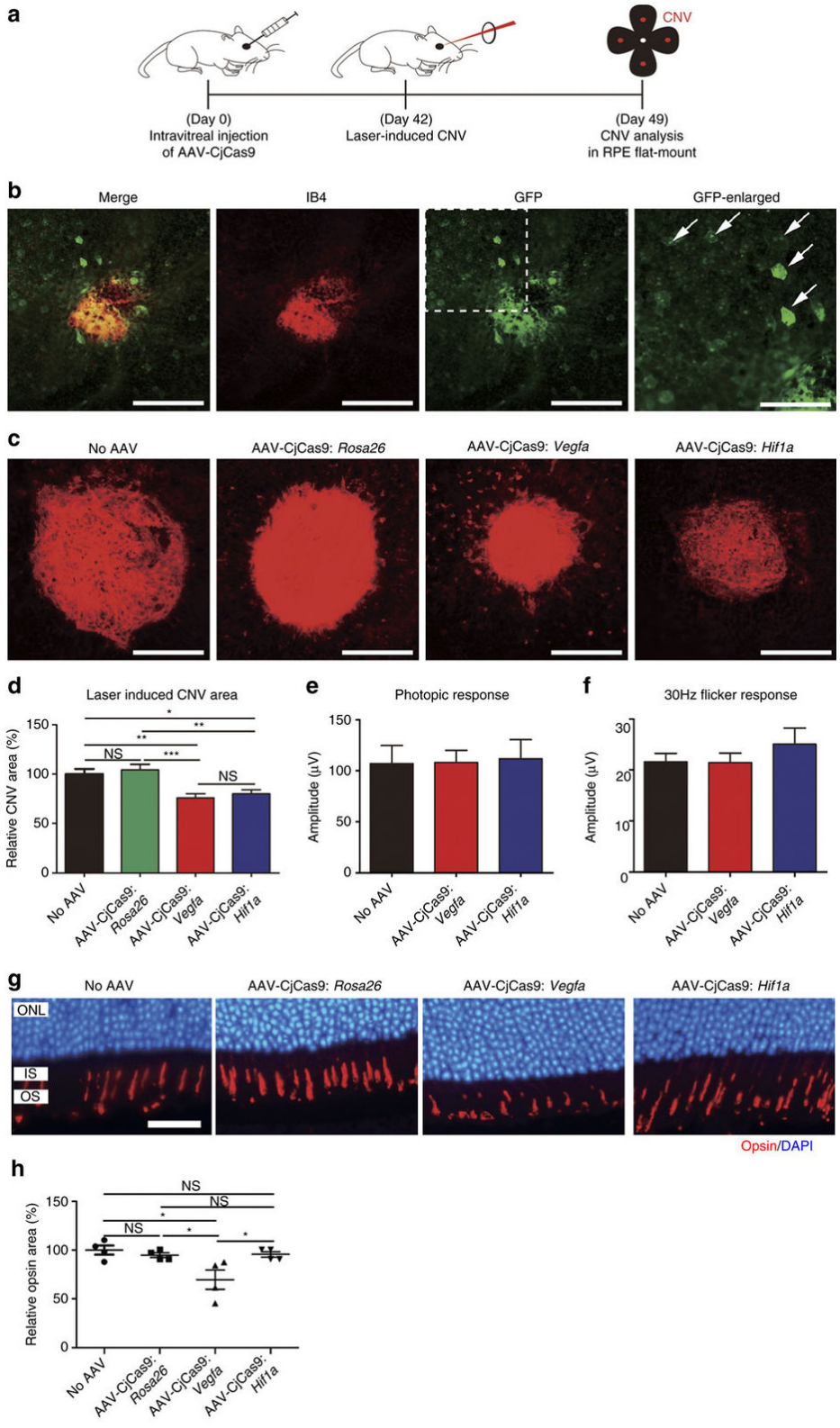
a
CNV
(Day 0)
Intravitreal injection
of AAV-CjCas9
(Day 42)
Laser-induced CNV
(Day 49)
CNV analysis
in RPE flat-mount
b
Merge
IB4
GFP
GFP-enlarged
c
No AAV
AAV-CjCas9: Rosa26
AAV-CjCas9: Vegfa
AAV-CjCas9: Hif1a
d
Laser induced CNV area
Relative CNV area (%)
150
100
50
0
NS
NS
No AAV
AAV-CjCas9: Rosa26
AAV-CjCas9: Vegfa
AAV-CjCas9: Hif1a
e
Photopic response
Amplitude (μV)
f
30Hz flicker response
Amplitude (μV)
30
20
10
0
g
No AAV
AAV-CjCas9: Rosa26
AAV-CjCas9: Vegfa
AAV-CjCas9: Hif1a
ONL
IS
OS
Opsin/DAPI
h
Relative opsin area (%)
NS
NS
NS

Figure 3-14. CjCas9 targeted to *Vegfa* or *Hif1a* reduces the area of laser-induced CNV in mice. (A) At day 42 post injection of AAV-CjCas9, mice were treated with laser to induce choroidal neovascularization (CNV). One week after laser treatment, the CNV area was analyzed. (B) *In vivo* expression of eGFP coexpressed with CjCas9 in laser-induced CNV. Representative confocal images of eGFP expression in the RPE of laser-induced CNV, 6 weeks after injection of AAV-CjCas9: *Hif1a*. eGFP was stained with anti-GFP antibody (green), CNV was stained with anti-IB4 antibody (red), and nuclei were counter-stained with DAPI (blue). Scale bars, 200 μm. Arrows indicate eGFP-expressing RPE cells. The scale bar in enlarged image is 100 μm. (C) Representative laser-induced CNV stained with isolectin B4 in the mouse eye injected with AAV-CjCas9 targeted to *Rosa26*, *Vegfa*, or *Hif1a*. Scale bar is 200 μm. (D) The CNV area. Error bars indicate s.e.m. (n = 17-18). One-way ANOVA and Tukey post-hoc tests, * $P < 0.05$, ** $P < 0.01$, *** $P < 0.001$, ns; not significant. (E and F) At day 56 post AAV injection, full-field electroretinogram (ERG) was performed to evaluate cone function in mice. There was no significant decrease of b-wave of photopic response (E) and 30Hz flicker response (F) in both AAV-CjCas9: *Vegfa* (n = 8) or AAV-CjCas9: *Hif1a* (n = 6) treated mice, compared to normal control mice (n = 8). Error bars indicate s.e.m. (n = 6-8). (G and H) Opsin positive areas in the retina at day 42 post injection. (G) Representative images of opsin positive areas in contact with RPE cells expressing HA-tagged CjCas9 in AAV-CjCas9: *Rosa26*, *Vegfa*, or *Hif1a* injected mice compared to the AAV-uninjected negative control mice (no AAV). Opsin (red) and DAPI (blue).

Scale bar is 20 μm. ONL: outer nuclear layer, IS: inner segment of photoreceptor cells, OS: outer segment of photoreceptor cells. (H) Relative opsin areas of the AAV-CjCas9-injected mice were normalized to that of the AAV-uninjected negative control mice. Error bars indicate SEM (n = 4). One-way ANOVA and Tukey post-hoc tests, * $P < 0.05$.

linked eGFP was expressed in RPE cells surrounding CNV, which are a major source of Vegfa in laser-induced CNV (Figure 3-14B). This result shows that the reduction of CNV area coincides with targeted *Vegfa* mutagenesis and partial suppression of Vegfa expression in RPE cells (Figure 3-14H).

I then investigated whether the partial gene knockout of *Vegfa* and *Hif1a* in RPE cells using AAV caused any side effect. It was reported that a conditional knockout of the *Vegfa* gene but not that of the *Hif1a* gene in mouse RPE cells leads to cone dysfunction (225). I measured cone function using full-field electroretinography (ERG) in laser-untreated CNV-free mice 8 weeks after injection of AAV-CjCas9: *Vegfa* and AAV-CjCas9: *Hif1a* (Figure 3-14E and F). No significant decrease in photopic response (Fig. 6e) or 30Hz flicker response (Figure 3-14F) was observed in these mice, compared to AAV-uninjected control mice. I also measured the size of the opsin positive area, which is closely related to cone function, in contact with RPE cells expressing CjCas9. The AAV-CjCas9: *Vegfa* reduced the size by 30 ± 10%, compared to the AAV-uninjected control (Figure 3-14G and H), suggesting that the partial *Vegfa* gene knockout using AAV can still cause local opsin dysfunction near *Vegfa*-edited RPE cells. As expected, however, the AAV-CjCas9: *Rosa26* or AAV-CjCas9: *Hif1a* did not cause any such cone dysfunction. Taken together, these results raise a concern about targeted inactivation of *Vegfa* in RPE cells using AAV and suggest that *Hif1*a could be inactivated without causing cone dysfunction to avoid neovascularization for the treatment of AMD.

DISCUSSION

In the first part of Chapter III, I showed that genome surgery using Cas9 RNPs has the potential for local, rather than systemic, treatment for non-genetic diseases such as AMD. Unlike previous studies involving RNA-guided genome editing *in vivo* to correct genetic defects, this report is focused on inactivating a disease-causing wild-type gene. This approach can broaden the scope of druggable targets from several protein families such as kinases, ion channels, G protein-coupled receptors, etc. to any protein-coding or non-coding genes.

I believe that eye diseases are well-suited for *in vivo* genome editing using Cas9 RNPs. Because of its compartmented anatomy, subretinal injection is an optimized technique to deliver Cas9 RNPs into RPE cells for the local treatment. The laser-induced CNV model in mice I used in this study is not suitable for multiple injections of Cas9 RNPs, because CNV formation peaks around 2 weeks after laser treatment and then slightly regressed over time. For multiple injection studies, large animal models such as non-human primates should be considered. In human or non-human primates, subretinal injection of RNPs in a volume of 100-150 μL would be enough to cover choroidal neovascularization. I envision that genome surgery is not just a metaphor but can be a graphic description of “operations” in the near future by which surgeons or physicians use Cas9 RNPs as micro-scalpels to cut and paste disease-causing genetic elements in patients.

In the second part of Chapter III, I have presented a small and highly specific Cas9 orthologue, derived from *C. jejuni*, that can be packaged with a reporter gene in an AAV vector for efficient gene surgery *in vivo*. The small size of CjCas9, compared to other orthologues including *Neisseria meningitidis* Cas9 (233), *Streptococcus thermophilus* Cas9 (233), SpCas9 (234), and SaCas9 (184, 235), allows more room for additional effectors or homology arms required for homologous recombination in AAV and other animal or plant viral vectors. Because CjCas9 is highly specific *in vitro* and *in vivo*, I expect that it will be widely used for precision genome editing in research and gene surgery in medicine.

In this study, I delivered the CjCas9 gene, its sgRNA sequence, and the GFP-coding gene to mutate three genes in two different tissues, TA muscles and eyes, in mice. CjCas9 induced indels at high frequencies in the *Vegfa* and *Hif1a* genes *in vivo*. HIF1α is a hypoxia-inducible transcription factor that activates the transcription of *VEGF A* (236). Unlike VEGF A, a secretory protein and a primary therapeutic target for the treatment of AMD, HIF1 α has not been considered as a drug target: Indeed, HIF1α in particular and transcription factors in general cannot be targeted directly by antibodies or aptamers or small molecules. In this study, I showed that CjCas9 targeted to the *Hif1a* gene in mouse eyes inactivated the gene in RPE cells efficiently and reduced the area of CNV in a mouse model of AMD. Because the CjCas9 target site in the mouse *Hif1a* gene is perfectly conserved in the human *HIF1A* gene, the AAV presented in this study or its variants could be used for the treatment of human patients in the future. I expect that CjCas9 can be

directed to other traditionally “undruggable” genes or non-coding sequences to broaden the range of therapeutic targets, making the entire human genome potentially druggable.

REFERENCES

1. Park SW, Yun JH, Kim JH, et al. Angiopoietin 2 Induces Pericyte Apoptosis via alpha3beta1 Integrin Signaling in Diabetic Retinopathy. Diabetes 2014;63:3057-3068

2. Yun JH, Park SW, Kim JH, et al. Angiopoietin 2 induces astrocyte apoptosis via alphavbeta5-integrin signaling in diabetic retinopathy. Cell Death Dis 2016;7:e2101

3. Yun JH, Park SW, Kim KJ, et al. Endothelial STAT3 Activation Increases Vascular Leakage Through Downregulating Tight Junction Proteins: Implications for Diabetic Retinopathy. J Cell Physiol 2017;232:1123-1134

4. Park SW, Kim JH, Mook-Jung I, et al. Intracellular amyloid beta alters the tight junction of retinal pigment epithelium in 5XFAD mice. Neurobiol Aging 2014;35:2013-2020

5. Park SW, Kim JH, Park SM, et al. RAGE mediated intracellular Abeta uptake contributes to the breakdown of tight junction in retinal pigment epithelium. Oncotarget 2015;6:35263-35273

6. Park SW, Im S, Jun HO, et al. Dry age-related macular degeneration like pathology in aged 5XFAD mice: Ultrastructure and microarray analysis. Oncotarget 2017;

7. Kim K, Park SW, Kim JH, et al. Genome surgery using Cas9 ribonucleoproteins for the treatment of age-related macular degeneration. Genome Res 2017;27:419-426

8. Kim E, Koo T, Park SW, et al. In vivo genome editing with a small Cas9

orthologue derived from Campylobacter jejuni. Nat Commun 2017;8:14500

9. Antonetti DA, Klein R, Gardner TW. Diabetic retinopathy. N Engl J Med 2012;366:1227-1239

10. Moss SE, Klein R, Klein BE. The incidence of vision loss in a diabetic population. Ophthalmology 1988;95:1340-1348

11. Klein R, Klein BE, Moss SE, Cruickshanks KJ. The Wisconsin Epidemiologic Study of Diabetic Retinopathy: XVII. The 14-year incidence and progression of diabetic retinopathy and associated risk factors in type 1 diabetes. Ophthalmology 1998;105:1801-1815

12. Cogan DG, Toussaint D, Kuwabara T. Retinal vascular patterns. IV. Diabetic retinopathy. Arch Ophthalmol 1961;66:366-378

13. Shepro D, Morel NM. Pericyte physiology. FASEB J 1993;7:1031-1038

14. Hammes HP, Lin J, Renner O, et al. Pericytes and the pathogenesis of diabetic retinopathy. Diabetes 2002;51:3107-3112

15. Romeo G, Liu WH, Asnaghi V, Kern TS, Lorenzi M. Activation of nuclear factor-kappaB induced by diabetes and high glucose regulates a proapoptotic program in retinal pericytes. Diabetes 2002;51:2241-2248

16. Miller AG, Smith DG, Bhat M, Nagaraj RH. Glyoxalase I is critical for human retinal capillary pericyte survival under hyperglycemic conditions. J Biol Chem 2006;281:11864-11871

17. Mizutani M, Kern TS, Lorenzi M. Accelerated death of retinal microvascular cells in human and experimental diabetic retinopathy. J Clin Invest 1996;97:2883-2890

18. Watanabe D, Suzuma K, Suzuma I, et al. Vitreous levels of angiopoietin 2

and vascular endothelial growth factor in patients with proliferative diabetic retinopathy. Am J Ophthalmol 2005;139:476-481

19. Hammes HP, Lin J, Wagner P, et al. Angiopoietin-2 causes pericyte dropout in the normal retina: evidence for involvement in diabetic retinopathy. Diabetes 2004;53:1104-1110

20. Cai J, Kehoe O, Smith GM, Hykin P, Boulton ME. The angiopoietin/Tie-2 system regulates pericyte survival and recruitment in diabetic retinopathy. Invest Ophthalmol Vis Sci 2008;49:2163-2171

21. Yao D, Taguchi T, Matsumura T, et al. High glucose increases angiopoietin-2 transcription in microvascular endothelial cells through methylglyoxal modification of mSin3A. J Biol Chem 2007;282:31038-31045

22. Pfister F, Feng Y, vom Hagen F, et al. Pericyte migration: a novel mechanism of pericyte loss in experimental diabetic retinopathy. Diabetes 2008;57:2495-2502

23. Pfister F, Wang Y, Schreiter K, et al. Retinal overexpression of angiopoietin-2 mimics diabetic retinopathy and enhances vascular damages in hyperglycemia. Acta Diabetol 2010;47:59-64

24. Feng Y, vom Hagen F, Pfister F, et al. Impaired pericyte recruitment and abnormal retinal angiogenesis as a result of angiopoietin-2 overexpression. Thromb Haemost 2007;97:99-108

25. Maisonpierre PC, Suri C, Jones PF, et al. Angiopoietin-2, a natural antagonist for Tie2 that disrupts in vivo angiogenesis. Science 1997;277:55-60

26. Augustin HG, Koh GY, Thurston G, Alitalo K. Control of vascular

morphogenesis and homeostasis through the angiopoietin-Tie system. Nat Rev Mol Cell Biol 2009;10:165-177

27. Hosaka K, Yang Y, Seki T, et al. Tumour PDGF-BB expression levels determine dual effects of anti-PDGF drugs on vascular remodelling and metastasis. Nat Commun 2013;4:2129

28. Felcht M, Luck R, Schering A, et al. Angiopoietin-2 differentially regulates angiogenesis through TIE2 and integrin signaling. J Clin Invest 2012;122:1991-2005

29. Abbott NJ, Ronnback L, Hansson E. Astrocyte-endothelial interactions at the blood-brain barrier. Nat Rev Neurosci 2006;7:41-53

30. Lee SW, Kim WJ, Choi YK, et al. SSeCKS regulates angiogenesis and tight junction formation in blood-brain barrier. Nat Med 2003;9:900-906

31. Cerani A, Tetreault N, Menard C, et al. Neuron-derived semaphorin 3A is an early inducer of vascular permeability in diabetic retinopathy via neuropilin-1. Cell Metab 2013;18:505-518

32. Barber AJ, Antonetti DA, Gardner TW. Altered expression of retinal occludin and glial fibrillary acidic protein in experimental diabetes. The Penn State Retina Research Group. Invest Ophthalmol Vis Sci 2000;41:3561-3568

33. Ly A, Yee P, Vessey KA, et al. Early inner retinal astrocyte dysfunction during diabetes and development of hypoxia, retinal stress, and neuronal functional loss. Invest Ophthalmol Vis Sci 2011;52:9316-9326

34. Pournaras CJ, Rungger-Brandle E, Riva CE, Hardarson SH, Stefansson E. Regulation of retinal blood flow in health and disease. Prog Retin Eye Res 2008;27:284-330

35. Choi YK, Kim JH, Kim WJ, et al. AKAP12 regulates human blood-retinal barrier formation by downregulation of hypoxia-inducible factor-1alpha. J Neurosci 2007;27:4472-4481

36. Kim JH, Kim JH, Yu YS, Kim DH, Kim KW. Recruitment of pericytes and astrocytes is closely related to the formation of tight junction in developing retinal vessels. J Neurosci Res 2009;87:653-659

37. Zhang Y, Stone J. Role of astrocytes in the control of developing retinal vessels. Invest Ophthalmol Vis Sci 1997;38:1653-1666

38. Gardner TW, Lieth E, Khin SA, et al. Astrocytes increase barrier properties and ZO-1 expression in retinal vascular endothelial cells. Invest Ophthalmol Vis Sci 1997;38:2423-2427

39. Chan-Ling T, Stone J. Degeneration of astrocytes in feline retinopathy of prematurity causes failure of the blood-retinal barrier. Invest Ophthalmol Vis Sci 1992;33:2148-2159

40. Medana IM, Chan-Ling T, Hunt NH. Redistribution and degeneration of retinal astrocytes in experimental murine cerebral malaria: relationship to disruption of the blood-retinal barrier. Glia 1996;16:51-64

41. Rungger-Brandle E, Dosso AA, Leuenberger PM. Glial reactivity, an early feature of diabetic retinopathy. Invest Ophthalmol Vis Sci 2000;41:1971-1980

42. Demircan N, Safran BG, Soylu M, Ozcan AA, Sizmaz S. Determination of vitreous interleukin-1 (IL-1) and tumour necrosis factor (TNF) levels in proliferative diabetic retinopathy. Eye (Lond) 2006;20:1366-1369

43. Krady JK, Basu A, Allen CM, et al. Minocycline reduces proinflammatory cytokine expression, microglial activation, and caspase-3 activation in a

rodent model of diabetic retinopathy. Diabetes 2005;54:1559-1565

44. Mocan MC, Kadayifcilar S, Eldem B. Elevated intravitreal interleukin-6 levels in patients with proliferative diabetic retinopathy. Can J Ophthalmol 2006;41:747-752

45. Nagai A, Nakagawa E, Hatori K, et al. Generation and characterization of immortalized human microglial cell lines: expression of cytokines and chemokines. Neurobiol Dis 2001;8:1057-1068

46. Nagai A, Mishima S, Ishida Y, et al. Immortalized human microglial cell line: phenotypic expression. J Neurosci Res 2005;81:342-348

47. Xu Q, Qaum T, Adamis AP. Sensitive blood-retinal barrier breakdown quantitation using Evans blue. Invest Ophthalmol Vis Sci 2001;42:789-794

48. Rabascio C, Muratori E, Mancuso P, et al. Assessing tumor angiogenesis: increased circulating VE-cadherin RNA in patients with cancer indicates viability of circulating endothelial cells. Cancer Res 2004;64:4373-4377

49. Bae JS, Lee W, Nam JO, et al. Transforming growth factor beta-induced protein promotes severe vascular inflammatory responses. Am J Respir Crit Care Med 2014;189:779-786

50. Ruoslahti E. RGD and other recognition sequences for integrins. Annu Rev Cell Dev Biol 1996;12:697-715

51. Silva R, D'Amico G, Hodivala-Dilke KM, Reynolds LE. Integrins: the keys to unlocking angiogenesis. Arterioscler Thromb Vasc Biol 2008;28:1703-1713

52. Lee J, Kim KE, Choi DK, et al. Angiopoietin-1 guides directional angiogenesis through integrin alphavbeta5 signaling for recovery of ischemic

retinopathy. Sci Transl Med 2013;5:203ra127

53. Yu H, Pardoll D, Jove R. STATs in cancer inflammation and immunity: a leading role for STAT3. Nat Rev Cancer 2009;9:798-809

54. Lampugnani MG. Endothelial cell-to-cell junctions: adhesion and signaling in physiology and pathology. Cold Spring Harb Perspect Med 2012;2

55. Wang Z, Li R, Tan J, et al. Syndecan-1 Acts in Synergy with Tight Junction Through Stat3 Signaling to Maintain Intestinal Mucosal Barrier and Prevent Bacterial Translocation. Inflamm Bowel Dis 2015;21:1894-1907

56. Jung JE, Lee HG, Cho IH, et al. STAT3 is a potential modulator of HIF-1-mediated VEGF expression in human renal carcinoma cells. FASEB J 2005;19:1296-1298

57. Suganami E, Takagi H, Ohashi H, et al. Leptin stimulates ischemia-induced retinal neovascularization: possible role of vascular endothelial growth factor expressed in retinal endothelial cells. Diabetes 2004;53:2443-2448

58. Xu Q, Briggs J, Park S, et al. Targeting Stat3 blocks both HIF-1 and VEGF expression induced by multiple oncogenic growth signaling pathways. Oncogene 2005;24:5552-5560

59. Wang W, Dentler WL, Borchardt RT. VEGF increases BMEC monolayer permeability by affecting occludin expression and tight junction assembly. Am J Physiol Heart Circ Physiol 2001;280:H434-440

60. Tigges U, Boroujerdi A, Welser-Alves JV, Milner R. TNF-alpha promotes cerebral pericyte remodeling in vitro, via a switch from alpha1 to alpha2

integrins. J Neuroinflammation 2013;10:33

61. Plow EF, Haas TA, Zhang L, Loftus J, Smith JW. Ligand binding to integrins. J Biol Chem 2000;275:21785-21788

62. Watson AR, Pitchford SC, Reynolds LE, et al. Deficiency of bone marrow beta3-integrin enhances non-functional neovascularization. J Pathol 2010;220:435-445

63. Lim Y, Jo DH, Kim JH, et al. Human apolipoprotein(a) kringle V inhibits ischemia-induced retinal neovascularization via suppression of fibronectin-mediated angiogenesis. Diabetes 2012;61:1599-1608

64. Carnevale E, Fogel E, Aplin AC, et al. Regulation of postangiogenic neovessel survival by beta1 and beta3 integrins in collagen and fibrin matrices. J Vasc Res 2007;44:40-50

65. Carlson TR, Feng Y, Maisonpierre PC, Mrksich M, Morla AO. Direct cell adhesion to the angiopoietins mediated by integrins. J Biol Chem 2001;276:26516-26525

66. Hu B, Jarzynka MJ, Guo P, et al. Angiopoietin 2 induces glioma cell invasion by stimulating matrix metalloprotease 2 expression through the alphavbeta1 integrin and focal adhesion kinase signaling pathway. Cancer Res 2006;66:775-783

67. Bezuidenhout L, Zilla P, Davies N. Association of Ang-2 with integrin beta 2 controls Ang-2/PDGF-BB-dependent upregulation of human peripheral blood monocyte fibrinolysis. Inflammation 2009;32:393-401

68. Thomas M, Felcht M, Kruse K, et al. Angiopoietin-2 stimulation of endothelial cells induces alphavbeta3 integrin internalization and degradation.

J Biol Chem 2010;285:23842-23849

69. Gale NW, Thurston G, Hackett SF, et al. Angiopoietin-2 is required for postnatal angiogenesis and lymphatic patterning, and only the latter role is rescued by Angiopoietin-1. Dev Cell 2002;3:411-423

70. Huang YQ, Li JJ, Hu L, Lee M, Karpatkin S. Thrombin induces increased expression and secretion of angiopoietin-2 from human umbilical vein endothelial cells. Blood 2002;99:1646-1650

71. Hackett SF, Wiegand S, Yancopoulos G, Campochiaro PA. Angiopoietin-2 plays an important role in retinal angiogenesis. J Cell Physiol 2002;192:182-187

72. Oh H, Takagi H, Suzuma K, et al. Hypoxia and vascular endothelial growth factor selectively up-regulate angiopoietin-2 in bovine microvascular endothelial cells. J Biol Chem 1999;274:15732-15739

73. Rangasamy S, Srinivasan R, Maestas J, McGuire PG, Das A. A potential role for angiopoietin 2 in the regulation of the blood-retinal barrier in diabetic retinopathy. Invest Ophthalmol Vis Sci 2011;52:3784-3791

74. Fiedler U, Scharpfenecker M, Koidl S, et al. The Tie-2 ligand angiopoietin-2 is stored in and rapidly released upon stimulation from endothelial cell Weibel-Palade bodies. Blood 2004;103:4150-4156

75. Fiedler U, Reiss Y, Scharpfenecker M, et al. Angiopoietin-2 sensitizes endothelial cells to TNF-alpha and has a crucial role in the induction of inflammation. Nat Med 2006;12:235-239

76. Ohashi H, Takagi H, Koyama S, et al. Alterations in expression of angiopoietins and the Tie-2 receptor in the retina of streptozotocin induced

diabetic rats. Mol Vis 2004;10:608-617

77. Group AS, Group AES, Chew EY, et al. Effects of medical therapies on retinopathy progression in type 2 diabetes. N Engl J Med 2010;363:233-244

78. The effect of intensive treatment of diabetes on the development and progression of long-term complications in insulin-dependent diabetes mellitus. The Diabetes Control and Complications Trial Research Group. N Engl J Med 1993;329:977-986

79. Intensive blood-glucose control with sulphonylureas or insulin compared with conventional treatment and risk of complications in patients with type 2 diabetes (UKPDS 33). UK Prospective Diabetes Study (UKPDS) Group. Lancet 1998;352:837-853

80. Shih A, Davis FB, Lin HY, Davis PJ. Resveratrol induces apoptosis in thyroid cancer cell lines via a MAPK- and p53-dependent mechanism. J Clin Endocrinol Metab 2002;87:1223-1232

81. Feit-Leichman RA, Kinouchi R, Takeda M, et al. Vascular damage in a mouse model of diabetic retinopathy: relation to neuronal and glial changes. Invest Ophthalmol Vis Sci 2005;46:4281-4287

82. Fernandez DC, Sande PH, Chianelli MS, Aldana Marcos HJ, Rosenstein RE. Induction of ischemic tolerance protects the retina from diabetic retinopathy. Am J Pathol 2011;178:2264-2274

83. Bringmann A, Pannicke T, Grosche J, et al. Muller cells in the healthy and diseased retina. Prog Retin Eye Res 2006;25:397-424

84. Dorfman D, Aranda ML, Gonzalez Fleitas MF, et al. Environmental enrichment protects the retina from early diabetic damage in adult rats. PLoS

One 2014;9:e101829

85. Cox D, Brennan M, Moran N. Integrins as therapeutic targets: lessons and opportunities. Nat Rev Drug Discov 2010;9:804-820

86. Hynes RO. Integrins: bidirectional, allosteric signaling machines. Cell 2002;110:673-687

87. Milner R, Huang X, Wu J, et al. Distinct roles for astrocyte alphavbeta5 and alphavbeta8 integrins in adhesion and migration. J Cell Sci 1999;112 (Pt 23):4271-4279

88. Ly PT, Wu Y, Zou H, et al. Inhibition of GSK3beta-mediated BACE1 expression reduces Alzheimer-associated phenotypes. J Clin Invest 2013;123:224-235

89. Zhang Y, Welzig CM, Picard KL, et al. Glycogen synthase kinase-3beta inhibition ameliorates cardiac parasympathetic dysfunction in type 1 diabetic Akita mice. Diabetes 2014;63:2097-2113

90. Lee MA, Park GS, Lee HJ, et al. Survivin expression and its clinical significance in pancreatic cancer. BMC Cancer 2005;5:127

91. Junod A, Lambert AE, Stauffacher W, Renold AE. Diabetogenic action of streptozotocin: relationship of dose to metabolic response. J Clin Invest 1969;48:2129-2139

92. Rossini AA, Appel MC, Williams RM, Like AA. Genetic influence of the streptozotocin-induced insulitis and hyperglycemia. Diabetes 1977;26:916-920

93. Barber AJ, Antonetti DA, Kern TS, et al. The Ins2Akita mouse as a model of early retinal complications in diabetes. Invest Ophthalmol Vis Sci

2005;46:2210-2218

94. Yang XP, Irani K, Mattagajasingh S, et al. Signal transducer and activator of transcription 3alpha and specificity protein 1 interact to upregulate intercellular adhesion molecule-1 in ischemic-reperfused myocardium and vascular endothelium. Arterioscler Thromb Vasc Biol 2005;25:1395-1400

95. Bromberg J, Darnell JE, Jr. The role of STATs in transcriptional control and their impact on cellular function. Oncogene 2000;19:2468-2473

96. Izumi-Nagai K, Nagai N, Ozawa Y, et al. Interleukin-6 receptor-mediated activation of signal transducer and activator of transcription-3 (STAT3) promotes choroidal neovascularization. Am J Pathol 2007;170:2149-2158

97. Joussen AM, Murata T, Tsujikawa A, et al. Leukocyte-mediated endothelial cell injury and death in the diabetic retina. Am J Pathol 2001;158:147-152

98. Funatsu H, Yamashita H, Noma H, et al. Increased levels of vascular endothelial growth factor and interleukin-6 in the aqueous humor of diabetics with macular edema. Am J Ophthalmol 2002;133:70-77

99. Rojas M, Zhang W, Lee DL, et al. Role of IL-6 in angiotensin II-induced retinal vascular inflammation. Invest Ophthalmol Vis Sci 2010;51:1709-1718

100. Kowluru RA, Odenbach S. Role of interleukin-1beta in the pathogenesis of diabetic retinopathy. Br J Ophthalmol 2004;88:1343-1347

101. Martin MU, Wesche H. Summary and comparison of the signaling mechanisms of the Toll/interleukin-1 receptor family. Biochim Biophys Acta 2002;1592:265-280

102. Pober JS, Sessa WC. Evolving functions of endothelial cells in

inflammation. Nat Rev Immunol 2007;7:803-815

103. Wung BS, Hsu MC, Wu CC, Hsieh CW. Resveratrol suppresses IL-6-induced ICAM-1 gene expression in endothelial cells: effects on the inhibition of STAT3 phosphorylation. Life Sci 2005;78:389-397

104. Zhang X, Dong H, Zhang S, et al. Enhancement of LPS-induced microglial inflammation response via TLR4 under high glucose conditions. Cell Physiol Biochem 2015;35:1571-1581

105. Aveleira CA, Lin CM, Abcouwer SF, Ambrosio AF, Antonetti DA. TNF-alpha signals through PKCzeta/NF-kappaB to alter the tight junction complex and increase retinal endothelial cell permeability. Diabetes 2010;59:2872-2882

106. Ohno-Matsui K. Parallel findings in age-related macular degeneration and Alzheimer's disease. Prog Retin Eye Res 2011;30:217-238

107. Johnson LV, Leitner WP, Rivest AJ, et al. The Alzheimer's A beta -peptide is deposited at sites of complement activation in pathologic deposits associated with aging and age-related macular degeneration. Proc Natl Acad Sci U S A 2002;99:11830-11835

108. Luibl V, Isas JM, Kayed R, et al. Drusen deposits associated with aging and age-related macular degeneration contain nonfibrillar amyloid oligomers. J Clin Invest 2006;116:378-385

109. Alexandrov PN, Pogue A, Bhattacharjee S, Lukiw WJ. Retinal amyloid peptides and complement factor H in transgenic models of Alzheimer's disease. Neuroreport 2011;22:623-627

110. Dentchev T, Milam AH, Lee VM, Trojanowski JQ, Dunaief JL. Amyloid-

beta is found in drusen from some age-related macular degeneration retinas, but not in drusen from normal retinas. Mol Vis 2003;9:184-190

111. Rosvall L, Rizzuto D, Wang HX, et al. APOE-related mortality: effect of dementia, cardiovascular disease and gender. Neurobiol Aging 2009;30:1545-1551

112. Adams MK, Simpson JA, Richardson AJ, et al. Apolipoprotein E gene associations in age-related macular degeneration: the Melbourne Collaborative Cohort Study. Am J Epidemiol 2012;175:511-518

113. Malek G, Johnson LV, Mace BE, et al. Apolipoprotein E allele-dependent pathogenesis: a model for age-related retinal degeneration. Proc Natl Acad Sci U S A 2005;102:11900-11905

114. Strohmeyer R, Shen Y, Rogers J. Detection of complement alternative pathway mRNA and proteins in the Alzheimer's disease brain. Brain Res Mol Brain Res 2000;81:7-18

115. LaFerla FM, Green KN, Oddo S. Intracellular amyloid-beta in Alzheimer's disease. Nat Rev Neurosci 2007;8:499-509

116. Yoshida T, Ohno-Matsui K, Ichinose S, et al. The potential role of amyloid beta in the pathogenesis of age-related macular degeneration. J Clin Invest 2005;115:2793-2800

117. Bruban J, Glotin AL, Dinet V, et al. Amyloid-beta(1-42) alters structure and function of retinal pigmented epithelial cells. Aging Cell 2009;8:162-177

118. Moon M, Hong HS, Nam DW, et al. Intracellular amyloid-beta accumulation in calcium-binding protein-deficient neurons leads to amyloid-beta plaque formation in animal model of Alzheimer's disease. J Alzheimers

Dis 2012;29:615-628

119. Kook SY, Hong HS, Moon M, et al. Abeta(1)(-)(4)(2)-RAGE interaction disrupts tight junctions of the blood-brain barrier via Ca(2)(+)-calcineurin signaling. J Neurosci 2012;32:8845-8854

120. Ning A, Cui J, To E, Ashe KH, Matsubara J. Amyloid-beta deposits lead to retinal degeneration in a mouse model of Alzheimer disease. Invest Ophthalmol Vis Sci 2008;49:5136-5143

121. Jager RD, Mieler WF, Miller JW. Age-related macular degeneration. N Engl J Med 2008;358:2606-2617

122. Lambert V, Lecomte J, Hansen S, et al. Laser-induced choroidal neovascularization model to study age-related macular degeneration in mice. Nat Protoc 2013;8:2197-2211

123. Pennesi ME, Neuringer M, Courtney RJ. Animal models of age related macular degeneration. Mol Aspects Med 2012;33:487-509

124. Ramkumar HL, Zhang J, Chan CC. Retinal ultrastructure of murine models of dry age-related macular degeneration (AMD). Prog Retin Eye Res 2010;29:169-190

125. Wirths O, Bayer TA. Intraneuronal Abeta accumulation and neurodegeneration: lessons from transgenic models. Life Sci 2012;91:1148-1152

126. Chaney MO, Stine WB, Kokjohn TA, et al. RAGE and amyloid beta interactions: atomic force microscopy and molecular modeling. Biochim Biophys Acta 2005;1741:199-205

127. Howes KA, Liu Y, Dunaief JL, et al. Receptor for advanced glycation

end products and age-related macular degeneration. Invest Ophthalmol Vis Sci 2004;45:3713-3720

128. Yamada Y, Ishibashi K, Ishibashi K, et al. The expression of advanced glycation endproduct receptors in rpe cells associated with basal deposits in human maculas. Exp Eye Res 2006;82:840-848

129. Mackic JB, Stins M, McComb JG, et al. Human blood-brain barrier receptors for Alzheimer's amyloid-beta 1- 40. Asymmetrical binding, endocytosis, and transcytosis at the apical side of brain microvascular endothelial cell monolayer. J Clin Invest 1998;102:734-743

130. Deane R, Du Yan S, Submamaryan RK, et al. RAGE mediates amyloid-beta peptide transport across the blood-brain barrier and accumulation in brain. Nat Med 2003;9:907-913

131. Takuma K, Fang F, Zhang W, et al. RAGE-mediated signaling contributes to intraneuronal transport of amyloid-beta and neuronal dysfunction. Proc Natl Acad Sci U S A 2009;106:20021-20026

132. Deane R, Singh I, Sagare AP, et al. A multimodal RAGE-specific inhibitor reduces amyloid beta-mediated brain disorder in a mouse model of Alzheimer disease. J Clin Invest 2012;122:1377-1392

133. Galasko D, Bell J, Mancuso JY, et al. Clinical trial of an inhibitor of RAGE-Abeta interactions in Alzheimer disease. Neurology 2014;82:1536-1542

134. Oakley H, Cole SL, Logan S, et al. Intraneuronal beta-amyloid aggregates, neurodegeneration, and neuron loss in transgenic mice with five familial Alzheimer's disease mutations: potential factors in amyloid plaque

formation. J Neurosci 2006;26:10129-10140

135. Gimenez E, Montoliu L. A simple polymerase chain reaction assay for genotyping the retinal degeneration mutation (Pdeb(rd1)) in FVB/N-derived transgenic mice. Lab Anim 2001;35:153-156

136. Mitter SK, Song C, Qi X, et al. Dysregulated autophagy in the RPE is associated with increased susceptibility to oxidative stress and AMD. Autophagy 2014;10:1989-2005

137. Dithmar S, Curcio CA, Le NA, Brown S, Grossniklaus HE. Ultrastructural changes in Bruch's membrane of apolipoprotein E-deficient mice. Invest Ophthalmol Vis Sci 2000;41:2035-2042

138. Huang da W, Sherman BT, Lempicki RA. Systematic and integrative analysis of large gene lists using DAVID bioinformatics resources. Nat Protoc 2009;4:44-57

139. Park SW, Kim JH, Park WJ, Kim JH. Limbal Approach-Subretinal Injection of Viral Vectors for Gene Therapy in Mice Retinal Pigment Epithelium. J Vis Exp 2015:e53030

140. Finnemann SC, Bonilha VL, Marmorstein AD, Rodriguez-Boulan E. Phagocytosis of rod outer segments by retinal pigment epithelial cells requires alpha(v)beta5 integrin for binding but not for internalization. Proc Natl Acad Sci U S A 1997;94:12932-12937

141. Nishiyama K, Sakaguchi H, Hu JG, Bok D, Hollyfield JG. Claudin localization in cilia of the retinal pigment epithelium. Anat Rec 2002;267:196-203

142. Sun H, Gilbert DJ, Copeland NG, Jenkins NA, Nathans J. Peropsin, a

novel visual pigment-like protein located in the apical microvilli of the retinal pigment epithelium. Proc Natl Acad Sci U S A 1997;94:9893-9898

143. Chowers I, Kim Y, Farkas RH, et al. Changes in retinal pigment epithelial gene expression induced by rod outer segment uptake. Invest Ophthalmol Vis Sci 2004;45:2098-2106

144. Edwards RL, Rickles FR, Bobrove AM. Mononuclear cell tissue factor: cell of origin and requirements for activation. Blood 1979;54:359-370

145. Hsu SL, Lin YF, Chou CK. Transcriptional regulation of transferrin and albumin genes by retinoic acid in human hepatoma cell line Hep3B. Biochem J 1992;283 (Pt 2):611-615

146. Ambati J, Anand A, Fernandez S, et al. An animal model of age-related macular degeneration in senescent Ccl-2- or Ccr-2-deficient mice. Nat Med 2003;9:1390-1397

147. Nikopoulos K, Avila-Fernandez A, Corton M, et al. Identification of two novel mutations in CDHR1 in consanguineous Spanish families with autosomal recessive retinal dystrophy. Sci Rep 2015;5:13902

148. Lang D, Knop J, Wesche H, et al. The type II IL-1 receptor interacts with the IL-1 receptor accessory protein: a novel mechanism of regulation of IL-1 responsiveness. J Immunol 1998;161:6871-6877

149. Emery M, Schorderet DF, Roduit R. Acute hypoglycemia induces retinal cell death in mouse. PLoS One 2011;6:e21586

150. Yang WJ, Hu J, Uemura A, et al. Semaphorin-3C signals through Neuropilin-1 and PlexinD1 receptors to inhibit pathological angiogenesis. EMBO Mol Med 2015;7:1267-1284

151. Chen X, Walker DG, Schmidt AM, et al. RAGE: a potential target for Abeta-mediated cellular perturbation in Alzheimer's disease. Curr Mol Med 2007;7:735-742

152. Proitsi P, Lupton MK, Dudbridge F, et al. Alzheimer's disease and age-related macular degeneration have different genetic models for complement gene variation. Neurobiol Aging 2012;33:1843 e1849-1817

153. Jawhar S, Trawicka A, Jenneckens C, Bayer TA, Wirths O. Motor deficits, neuron loss, and reduced anxiety coinciding with axonal degeneration and intraneuronal Abeta aggregation in the 5XFAD mouse model of Alzheimer's disease. Neurobiol Aging 2012;33:196 e129-140

154. Omtri RS, Davidson MW, Arumugam B, Poduslo JF, Kandimalla KK. Differences in the cellular uptake and intracellular itineraries of amyloid beta proteins 40 and 42: ramifications for the Alzheimer's drug discovery. Mol Pharm 2012;9:1887-1897

155. Neeper M, Schmidt AM, Brett J, et al. Cloning and expression of a cell surface receptor for advanced glycosylation end products of proteins. J Biol Chem 1992;267:14998-15004

156. Schmidt AM, Yan SD, Yan SF, Stern DM. The multiligand receptor RAGE as a progression factor amplifying immune and inflammatory responses. J Clin Invest 2001;108:949-955

157. Zhou J, Cai B, Jang YP, et al. Mechanisms for the induction of HNE-MDA- and AGE-adducts, RAGE and VEGF in retinal pigment epithelial cells. Exp Eye Res 2005;80:567-580

158. Lue LF, Walker DG, Brachova L, et al. Involvement of microglial

receptor for advanced glycation endproducts (RAGE) in Alzheimer's disease: identification of a cellular activation mechanism. Exp Neurol 2001;171:29-45

159. Tai LM, Holloway KA, Male DK, Loughlin AJ, Romero IA. Amyloid-beta-induced occludin down-regulation and increased permeability in human brain endothelial cells is mediated by MAPK activation. J Cell Mol Med 2010;14:1101-1112

160. Ding JD, Johnson LV, Herrmann R, et al. Anti-amyloid therapy protects against retinal pigmented epithelium damage and vision loss in a model of age-related macular degeneration. Proc Natl Acad Sci U S A 2011;108:E279-287

161. Rakoczy PE, Zhang D, Robertson T, et al. Progressive age-related changes similar to age-related macular degeneration in a transgenic mouse model. Am J Pathol 2002;161:1515-1524

162. Toomey CB, Kelly U, Saban DR, Bowes Rickman C. Regulation of age-related macular degeneration-like pathology by complement factor H. Proc Natl Acad Sci U S A 2015;112:E3040-3049

163. Klein RJ, Zeiss C, Chew EY, et al. Complement factor H polymorphism in age-related macular degeneration. Science 2005;308:385-389

164. Edwards AO, Ritter R, 3rd, Abel KJ, et al. Complement factor H polymorphism and age-related macular degeneration. Science 2005;308:421-424

165. Ding JD, Kelly U, Landowski M, et al. Expression of human complement factor H prevents age-related macular degeneration-like retina damage and kidney abnormalities in aged Cfh knockout mice. Am J Pathol

2015;185:29-42

166. Anderson DH, Talaga KC, Rivest AJ, et al. Characterization of beta amyloid assemblies in drusen: the deposits associated with aging and age-related macular degeneration. Exp Eye Res 2004;78:243-256

167. Mayerson PL, Hall MO. Rat retinal pigment epithelial cells show specificity of phagocytosis in vitro. J Cell Biol 1986;103:299-308

168. More SS, Vince R. Hyperspectral imaging signatures detect amyloidopathy in Alzheimer's mouse retina well before onset of cognitive decline. ACS Chem Neurosci 2015;6:306-315

169. Nagele RG, D'Andrea MR, Anderson WJ, Wang HY. Intracellular accumulation of beta-amyloid(1-42) in neurons is facilitated by the alpha 7 nicotinic acetylcholine receptor in Alzheimer's disease. Neuroscience 2002;110:199-211

170. Bi X, Gall CM, Zhou J, Lynch G. Uptake and pathogenic effects of amyloid beta peptide 1-42 are enhanced by integrin antagonists and blocked by NMDA receptor antagonists. Neuroscience 2002;112:827-840

171. Deane R, Wu Z, Sagare A, et al. LRP/amyloid beta-peptide interaction mediates differential brain efflux of Abeta isoforms. Neuron 2004;43:333-344

172. Glenn JV, Stitt AW. The role of advanced glycation end products in retinal ageing and disease. Biochim Biophys Acta 2009;1790:1109-1116

173. Dahrouj M, Alsarraf O, Liu Y, Crosson CE, Ablonczy Z. C-type natriuretic peptide protects the retinal pigment epithelium against advanced glycation end product-induced barrier dysfunction. J Pharmacol Exp Ther 2013;344:96-102

174. Siddiqui SS, Siddiqui ZK, Uddin S, Minshall RD, Malik AB. p38 MAPK activation coupled to endocytosis is a determinant of endothelial monolayer integrity. Am J Physiol Lung Cell Mol Physiol 2007;292:L114-124

175. Ablonczy Z, Dahrouj M, Tang PH, et al. Human retinal pigment epithelium cells as functional models for the RPE in vivo. Invest Ophthalmol Vis Sci 2011;52:8614-8620

176. Leung DW, Cachianes G, Kuang WJ, Goeddel DV, Ferrara N. Vascular endothelial growth factor is a secreted angiogenic mitogen. Science 1989;246:1306-1309

177. Group CR, Martin DF, Maguire MG, et al. Ranibizumab and bevacizumab for neovascular age-related macular degeneration. N Engl J Med 2011;364:1897-1908

178. Schmidt-Erfurth U, Kaiser PK, Korobelnik JF, et al. Intravitreal aflibercept injection for neovascular age-related macular degeneration: ninety-six-week results of the VIEW studies. Ophthalmology 2014;121:193-201

179. Woo JW, Kim J, Kwon SI, et al. DNA-free genome editing in plants with preassembled CRISPR-Cas9 ribonucleoproteins. Nat Biotechnol 2015;33:1162-1164

180. Zuris JA, Thompson DB, Shu Y, et al. Cationic lipid-mediated delivery of proteins enables efficient protein-based genome editing in vitro and in vivo. Nat Biotechnol 2015;33:73-80

181. Kim S, Kim D, Cho SW, Kim J, Kim JS. Highly efficient RNA-guided genome editing in human cells via delivery of purified Cas9 ribonucleoproteins. Genome Res 2014;24:1012-1019

182. Maeder ML, Gersbach CA. Genome-editing Technologies for Gene and Cell Therapy. Mol Ther 2016;

183. Yin H, Xue W, Chen S, et al. Genome editing with Cas9 in adult mice corrects a disease mutation and phenotype. Nat Biotechnol 2014;32:551-553

184. Ran FA, Cong L, Yan WX, et al. In vivo genome editing using Staphylococcus aureus Cas9. Nature 2015;520:186-191

185. Nelson CE, Hakim CH, Ousterout DG, et al. In vivo genome editing improves muscle function in a mouse model of Duchenne muscular dystrophy. Science 2016;351:403-407

186. Long C, Amoasii L, Mireault AA, et al. Postnatal genome editing partially restores dystrophin expression in a mouse model of muscular dystrophy. Science 2016;351:400-403

187. Tabebordbar M, Zhu K, Cheng JK, et al. In vivo gene editing in dystrophic mouse muscle and muscle stem cells. Science 2016;351:407-411

188. Calcedo R, Franco J, Qin Q, et al. Preexisting Neutralizing Antibodies to Adeno-Associated Virus Capsids in Large Animals Other Than Monkeys May Confound In Vivo Gene Therapy Studies. Hum Gene Ther Methods 2015;26:103-105

189. Shankar G, Pendley C, Stein KE. A risk-based bioanalytical strategy for the assessment of antibody immune responses against biological drugs. Nat Biotechnol 2007;25:555-561

190. Chew WL, Tabebordbar M, Cheng JK, et al. A multifunctional AAV-CRISPR-Cas9 and its host response. Nat Methods 2016;13:868-874

191. Schumann K, Lin S, Boyer E, et al. Generation of knock-in primary

human T cells using Cas9 ribonucleoproteins. Proc Natl Acad Sci U S A 2015;112:10437-10442

192. Kim H, Kim JS. A guide to genome engineering with programmable nucleases. Nat Rev Genet 2014;15:321-334

193. Jinek M, Chylinski K, Fonfara I, et al. A programmable dual-RNA-guided DNA endonuclease in adaptive bacterial immunity. Science 2012;337:816-821

194. Cho SW, Kim S, Kim JM, Kim JS. Targeted genome engineering in human cells with the Cas9 RNA-guided endonuclease. Nat Biotechnol 2013;31:230-232

195. Cho SW, Lee J, Carroll D, Kim JS, Lee J. Heritable gene knockout in Caenorhabditis elegans by direct injection of Cas9-sgRNA ribonucleoproteins. Genetics 2013;195:1177-1180

196. Mali P, Yang L, Esvelt KM, et al. RNA-guided human genome engineering via Cas9. Science 2013;339:823-826

197. Cong L, Ran FA, Cox D, et al. Multiplex genome engineering using CRISPR/Cas systems. Science 2013;339:819-823

198. Wang H, Yang H, Shivalila CS, et al. One-step generation of mice carrying mutations in multiple genes by CRISPR/Cas-mediated genome engineering. Cell 2013;153:910-918

199. Sung YH, Kim JM, Kim HT, et al. Highly efficient gene knockout in mice and zebrafish with RNA-guided endonucleases. Genome Res 2014;24:125-131

200. Jinek M, East A, Cheng A, et al. RNA-programmed genome editing in

human cells. Elife 2013;2:e00471

201. Wu Z, Yang H, Colosi P. Effect of genome size on AAV vector packaging. Mol Ther 2010;18:80-86

202. Swiech L, Heidenreich M, Banerjee A, et al. In vivo interrogation of gene function in the mammalian brain using CRISPR-Cas9. Nat Biotechnol 2015;33:102-106

203. Wright AV, Sternberg SH, Taylor DW, et al. Rational design of a split-Cas9 enzyme complex. Proc Natl Acad Sci U S A 2015;112:2984-2989

204. Zetsche B, Volz SE, Zhang F. A split-Cas9 architecture for inducible genome editing and transcription modulation. Nat Biotechnol 2015;33:139-142

205. Chew WL, Tabebordbar M, Cheng JK, et al. A multifunctional AAV-CRISPR-Cas9 and its host response. Nat Methods 2016;

206. Truong DJ, Kuhner K, Kuhn R, et al. Development of an intein-mediated split-Cas9 system for gene therapy. Nucleic Acids Res 2015;43:6450-6458

207. Kim D, Bae S, Park J, et al. Digenome-seq: genome-wide profiling of CRISPR-Cas9 off-target effects in human cells. Nat Methods 2015;12:237-243, 231 p following 243

208. Kim D, Kim S, Kim S, Park J, Kim JS. Genome-wide target specificities of CRISPR-Cas9 nucleases revealed by multiplex Digenome-seq. Genome Res 2016;

209. Fernandez-Godino R, Garland DL, Pierce EA. Isolation, culture and characterization of primary mouse RPE cells. Nat Protoc 2016;11:1206-1218

210. Kim H, Um E, Cho SR, Jung C, Kim JS. Surrogate reporters for

enrichment of cells with nuclease-induced mutations. Nat Methods 2011;8:941-943

211. Kim D, Kim J, Hur JK, et al. Genome-wide analysis reveals specificities of Cpf1 endonucleases in human cells. Nat Biotechnol 2016;

212. Raczy C, Petrovski R, Saunders CT, et al. Isaac: ultra-fast whole-genome secondary analysis on Illumina sequencing platforms. Bioinformatics 2013;29:2041-2043

213. Wei H, Xun Z, Granado H, Wu A, Handa JT. An easy, rapid method to isolate RPE cell protein from the mouse eye. Exp Eye Res 2016;145:450-455

214. Gresh J, Goletz PW, Crouch RK, Rohrer B. Structure-function analysis of rods and cones in juvenile, adult, and aged C57bl/6 and Balb/c mice. Vis Neurosci 2003;20:211-220

215. Park J, Bae S, Kim JS. Cas-Designer: a web-based tool for choice of CRISPR-Cas9 target sites. Bioinformatics 2015;31:4014-4016

216. Bae S, Park J, Kim JS. Cas-OFFinder: a fast and versatile algorithm that searches for potential off-target sites of Cas9 RNA-guided endonucleases. Bioinformatics 2014;30:1473-1475

217. Deng W, Shi X, Tjian R, Lionnet T, Singer RH. CASFISH: CRISPR/Cas9-mediated in situ labeling of genomic loci in fixed cells. Proc Natl Acad Sci U S A 2015;112:11870-11875

218. Krzywinski M, Schein J, Birol I, et al. Circos: an information aesthetic for comparative genomics. Genome Res 2009;19:1639-1645

219. Zetsche B, Gootenberg JS, Abudayyeh OO, et al. Cpf1 is a single RNA-guided endonuclease of a class 2 CRISPR-Cas system. Cell 2015;163:759-771

220. Kim D, Kim J, Hur JK, et al. Genome-wide analysis reveals specificities of Cpf1 endonucleases in human cells. Nat Biotechnol 2016;34:863-868

221. Kleinstiver BP, Pattanayak V, Prew MS, et al. High-fidelity CRISPR-Cas9 nucleases with no detectable genome-wide off-target effects. Nature 2016;529:490-495

222. Slaymaker IM, Gao L, Zetsche B, et al. Rationally engineered Cas9 nucleases with improved specificity. Science 2016;351:84-88

223. Fu Y, Sander JD, Reyon D, Cascio VM, Joung JK. Improving CRISPR-Cas nuclease specificity using truncated guide RNAs. Nat Biotechnol 2014;32:279-284

224. Cho SW, Kim S, Kim Y, et al. Analysis of off-target effects of CRISPR/Cas-derived RNA-guided endonucleases and nickases. Genome Res 2014;24:132-141

225. Kurihara T, Westenskow PD, Bravo S, Aguilar E, Friedlander M. Targeted deletion of Vegfa in adult mice induces vision loss. J Clin Invest 2012;122:4213-4217

226. Fonfara I, Le Rhun A, Chylinski K, et al. Phylogeny of Cas9 determines functional exchangeability of dual-RNA and Cas9 among orthologous type II CRISPR-Cas systems. Nucleic Acids Res 2013;

227. Hur JK, Kim K, Been KW, et al. Targeted mutagenesis in mice by electroporation of Cpf1 ribonucleoproteins. Nat Biotechnol 2016;

228. Kleinstiver BP, Tsai SQ, Prew MS, et al. Genome-wide specificities of CRISPR-Cas Cpf1 nucleases in human cells. Nat Biotechnol 2016;34:869-874

229. Bae S, Park J, Kim JS. Cas-OFFinder: A fast and versatile algorithm that

searches for potential off-target sites of Cas9 RNA-guided endonucleases. bioinformatics 2014;

230. Wu Z, Asokan A, Samulski RJ. Adeno-associated virus serotypes: vector toolkit for human gene therapy. Mol Ther 2006;14:316-327

231. Kwak N, Okamoto N, Wood JM, Campochiaro PA. VEGF is major stimulator in model of choroidal neovascularization. Invest Ophthalmol Vis Sci 2000;41:3158-3164

232. Andre H, Tunik S, Aronsson M, Kvanta A. Hypoxia-Inducible Factor-1alpha Is Associated With Sprouting Angiogenesis in the Murine Laser-Induced Choroidal Neovascularization Model. Invest Ophthalmol Vis Sci 2015;56:6591-6604

233. Esvelt KM, Mali P, Braff JL, et al. Orthogonal Cas9 proteins for RNA-guided gene regulation and editing. Nat Methods 2013;10:1116-1121

234. Anders C, Niewoehner O, Duerst A, Jinek M. Structural basis of PAM-dependent target DNA recognition by the Cas9 endonuclease. Nature 2014;513:569-573

235. Nishimasu H, Cong L, Yan WX, et al. Crystal Structure of Staphylococcus aureus Cas9. Cell 2015;162:1113-1126

236. Forsythe JA, Jiang BH, Iyer NV, et al. Activation of vascular endothelial growth factor gene transcription by hypoxia-inducible factor 1. Mol Cell Biol 1996;16:4604-4613

국문 초록

서론: 당뇨망막병증과 노인성 황반변성은 대표적인 실명을 일으키는 안과 질환이다. 당뇨망막병증에서는 황반부종(혈관 누출)과 혈관신생(혈관형성)이 시력 저하의 주요 원인이다. 혈관신생은 당뇨망막병증의 후기 단계에서 주로 심각한 시력 저하를 초래하지만 황반부종은 당뇨망막병증의 어느 단계에서나 발생하여 시력 저하를 일으킬 수 있다. 노인성 황반변성은 크게 건성 노인성 황반변성과 습성 노인성 황반변성으로 나뉜다. 습성 노인성 황반변성에서는 맥락막 혈관신생이 황반부에 발생하여 망막을 손상시킨다. 건성 노인성 황반변성은 드루젠과 망막색소상피세포의 위축이 특징적이다.

당뇨망막병증의 치료를 위해서, 내측 혈액망막장벽의 3 가지 세포구성요소인 혈관내피세포, 혈관주변세포, 성상세포를 중심으로 연구하였다. 특히, 당뇨망막병증에서 안지오포이에틴 2 가 혈관주변세포 소실과 성상세포 소실에 미치는 기전에 대해서 연구를 하였다.

습성 노인성 황반변성 연구를 위해서 레이저유발 맥락막 혈관신생 동물 모델이 널리 이용되었지만, 건성 노인성 황반변성을 완벽하게 모사하는 생쥐모델은 아직까지 확립되어 있지 않다. 이에 5XFAD 생쥐와 아밀로이드 베타 주사 생쥐를 이용하여 아밀로이드 베타와

관련된 건성 노인성 황반변성의 질병 기전을 연구하였다. 특히, 아밀로이드 베타의 세포내 이동과 세포내 아밀로이드 베타의 자가포식현상 장애 기전이 건성 노인성 황반변성의 질병 기전에 미치는 영향에 대해 연구하였다.

습성 노인성 황반변성은 망막에서 혈관내피성장인자 유전자의 과발현과 관련이 있다. 크리스퍼-Cas9 뉴클라아제를 이용한 RNA 유도 유전자 수술은 다양한 유전성 질환의 치료를 위해 연구되고 있다. 하지만, 아직까지 크리스퍼-Cas9 뉴클라아제의 비유전성 질환에서의 적용은 거의 연구되지 않고 있다. 본 연구에서 2 가지 형태의 유전자 가위(Cas9 단백질핵산복합체와 가장 작은 Cas9 상동체인 캄필로박터 제주니 유래 Cas9)를 이용하여 망막색소상피세포 내의 혈관내피성장인자 유전자와 저산소유도인자 1a 유전자의 교정의 치료효과에 대해 연구하였다.

방법: 생체 실험으로는 당뇨망막병증 연구를 위해 스트렙토조토신 유발 당뇨생쥐, 건성 노인성 황반변성 연구를 위해 5XFAD 생쥐와 아밀로이드 베타 주사 생쥐, 습성 노인성 황반변성 연구를 위해 레이저 유발 맥락막 혈관신생 생쥐 모델을 이용하였다. 생체 외 실험으로는 세포 활성 측정, 웨스턴 블롯팅, 중합효소 연쇄 반응, 유세포 분석, 면역형광염색, 효소결합면역흡착측정법, 차세대 염기서열분석법, 절단 유전체 시퀀싱 기법 등을 이용하였다.

결과: 안지오포이에틴 2 는 고혈당 조건에서 인테그린 α3β1/p53 신호전달을 통해서 혈관주위세포의 세포사멸을 유발하였다. 또한, 안지오포이에틴 2 는 고혈당 조건에서 인테그린 αvβ5/GSK3β/β-카테닌 신호전달을 통해서 성상세포의 세포사멸을 유발하였다. 그리고 소교세포 유래 인터루킨 6 은 혈관내피세포에서 STAT3 신호전달을 통해 치밀이음부 단백을 줄임으로써 혈관 누출을 일으켰다.

세포 내 아밀로이드 베타는 5XFAD 생쥐에서의 건성 노인성 황반변성 병리에 기여하였다. 최종당화산물 수용체 매개 p38 MAPK 신호전달은 망막색소상피세포에서 아밀로이드 베타의 세포 내 이동에 관여하였다. 또한, 세포 내 아밀로이드 베타는 치밀이음부의 손상을 유발하였으며, 특히 리소좀 기능 장애에 의한 자가포식현상의 장애를 유발하였다.

Cas9 핵산단백복합체 와 캄필로박터 제주니 유래 Cas9 을 이용하여 망막색소상피세포에서 생체 내 유전자 교정을 효과적으로 달성하였다. 2 가지 방법 모두 습성 노인성 황반변성의 생쥐 모델인 레이저 유발 맥락막 혈관신생의 크기를 효과적으로 줄였다. 절단 유전체 시퀀싱 기법을 이용한 유전체 전장 분석에서 오프 타겟 변이는 관찰되지 않았다.

결론: 안지오포이에틴 2/인테그린 신호전달은 당뇨망막병증에서 혈관주위세포 소실과 성상아교세포 소실에 의한 혈관 누출을

예방하기 위한 치료제 개발에 이용될 수 있다. 또한, 인터루킨 6/STAT3 신호 전달은 당뇨망막병증 혈관 누출을 막기 위한 또 다른 치료제 개발에 이용될 수 있다. 세포 내 아밀로이드 베타는 건성 노인성 황반변성의 질병 기전에 기여한다. 따라서, 5XFAD 생쥐는 건성 노인성 황반변성에 이용될 수 있으며, 아밀로이드 베타를 조절하거나 자가포식현상을 조절하는 것은 건성 노인성 황반변성 치료의 새로운 접근법이 될 수 있다. Cas9 핵산단백복합체나 캄필로박터제주니 유래 Cas9 을 이용한 생체 내 유전자 교정은 습성 노인성 황반변성 치료를 위한 국소 치료제로 이용될 수 있다. 이는 유전자 수술을 유전성 질환뿐 아니라, 비유전성 질환까지 확대 적용할 수 있는 의미가 있다.

* 본 학위 논문은 Diabetes 학술지(1), Cell Death and Disease 학술지(2) , Journal of Cellular Physiology 학술지(3), Neurobiology of Aging 학술지(4), Oncotarget 학술지(5, 6), Genome Research 학술지(7), Nature Communications 학술지(8)에 출판 완료된 내용을 기반으로 작성됨.

주요어 : 망막혈액장벽, 망막, 노인성 황반변성, 당뇨망막병증, 당뇨망막병증 황반부종, 혈관주위세포 소실, 혈관누출, 혈관신생, 항체, 유전자 교정, 유전자치료

학 번 : 2012-31158